SAPIENZA
UNIVERSITÀ DI ROMA

Department of Mechanical and Aerospace Engineering
PhD in Aeronautical and Space Engineering

PhD Thesis

Characterization of the behavior of cryogenic propellants in tanks

Supervisor
Prof. Matteo Bernardini

Co-supervisor
Eng. Marco Pizzarelli

Candidate
Francesca Rossetti

Academic Year 2022-2023 (XXXVI cycle)

Abstract

With the introduction of cryogenic propellant combinations for space engines, there has been an increasing interest in the study of the behavior of the propellant in the tanks in which it is stored. This study can be carried out in two ways. The first approach involves both the dynamic behavior of the propellant, i.e. the sloshing analysis, and the thermo-fluid-dynamics behavior, which are analyzed as coupled phenomena. Conversely, in the second approach, the two phenomena are studied separately. In this thesis, the second approach has been used, and only the thermo-fluid-dynamics characterization of the behavior of cryogenic propellant in tanks has been carried out, since a consolidated reduced order activity on the sloshing analysis is already present in the literature.

Cryogenic propellants, having a very low boiling point, are subject to phase transitions even when exposed to very low heat leaks. As a result, the pressure raises inside a closed non-venting tank. Moreover, the tanks, especially those belonging to the upper stages of space launchers, are subjected to time-varying heat leaks and gravity levels during their operating life. The thermo-fluid-dynamics characterization mainly aims at estimating the evolutions of tank pressure, of the local fluid temperatures, of the phase change rate, and of the propellant location (in the case of reduced gravity). All these analyses, are necessary in order to guarantee the reliability and safety of a tank operation (feed turbopumps with propellant at appropriate temperature and pressure conditions, guarantee that only liquid drains from the tank outlet, ensure that only vapor comes out of the venting valve, etc.).

Due to the cost and complexity associated with the experiments, numerical tools of various levels of complexity have been implemented over the years to carry out the thermo-fluid-dynamics characterization. The first approach is characterized by the use of reduced order models. The latter allow quick estimates of the main observables, and, therefore, represent an engineering tool necessary in the case when a large number of parametric analyses has to be carried out, as in an industrial design process. The second approach involves Computational Fluid Dynamics (CFD) simulations. These last allow to perform more accurate analyses than the previous approach, and to study the complex physical phenomena at play. However, the drawback of CFD simulations is the elevated computational cost with respect to the reduced order models.

The aim of this study is twofold. On the one hand, a suitable zero-dimensional model has been developed, implemented in Matlab, and successfully verified through the comparison with the results of a one-dimensional code developed by NASA (see Chap. 2). Later, it has been used to simulate two tank characteristic operating conditions, for which experimental data were also available. A ground-based self-pressurization experiment in a small-scale liquid N_2 tank (see Chap. 4) and a ground-based active-pressurization experiment in a different small-scale liquid N_2 tank (see Chap. 5). On the other hand, the aim of the study has been the development of a state-of-the-art CFD methodology (see Chap. 3), capable of estimating the main thermo-fluid-dynamics observables, and to study the main physical phenomena at play inside tanks of various species of cryogenic propellant, and characterized by different operating conditions. The proposed methodology has been successfully validated through the comparison with the experimental data of three benchmark test cases, characterized by different propellants, geometries, and operating conditions. This has been done in order to develop a computational tool which guarantees reliability during most of the operating life of the tank. Moreover, for the various validation test cases, different physical and

numerical models and parameters have been tested, in order to find the ones which allow the best reproduction of a particular operating condition, as well as the optimal parameters in terms of the trade-off between accuracy and computational time. The three validation test cases which have been simulated are:

- A ground-based liquid N_2 self-pressurization test case, inside a small-scale tank (see Chap. 4).
- A ground-based liquid N_2 active-pressurization test case, inside a small-scale tank (see Chap. 5).
- A self-pressurization test case carried out in the liquid H_2 tank of the second stage of the Saturn IB AS-203 vehicle, while it was into circular low Earth orbit (see Chap. 6).

Then, the validated CFD methodology has been used to carry out a parametric study on the gravity level. In particular, four gravity levels, from normal gravity ($g_E = 9.81$ m/s^2) until the reduced gravity of $10^{-3} g_E$, have been considered. This study has been performed using the same geometry, fluid, and operating conditions of the first validation test case. The parametric study has allowed to see the effect of the gravity level on the pressurization behavior, phase change, and liquid-ullage interface shape.

Finally, the developed, and repeatedly validated zero-dimensional model and CFD methodology have demonstrated to allow to perform, with a different level of detail, the thermo-fluid-dynamics characterization of the behavior of cryogenic propellant, under most of the operating conditions of interest for tank design. Nevertheless, the operating conditions considered in the present thesis do not involve the case of fluid with sloshing. In order to carry out a more comprehensive study of the actual behaviour of cryogenic propellant in tanks, the sloshing phenomenon should be included in future work. Indeed, sloshing happens very often in cryogenic propellant tanks and, although being a mainly dynamic in nature process, it has a strong influence on the propellant thermal physical phenomena.

Contents

List of Figures

List of Tables

Nomenclature

Greek letters

α	volume fraction or thermal diffusivity
β	thermal expansion coefficient
γ	convection heat transfer coefficient
δ_s	Dirac delta function
Δx	thickness of each interface layer
ε	dissipation rate of turbulence kinetic energy
λ	thermal conductivity
μ	dynamic viscosity
μ_t	eddy dynamic viscosity
ν	kinematic viscosity
ν_t	eddy kinematic viscosity
ρ	density
$\bar{\rho}\tau_{ij}^R$	Favre-averaged Reynolds Stress Tensor
σ	surface tension
ω	specific dissipation rate of turbulence kinetic energy

Roman letters

a	sound speed
$\widetilde{a_{ij}}$	anisotropy tensor
Bo	Bond number
c	specific heat
C_0	empirical constant in the curve-fit equation used for the surface tension of a pure substance
C_1	empirical constant in the curve-fit equation used for the surface tension of a pure substance
c_p	specific heat at constant pressure
c_v	specific heat at constant volume
D	tank inner diameter

e	specific internal energy
E	specific total energy
$E_{r\%}$	percentage error
$\boldsymbol{F_{vol}}$	surface tension force
g	gravity level
$\boldsymbol{g}$	gravity vector
g_E	normal gravity
Gr	Grashof number
h	specific enthalpy
h_{lv}	latent heat of evaporation
H	tank inner height
$\mathcal{H}(x)$	Heaviside step function
H_l	liquid height
H_v	ullage height
J	mass flow rate
k	turbulence kinetic energy
κ	surface curvature
κ_T	isothermal compressibility
L	reference length
m	mass
M	molar mass
M_t	turbulent Mach number
$\dot{m}_{lv}$	volumetric mass source due to evaporation
$\dot{m}_{vl}$	volumetric mass source due to condensation
n	number of interface layers or number of moles
$\hat{\boldsymbol{n}}$	surface unit normal
p	pressure
Pr	Prandtl number
$\boldsymbol{q}$	heat flux vector
$\dot{Q}$	heat transfer rate
r	mass transfer intensity factor
R	tank inner radius or specific gas constant

Ra Rayleigh number

Ra^* modified Rayleigh number

Re Reynolds number

R_u universal gas constant

$\widetilde{S_{ij}}$ Favre-mean strane rate tensor

S_h volumetric heat source due to phase change

t time or thickness

T temperature

v velocity magnitude or specific volume

$\boldsymbol{v}$ velocity vector

$\widetilde{v}$ Favre-averaged velocity

V volume

$\dot{W}$ power associated to the change in volume of the liquid or ullage control volume

X molar fraction

Y mass fraction

Subscripts

$bott$ bottom internal surface of the tank

c critical state

CV control volume

eff effective

f film, i.e. interface between liquid and ullage

g gas

ge exchanged between the gas and the external

l liquid

lat lateral internal surface of the tank

le exchanged between the liquid and the external

lid lid

lv from liquid to vapor or at liquid/vapor interface

mix mixture made by the vapor and the gas contained in the ullage

$press$ active-pressurization phase

s saturation condition

top top internal surface of the tank

u ullage

v vapor

ve exchanged between the vapor and the external

vl from vapor to liquid

w wall

wl wall adjacent to the liquid

wv wall adjacent to the the ullage

Superscripts

$cond$ conduction

$conv$ convection

Acronyms

ASD Anti-Sloshing Device

AVD Anti-Vortices Device

CFD Computational Fluid Dynamics

CHF Critical Heat Flux

CSF Continuum Surface Force

CV Control Volume

EoS Equation of State

ISRU In-Situ Resource Utilization

ISS International Space Station

LEO Low Earth Orbit

LEVM Linear Eddy Viscosity Models

MLI Multilayer Insulation

NIST National Institute of Standards and Technology

ODE Ordinary Differential Equation

PIV Particle Image Velocimetry

PMD Propellant Management Device

RANS Reynolds-Averaged Navier-Stokes

RTD Resistance Temperature Detector

SI Sharp Interface

SST Shear Stress Transport

URANS Unsteady Reynolds-Averaged Navier-Stokes

VOF Volume-of-Fluid

Chapter 1

Introduction

This study aims at improving the understanding of the complex physical phenomena occurring inside the tanks for cryogenic propellant. These phenomena, although being coupled, can be studied, in the first instance, as decoupled, and can be divided into two macro categories, the first is the thermo-fluid-dynamics characterization, the second is the sloshing analysis. Sloshing is the movement of the unrestrained free-surface of the liquid contained in a partially filled tank, which happens when the latter is subject to a sudden movement or acceleration. We have concentrated only on the first category, because a well established reduced literature can be found about the sloshing topic [2], even if it is not strictly focused on the cryogenic propellant.

Our study is carried out mainly through CFD simulations. These, although being very computationally time-consuming for a two-phase flow problem, such as propellant tanks, allow to account for the complex physical phenomena at play. But, we have considered also reduced order models because, even if they simplify the physics involved, they offer an engineering tool suitable to compute the principal operating parameters of a cryogenic tank, in a reduced computational time.

Cryogenic fluid tanks are extremely interesting for many current and future applications. One of them is the transportation of liquefied natural gas (LNG), a rapidly expanding non-renewable energy source, over great distances, such as across oceans. Furthermore, because of its numerous uses in the energy, automotive, and aerospace industries, there is an increasing demand for the storage and transportation of huge amounts of liquid hydrogen (H_2). Due to their higher specific impulse than storable hypergolic propellants, cryogenic propellants are particularly appealing in the aerospace field, but their storage is tricky, especially for long-term applications. Alongside the traditional cryogenic propellant combination of liquid oxygen (O_2) and liquid H_2, the combination of liquid O_2 and liquid methane (CH_4) is receiving growing interest in liquid rocket engines, as it will be clear in Sec. 1.2. Despite not being a fluid of interest as a rocket fuel, liquid nitrogen (N_2) is very often used to test experimental equipment [56, 57, 84, 93], since it is more readily available and manageable than, for instance, liquid H_2.

Experimental measurements provide an effective method for studying thermo-fluid-dynamics phenomena of self-pressurization but, to the high costs of the test equipment and the challenges associated with the management of cryogenic fluids, CFD analyses have become an appealing tool for supporting both the design of cryogenic propellant tanks and the reconstruction of the experimental tests. The latter might be used to validate, verify, and improve the CFD models. Although there have been many experiments in cryogenic tanks, not all of them have clear and reproducible initial

and boundary conditions, making them acceptable for comparison with CFD results. A review of significant experimental literature data for the validation of cryogenic tank models in case of self-pressurization in normal gravity, of active-pressurization in normal gravity, and of self-pressurization in reduced gravity can be found in Sec. 4.1, in Sec. 5.1, and in Sec. 6.1, respectively. The experimental studies carried out in cryogenic tanks can be separated in experiments carried out in large-scale tanks and in small-scale tanks. When the characteristic dimensions of an experimental tank closely resemble those of a tank used in a real application (for example of the order of a few meters for rocket or satellite tanks), the tank is said to be large-scale. Small-scale experimental tanks, on the other hand, have dimensions of the order of tens of centimeters, and are frequently used for model validation and tank design development.

In this chapter, once the cryogenics concept is introduced (see Sec. 1.1), the international interest in cryogenic propellant is explained (see Sec. 1.2). Then, the basic concepts of tank design are shown (see Sec. 1.3), and the attention is focused on the thermo-fluid-dynamics characterization (see Sec. 1.4). Next, the aspects characterizing the study of cryogenic tanks in reduced gravity environment are discussed (see Sec. 1.5). Finally, an outline of the thesis is provided (see Sec. 1.6).

Due to the numerous physical phenomena involved, the thermo-fluid-dynamics characterization of cryogenic tanks is a challenging task, and which would require a further deepening.

1.1 Cryogenic matters

The practice of creating extremely low temperatures and the effects created by low temperatures is known as cryogenic engineering. The cryogenic temperature range is commonly defined as from -150°C to absolute zero (i.e., -273°C or 0 K) [109]. Theoretically, the molecular mobility is close to halting altogether at 0 K. The temperatures experienced in cryogenic environments are far lower than those in regular physical processes. The alteration in thermal conductivity, ductility, strength, and electric resistance under these harsh circumstances is crucial. As heat is thought to be produced by the random motion of molecules, this suggests that substances at cryogenic temperatures are extremely near to a static and highly ordered state.

Cryogens have become very significant because of their application in space propulsion systems, in medicine and surgery, and in studies of basic physical phenomena at low temperatures. The creation of superconducting electromagnets for particle accelerators makes extensive use of the superconductivity of materials that have been cooled to extremely low temperatures. Many satellites need cryocoolers (heat exchangers that operate at very low temperatures) to chill the infrared and microwave detectors, allowing for the reception of sharper images.

Cryogens, often liquefied gases, are substances used to achieve or sustain cryogenic temperatures. Liquid N_2, H_2, O_2, and helium (He) are examples of common cryogens. The boiling points at 1 atm of the most common cryogens are summarized in Tab. 1.1.

Since the liquid phase takes up significantly less volume per kilogram than the gaseous phase does, the storage of liquefied gases is crucial from a commercial standpoint. The storage and transportation of LNG is a crucial commercial use of cryogenic liquefaction techniques. Natural gas is liquefied at about 110 K, and it becomes very compact, so that it may be transported effectively in properly insulated tanks. Cryogens like liquid O_2 and liquid H_2 are utilized as propellants for spacecrafts and rockets. The major drawback of using H_2 as fuel in aerospace vehicles is its need for a

Table 1.1: Boiling points at 1 atm of the most common cryogens, taken from NIST Chemistry WebBook [65].

Species	Boiling point at 1 atm [K]
N_2	77.36
H_2	20.37
O_2	90.2
He	4.22
CH_4	111.67

large storage volume. H_2 has a density of around 0.09 kg/m^3 at standard pressure and temperature, compared to about 800 kg/m^3 for gasoline and kerosene. This is the major reason for storing H_2 in liquid form at cryogenic temperatures. At a given amount of energy the volume of H_2 would be four times larger than that of kerosene. Liquid H_2 is also expected to play a significant role in clean and fossil-free transportation energy systems.

Since cryogens are by definition colder than their surroundings, they are constantly in a hostile environment. This significant temperature differential makes boiling easy to achieve. Film boiling happens often, especially when cooling down an equipment. In many circumstances, two-phase flow and the ensuing unsteadiness are to be expected. Experiments with cryogens are required because the boiling correlations for noncryogens are not suitable.

He is the sole cryogen that exhibits anomalous fluid flow and heat transfer behavior. He is liquefied at 4.2 K, and this liquid is called helium I. At a temperature of 2.17 K at 1 atm, known as the lambda point, it is abruptly transferred to helium II. This last exhibits very uncommon properties including superconductivity and superfluidity, i.e., exceptionally high thermal conductivity and low viscosity.

Liquid gas storage at low temperatures necessitates insulations with significantly lower thermal conductivity than standard insulations. New insulation materials and techniques have been developed for this purpose. A remarkable example is the so-called superinsulation materials, which consist of many layers of highly reflective material separated by low-conductivity spacers of some type, and evacuated to low pressures.

1.2 International growing interest in cryogenic propellant

With high specific impulse and non-pollution, cryogens have been widely recognized as a powerful and promising fuel for space exploration. In the cryogenic field, in recent years, international attention has been increasingly focused on the use of CH_4 for the future space exploration. Indeed liquid CH_4, despite having a lower specific impulse with respect to liquid H_2, is easier to store, due to its higher boiling point and density, as well as its lack of H_2 embrittlement. It also leaves less residue in the engines compared to kerosene, which is a favorable characteristic for reusability. Moreover its possible use with In-Situ Resource Utilization (ISRU) enables sustained exploration of Mars [97]. Among the CH_4-powered engines currently under development there are Prometheus, ESA's M10, Blue Origin's BE-4, and SpaceX's Raptor. M10 engine, that will be used on the third stage of Vega-E launcher, is the first European engine powered by CH_4. The progress achieved in Europe with cryogenic systems and, in particular, with liquid O_2/liquid H_2 propellant combination, has allowed the development of the Vinci upper-stage engine, which is a derivative design of the

predecessors HM7, Vulcain and Vulcain 2 thrust chambers, and which represents Europe's first approach to an expander cycle engine. M10 engine arises from the acquired European expertise with the expander cycle engine, but with the objective to use the "soft" cryogenic CH_4.

European Space Agency (ESA), in 2017, started funding the development of Prometheus, a reusable rocket engine powered by liquid CH_4 and liquid oxygen O_2, which will likely be used on a future version of Ariane 6, the Ariane Next.

SpaceX's Raptor engine will power, with high performance, the upper (Starship) and lower (Super Heavy) stages of SpaceX's new class of fully reusable launchers. The choice of CH_4 for this engine has been dictated not only by the relative ease of storage compared to liquid H_2 and the chemical properties of its combustion, but also by the possibility of producing CH_4 in situ from the Martian atmosphere, which mostly contains carbon dioxide. This class of SpaceX's launchers was born, in fact, with the aim of colonizing Mars. Both the Starship and the Super Heavy will allow the propellant to be kept in a cryogenic state in innovative stainless steel structures. Furthermore, the Starship has three possible versions of integrated payload: either a spacecraft, or a vehicle to deploy satellites, or a tanker, i.e. a structure for the supply of propellant in Earth orbit. The tanker will allow to launch a heavy vehicle into interplanetary space, since the vehicle, being refueled in obit, will be able to consume the tank twice, once to enter Low Earth Orbit (LEO) and then to leave Earth's orbit. This design allows for a velocity increase similar to that of three-stage rockets, without the need for the corresponding mass ratios. Such an ambitious program requires propellant transfers in orbit from the tanker to the Starship, an objective that could not be achieved without studying the behavior of the propellant in microgravity, and without the design of specific devices to know and control propellant position over time. Transferring liquid CH_4 in microgravity is, also, one of the primary goals of the NASA's mission Robotic Refueling Mission 3 (RRM3). The techniques required to perform cryogenic transfer will allow to replenish depleted satellite tanks, advancing satellite servicing capabilities, and enabling long duration, deep space exploration. Moreover, using cryocoolers and advanced Multilayer Insulation (MLI) to balance temperatures, RRM3 has demonstrated the first ever long-term storage of cryogenic fluid with zero boil-off, having successfully stored cryogenic fluid for four months on the International Space Station (ISS), prior to the venting operation. Moreover, NASA, with its Evolvable Cryogenic (eCryo) Project, is currently playing a critical role in the maturation of cryogenic fluid management (CFM) technologies. eCryo is addressing four focus areas: analysis tools, MLI characterization, vapor-based heat intercept, and radio frequency mass gauging (RFMG).

Finally, the use of cryogenic propellants is also envisaged in the aeronautical field, given Airbus' goal of decarbonising the skies, putting a H_2 aircraft on the market in 2035.

1.3 Tank design

Cryogenic tanks' primary purpose is to store and deliver propellants in adequate thermodynamic conditions for all phases of a space launcher mission (ground, flight coasting, and flight firing). In this section, a summary of the main aspects concerning the cryogenic tank design for space applications (e.g. the typically used configurations, shapes, materials etc.) is provided.

Tank subsystem

Typically, a tank assembly or subsystem consists of:

- A bare tank to ensure the storage of the propellant and the mechanical strength;
- Insulations to ensure the thermal performance;
- Propellant Management Devices (PMDs), which will be extensively discussed in Sec. 1.5;
- Lines to be able to pressurize, fill and drain the tanks;
- Measurement tools (pressure, propellant level, temperature), not always present;
- Additional tank devices.

Additional propellant tank devices

Other devices typically used in space tanks are:

- Anti-Sloshing Devices (ASDs) to limit and damp sloshing;
- Anti-Vortices Devices (AVDs) to prevent the creation of vortices, and, consequently, help to feed the turbopumps with a liquid flow free of bubbles and with a velocity profile as uniform as possible;
- Baffles to limit the de-spin phase duration prior to engine reignition;
- Diffusors to prevent liquid ingestion in the pressurization lines and strong deformation of the free surface during pressurization phases.

Design configurations

There are two basic cryogenic propellant tank configurations for liquid rocket applications: one for pressure-fed upper-stage systems and one for booster-stage systems [40]. The specific application affects the working tank pressure level. In fact, the employment of a turbopump-fed engine system is necessary for booster applications and frequently also for upper-stage applications, allowing for relatively low working tank pressures (below 10 bar). Instead, pressure-fed upper-stage propulsion systems for relatively moderate thrust applications use a gas-pressurized propellant feed system, resulting in greater operational tank pressures (from around 10 to 30 bar).

Fig. 1.1 shows the propellant tank configuration of a typical booster-stage propulsion system of a large launch vehicle. Such a system can be used for either storable or cryogenic propellants. The tanks are arranged in tandem, and form the walls of the vehicle structure. The tanks represent a large percentage of the vehicle inert weight. Low pressure levels allow constructing the tanks with extremely thin walls, but the often huge tank structures develop sensitivity to external buckling loads. Two design options are available to stabilize the tank: pressure-stabilization and self-supporting structures. When using the first option, tank pressure must be kept above a specific minimum by using controls. However, at least until the 90s, in most booster-stage systems, the

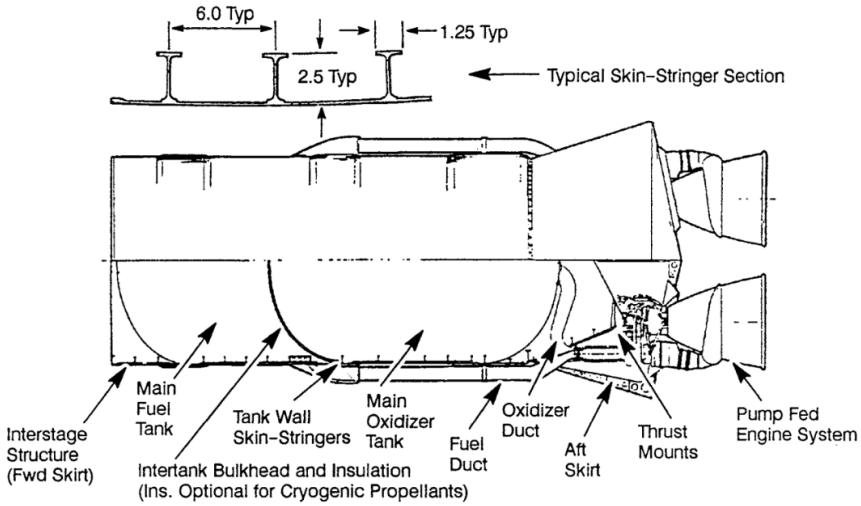

Figure 1.1: Propellant tank configuration of a typical booster-stage propulsion system, from [40].

second option was selected, and tank wall was reinforced by skin stringers or by other structural means [40].

The propellant tank configuration of a typical upper-stage propulsion system is shown in Fig. 1.2. The tanks are contained in an outer cylindrical shell, designed to withstand all boost and flight loads. The tanks are two modified spheres, faired into conical sections at the bottom for propellant discharge. Moreover, they are bolted to the shell structure around their support ring. The system shown is gas-pressurized using He gas, which is stored, at an initial pressure level higher than 300 bar, in two liquid-nitrogen-jacketed, high pressure spherical tanks, placed between the two primary propellant tanks.

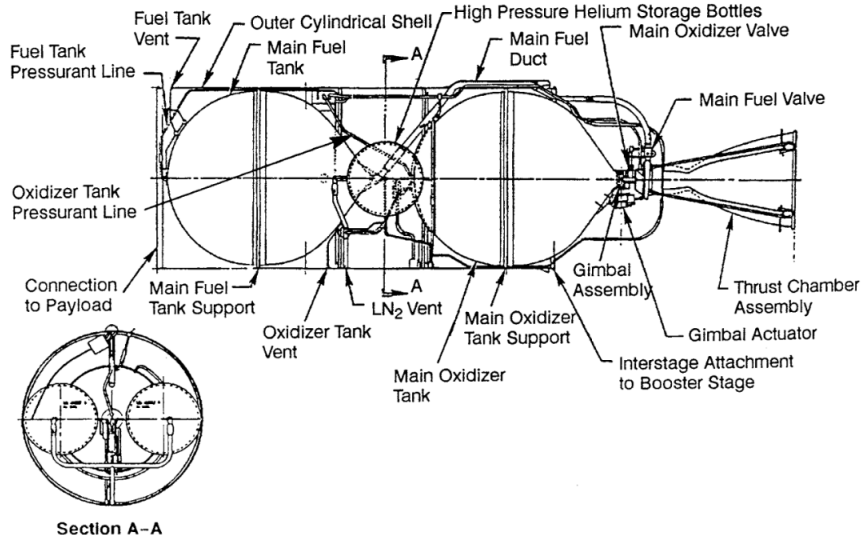

Figure 1.2: Propellant tank configuration of a typical upper-stage propulsion system, from [40].

Shape

Propellant tank shape is influenced by both vehicle design and tank pressure. Vehicles with relatively high length-to-diameter ratios and small diameters typically use cylindrical-shaped tanks. When

tank pressures are reasonably high, and there are less restrictions on tank diameter and slenderness, spherical tanks may be advantageous. As a propellant tank, a sphere offers the smallest surface-to-volume ratio and the smallest shell stress for a given internal pressure, but the combination of several spheres into the rocket structure, which is typically cylindrical, causes weight and volume penalties. Moreover, a sphere does not allow to the tank wall to be used as a load-carrying member of the rocket structure, resulting in additional weight and volume penalties. Additionally, the ends of cylindrical tanks might be spherical or elliptical. The cylindrical tank with spherical ends weighs less than the one with ellipsoidal ends, but, overall, a tank with ellipsoidal ends may lead to a weight reduction, because it allows for a shorter interstage structure. In some cases, the propellant tank ends are designed with particular shapes, such to accomodate structural loads, minimize residual propellant, and utilize available envelope.

Structural loads

Being structural members, propellant tanks must be designed in such a way to withstand a combination of the following structural loads:

- Internal pressures and their dynamic effects
- Axial thrust loads and their dynamic effects
- Bending moments due to vehicle transverse accelerations, wind loads, and shifting of the center of gravity
- Aerodynamic forces
- Thrust-vector-control forces
- Vibration and shock loads
- Loads produced by mounting arrangement
- Loads caused by thermal transients and gradients
- Loads produced during ground handling

Internal tank pressures and axial-thrust loads are the main ones in the majority of vehicle systems. The evaluation of these and other loads must be thorough, and should involve experimental testing. Finally, the relatively thin, highly stressed shells make it challenging to attach concentrated loads. For this reason, the loads must be spread out in order to prevent localized overstresses.

Wall material

The selection of the proper material for a cryogenic tank is based not only on consideration of compatibility with the propellant, of maximization of the strength-to-density ratio at a given temperature and on ductility requirement. Indeed, an important prerequisite for material selection is knowing the precise strength characteristics, degree of brittleness, and notch sensitivity of the tank

construction material at the cryogenic propellant service temperature range (as low as approximately 20 K for liquid H_2 services). Most austenitic and semiaustenitic stainless steels, as well as the majority of aluminum (Al) alloys, have good mechanical properties at cryogenic temperatures.

Insulation types

In order to reduce the heat influx into a cryogenic system, a thermal insulation is sometimes used. Liquid H_2 offers the most significant tank design issues among the cryogenic propellants, primarily because of its extremely low service temperature and its relatively high specific volume. Thus, the tank insulation becomes one of the most critical design factors in a H_2-fueled rocket. Some design features required by a thermal insulation are: light weight, uniform and repeatable insulation characteristics, ease of application, low cost, low hazard, reasonable ruggedness, ease of repair, good reliability, and, above all, low heat-conductivity. Excellent performances can be reached with a laminated-type insulation, made by an aluminum foil and a structural material, often in multiple layers. The aluminum foils, being reflectors, reject radiative heat, while the void space in between prevents conductive heat transfer. This type of insulation has been rarely used in atmospheric applications, since it can be easily damaged, and subjected to cracks and infiltration of gas. Another type of insulation, which is finding wide application, are the honeycomb-supported structures. They are composed by a plastic honeycomb, which goes between an inner and an outer facing sheets. The cells may or may not be filled with an isocyanate-type foam, depending on weight limitations. The foam bubbles or the properly sealed cells form individual vacuum spaces when cold (cryopumping). Thermal conductivity and density vary from one kind of insulation to the other, as well as their cost, so an optimization study based on mission characteristics has to be carried out before selecting the insulation type.

The tank insulation may be located internally or externally with respect to the tank wall. It can be integral, i.e. bonded in place, or disposable during boost, i.e. mechanically retained. Each insulation design choice has its own advantages and drawbacks. For example, the insulation located inside the wall has the advantage of isolating the tank wall from the low-temperature effects due to the direct contact with the propellant, but it is uneasy to install and to repair in case of leaks. Instead, the external insulation isolates the tank structure from the extreme temperature of the aerodynamic heating during the boost phase, and it is easily accessible for installation and repair. However, a tank leak is more difficultly detected with that kind of insulation, and the presence of a crack causes air liquefaction, with a consequent increase in heat transfer.

Finally, when a common bulkhead is used between cryogenic propellant tanks, as in Fig. 1.1, the common bulkhead has to be insulated in order to prevent freezing of the propellant with the higher boiling point.

1.4 Thermo-fluid-dynamics characterization

Cryogenic tanks need stringent control and accurate characterization of the main thermo-fluid-dynamics phenomena occurring inside them, a scheme of the main ones is shown in Fig. 1.3.

In fact, heat leaks from the outside environment are inevitable in cryogenic tanks due to the asperity of the cryogenic condition (low boiling point) and to the presence of various conduction

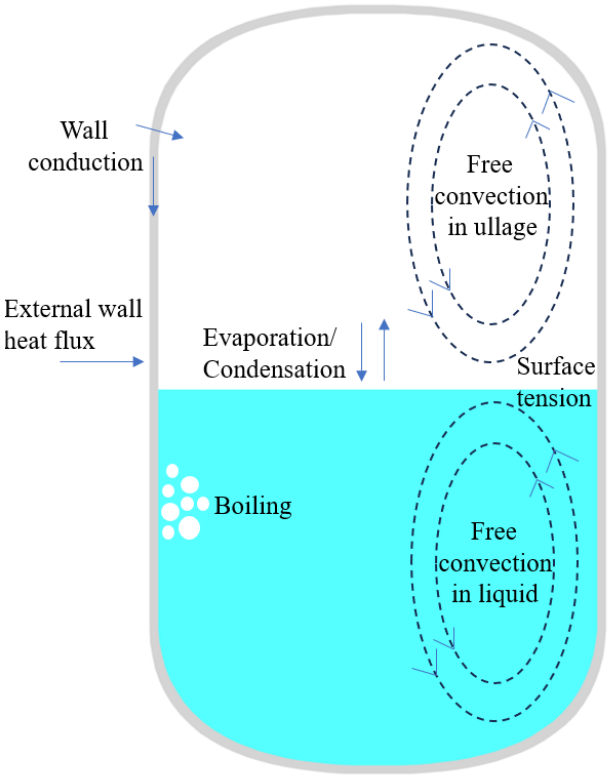

Figure 1.3: Typical thermo-fluid-dynamics phenomena occurring inside cryogenic tanks.

paths (due to the tank support structures and the propellant lines and valves). The conduction paths are not the only source of heat leak, indeed, another important contribution is linked to the particular phase of the vehicle mission: ground hold, boost phase, and coast in space phase. Long ground hold periods cause large propellant evaporative losses because of the heat leaks mainly due to solar radiation and natural convection. The boost phase, although of short duration, dictates the requirements of the thermal insulation. Indeed, this phase is characterized by large aerodynamic heating. During the coast in space phase, the principal source of thermal energy is radiation from the sun and the planets, which can be minimized using radiation shields, surrounding the basic tank insulation. These shields are characterized by proper values of surface absorptivity and emissivity.

Tank heat leaks are the cause of propellant vaporization, which can occur both in the form of evaporation at the liquid-vapor interface, and in the form of boiling in the bulk liquid, usually originating near the tank walls. Also condensation at the liquid-vapor interface is common in some tank operative conditions, for example during some procedures of active-pressurization, as it has been noticed in some experimental [72, 79] and numerical [67] studies. Propellant vaporization, together with the heating of the vapor phase located above the liquid, which is commonly referred as ullage, causes tank self-pressurization, in the case of a closed tank without venting. Pressurization can also be actively performed in some situations. For example, the loading of the propellant is done on the launch pad a few hours prior the flight, and the initial pressurization is done just prior the lift-off (in order to make the propellant subcooled), and then maintained at the required levels during all the flight phases for the good draining of the propellants to the engine. In the design phase of cryogenic tanks, tank pressurization has to be reliably quantified in order to estimate the range of tank operating pressures. Indeed, to design the wall thickness, it is required to estimate the

maximum operating pressure. In addition, a minimum operating pressure limitation must be set in order for the entire liquid propellant system to function. For instance, in pressure-stabilized large booster-stage systems, a minimum pressure value must be exceeded, in order to resist to external buckling loads. Control of instantaneous propellant tank pressures and temperatures is furthermore required to ensure proper inlet conditions for the turbopumps.

In addition to pressurization and phase changes, the application of a heat flux to the tank walls causes heating of the fluid layers adjacent to it, which, due to buoyancy, move upward into the denser fluid, and generate convective recirculations, both in the liquid and in the ullage. Convective recirculations in the ullage cause its thermal stratification, indeed the hottest and lightest vapor layers move in the uppermost part of the ullage, while the coldest and heaviest layers reach the lowest part of the ullage. Convective recirculations in the liquid transport heat towards the interface between the two phases. The interface temperature is approximately the saturation temperature corresponding to tank pressure at a given time [6]. Additionally, the heat input causes the liquid's bulk temperature to rise, although at a slower rate than the interface temperature does since, as previously stated, the interface temperature rise is correlated with the rise in tank pressure via the saturation curve. This difference in the rate of growth causes a liquid thermal stratification near to the free-surface, whose extension grows over time, in a closed self-pressurizing tank.

Among the thermal phenomena, an important role is played by the heat conduction inside the solid wall. For example, for an Al tank partially filled with liquid H_2, and having only gaseous H_2 in the ullage, as the ratio of thermal conductivities for gaseous H_2, liquid H_2, and Al is 1:6:1180, the heat flux through the walls is much higher than that in the fluid phases, and thin walls only partially alleviate it [102]. Moreover, the wall divert the heat coming from the upper part of the tank, in correspondence of the ullage, to the lower part of the tank, by conduction. This happens both in the case of a closed tank exposed to a uniform heat flux on its exterior wall [89], and in the case of a tank actively-pressurized with a pressurant gas having a higher temperature with respect to the fluids already present in the tank [88, 90]. Generally, tank wall thickness has a noticeable influence on the pressurization characteristics. A thinner wall is preferred not only for lowering the vehicle weight, but also for a higher pressure produced by a given pressurant gas flow rate [115].

It is well established that the sloshing, although being a mainly dynamic in nature process, has a strong influence on the thermal physical processes occurring in cryogenic tanks [45, 47, 60, 63, 66]. During sloshing there is thermal de-stratification induced by fluid mixing, as well as heat and mass transfer at the liquid-ullage interface, which cause large pressure drops in the tank. Moreover, oscillating liquid cools a large portion of the tank surface, which was previously in contact with the hot gas. As a consequence, there is a temperature and pressure reduction in the ullage [45, 47]. In addition, the interface deformation and splashing causes the increment of the liquid-ullage interface area. This factor enhances the heat transfer from the ullage to the liquid, leading to a further reduction of the tank pressure. In cryogenic propellants, in conjunction to the heat transfer, there is a more significant mass transfer, which additionally leads to the pressure decrease. In this thesis, the thermo-fluid-dynamics characterization has been carried out only in the static case, i.e. without considering the sloshing phenomenon, even if during an upper-stage tank mission sloshing can be induced by various sources. The latter can be vibrations during the propulsive phases, as well as different external perturbations (the engine shut-down, the separation phases, the reorientation before reignition, etc.), which cause large deformations of the liquid-ullage interface. Hence, due to the

aforementioned motivations, having neglected the sloshing influence on the thermo-fluid-dynamics characterization is a limitation of this thesis, and this aspect should be explored in future work.

As just seen, the thermo-fluid-dynamics phenomena occurring in cryogenic tanks are numerous, and all affect the propellant behavior. The objective of this thesis is to study these phenomena in tanks characterized by different operating conditions. In particular, the self-pressurization and the active-pressurization on ground, and the self-pressurization in reduced-gravity conditions are taken into account. The main observables we focus on are: the pressurization rate, the temperature stratification, in particular that in proximity of the free-surface, and the phase change rate.

1.5 Reduced gravity aspects

For the design of upper stage cryogenic storage tanks, it is necessary to study the thermo-fluid-dynamics behavior of cryogenic propellant not only in normal gravity (e.g. $g_E = 9.81$ m/s^2), but at different gravity levels, g. Indeed, upper stage cryogenic tanks, during their operating life, experience extreme gravity levels, varying from the high gravity, during the boost flight, to the low gravity, during the ballistic and space flight.

Different microgravity testing platforms have been exploited over the years to carry out experiments in order to study the two-phase fluid behavior at various gravity levels. Among these, the NASA's Space Shuttles and the ISS have allowed to reach all testing benefits, among which long duration experiments, high quality microgravity ($g < 10^{-4} g_E$), and operator access to the experimental package. However, this kind of microgravity experiments is very costly, and requires many years of development.

In this section, different topics related to the reduced gravity environment are addressed: the influence of the gravity level on the boiling behavior as well as on the dynamics of the free surface, and the propellant expulsion under reduced-gravity conditions.

Influence of the gravity level on the boiling characteristics

The gravity level influences the boiling process, as pointed out in both numerical and experimental studies on pool boiling. According to Fritz expression [27], the bubble diameter at departure varies as $g^{-1/2}$ on an upward-facing horizontal surface, this expression is approximately consistent with the numerical results of [23]. Microgravity pool boiling experiments with n-Pentane, R-113, and water, carried out in parabolic flight [77], and with R-113 and water, carried out in drop shaft [78], showed the strong influence of the fluid surface tension and of the latent heat of vaporization on bubble nucleation, growth and coalescence, and on heat transfer effectiveness. Microgravity pool boiling experiments pointed out two fundamental aspects of pool boiling in space applications: the first is the formation of an unusually large bubble that engulfs the entire heater surface, and the second is the appreciable reduction in Critical Heat Flux (CHF) compared to terrestrial data. Fig. 1.4 [55] shows snapshots of bubble formation during pool boiling of R-113 in normal gravity (left) and microgravity (right).

In normal gravity, many small bubbles form, which depart from the heater surface due to buoyancy. Instead, in microgravity, a single large bubble forms, which remains attached to the heater surface. The Capillary or Laplace length, defined as $l_c = \sqrt{\frac{\sigma}{\rho g}}$, determines the bubble's size in

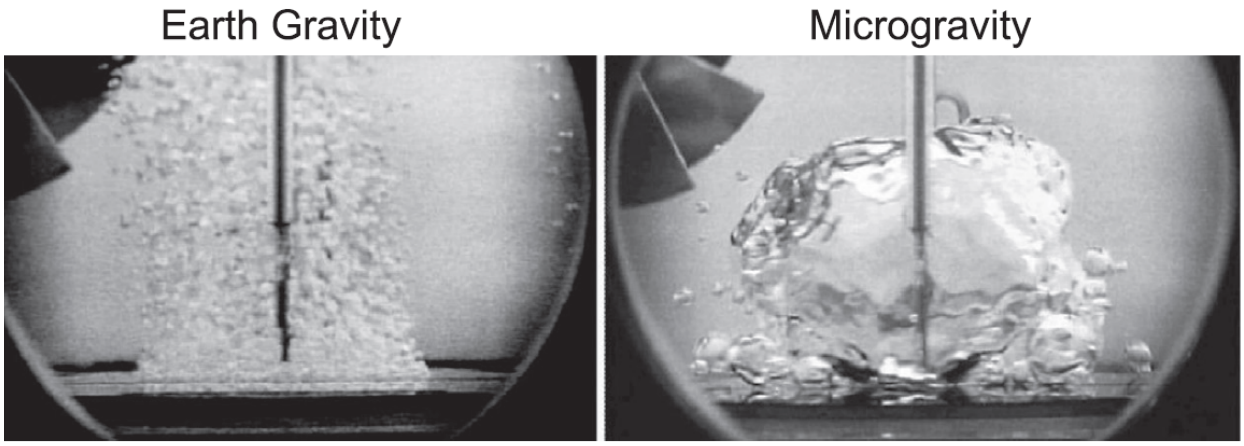

Figure 1.4: Snapshots of pool boiling of R-113 in normal gravity and microgravity (courtesy NASA), from [55].

response to surface tension, σ, and gravity, g, and it is very large in microgravity, explaining the phenomenon visible in Fig. 1.4. Another important consideration is how the Capillary length compares to heater size. In particular, experimental results from Microheater Array Boiling Experiment (MABE), carried out onboard the ISS, showed that the boiling curve for high gravity is heater size dependent [85].

Boiling happens whenever the system becomes superheated. Even if superheat is typically associated to the application of a heat flow, it can also be induced by a decrease in the system pressure. An example are the depressurization maneuvers which can be carried out for cryogenic propellant in spacecraft tanks to transfer thermal energy from the liquid to the ullage [118]. The behavior of a single nucleation site during a depressurization conducted under compensated gravity, in the drop tower of the university of Bremen, was presented in [118]. The data gathered on the growth of a single bubble of CH_4 under compensated gravity could be exploited for comparison against numerical and analytical models, and hopefully for the development of a sub-scale modeling of bubble behavior to be used in numerical simulations.

Influence of surface tension

Some researchers hypothesized that bubble nucleation and growth in microgravity are significantly influenced by thermocapillary or Marangoni convection. The Marangoni effect is the fluid motion along a liquid-vapor interface due to a gradient of the surface tension, this type of convection is normally hidden by dominating buoyancy-driven convection in normal gravity. In the case of temperature dependence, this phenomenon may be called thermocapillary convection.

The surface tension of a multicomponent liquid that is in equilibrium with the vapor is a function of temperature and composition of the mixture [25], i.e.:

$$\sigma = \sigma(T, X_1, X_2, ..., X_{N-1}) \tag{1.1}$$

where X_i is the molar fraction of the i^{th} component in the liquid phase, and N is the total number of components in the liquid phase. The change of surface tension can be caused by either change

in temperature or composition, i.e.:

$$d\sigma = \left(\frac{\partial \sigma}{\partial T}\right)_{X_i} dT + \sum_{i=1}^{N-1} \left(\frac{\partial \sigma}{\partial X_i}\right)_{T, X_{j \neq i}} dX_i \tag{1.2}$$

From thermodynamics, it is known that as the critical temperature for a given fluid is approached, the properties of the liquid and vapor phases of the fluid become identical, and so σ becomes zero. It ensues that the surface tension decreases with temperature, namely $\left(\frac{\partial \sigma}{\partial T}\right)_{X_i} < 0$.

For a pure substance, surface tension is a function of temperature only. The curve-fit equations for surface tension are almost linear for the majority of fluids, and can have the form:

$$\sigma = C_0 - C_1 T \tag{1.3}$$

where C_0 and C_1 are empirical constants that vary between substances. The unit of the temperature in Eq. (1.3) is °C. As the surface tension varies with temperature, it will not be uniform if the temperature, along the liquid-vapor interface, is not uniform. The flow driven by surface tension moves away from the region of the interface with high temperature (or, equivalently, low surface tension) towards the region of the interface with low temperature (or, equivalently, high surface tension).

The most well-known example of surface-tension-driven flow is Bernard cellular flow, which occurs in a thin horizontal liquid layer heated from below. A steady cellular flow driven by the Marangoni effect is shown in Fig. 1.5. When a steady Marangoni flow is developed, the liquid

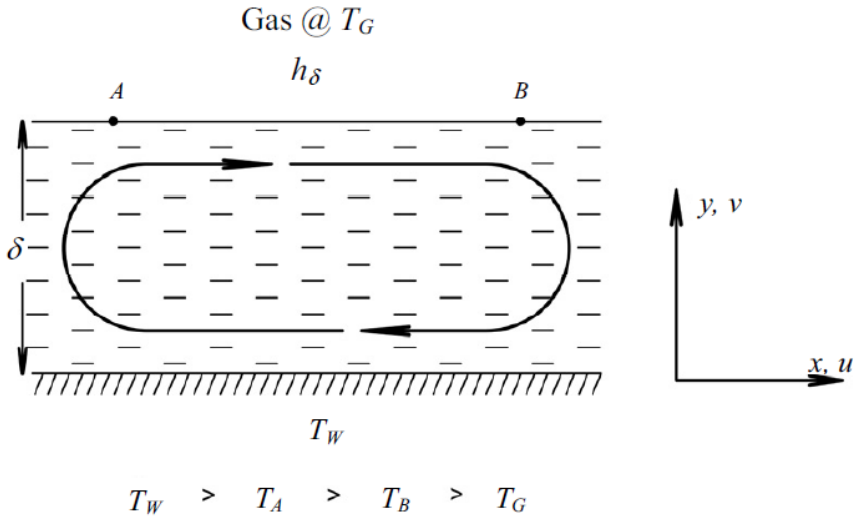

Figure 1.5: Steady cellular flow driven by the Marangoni effect, from [25].

velocity is upward at point A and downward at point B. The temperature at point A is higher than that at point B because the liquid at the surface point A arrives directly from the hot surface. As a consequence, point A has a lower surface tension than point B, and the fluid is pulled from point A to point B. This means that, although a temperature gradient exists in the vertical direction, the actual driving force is the surface tension gradient in the horizontal direction.

The effect of thermocapillary convection on bubble behavior in pool boiling experiments in microgravity was studied both with R-11 fluid in Spacelab mission IML-2 [107] and with R-113

fluid onboard NASA's Space Shuttle (STS-47, 57, 60, 72, 77) [75, 76]. Moreover, the contributions of thermocapillary convection in microgravity were later thoroughly analyzed by Straub [108]. The effect of Marangoni convection was mostly seen in subcooled boiling, and it produced jet streams around the nucleating bubbles, which aided in the transfer of heat from the bubbles to the bulk liquid. The strength of the thermocapillary jet, which was measured by Particle Image Velocimetry (PIV), increased by increasing the heat flux. However, this behavior was highly influenced by the degree of subcooling. In saturated conditions, a zero jet velocity was measured. Upon slightly increasing the subcooling, the jet velocity increased rapidly to a maximum level, but decreased back to zero at high subcooling. In subcooled boiling, it was proposed that bubble growth is driven by a balance between evaporation at the bubble base and condensation at the bubble cap. Differences between the rates of the two processes resulted in temperature gradients that induced vapor flow within the bubble.

Finally, it is important to remark that the level of gravity influences the dynamics of the free-surface, whose behavior can be predicted by looking at the value of the Bond number, Bo, which is the ratio of buoyancy forces to surface tension force:

$$Bo = \frac{g(\rho_l - \rho_v)L^2}{\sigma} \tag{1.4}$$

where, ρ_l is the liquid density, ρ_v is the vapor density, L is a reference length, and g is the gravity level. In normal gravity, the Bo is quite high, and the role of the surface tension is negligible, whereas, in microgravity, the Bo is low, and the surface tension force prevails over the gravity force, leading to motions of the free-surface along the tank walls.

There are recent valuable experiments in the literature that have further enhanced the knowledge of these phenomena [29, 33]. For example, in [33], the reorientation of the liquid HFE-7500, during three microgravity experiments, a drop test and two catapult tests, was analyzed. While, in [29], results of free-surface deformations and heat transfer by thermocapillary convection, for a sounding rocket experiment, were discussed. In this case, the system considered was a two species system, as the ullage contained a mixture of vapor (HFE-7000) and non-condensable gaseous N_2.

Finally, the rising of the liquid along the tank walls has to be countered in the cases when in-orbit engine start-up and operation is necessary, as it will be described in the following paragraph.

Propellant expulsion under zero-gravity or oscillatory g-loading conditions

Under zero-gravity or oscillatory g-loading conditions typical of many vehicle trajectories, the propellant's location in a tank becomes uncertain, and a means to prevent gas from being expelled with the propellant is necessary. There are two possible approaches to do this, the first is "impulse settling", the second is "propellant management" [40].

In case of "impulse settling", a small propulsive force directed axially, parallel to the vehicle center line of thrust, is used to confine the propellant to the tank outlet, before starting the main-engine operation. This approach is suited to the majority of space vehicles, because their low-thrust reaction control units can also provide the thrust for propellant settling. This method offers the advantage of eliminating the need for propellant management devices for the main propellant tanks, but has the possible disadvantages of no control of vehicle center-of-gravity shifts and low thrust-to-weight ratio under these conditions, which may increase response time beyond tolerable limits.

The second method, i.e. "propellant management", consists in continuously confining the propellant to the vicinity of the tank outlet. This is done either by displacing the propellant with a moving device (called non-capillary PMD or positive expulsion device), or by exploiting the surface tension properties of the propellant with a, so called, capillary PMD, e.g. a porous plate or screen.

PMD performance depends on three principal characteristics: PMD system mass, demand mass flow rate, and expulsion efficiency EE, which is defined as [35]:

$$EE = \frac{V_{residuals}}{V_{tank}} \tag{1.5}$$

where $V_{residuals}$ indicates the volume of the residual propellant left in tank when the PMD breaks down, and lets vapor enter the transfer line, and V_{tank} is the tank internal volume. So, EE indicates how much the tank is drained by means of the PMD before the PMD breaks down.

A positive-expulsion propellant tank is made of an outer structural shell and an inner movable expulsion device, such as metallic diaphragms or bladders, elastomeric diaphragms or bladders, bellows, and pistons. Pistons were characterized by leakage and low EE, therefore the design of better devices was necessary. The bladder is similar to a balloon, where there is a membrane housing the propellant, with a narrow opening leading the propellant to the tank outlet, as shown in Fig. 1.6. The diaphragm is made of a flexible membrane which separates the pressurant gas from the

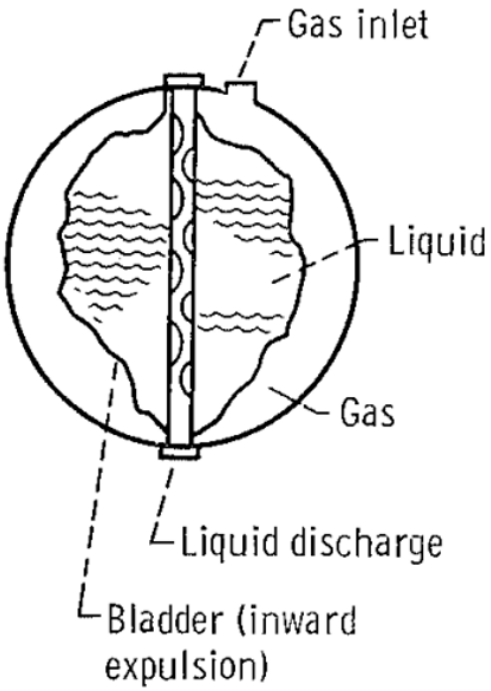

Figure 1.6: Schematics of a spherical bladder lying within the tank shell, from [61].

liquid propellant. Fig. 1.7 shows the progression of an apex-initiated diaphragm during expulsion. Bladders and diaphragms are useful in systems which require effective slosh control and suppression of reactions between pressurant gas and propellant. However, because they span across all the tank, their mass can be too large to make them eligible for large scale applications. Moreover, elastomeric material is not appropriate for long duration missions [21].

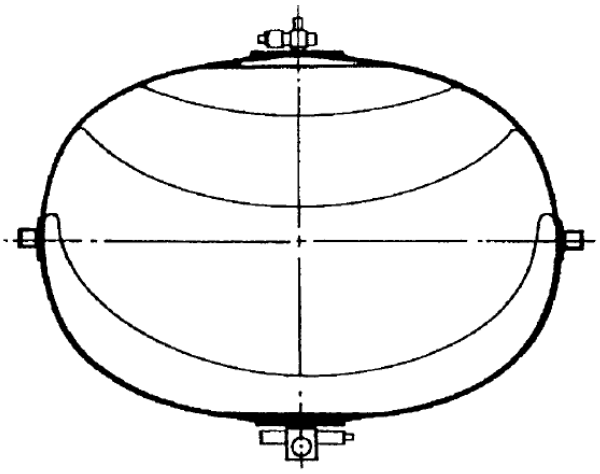

Figure 1.7: Progression of an apex-initiated diaphragm during expulsion, from [40].

New missions tend to use surface tension PMDs, which can be lighter and more reliable than positive expulsion devices [35]. Surface tension propellant management devices are passive systems, whose role is to increase the effective surface tension forces enough to hold the liquid at the desired position against adverse accelerations [24]. They can be divided into three types: partial communication (sometimes called "partial control"), total control, and total communication systems [24]. Another possible classification is based on the range of acceleration level, or effective acceleration, for which they manage to control the position of the liquid.

Partial communication PMDs maintain only a part of the liquid over the outlet, and leave the remaining liquid free. They are employed when significant spacecraft maneuvering or numerous small engine firings are required. In the case when thrusting is sufficient to settle the liquid, they are refilled during settling operations, and their size is such to contain the gas-free propellant needed to start the engines each time. If the thrust level is not always sufficient to settle the liquid, the PMDs must be large enough to contain all the propellant needed for the situations when settled liquid is not available. In this case, they do not need to be refillable. Both kinds are typically characterized by walls made of fine-mesh screens or similar "porous" materials. Capillary forces in the pores avoid the entrance of the ullage gas in the PMD during disturbances.

Total control PMDs retain all the liquid over the outlet. They are mainly used in the spacecrafts where the sloshing control is prominent.

Total communication PMDs are designed to create a flow path from the bulk liquid to the tank outlet at all instants. Since the liquid tends to remain attached to a wall, common types of total communication PMD are formed by a liner and a series of galleries, both made of fine-mesh screens, and positioned near the wall. A schematic of this device is shown in Fig. 1.8. The galleries are all joined to a manifold at the tank outlet. Tank pressurization will lead the bulk liquid into the gallery and then along the gallery into the manifold, as long as at least one of the galleries remains in contact with the bulk liquid. Capillary forces prevent the penetration of gas into the adjacent exposed channels. Due to their large size, total communication PMDs are stable in case of moderate accelerations but will allow gas access in case of large accelerations. There is also another type of total communication PMD, it composed of a set of central vanes connected to a standpipe. The vaned PMD used in the Viking spacecraft is shown in Fig. 1.9. If any vane comes in touch with the liquid, liquid is drawn to the standpipe. The liquid position is relatively unstable in this kind of

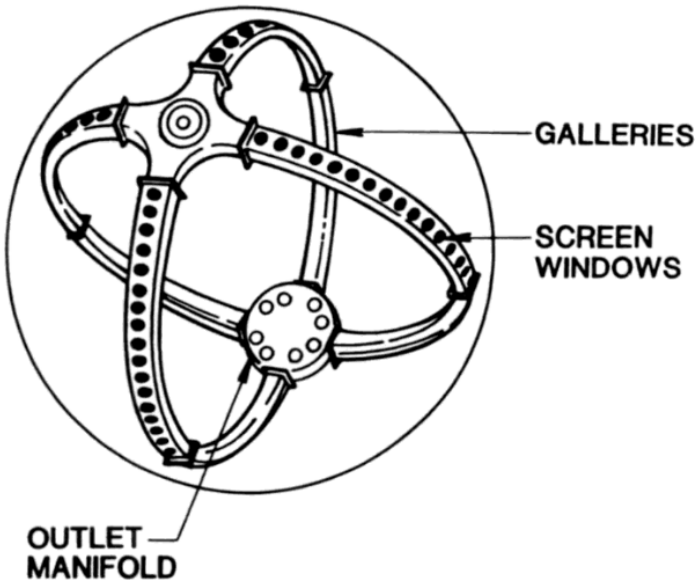

Figure 1.8: Schematic of a gallery-type PMD, from [24].

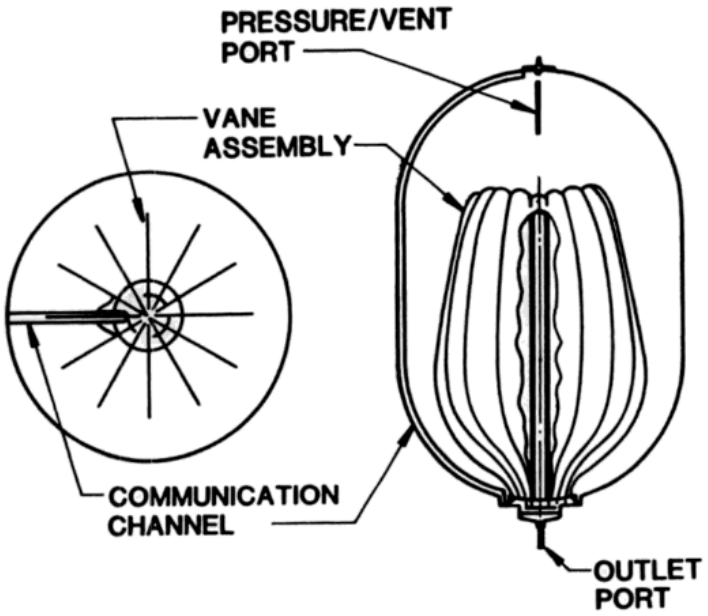

Figure 1.9: Vaned PMD used in the Viking spacecraft, from [24].

device because the interfaces are large. Therefore, this device can be selected when the disturbing accelerations are small, as in the case of deep space probes. It can also be used when the thrust level is high enough to keep the liquid settled, but, after the thrust ends, it takes a certain time to the PMD to reacquire the liquid before any subsequent small thrust operation can happen.

Finally, although scientific knowledge on surface tension PMDs has grown since 1960s, and the design and development of PMDs for storable propellants are mature, the fundamental research to include data collection for cryogenic and green propellants should be expanded [111]. Indeed, when cryogenic liquid is supplied to the outlet of the tank, low gravity fluid acquisition is more complex with respect to storable liquid due to the low surface tension and high susceptibility to heat leak associated with cryogenic propellants [35].

Three crucial factors are taken into account when choosing a propellant management strategy: the impulse on the vehicle generated by propellant movement, variation in the propellant center of gravity, and available tank envelope. If the impulse created by propellant sloshing within a tank with a surface tension device cannot be sufficiently controlled by reasonable sized baffles, positive expulsion may be the only option. If the center-of-gravity shift caused by propellant movement during vehicle maneuvers with a surface tension device results in excessive attitude control system needs, positive expulsion can also be necessary. Finally, if the required propellant amount cannot be packaged into cylindrical tanks in the available envelopes, bellows and pistons are not suitable.

1.6 Thesis outline

In this thesis, two approaches for the thermo-fluid-dynamics characterization of the behavior of cryogenic propellant in tanks are proposed.

The first approach, presented in Chap. 2, is an engineering tool for rapid analyses, i.e. a 0D model, which has been implemented in Matlab, and verified through the comparison with the results of a 1D model, developed by NASA. This tool has been also used to simulate two test cases: a liquid N_2 self-pressurization one, in Chap. 4, and a liquid N_2 active-pressurization one, in Chap. 5.

The second proposed approach involves the use of CFD, which, differently from reduced order models, allows to make a more detailed analysis, and to study most of the physical phenomena at play. In particular, in Chap. 3, the numerical setup selected to perform the analyses presented in the following chapters is shown. Then, in Chap. 4, the results of a test case characterized by liquid N_2 self-pressurization in a small-scale tank are presented. Later, the active-pressurization phenomenon is investigated in Chap. 5, in particular a liquid N_2 tank, pressurized with gaseous N_2, injected by a radial diffuser, is taken into account. For each test case, the effect of using various numerical models and parameters is studied, and the most appropriate ones are selected, namely those giving the best agreement between CFD and experimental results.

Once the setup for the thermo-fluid-dynamics characterization in normal gravity is defined and validated, in the last chapter (Chap. 6) the attention is focused on the reduced gravity environment. In particular, the results of a test case, characterized by liquid H_2 self-pressurization in low Earth orbit, are presented. Finally, a parametric study is carried out, where the gravity level is varied from normal gravity to a level of gravity three orders of magnitude lower, in order to see the effect of the gravity level on various thermo-fluid-dynamics observables, among which the pressurization rate, the phase change mass flow rate, and the liquid-ullage interface shape.

Chapter 2

0D model

The objective of this chapter is to analyze the cryogenic tank system, in different operating conditions, by means of a zero-dimensional transient model. This model has been implemented using the software Matlab®, and has been verified through comparison with the results obtained with a one-dimensional code developed by NASA [19, 20].

Numerous theoretical and computational models of varying levels of sophistication were developed over the years to both interpret and predict the tank pressurization behavior. The first analytical tool developed for this goal was the homogeneous thermodynamic model [5, 9, 81, 82]. Typically, in this model, an energy balance is performed over the entire liquid-vapor system, and the temperatures of both the liquid and the vapor phase are set equal to the saturation temperature. Naturally, the simplifying assumptions made led to a poor agreement between the thermodynamic predictions and the experimental results.

In order to address these shortcomings, a number of investigators developed models which include energy and mass transport. These models can be classified as zonal methods, where the liquid-vapor system is divided into zones of uniform temperature, and engineering correlations are used to model the energy and mass transport among these zones. The number of zones is completely arbitrary. For example, a zonal model in which the liquid-vapor system is divided into three control volumes (liquid, ullage, and interface) was developed in [9]. These zones were coupled to a 2D axisymmetric finite element conduction model of the tank wall. The predictive capability of the model was assessed by comparing the model's predictions with experimental results presented in a companion paper [8]. The results of zonal models are unfortunately not consistent, and can vary depending on the correlations used to model the heat and mass transport between the different zones.

Both the homogeneous and zonal thermodynamic models describe the tank in a lumped approach and are, therefore, unable to capture the thermal stratification which develops inside the two phases as a result of fluid convection and the thermal boundary layer at the tank wall. To overcome the limitations of the previous models a one-dimensional dynamic model describing temperature stratification effects driven by natural convection was developed in [20]. Another approach was used by Panzarella and Kassemi, who coupled a lumped thermodynamic model of the vapor region to the full set of conservation equations inside the liquid region [81–83]. This model allowed to visualize liquid thermal stratification and flow field and the effects caused by the variation of the heat flux application point.

The model that we have implemented belongs to the class of the zonal models, and it has been developed in order to have an engineering tool for preliminary and rapid estimation of the main quantities of interest for the thermo-fluid-dynamics characterization of the behavior of cryogenic propellant in tanks (pressurization rate, evaporated mass, etc.). For this reason, this model will also be used, in Chaps. 4 and 5, to make a comparison with the results obtained with our CFD model.

2.1 Description of the model

A cylindrical tank of volume, V, radius, R, height, H, and liquid height, H_l, is considered in the case when the gravity/inertia force is parallel to its axis. It is partially filled with a liquid propellant, and its ullage can be filled either with a mixture of the propellant in the vapor phase and of a pressurant gas, or only with the propellant in the vapor phase. The 0D model schematizes the tank as a volume consisting of 5 Control Volumes (CVs): one for the liquid phase, one for the ullage (which can also be multi-component), one for the film, one for the wall in contact with the ullage, and one for the wall in contact with the liquid phase. Control volumes are schematized in Fig. 2.1 (a).

Film refers to the saturated vapor layer that separates the liquid and vapor control volumes, and it is assumed to be in quasi-equilibrium conditions (although the conditions in the tank are of non-equilibrium), and having negligible mass.

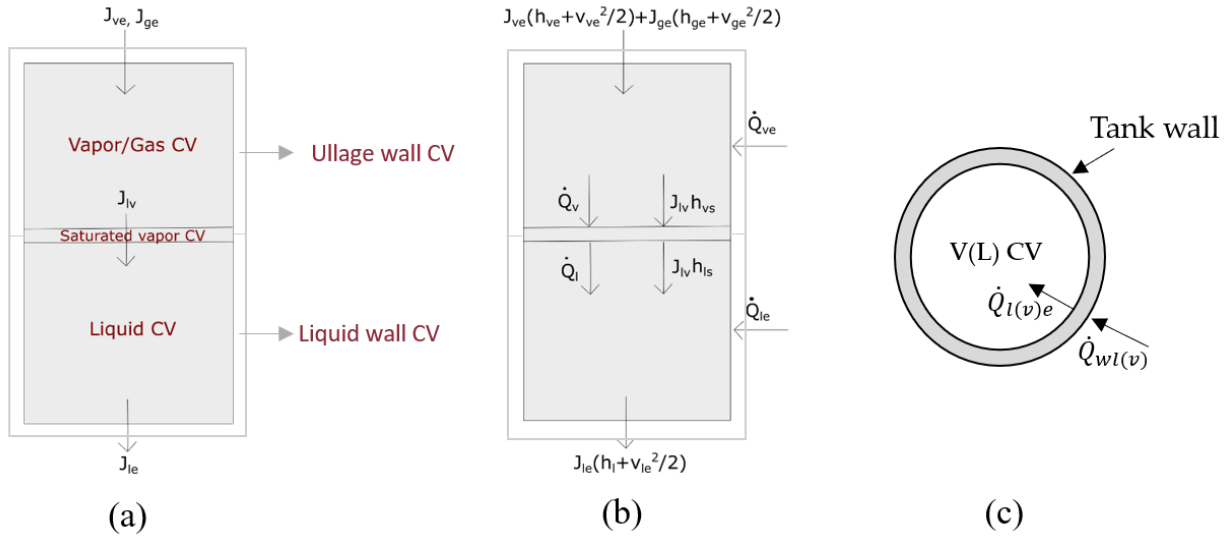

Figure 2.1: 0D model schematics of: (a) control volumes and mass transfers (b) heat transfers for the fluid control volumes (c) heat transfers for the wall control volumes.

The system is described by 12 state variables:

- 3 masses (liquid mass, m_l, vapor mass, m_v, and gas mass, m_g);
- 5 temperatures (liquid temperature, T_l, ullage temperature, T_u, film temperature, T_f, temperature of the wall adjacent to the liquid, T_{wl}, and temperature of the wall adjacent to the vapor, T_{wv});

- 2 partial pressures (the vapor partial pressure, p_v, and the gas partial pressure, p_g, whose sum is expressed as p);
- the ullage volume, V_u;
- the interface phase change mass flow rate, J_{lv}.

The conservation equations are 8:

- 3 mass conservation equations (for the liquid, vapor, and gas, respectively);
- 5 energy conservation equations (for the liquid, ullage, film, wall adjacent to the ullage, and wall adjacent to the liquid, respectively).

In order to close the system, 4 Equation of States (EoSs) have been used:

- the ideal gas EoS for the vapor;
- the ideal gas EoS for the gas;
- the equation of saturation vapor pressure for the film;
- the incompressible EoS for the liquid.

2.2 Conservation equations for the fluid control volumes

The mass conservation equations for the liquid, vapor and gas phases are:

$$\dot{m}_l = J_{lv} - J_{le} \tag{2.1}$$

$$\dot{m}_v = -J_{lv} + J_{ve} \tag{2.2}$$

$$\dot{m}_g = J_{ge} \tag{2.3}$$

where J_{le}, J_{ve} and J_{ge} are mass flow rates of liquid, vapor and gas, respectively. Their sign is positive or negative depending on whether the fluids enter (liquid filling, active pressurization) or leave (liquid draining, ullage venting) the respective control volumes. J_{lv} is an interfacial mass flow rate due to phase change. The mass transfers are schematized in Fig. 2.1 (a).

The energy conservation equations for the ullage and for the liquid are:

$$\frac{d}{dt}(m_v e_v + m_g e_g) = \dot{Q}_{ve} - \dot{Q}_v + \dot{W} - J_{lv} h_{vs} + J_{ve}\left(h_{ve} + \frac{v_{ve}^2}{2}\right) + J_{ge}\left(h_{ge} + \frac{v_{ge}^2}{2}\right) \tag{2.4}$$

$$\frac{d}{dt}(m_l e_l) = \dot{Q}_{le} + \dot{Q}_l + \dot{W} + J_{lv} h_{ls} - J_{le}\left(h_l + \frac{v_{le}^2}{2}\right) \tag{2.5}$$

where $\dot{Q}_{ve}$ and $\dot{Q}_{le}$ are the heat transfer rates of the vapor and liquid control volumes with the adjacent walls. $\dot{Q}_l$ and $\dot{Q}_v$ are heat transfer rates between the interface and the adjacent phases, liquid and ullage, respectively. $\dot{W}$ is the power associated to the change in volume of the liquid or

ullage CV. h_{vs} and h_{ls} are the enthalpies of saturated vapor and of saturated liquid, respectively. h_{ve}, h_{ge} are the enthalpies of the vapor and of the gas, respectively, entering or leaving the ullage CV. While, v_{ve}, v_{ge} are their velocities. h_l is the enthalpy of the liquid entering or leaving the liquid CV. While, v_{le} is its velocity. The heat transfers for the fluid control volumes are schematized in Fig. 2.1 (b).

A few passages can be made on the left-hand side of Eq. (2.4) to make the derivatives of the state variables explicit:

$$\frac{d}{dt}(m_v e_v + m_g e_g) = e_v \frac{dm_v}{dt} + m_v \frac{de_v}{dt} + e_g \frac{dm_g}{dt} + m_g \frac{de_g}{dt} \tag{2.6}$$

Using the definition of partial derivative:

$$\frac{de_v}{dt} = \left(\frac{\partial e_v}{\partial T_u}\right)_{V_u} \frac{dT_u}{dt} + \left(\frac{\partial e_v}{\partial V_u}\right)_{T_u} \frac{dV_u}{dt} \tag{2.7}$$

$$\frac{de_g}{dt} = \left(\frac{\partial e_g}{\partial T_u}\right)_{V_u} \frac{dT_u}{dt} + \left(\frac{\partial e_g}{\partial V_u}\right)_{T_u} \frac{dV_u}{dt} \tag{2.8}$$

and remembering that:

$$\left(\frac{\partial e_v}{\partial T_u}\right)_{V_u} = c_{v,v} \tag{2.9}$$

$$\left(\frac{\partial e_v}{\partial V_u}\right)_{T_u} = 0 \tag{2.10}$$

$$\left(\frac{\partial e_g}{\partial T_u}\right)_{V_u} = c_{v,g} \tag{2.11}$$

$$\left(\frac{\partial e_g}{\partial V_u}\right)_{T_u} = 0 \tag{2.12}$$

one gets:

$$\frac{d}{dt}(m_v e_v + m_g e_g) = e_v \frac{dm_v}{dt} + e_g \frac{dm_g}{dt} + (m_v c_{v,v} + m_g c_{v,g}) \frac{dT_u}{dt} \tag{2.13}$$

A few passages can be made on the left-hand side of Eq. (2.5) to make the derivatives of the state variables explicit:

$$\frac{d}{dt}(m_l e_l) = m_l \frac{de_l}{dt} + e_l \frac{dm_l}{dt} \tag{2.14}$$

Using the definition of partial derivative:

$$\frac{de_l}{dt} = \left(\frac{\partial e_l}{\partial T_l}\right)_{p} \frac{dT_l}{dt} + \left(\frac{\partial e_l}{\partial p}\right)_{T_l} \frac{dp}{dt} \tag{2.15}$$

and remembering that:

$$\left(\frac{\partial e_l}{\partial T_l}\right)_{p} = c_l \tag{2.16}$$

$$\left(\frac{\partial e_l}{\partial p}\right)_{T_l} = 0 \tag{2.17}$$

one gets:

$$\frac{d}{dt}(m_l e_l) = e_l \frac{dm_l}{dt} + m_l c_l \frac{dT_l}{dt} \tag{2.18}$$

The term $\dot{W}$, as already said, is the power associated to the change in volume of the liquid or of the ullage CV (the volume of the the CV is indicated as V_{CV}):

$$\dot{W} = -p\frac{dV_{CV}}{dt} = \begin{cases} -p\dfrac{dV_u}{dt} & for\ ullage\ CV \\ -p\dfrac{d(V - V_u)}{dt} = p\dfrac{dV_u}{dt} & for\ liquid\ CV \end{cases} \tag{2.19}$$

So, Eq. (2.4) can be rewritten, using Eqs. (2.13) and (2.19), in its final form:

$$\begin{aligned} &e_v \frac{dm_v}{dt} + e_g \frac{dm_g}{dt} + \left(m_v c_{v,v} + m_g c_{v,g}\right) \frac{dT_u}{dt} + p\frac{dV_u}{dt} = \\ &\dot{Q}_{ve} - \dot{Q}_v + \dot{W} - J_{lv} h_{vs} + J_{ve}\left(h_{ve} + \frac{v_{ve}^2}{2}\right) + J_{ge}\left(h_{ge} + \frac{v_{ge}^2}{2}\right) \end{aligned} \tag{2.20}$$

Finally, Eq. (2.5) can be rewritten, using Eqs. (2.18) and (2.19), in its final form:

$$e_l \frac{dm_l}{dt} + m_l c_l \frac{dT_l}{dt} - p\frac{dV_u}{dt} = \dot{Q}_{le} + \dot{Q}_l + \dot{W} + J_{lv} h_{ls} - J_{le}\left(h_l + \frac{v_{le}^2}{2}\right) \tag{2.21}$$

The heat balance in the film control volume is:

$$\dot{Q}_v - \dot{Q}_l + J_{lv} h_{lv} = \frac{d}{dt}(m_f e_f) = 0 \tag{2.22}$$

where the right-hand side term is null because of the assumption of negligible mass for the film CV. In Eq. (2.22), h_{lv} indicates the latent heat of evaporation. The interfacial phase change mass flow rate, J_{lv}, as shown in Fig. 2.1 (a), is considered positive in case of condensation and negative in case of evaporation, and it is computed, from Eq. (2.22), as:

$$J_{lv} = \frac{\dot{Q}_l - \dot{Q}_v}{h_{vs} - h_{ls}} \tag{2.23}$$

2.3 Heat transfer rates

The total heat transfer rate of the vapor CV with the adjacent wall, $\dot{Q}_{ve}$, is the sum of two heat transfer rates due to convection, one with the top wall, $\dot{Q}_{top}$, and the other with the lateral wall, $\dot{Q}_{lat,v}$:

$$\dot{Q}_{ve} = \dot{Q}_{top} + \dot{Q}_{lat,v} \tag{2.24}$$

where $\dot{Q}_{top}$ is defined as:

$$\dot{Q}_{top} = \pi R^2 \gamma_{top,v}(T_{wv} - T_u) \tag{2.25}$$

with the heat transfer coefficient from a horizontal surface $\gamma_{top,v}$ expressed as [20, 41]:

$$\gamma_{top,v} = \frac{\lambda_{mix}}{R} \begin{cases} 0.54 Ra_{top,v}^{1/4} & 10^4 < Ra_{top,v} < 10^7 \\ 0.15 Ra_{top,v}^{1/3} & 10^7 \leq Ra_{top,v} < 10^{11} \end{cases} \tag{2.26}$$

Here, λ_{mix} is the thermal conductivity of the mixture made by the vapor and the gas. In addition, the Rayleigh number $Ra_{top,v}$, is defined as:

$$Ra_{top,v} = Gr_{top,v} Pr_{mix} \tag{2.27}$$

where Pr_{mix} is the Prandtl number of the mixture made by the vapor and the gas. Moreover, the Grashof number $Gr_{top,v}$ is defined as:

$$Gr_{top,v} = \frac{g\beta_{mix}(T_{wv} - T_u)R^3}{\nu_{mix}^2} \tag{2.28}$$

where, the coefficient of volumetric expansion, β_{mix}, has been expressed as that of an ideal gas (for which $\rho = p/(RT)$), being the ullage a mixture of ideal gases:

$$\beta_{mix} = -\frac{1}{\rho_{mix}}\left(\frac{\partial \rho_{mix}}{\partial T_u}\right)_p = \frac{1}{\rho_{mix}}\frac{p}{RT_u^2} = \frac{1}{T_u} \tag{2.29}$$

Instead, ν_{mix} is the kinematic viscosity of the mixture made by the vapor and the gas. The heat transfer rate with the lateral wall, $\dot{Q}_{lat,v}$ is expressed as:

$$\dot{Q}_{lat,v} = 2\pi R H_v \overline{\gamma}_{lat,v}(T_{wv} - T_u) \tag{2.30}$$

where H_v is the height of the ullage, defined as $H_v = H - H_l$, and $\overline{\gamma}_{lat,v}$ is the average of the local convection heat transfer coefficients for a vertical surface, and is defined as [20, 41]:

$$\overline{\gamma}_{lat,v} = \frac{\lambda_{mix}}{H_v}\begin{cases} 0.68 + 0.67(Ra_{H_v}\psi)^{1/4} & 10^5 < Ra_{H_v} < 10^9 \\ 0.15(Ra_{H_v}\psi)^{1/3} & 10^9 \leq Ra_{H_v} < 10^{11} \end{cases} \tag{2.31}$$

where $Ra_{H_v} = Gr_{H_v} Pr_{mix}$. Moreover, Gr_{H_v} is defined as:

$$Gr_{H_v} = \frac{g\beta_{mix}(T_{wv} - T_u)H_v^3}{\nu_{mix}^2} \tag{2.32}$$

and:

$$\psi = \left(1 + \left(\frac{0.492}{Pr_{mix}}\right)^{9/16}\right)^{-16/9} \tag{2.33}$$

The total heat transfer rate of the liquid CV with the adjacent wall, $\dot{Q}_{le}$, is the sum of the heat transfer rate with the bottom wall, $\dot{Q}_{bott}$, and of the heat transfer rate with the lateral wall, $\dot{Q}_{lat,l}$:

$$\dot{Q}_{le} = \dot{Q}_{bott} + \dot{Q}_{lat,l} \tag{2.34}$$

where $\dot{Q}_{bott}$ is defined as:

$$\dot{Q}_{bott} = \pi R^2 \gamma_{bott,l}(T_{wl} - T_l) \tag{2.35}$$

with the heat transfer coefficient from a horizontal surface $\gamma_{bott,l}$ expressed as in Eq. (2.26), but using, instead of λ_{mix} and $Ra_{top,v}$, the liquid thermal conductivity, λ_l, and the Rayleigh number, $Ra_{bott,l}$, defined as $Ra_{bott,l} = Gr_{bott,l} Pr_l$. Where, Pr_l is the liquid Prandtl number, and $Gr_{bott,l}$ is

expressed as:

$$Gr_{bott,l} = \frac{g\beta_l(T_{wl} - T_l)R^3}{\nu_l^2} \tag{2.36}$$

where, β_l is the coefficient of volumetric expansion of the liquid, and ν_l is the kinematic viscosity of the liquid. The heat transfer rate with the lateral wall, $\dot{Q}_{lat,l}$ is expressed as:

$$\dot{Q}_{lat,l} = 2\pi R H_l \overline{\gamma}_{lat,l}(T_{wl} - T_l) \tag{2.37}$$

where $\overline{\gamma}_{lat,l}$ is defined as in Eq. (2.31), but using, instead of λ_{mix}, H_v, and Ra_{H_v}, the liquid thermal conductivity, λ_l, and the Rayleigh number, Ra_{H_l}, defined as $Ra_{H_l} = Gr_{H_l}Pr_l$. Where Gr_{H_l} is expressed as in Eq. (2.36), but using H_l instead of R as reference length, and ψ is defined as in Eq. (2.33) but using Pr_l instead of Pr_{mix}.

The heat transfer rates between the interface and the adjacent phases, $\dot{Q}_l$ and $\dot{Q}_v$, are computed as the maximum between the heat transfer rate due to conduction and the one due to convection:

$$\dot{Q}_l = \pm max\left(\dot{Q}_l^{cond}, \dot{Q}_l^{conv}\right) \tag{2.38}$$

$$\dot{Q}_v = \pm max\left(\dot{Q}_v^{cond}, \dot{Q}_v^{conv}\right) \tag{2.39}$$

The positive sign in Eq. (2.38) is used when the film temperature is higher than the liquid temperature, and the negative sign is used in the opposite case. This convention leads to a positive heat transfer rate when it is from the film CV to the liquid CV, as shown in Fig. 2.1 (b). Instead, the positive sign in Eq. (2.39) is used when the vapor temperature is higher than the film temperature, and the negative sign is used in the opposite case. This convention leads to a positive heat transfer rate when it is from the vapor CV to the film CV, as shown in Fig. 2.1 (b). The heat transfer rates due due convection, $\dot{Q}_l^{conv}$ and $\dot{Q}_v^{conv}$, are computed as:

$$\dot{Q}_l^{conv} = \pi R^2 \gamma_{f,l}(T_l - T_f)H(T_l - T_f) \tag{2.40}$$

$$\dot{Q}_v^{conv} = \pi R^2 \gamma_{f,v}(T_f - T_v)H(T_f - T_v) \tag{2.41}$$

where $\gamma_{f,l}$ and $\gamma_{f,v}$ are computed from:

$$\gamma_{f,l} = \frac{\lambda_l}{R}\begin{cases} 0.54Ra_{f,l}^{1/4} & 10^4 < Ra_{f,l} < 10^7 \\ 0.15Ra_{f,l}^{1/3} & 10^7 \leq Ra_{f,l} < 10^{11} \end{cases} \tag{2.42}$$

$$Ra_{f,l} = Gr_{f,l}Pr_l = \frac{g\beta_l(T_l - T_f)R^3}{\nu_l^2}Pr_l \tag{2.43}$$

$$\gamma_{f,v} = \frac{\lambda_v}{R}\begin{cases} 0.54Ra_{f,v}^{1/4} & 10^4 < Ra_{f,v} < 10^7 \\ 0.15Ra_{f,v}^{1/3} & 10^7 \leq Ra_{f,v} < 10^{11} \end{cases} \tag{2.44}$$

$$Ra_{f,v} = Gr_{f,v}Pr_{mix} = \frac{g\beta_{mix}(T_f - T_v)R^3}{\nu_{mix}^2}Pr_{mix} \tag{2.45}$$

The Heaviside function, H, in Eqs. (2.40) and (2.41), takes into account the proper temperature condition required for natural convection to happen. Namely, natural convection can verify when, in a control volume, the lowermost fluid layers have a higher temperature than the uppermost ones. In the case when this condition is not verified, the Heaviside function cancels the convection term. The heat transfer rate between the interface and the adjacent phases due to conduction is computed through the Fourier's law. For this purpose, an interfacial temperature distribution has been derived through a finite difference discretization of the thermal diffusion equation, as it will be described in Sec. 2.4.

2.4 Stratified model at the interface

The heat transfer rate between the interface and the adjacent phases due to conduction is computed using the Fourier's law for the conductive heat flux, $\boldsymbol{q}^{cond}$:

$$\boldsymbol{q}^{cond} = -\lambda \nabla T \tag{2.46}$$

where λ is the material conductivity. In order to use this expression, it is necessary to know the liquid and ullage temperature in close proximity of the interface. Even if the interface is assumed massless, ans so with null thickness, an interfacial temperature distribution has been derived assuming the interface as 1D stratified, i.e. made by a certain number of layers, n_l, in the liquid CV, and a certain number of layers, n_v, in the vapor CV. Each interface layer belonging to the liquid CV has a fixed thickness, Δx_l, while, each interface layer belonging to the ullage CV has a fixed thickness, Δx_v. The interfacial temperature distribution has been, then, derived through the thermal diffusion equation:

$$\frac{\partial T}{\partial t} = \alpha \frac{\partial^2 T}{\partial x^2} \tag{2.47}$$

where α is the thermal diffusivity. This equation has been discretized using a finite difference scheme:

$$\frac{\partial T(i)}{\partial t} \approx \frac{\alpha}{\Delta x^2} \left[T(i+1) + T(i-1) - 2T(i) \right] \tag{2.48}$$

In particular, the following differential equations have been integrated to compute the temperatures in the $n_l - 1$ nodes close to the interface, and belonging to the liquid CV, $T_{f,l}$:

$$\frac{\partial T_{f,l}(i)}{\partial t} \approx \frac{\alpha_l}{\Delta x_l^2} \left[T_{f,l}(i+1) + T_{f,l}(i-1) - 2T_{f,l}(i) \right] \tag{2.49}$$

$$\frac{\partial T_{f,l}(1)}{\partial t} \approx \frac{\alpha_l}{\Delta x_l^2} \left[T_{f,l}(2) + T_f - 2T_{f,l}(1) \right] \tag{2.50}$$

$$\frac{\partial T_{f,l}(n_l - 1)}{\partial t} \approx \frac{\alpha_l}{\Delta x_l^2} \left[T_l + T_{f,l}(n_l - 2) - 2T_{f,l}(n_l - 1) \right] \tag{2.51}$$

where α_{mix} is the thermal diffusivity of the mixture made by the vapor and the gas. While, the following differential equations have been used to compute the temperatures in the $n_v - 1$ nodes

close to the interface, and belonging to the ullage CV, $T_{f,v}$:

$$\frac{\partial T_{f,v}(i)}{\partial t} \approx \frac{\alpha_{mix}}{\Delta x_v^2} \left[T_{f,v}(i+1) + T_{f,v}(i-1) - 2T_{f,v}(i)\right] \tag{2.52}$$

$$\frac{\partial T_{f,v}(1)}{\partial t} \approx \frac{\alpha_{mix}}{\Delta x_v^2} \left[T_{f,v}(2) + T_f - 2T_{f,v}(1)\right] \tag{2.53}$$

$$\frac{\partial T_{f,v}(n_v-1)}{\partial t} \approx \frac{\alpha_{mix}}{\Delta x_v^2} \left[T_u + T_{f,v}(n_v-2) - 2T_{f,v}(n_v-1)\right] \tag{2.54}$$

With this procedure, the 0D model has been coupled with a stratified model at the interface.

So, once the temperatures of the vapor and liquid interface layers closest to the film CV are found, they are use to compute the heat transfer rates between the interface and the adjacent phases due to conduction, through the Fourier's law:

$$\dot{Q}_l^{cond} = -\lambda_l \pi R^2 \frac{T_{f,l}(1) - T_f}{\Delta x} \tag{2.55}$$

$$\dot{Q}_v^{cond} = -\lambda_{mix} \pi R^2 \frac{T_{f,v}(1) - T_f}{\Delta x} \tag{2.56}$$

2.5 Internal energy and enthalpy

In this section, the thermodynamic relations used to compute the specific internal energy and the specific enthalpy for the liquid, the vapor, and the gas are given.

2.5.1 Ideal gas

Considering the specific internal energy of a perfect gas as a function of specific volume and temperature, and differentiating it [92]:

$$\begin{cases} e = e(T, v) \\ de = \left(\dfrac{\partial e}{\partial T}\right)_v dT + \left(\dfrac{\partial e}{\partial v}\right)_T dv \end{cases} \tag{2.57}$$

and, remembering that, for a perfect gas ($p = \rho RT$):

$$\begin{cases} \left(\dfrac{\partial e}{\partial T}\right)_v = c_v = const \\ \left(\dfrac{\partial e}{\partial v}\right)_T = 0 \end{cases} \tag{2.58}$$

the expression of the specific internal energy for the vapor and for the gas is obtained:

$$e = e^0 + c_v(T - T^0) \tag{2.59}$$

where c_v is the specific heat capacity at constant volume. In this work, a reference temperature of $T^0 = 0$ K has been considered, to which corresponds $e^0 = 0$ J/kg.

Considering the specific enthalpy of a perfect gas as a function of temperature and pressure, and differentiating it [92]:

$$\begin{cases} h = h(T,p) \\ dh = \left(\dfrac{\partial h}{\partial T}\right)_p dT + \left(\dfrac{\partial h}{\partial p}\right)_T dp \end{cases} \tag{2.60}$$

and remembering that, for a perfect gas:

$$\begin{cases} \left(\dfrac{\partial h}{\partial T}\right)_p = c_p \\ \left(\dfrac{\partial h}{\partial p}\right)_T = 0 \end{cases} \tag{2.61}$$

the expression of the specific enthalpy for the vapor and for the gas is obtained:

$$h = h^0 + c_p(T - T^0) \tag{2.62}$$

where c_p is the specific heat capacity at constant pressure. In this work, a reference pressure of $p^0 = 0$ Pa has been considered, to which corresponds $h^0 = 0$ J/kg.

2.5.2 Incompressible liquid

The liquid is treated as incompressible ($\rho_l = const$). Considering its specific internal energy as a function of temperature and pressure, and differentiating it:

$$\begin{cases} e = e(T,p) \\ de = \left(\dfrac{\partial e}{\partial T}\right)_p dT + \left(\dfrac{\partial e}{\partial p}\right)_T dp \end{cases} \tag{2.63}$$

and remembering that, for an incompressible liquid:

$$\begin{cases} \left(\dfrac{\partial e}{\partial T}\right)_p = c = const \\ \left(\dfrac{\partial e}{\partial p}\right)_T = 0 \end{cases} \tag{2.64}$$

the expression of the specific internal energy for the liquid is obtained:

$$e = e^0 + c(T - T^0) \tag{2.65}$$

where c is the specific heat capacity of the liquid. Considering the specific enthalpy of an incompressible liquid as a function of temperature and pressure, and differentiating it [92]:

$$\begin{cases} h = h(T,p) \\ dh = \left(\dfrac{\partial h}{\partial T}\right)_p dT + \left(\dfrac{\partial h}{\partial p}\right)_T dp \end{cases} \tag{2.66}$$

and remembering that, for an incompressible liquid:

$$\begin{cases} \left(\frac{\partial h}{\partial T}\right)_p = c = const \\ \left(\frac{\partial h}{\partial p}\right)_T = \frac{1}{\rho} \end{cases} \tag{2.67}$$

the expression of the specific enthalpy for the liquid is obtained:

$$h = h^0 + c(T - T^0) + \frac{p - p^0}{\rho} \tag{2.68}$$

2.6 Mixture properties for ullage gas

The ullage is considered a homogeneous mixture of pressurant gas and evaporated propellant. Mixture properties, i.e. specific heat at constant pressure, $c_{p,mix}$, thermal conductivity, λ_{mix}, and kinematic viscosity, ν_{mix}, can be obtained using formulas suggested by various sources in the literature [18, 87]:

$$c_{p,mix} = c_{p,g}Y_g + c_{p,v}Y_v \tag{2.69}$$

$$\lambda_{mix} = \lambda_g X_g + \lambda_v X_v \tag{2.70}$$

$$\nu_{mix} = \frac{\nu_g X_g \sqrt{M_g} + \nu_v X_v \sqrt{M_v}}{X_g \sqrt{M_g} + X_v \sqrt{M_v}} \tag{2.71}$$

In the previous relations, subscripts "g" and "v" are used for pressurant gas and vapor, respectively. Moreover, M_i is the molar mass of the i element, Y_i is its mass fraction, and X_i is its molar fraction:

$$Y_i = \frac{m_i}{\sum_{i=v,g} m_i} \tag{2.72}$$

$$X_i = \frac{\frac{m_i}{M_i}}{\sum_{i=v,g} \frac{m_i}{M_i}} \tag{2.73}$$

2.7 Equations of state

The ideal gas law is:

$$pV = nR_u T = mRT \tag{2.74}$$

where p, V, T, and m are the pressure, volume, temperature, and mass respectively, n is the number of moles of the gas, R_u is the ideal gas constant, and R is the specific gas constant, $R = R_u/M_i$. Making the derivative of Eq. (2.74), and writing it in a useful form, where the derivatives of the state variables are made explicit:

$$\frac{d}{dt}(pV) = \frac{d}{dt}(mRT) \tag{2.75}$$

$$p\frac{dV}{dt} + V\frac{dp}{dt} - Rm\frac{dT}{dt} - RT\frac{dm}{dt} = 0 \tag{2.76}$$

Eq. (2.76) can be written for the vapor as:

$$p_v\frac{dV_u}{dt} + V_u\frac{dp_v}{dt} - R_v m_v\frac{dT_u}{dt} - R_v T_u\frac{dm_v}{dt} = 0 \tag{2.77}$$

and for the gas as:

$$p_g\frac{dV_u}{dt} + V_u\frac{dp_g}{dt} - R_g m_g\frac{dT_u}{dt} - R_g T_u\frac{dm_g}{dt} = 0 \tag{2.78}$$

The liquid EoS is derived by using the assumption of incompressibility ($\rho_l = const$), and making the derivative of the expression of the liquid mass:

$$\rho_l = const = \frac{m_l}{V_l} \tag{2.79}$$

$$\frac{dm_l}{dt} = \frac{d}{dt}\left(\rho_l V_l\right) = \rho_l\frac{dV_l}{dt} = -\rho_l\frac{dV_u}{dt} \tag{2.80}$$

$$\frac{dm_l}{dt} + \frac{m_l}{V - V_u}\frac{dV_u}{dt} = 0 \tag{2.81}$$

Finally, the equation of saturation vapor pressure for the film is added to complete the set of governing equations. In particular, when the propellant is H_2, the following equation is used [17, 20, 80]:

$$p_v = p_c\left(\frac{T_f}{T_c}\right)^n \tag{2.82}$$

where p_c and T_c are the critical pressure and temperature for H_2 ($p_c = 1.315$ MPa and $T_c = 33.2$ K) and $n = 5$. Eq. (2.82) is used to compute the film temperature, once the vapor partial pressure is calculated by integrating the Ordinary Differential Equations (ODEs) system that will be presented in Sec. 2.8.

2.8 Governing equations: Matrix format

ODEs (2.1), (2.2), (2.3), (2.20), (2.21), (2.77), (2.78), and (2.81) can be rewritten in a matrix format:

$$A\,[8,8] \cdot X\,[8] = B\,[8] \tag{2.83}$$

where A is the "mass" matrix, X is the unknown vector, which is made by the derivatives of

the state variables, and B is the vector with the constant terms:

$$A = \begin{bmatrix} 1 & 0 & 0 & 0 & 0 & 0 & 0 & 0 \\ 0 & 1 & 0 & 0 & 0 & 0 & 0 & 0 \\ 0 & 0 & 1 & 0 & 0 & 0 & 0 & 0 \\ e_l & 0 & 0 & m_l c_l & 0 & 0 & 0 & -p \\ 0 & e_v & e_g & 0 & m_v c_{v,v} + m_g c_{v,g} & 0 & 0 & p \\ 0 & -R_v T_u & 0 & 0 & -R_v m_v & V_u & 0 & p_v \\ 0 & 0 & -R_g T_u & 0 & -R_g m_g & 0 & V_u & p_g \\ 1 & 0 & 0 & 0 & 0 & 0 & 0 & \frac{m_l}{V - V_u} \end{bmatrix} \tag{2.84}$$

$$X = \begin{bmatrix} \frac{dm_l}{dt} \\ \frac{dm_v}{dt} \\ \frac{dm_g}{dt} \\ \frac{dT_l}{dt} \\ \frac{dT_u}{dt} \\ \frac{dp_v}{dt} \\ \frac{dp_g}{dt} \\ \frac{dV_u}{dt} \end{bmatrix} \tag{2.85}$$

$$B = \begin{bmatrix} J_{lv} - J_{le} \\ -J_{lv} + J_{ve} \\ J_{ge} \\ \dot{Q}_{le} + \dot{Q}_l + J_{lv} h_{ls} - J_{le} \left(h_l + \frac{v_{le}^2}{2} \right) \\ \dot{Q}_{ve} - \dot{Q}_v - J_{lv} h_{vs} + J_{ve} \left(h_{ve} + \frac{v_{ve}^2}{2} \right) + J_{ge} \left(h_{ge} + \frac{v_{ge}^2}{2} \right) \\ 0 \\ 0 \\ 0 \end{bmatrix} \tag{2.86}$$

The unknown vector is found from Eq. (2.83):

$$X = A^{-1} B \tag{2.87}$$

The matrix format just derived is very useful because it can be easily integrated in order to find 8 of the state variables. In this work, ODE45 Matlab® algorithm has been used to solve the 8 ODEs system.

2.9 Conservation equations for the wall control volumes

The energy conservation equations for the wall in contact with the liquid CV and for the wall in contact with the ullage CV are:

$$c_w \frac{d}{dt}(m_{wl} T_{wl}) = \begin{cases} \dot{Q}_{wl} - \dot{Q}_{le} + c_w \dot{m}_{wl} T_{wl} & \dot{m}_{wl} < 0 \\ \dot{Q}_{wl} - \dot{Q}_{le} + c_w \dot{m}_{wl} T_{wv} & \dot{m}_{wl} \geq 0 \end{cases} \tag{2.88}$$

$$c_w \frac{d}{dt}(m_{wv} T_{wv}) = \begin{cases} \dot{Q}_{wv} - \dot{Q}_{ve} + c_w \dot{m}_{wv} T_{wl} & \dot{m}_{wl} < 0 \\ \dot{Q}_{wv} - \dot{Q}_{ve} + c_w \dot{m}_{wv} T_{wv} & \dot{m}_{wl} \geq 0 \end{cases} \tag{2.89}$$

where, m_{wv} and m_{wl} are the mass of the wall adjacent to the vapor CV and liquid CV, respectively. $\dot{Q}_{wv}$ and $\dot{Q}_{wl}$ are the heat transfer rates entering the wall in contact with the ullage and the wall in contact with the liquid, from the outside. While, the last terms in the right-hand sides of Eqs. (2.88) - (2.89) represent the flow of internal energy along the tank walls due to motion of the liquid level (note that $\dot{m}_{wl}$ = - $\dot{m}_{wv}$). The direct heat exchange, due to conduction, between the two parts of the wall has been ignored. The heat transfers for the wall CVs are schematized in Fig. 2.1 (c).

2.10 Results

In this section, at first the 0D model is verified through the comparison, for two operating conditions, with the results obtained with a 1D model developed by NASA. Secondly, a parametric study necessary to find proper values for the parameters of the stratified interface model is presented.

2.10.1 Verification with NASA 1D code results

The previously described model has been verified with the results of a 1D model developed and implemented by NASA [20]. The related code is open source [19]. Two operating conditions have been simulated, the first is the storage regime, and the second is the blowdown regime. The geometry and the initial conditions are the same for the two cases, and the physical time simulated is 5000 s in each case.

NASA 1D model

The 1D model developed by NASA [20] has the same control volumes of the 0D model just presented, but the liquid and ullage CVs are divided into multiple horizontal control volumes. Moreover, each of the latter is subdivided in two sub volumes: a torus-shaped element of the boundary layer, adjacent to the lateral wall of the tank, and exchanging heat with it, and a cylinder-shaped bulk element, which is coaxial with the tank vertical axis. A schematics of this stratified model is presented in Fig. 2.2. This model, differently from the 0D model, allows to describe the temperature stratification effects driven by natural convection.

Test case description

The considered tank is a liquid H_2 tank. The parameters of the cylindrical tank have been taken similar to those of the Space Shuttle external tank [100], i.e. radius, height, and wall thickness of R = 4.21 m, H = 29.56 m, and t_w= 0.1 m, respectively. The wall material is aluminum, whose specific heat and density have been considered constant and equal to c_w = 500 J/(kg K) and ρ_w = 2700 kg/m^3, respectively. The tank is initially filled at 50% of its volume with liquid H_2. The ullage is initially filled with a mixture of gaseous H_2 and gaseous He, whose partial pressures are $p_v(0) = p_g(0)$ = 1 atm. The liquid volume is made only by liquid H_2, because of the non-condensable He gas assumption (indeed the He gas saturation temperature at $p_v(0)$ is 4.2238 K).

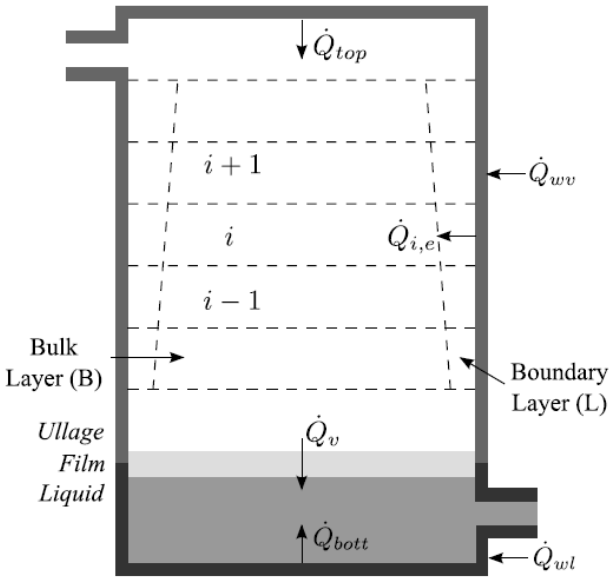

Figure 2.2: Schematics of the 1D NASA model, from [20].

Table 2.1: Liquid, vapor, and gas parameters.

Component	Parameters values
Liquid H_2	$\rho_l = 71.1$ [kg/m^3], $c_l = 9450$ [J/(kg K)], $\lambda_l = 0.0984$ [W/(m K)], $\mu_l = 1.3 \cdot 10^{-5}$ [Pa s], $\beta_l = 0.02$ [1/K]
Gaseous H_2	$M_v = 2.01588 \cdot 10^{-3}$ kg/mol, , $c_{p,v} = 14320$ [J/(kg K)], $c_{v,v} = 10160$ [J/(kg K)], $\lambda_v = 0.0166$ [W/(m K)], $\mu_v = 3.4 \cdot 10^{-6}$ [Pa s]
Gaseous He	$M_g = 4.002602 \cdot 10^{-3}$ kg/mol, , $c_{p,g} = 5193$ [J/(kg K)], $c_{v,g} = 3121$ [J/(kg K)], $\lambda_g = 0.0262$ [W/(m K)], $\mu_g = 3.5821 \cdot 10^{-6}$ [Pa s]

The initial temperatures of the liquid and of the ullage are $T_l(0) = T_u(0) = 20$ K, and the initial temperature of the wall is $T_w(0) = 21$ K. Moreover, the tank absorbs heat from the environment, and the heat transfer rate is different under the two operating conditions considered. The liquid, vapor, and gas parameters have been modeled as constant, and are summarized in Tab. 2.1.

Storage regime

The first operating condition considered is the storage regime. During it, the tank is closed, thus no mass is removed or added to it, and the tank absorbs heat at a rate of 10 kW, which, for the chosen tank, roughly equates the radiation heat flux from the Sun. The tank is in normal gravity ($g_E = 9.81$ m/s^2). The absorbed heat causes tank self-pressurization, as it is apparent in Fig. 2.3, showing the evolutions of the vapor (top) and the gas (bottom) partial pressures, obtained both with the 0D model and with the 1D model developed by NASA. Fig. 2.4 shows the temperature evolutions obtained with the 0D model in the the liquid CV (top) and in the ullage CV (bottom). In the same figure, the average of the bulk temperatures in the ullage and liquid CVs obtained with the 1D NASA model are also shown for comparison. The qualitative behavior described by the two models is the the same both for the pressure and for the temperature evolutions, and there is also a reasonably good quantitative agreement between the two models. On the contrary, greater discrepancies between the estimations made with the two models are obtained for the liquid

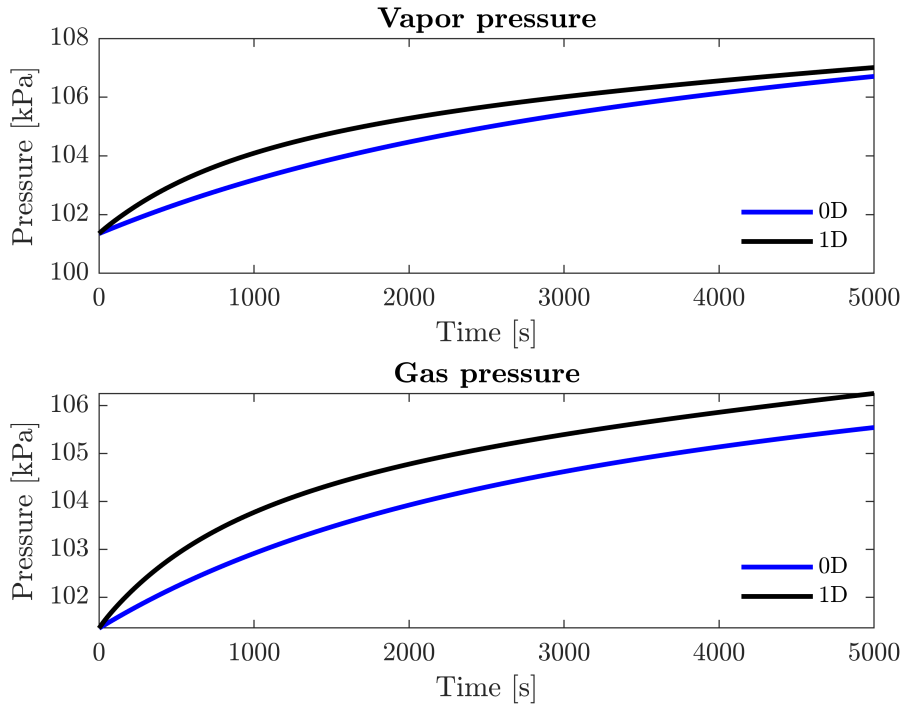

Figure 2.3: Storage regime: evolutions of the vapor (top) and the gas (bottom) partial pressures, obtained with the 0D and with the 1D NASA models.

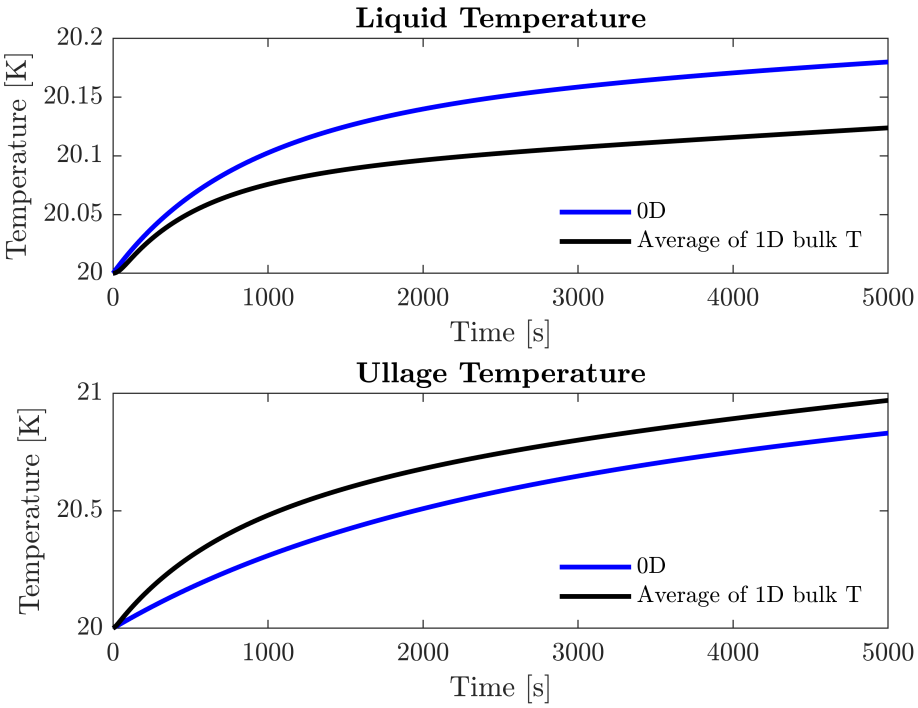

Figure 2.4: Storage regime: temperature evolutions obtained with the 0D and with the 1D NASA model in the the liquid CV (top) and in the ullage CV (bottom). The 1D results are the average of the bulk temperatures in the respective control volumes.

and vapor mass evolutions, which are shown in Fig. 2.5. Even if the 0D model predicts a higher evaporated mass than the 1D model after approximately 1500 s, the vapor pressure estimated

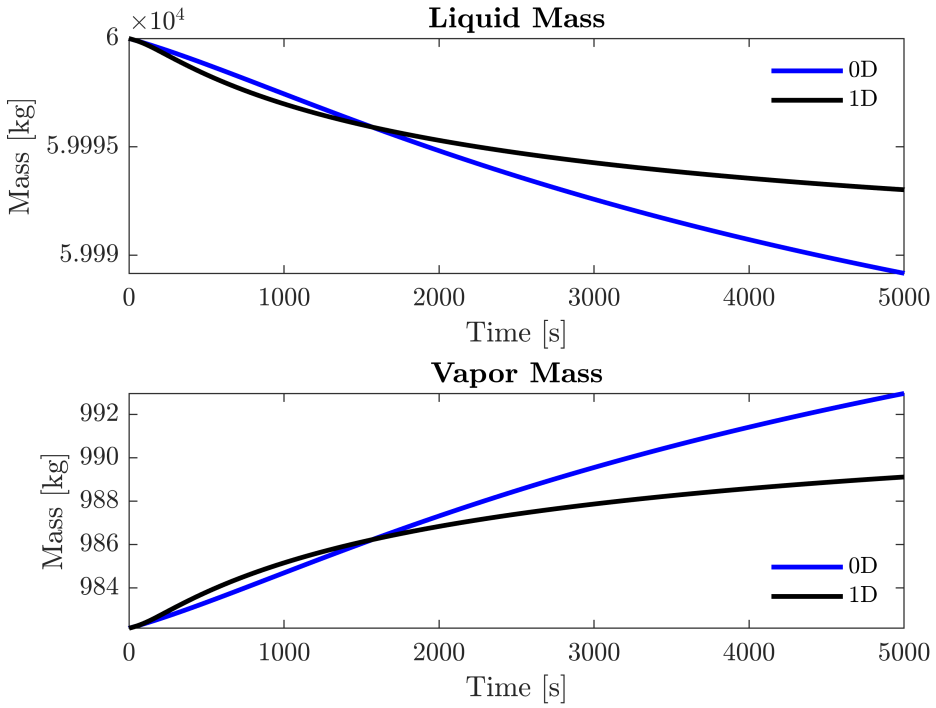

Figure 2.5: Storage regime: evolutions of the liquid mass (top) and of the vapor mass (bottom) obtained with the 0D and with the 1D NASA models.

with the 1D model is higher, this suggests that the pressure increase is mainly due to the ullage temperature increase than to the evaporation. This is confirmed by the average of the 1D bulk temperature in the ullage, which is higher than the 0D estimation.

Blowdown regime

The second operating condition considered is the blowdown regime. During it, liquid H_2 is removed from the tank bottom, with a constant mass flow rate, $J_{le} = 10$ kg/s, and the tank absorbs heat at a rate of 20 kW. Moreover, the tank is in normal gravity. Fig. 2.6 shows the evolutions of the vapor (top) and the gas (bottom) partial pressures, obtained both with the 0D model and with the 1D model developed by NASA. Both the qualitative and quantitative agreement between the pressure evolutions obtained with the two models is very good. Both vapor and gas partial pressures show a rapidly decreasing behavior because of the increase in ullage volume, due to the propellant draining. Fig. 2.7 shows the temperature evolutions obtained with the 0D model in the the liquid CV (top) and in the ullage CV (bottom). On the same figure, the average of the bulk temperatures in the ullage and liquid CVs obtained with the 1D NASA model are also shown for comparison. Even if the temperature evolutions obtained with the 0D model are qualitatively similar to the ones obtained with the 1D model, there are some quantitative discrepancies, with a maximum temperature difference of approximately 0.5 K in the ullage temperature estimates, at about 2000 s. But, in this case, a better quantitative agreement between the estimations made with the two models are obtained for the liquid and vapor mass evolutions, which are shown in Fig. 2.8. Both models predict a decrease of the liquid mass due to both the propellant draining and to evaporation. Instead, the vapor mass increases due to evaporation, and the 0D model predicts a

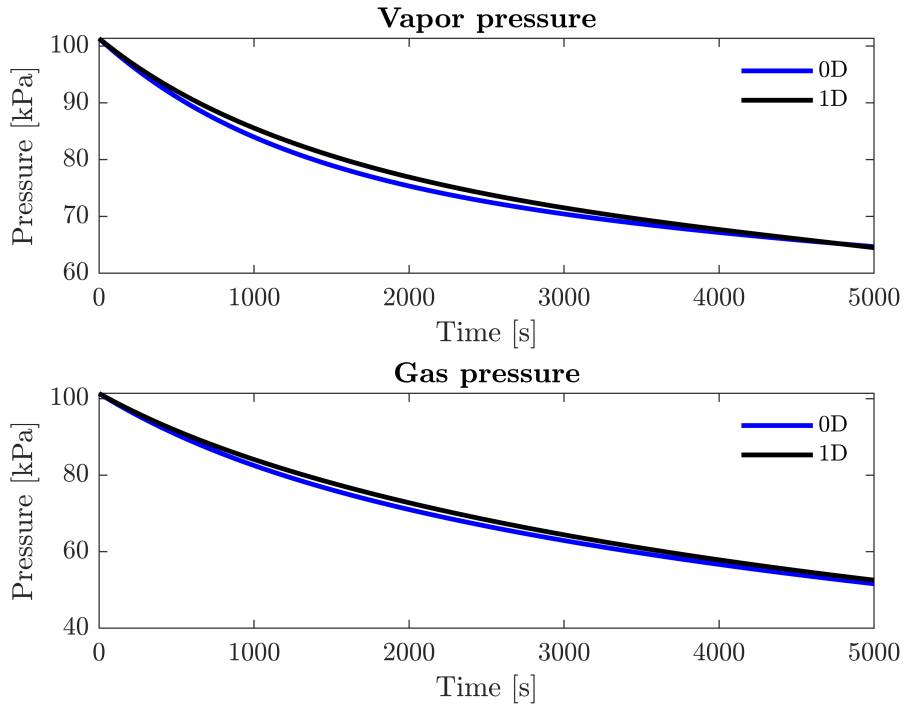

Figure 2.6: Blowdown regime: evolutions of the vapor (top) and the gas (bottom) partial pressures, obtained with the 0D and with the 1D NASA models.

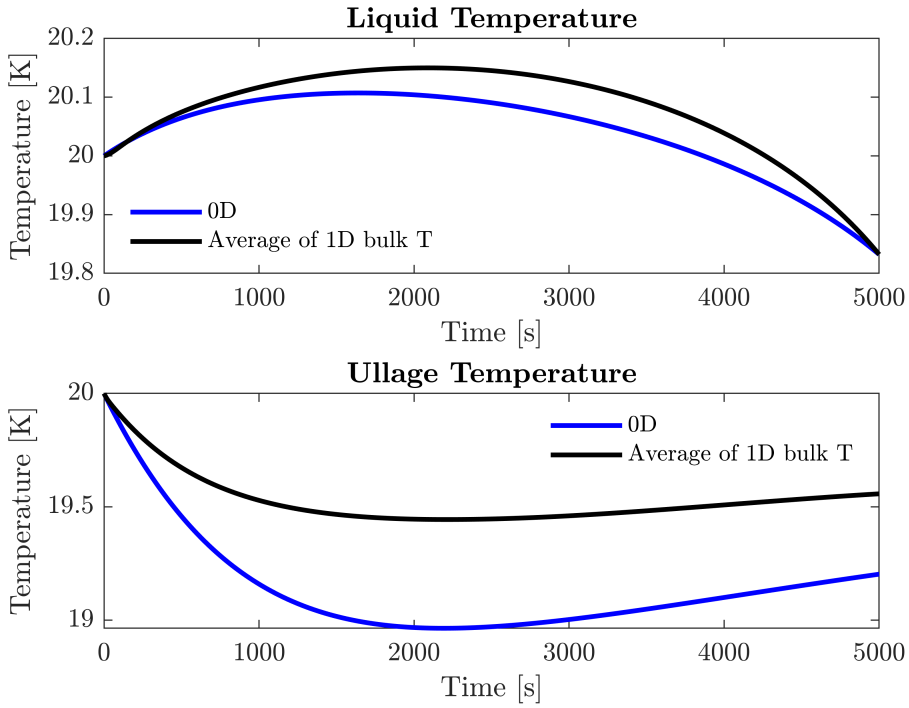

Figure 2.7: Blowdown regime: temperature evolutions obtained with the 0D and with the 1D NASA model in the the liquid CV (top) and in the ullage CV (bottom). The 1D results are the average of the bulk temperatures in the respective control volumes.

higher evaporation rate than the 1D model after about 1800 s.

Finally, a comparison between the results of the two models shows that the 0D model is able to

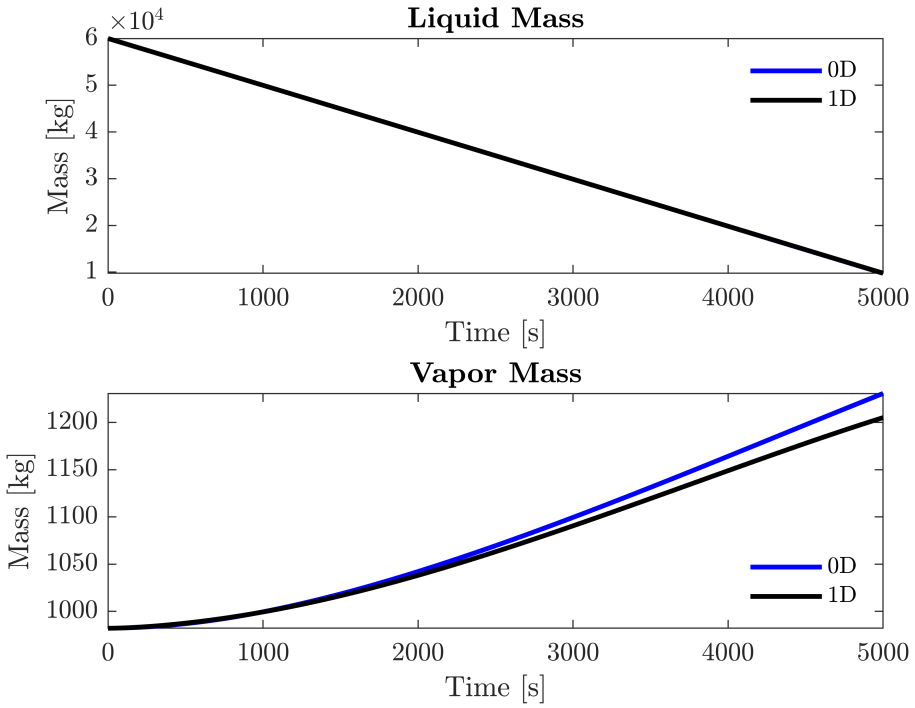

Figure 2.8: Blowdown regime: evolutions of the liquid mass (top) and of the vapor mass (bottom) obtained with the 0D and with the 1D NASA models.

describe, with reasonable accuracy, the main observables of the thermo-fluid-dynamics characterization, both during the storage and the during the blowdown regime. The greatest discrepancies arise, during the storage regime, for the evolution of the liquid and vapor mass, even if these last only marginally affect the pressure evolution, and, during the blowdown regime, for the evolution of liquid and ullage temperature. This result underscores the potential of the 0D model, which, moreover, requires less effort to be implemented with respect to the 1D model. However, the latter is essential in the case when the effects related to the temperature stratification have to be considered.

2.10.2 Parametric study for the variables of the stratified interface model

The proper value for the integration distance, i.e. the total thickness of the interface layers, which is called $t_{f,v}$ in the ullage CV and $t_{f,l}$ in the liquid CV, and the proper values for the thickness of each interface layer in the liquid CV and ullage CV, Δx_l and Δx_v, respectively, can be found through a parametric study. Here, the parametric study carried out in the case of the storage regime is presented, as an example.

In this work, the proper value for $t_{f,l}$ has been found by fixing the values of $t_{f,v} = 10$ cm and $\Delta x_l = \Delta x_v = 1$ mm, and letting $t_{f,l}$ assume the following values $t_{f,l} = [2, 5, 10, 15, 17, 18, 20, 30, 40, 60]$ cm. In Fig. 2.9, the interface temperature distributions, in the liquid CV, obtained for the different values of $t_{f,l}$ are plotted. In each subfigure, the temperature distribution is plotted at the three times of 1000 s, 3000 s, and 5000 s. As $t_{f,l}$ increases, the interface temperature distribution, far from both T_l and T_f, becomes independent of the value of both $t_{f,l}$ and time. The conductive heat transfer rate between the liquid CV and the film CV, at 3000 s, is plotted, in Fig. 2.10, as a function of $t_{f,l}$. Convergence in the values of $\dot{Q}_l^{cond}$ and $\dot{Q}_v^{cond}$ is reached for a value of $t_{f,l} = 15$ cm, as it is

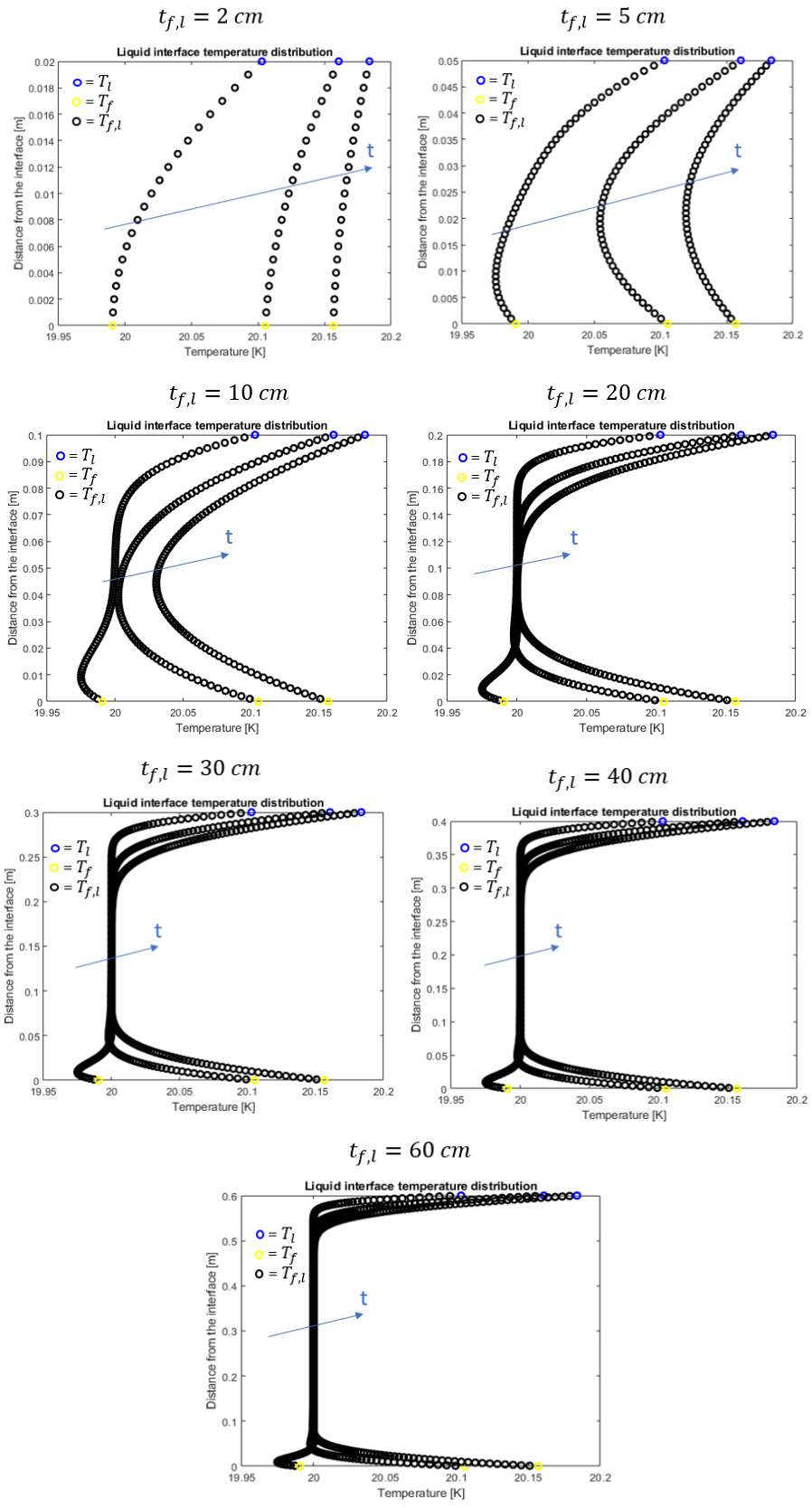

Figure 2.9: $t_{f,l}$ parametric study: interface temperature distributions, in the liquid CV, obtained for the different values $t_{f,l}$. In each subfigure, the temperature distribution is plotted at the three times of 1000 s, 3000 s, and 5000 s.

clear both in Fig. 2.10 and in Tab. 2.2, so this value of $t_{f,l}$ has been selected.

Table 2.2: $t_{f,l}$ parametric study: conductive heat transfer rate between the liquid CV and the film CV, $\dot{Q}_l^{cond}$, and conductive heat transfer rate between the ullage CV and the film CV, $\dot{Q}_v^{cond}$, for different values of $t_{f,l}$. Both $\dot{Q}_l^{cond}$ and $\dot{Q}_v^{cond}$ are taken at 3000 s.

$t_{f,l}$ [cm]	$\dot{Q}_l^{cond}$ [W]	$\dot{Q}_v^{cond}$ [W]
2	3.816227	-2.161077
5	-27.904290	-2.161077
10	-35.212929	-2.161077
15	-35.265658	-2.161077
17	-35.265683	-2.161077
18	-35.265683	-2.161077
20	-35.265683	-2.161077
30	-35.265683	-2.161077
40	-35.265683	-2.161077
60	-35.265683	-2.161077

After selecting $t_{f,l}$, a parametric study can be done to find the proper value of the parameter $t_{f,v}$, always leaving Δx_l and Δx_v fixed at the value of $\Delta x_l = \Delta x_v = 1$ mm. In this case, $t_{f,v}$ has been varied using the following values $t_{f,v} = [10, 30, 35, 40, 50, 60, 65]$ cm. In Fig. 2.11, the interface temperature distributions, in the ullage CV, obtained for the different values of $t_{f,v}$ are plotted. In each subfigure, the temperature distribution is plotted at the three times of 1000 s, 3000 s, and 5000 s. As $t_{f,v}$ increases, the interface temperature distribution, far from both T_u and T_f, becomes independent of the value of both $t_{f,v}$ and time. The conductive heat transfer rate between the ullage CV and the film CV, at 3000 s, is plotted, in Fig. 2.12, as a function of $t_{f,v}$. Convergence in the values of $\dot{Q}_v^{cond}$ and $\dot{Q}_l^{cond}$ is reached for a value of $t_{f,v} = 35$ cm, as it is clear both in Fig. 2.12 and in Tab. 2.3.

After finding the appropriate values for $t_{f,v}$ and $t_{f,l}$, the proper values for the thickness of each layer in the vapor and liquid CV, Δx_v and Δx_l respectively, can be found also through a parametric

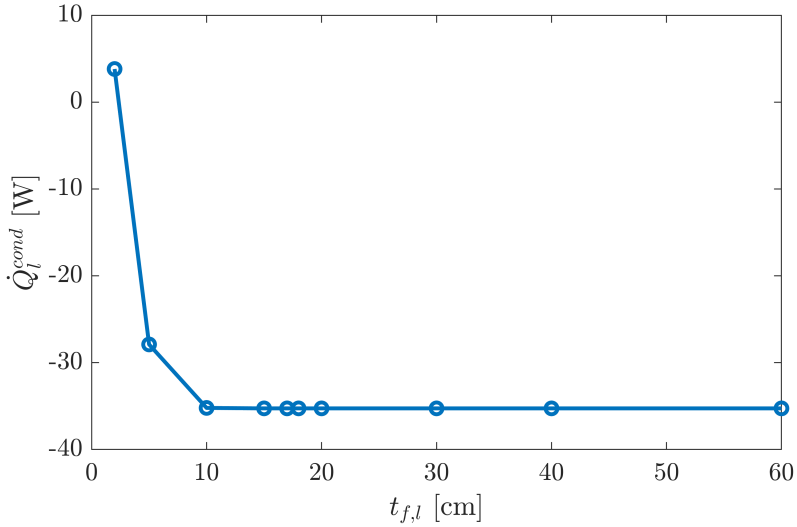

Figure 2.10: $t_{f,l}$ parametric study: conductive heat transfer rate between the liquid CV and the film CV, at 3000 s, $\dot{Q}_l^{cond}$, as a function of the total thickness of the interface layers in the liquid CV, $t_{f,l}$.

study. In this work, the parametric study for Δx_l has been done by fixing the values just found of $t_{f,l} = 15$ cm and $t_{f,v} = 35$ cm, using a value of $\Delta x_v = 1$ mm, and letting Δx_l assume the following values $\Delta x_l = [0.05, 0.1, 0.5, 1]$ mm. As the values of $\dot{Q}_v^{cond}$ and $\dot{Q}_l^{cond}$ obtained with $\Delta x_l = 0.1$ mm show a little discrepancy with respect to the ones obtained with $\Delta x_l = 0.05$ mm, as it is clear both in Fig. 2.13 and in Tab. 2.4, the former value has been selected for a trade-off between accuracy and computational time.

Finally, the parametric study for Δx_v has been done by fixing the values just found of $t_{f,l} = 15$ cm, $t_{f,v} = 35$ cm, and $\Delta x_l = 0.1$ mm, and letting Δx_v assume the following values $\Delta x_v = [0.5, 0.8, 1]$ mm. A value of $\Delta x_v = 1$ mm has been selected for a trade-off between accuracy and computational time, as the values of $\dot{Q}_v^{cond}$ and $\dot{Q}_l^{cond}$ obtained with this value of Δx_v are comparable to the ones

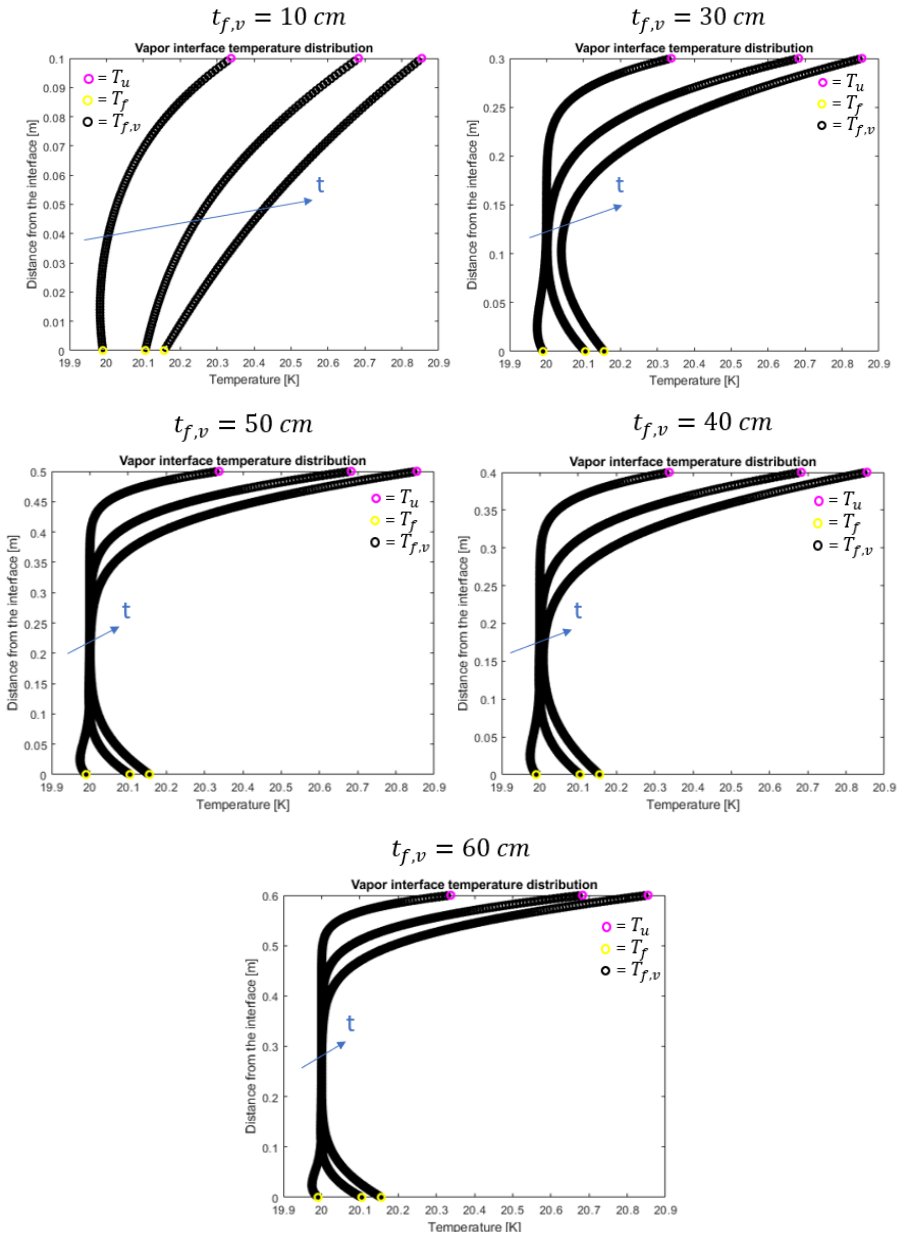

Figure 2.11: $t_{f,v}$ parametric study: interface temperature distributions, in the ullage CV, obtained for different values of $t_{f,v}$. In each subfigure, the temperature distribution is plotted at the three times of 1000 s, 3000 s, and 5000 s.

Table 2.3: $t_{f,v}$ parametric study: conductive heat transfer rate between the liquid CV and the film CV, $\dot{Q}_l^{cond}$, and conductive heat transfer rate between the ullage CV and the film CV, $\dot{Q}_v^{cond}$, for different values of $t_{f,v}$. Both $\dot{Q}_l^{cond}$ and $\dot{Q}_v^{cond}$ are taken at 3000 s.

$t_{f,v}$ [cm]	$\dot{Q}_l^{cond}$ [W]	$\dot{Q}_v^{cond}$ [W]
10	-35.265658	-2.161077
30	-35.196234	2.885266
35	-35.196215	2.887647
40	-35.196213	2.887803
50	-35.196213	2.887809
60	-35.196213	2.887809
65	-35.196213	2.887809

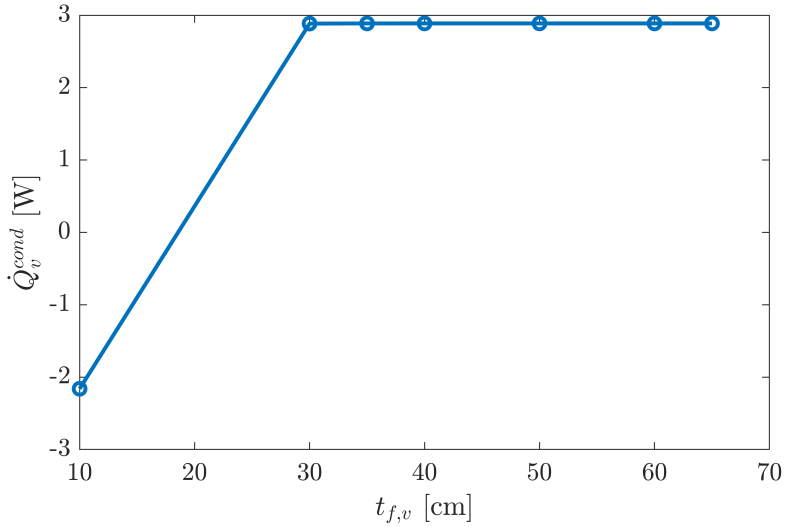

Figure 2.12: $t_{f,v}$ parametric study: conductive heat transfer rate between the ullage CV and the film CV, $\dot{Q}_v^{cond}$, at 3000 s, as a function of the total thickness of the interface layers in the ullage CV, $t_{f,v}$.

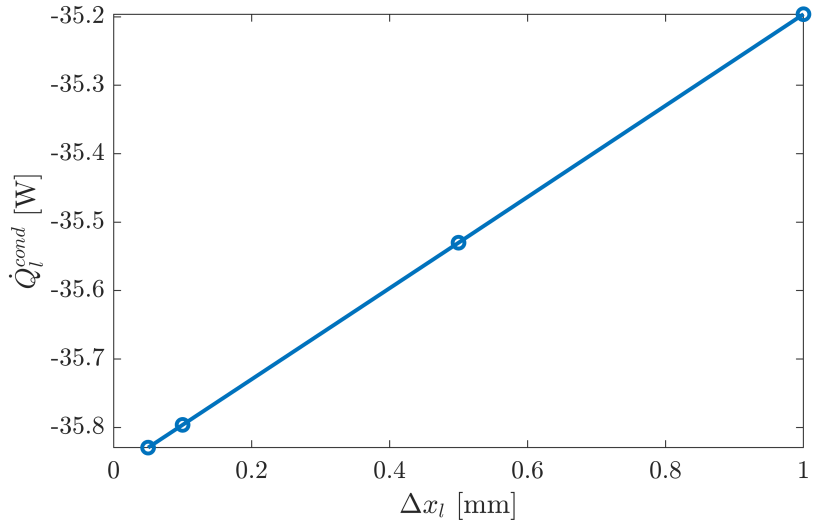

Figure 2.13: Δx_l parametric study: conductive heat transfer rate between the liquid CV and the film CV, $\dot{Q}_l^{cond}$, at 3000 s as a function of the thickness of each layer in the liquid CV, Δx_l.

Table 2.4: Δx_l parametric study: conductive heat transfer rate between the liquid CV and the film CV, $\dot{Q}_l^{cond}$, and conductive heat transfer rate between the ullage CV and the film CV, $\dot{Q}_v^{cond}$, for different values of Δx_l. Both $\dot{Q}_l^{cond}$ and $\dot{Q}_v^{cond}$ are taken at 3000 s.

$\boldsymbol{\Delta x_l}$ [mm]	$\boldsymbol{\dot{Q}_l^{cond}}$ [W]	$\boldsymbol{\dot{Q}_v^{cond}}$ [W]
0.05	-35.829423	2.887560
0.1	-35.796195	2.887570
0.5	-35.530036	2.887635
1	-35.196215	2.887647

obtained choosing lower values of this parameter, as it is clear both in Fig. 2.14 and in Tab. 2.5.

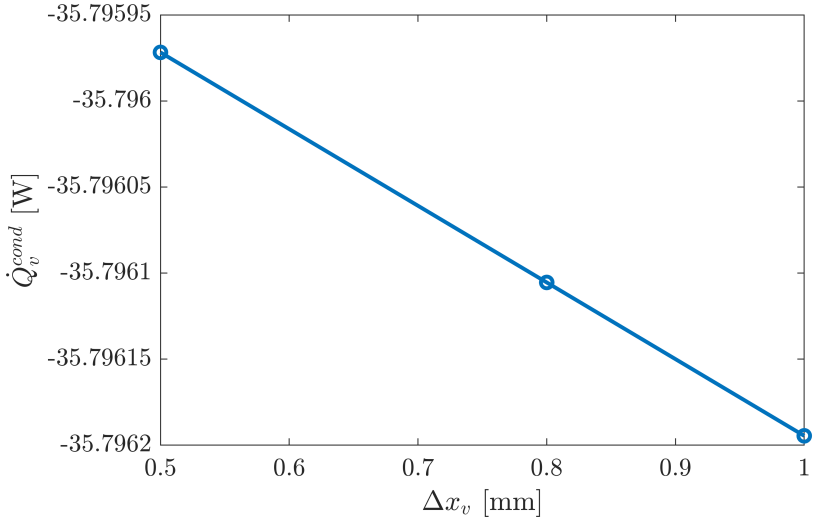

Figure 2.14: Δx_v parametric study: conductive heat transfer rate between the ullage CV and the film CV, $\dot{Q}_v^{cond}$, at 3000 s, as a function of the thickness of each layer in the ullage CV, Δx_v.

Table 2.5: Δx_v parametric study: conductive heat transfer rate between the liquid CV and the film CV, $\dot{Q}_l^{cond}$, and conductive heat transfer rate between the ullage CV and the film CV, $\dot{Q}_v^{cond}$, for different values of Δx_v. Both $\dot{Q}_l^{cond}$ and $\dot{Q}_v^{cond}$ are taken at 3000 s.

$\boldsymbol{\Delta x_v}$ [mm]	$\boldsymbol{\dot{Q}_l^{cond}}$ [W]	$\boldsymbol{\dot{Q}_v^{cond}}$ [W]
0.5	-35.795972	2.897678
0.8	-35.796105	2.891618
1	-35.796195	2.887570

It is evident, in Figs. 2.9 and 2.11, that the temperature far from T_f and T_l or T_u, respectively, tends to the initial temperature when the results reach the convergence. So, if the initial temperature is imposed as a boundary condition, instead of using liquid and ullage temperatures in Eqs. (2.51) and (2.54), respectively, the integration distance at which the results reach the convergence becomes lower. When the initial liquid temperature, $T_l(0)$, is used, instead of the instantaneous liquid temperature, Eq. (2.51) becomes:

$$\frac{\partial T_{f,l}(n_l-1)}{\partial t} \approx \frac{\alpha_l}{\Delta x_l^2}\left[T_l(0) + T_{f,l}(n_l-2) - 2T_{f,l}(n_l-1)\right] \tag{2.90}$$

Figs. 2.15 and 2.16 and Tab. 2.6 show that, in this way, a convergence both in the interface

temperature values, $T_{f,l}$, and in the heat transfer rates, $\dot{Q}_l^{cond}$ and $\dot{Q}_v^{cond}$, is reached with a lower value of the interface thickness in the liquid CV, $t_{f,l} = 10$ cm.

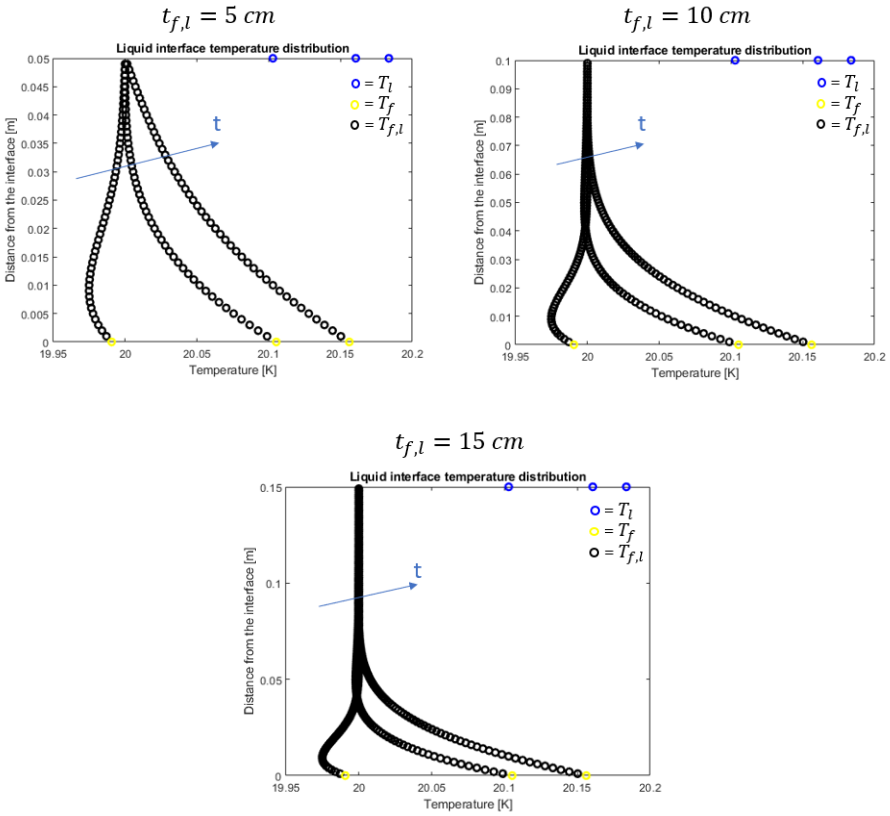

Figure 2.15: $t_{f,l}$ parametric study: interface temperature distributions in the liquid CV obtained for different values of $t_{f,l}$, in the case of the use of $T_l(0)$ as boundary condition. In each subfigure, the temperature distribution is plotted at the three times of 1000 s, 3000 s, and 5000 s.

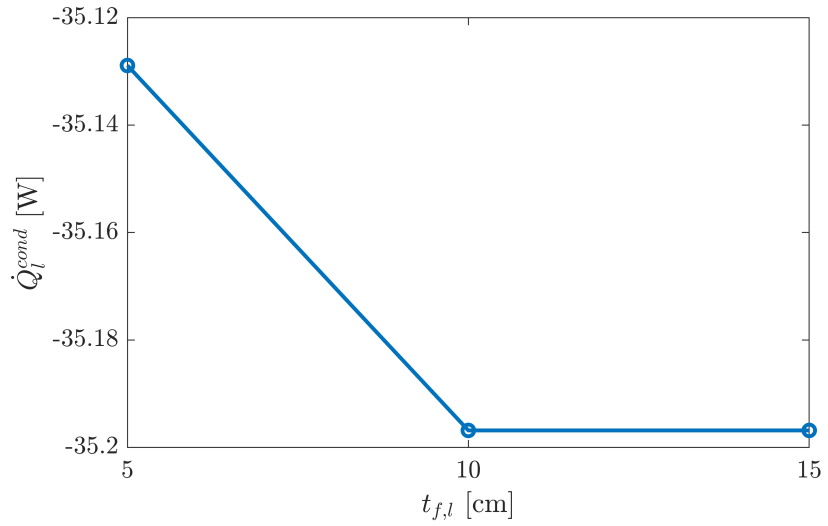

Figure 2.16: $t_{f,l}$ parametric study: conductive heat transfer rate between the liquid CV and the film CV, $\dot{Q}_l^{cond}$, at 3000 s, as a function of the total thickness of the interface layers in the liquid CV, $t_{f,l}$, in the case of the use of $T_l(0)$ as boundary condition.

The same procedure can be adopted to reduce the total interface layer thickness in the ullage CV. Using, as boundary condition, the initial ullage temperature, $T_u(0)$, instead of the instantaneous

Table 2.6: $t_{f,l}$ parametric study: conductive heat transfer rate between the liquid CV and the film CV, $\dot{Q}_l^{cond}$, and conductive heat transfer rate between the ullage CV and the film CV, $\dot{Q}_v^{cond}$, for different values of $t_{f,l}$. Both $\dot{Q}_l^{cond}$ and $\dot{Q}_v^{cond}$ are taken at 3000 s, and refer to the case of the use of $T_l(0)$ as boundary condition.

$t_{f,l}$ [cm]	$\dot{Q}_l^{cond}$ [W]	$\dot{Q}_v^{cond}$ [W]
5	-35.128876	2.843580
10	-35.196854	2.843580
15	-35.196854	2.843580

ullage temperature, Eq. (2.54) becomes:

$$\frac{\partial T_{f,v}(n_v-1)}{\partial t} \approx \frac{\alpha_{mix}}{\Delta x_v^2}\left[T_u(0) + T_{f,v}(n_v-2) - 2T_{f,v}(n_v-1)\right] \tag{2.91}$$

Figs. 2.17 and 2.18 and Tab. 2.7 show that, in this way, a convergence both in the interface temperature values, $T_{f,v}$, and in the heat transfer rates, $\dot{Q}_l^{cond}$ and $\dot{Q}_v^{cond}$, is reached with a lower value of the interface thickness in the ullage CV, $t_{f,v} = 20$ cm.

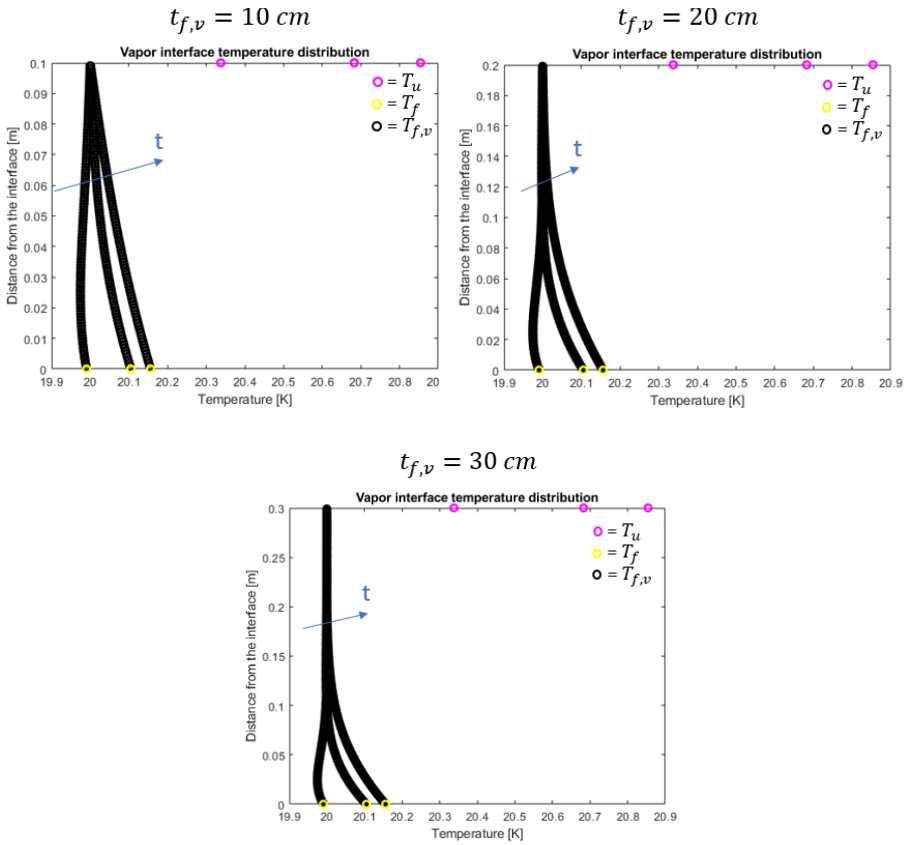

Figure 2.17: $t_{f,v}$ parametric study: interface temperature distributions in the ullage CV obtained for different values of $t_{f,v}$, in the case of the use of $T_u(0)$ as boundary condition. In each subfigure, the temperature distribution is plotted at the three times of 1000 s, 3000 s, and 5000 s.

A parametric study on Δx_l has been also carried out, using $T_l(0)$ as boundary condition. In particular, fixed values of $t_{f,l} = 10$ cm, $t_{f,v} = 20$ cm, and $\Delta x_v = 1$ mm have been used, and Δx_l has assumed the following values $\Delta x_l = [0.1, 0.5, 1]$ mm. Fig. 2.19 and Tab. 2.8 show that a value of $\Delta x_l = 0.1$ mm allows a good trade-off between accuracy and computational time.

Table 2.7: $t_{f,v}$ parametric study: conductive heat transfer rate between the liquid CV and the film CV, $\dot{Q}_l^{cond}$, and conductive heat transfer rate between the ullage CV and the film CV, $\dot{Q}_v^{cond}$, for different values of $t_{f,v}$. Both $\dot{Q}_l^{cond}$ and $\dot{Q}_v^{cond}$ are taken at 3000 s, and refer to the case of the use of $T_u(0)$ as boundary condition.

$t_{f,v}$ [cm]	$\dot{Q}_l^{cond}$ [W]	$\dot{Q}_v^{cond}$ [W]
10	-35.196854	2.843580
15	35.196253	2.886339
20	-35.196239	2.887802
30	-35.196239	2.887809

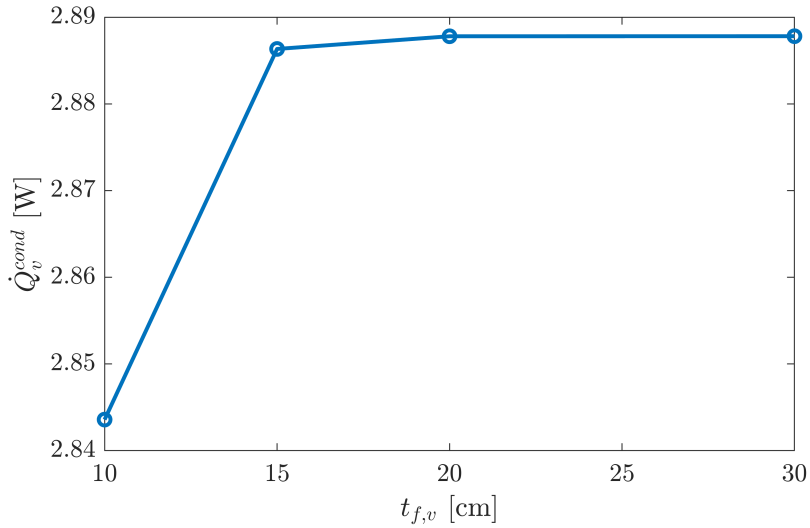

Figure 2.18: $t_{f,v}$ parametric study: conductive heat transfer rate between the ullage CV and the film CV, $\dot{Q}_v^{cond}$, at 3000 s, as a function of the total thickness of the interface layers in the ullage CV, $t_{f,v}$, in the case of the use of $T_u(0)$ as boundary condition.

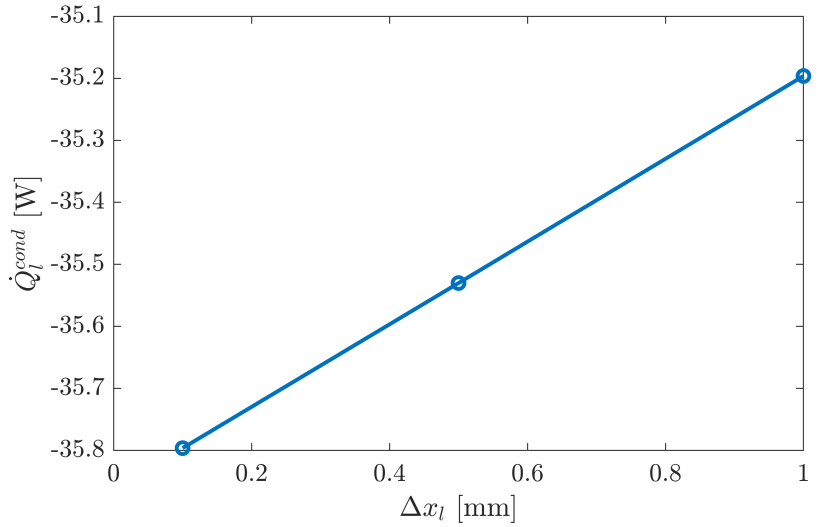

Figure 2.19: Δx_l parametric study: conductive heat transfer rate between the liquid CV and the film CV, $\dot{Q}_l^{cond}$, at 3000 s, as a function of the thickness of each layer in the liquid CV, Δx_l, in the case of the use of $T_l(0)$ as boundary condition.

Table 2.8: Δx_l parametric study: conductive heat transfer rate between the liquid CV and the film CV, $\dot{Q}_l^{cond}$, and conductive heat transfer rate between the ullage CV and the film CV, $\dot{Q}_v^{cond}$, for different values of Δx_l. Both $\dot{Q}_l^{cond}$ and $\dot{Q}_v^{cond}$ are taken at 3000 s, and refer to the case of the use of $T_l(0)$ as boundary condition.

Δx_l [mm]	$\dot{Q}_l^{cond}$ [W]	$\dot{Q}_v^{cond}$ [W]
0.1	-35.796218	2.887726
0.5	-35.530059	2.887791
1	-35.196239	2.887802

Finally, a parametric study on the Δx_v has been carried out, using $T_u(0)$ as boundary condition. In particular, fixed values of $t_{f,l} = 10$ cm, $t_{f,v} = 20$ cm, and $\Delta x_l = 0.1$ mm have been used, and Δx_v has assumed the following values $\Delta x_v = [0.5, 0.7, 1]$ mm. Fig. 2.20 and Tab. 2.9 show that a value of $\Delta x_v = 0.7$ mm allows a good trade-off between accuracy and computational time.

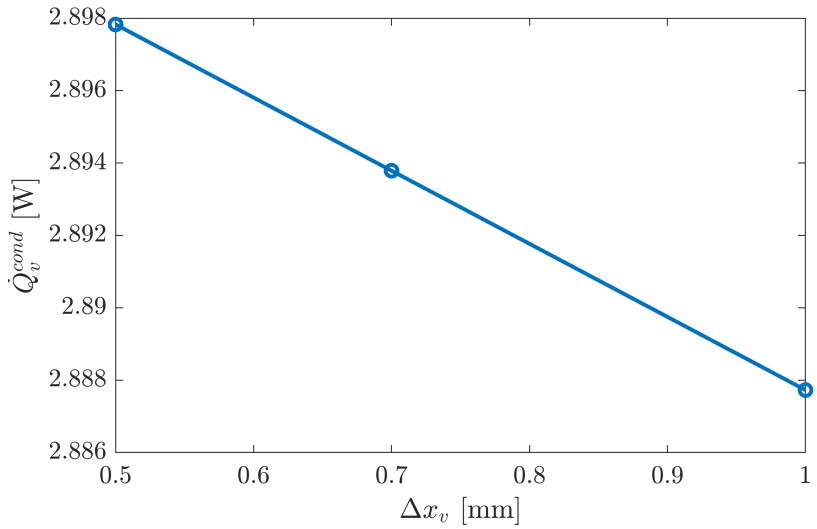

Figure 2.20: Δx_v parametric study: conductive heat transfer rate between the ullage CV and the film CV, $\dot{Q}_v^{cond}$, at 3000 s, as a function of the thickness of each layer in the ullage CV, Δx_v, in the case of the use of $T_u(0)$ as boundary condition.

Table 2.9: Δx_v parametric study: conductive heat transfer rate between the liquid CV and the film CV, $\dot{Q}_l^{cond}$, and conductive heat transfer rate between the ullage CV and the film CV, $\dot{Q}_v^{cond}$, for different values of Δx_v. Both $\dot{Q}_l^{cond}$ and $\dot{Q}_v^{cond}$ are taken at 3000 s, and refer to the case of the use of $T_u(0)$ as boundary condition.

Δx_v [mm]	$\dot{Q}_l^{cond}$ [W]	$\dot{Q}_v^{cond}$ [W]
0.5	-35.795996	2.897829
0.7	-35.796085	2.893788
1	-35.796218	2.887726

Chapter 3

Numerical setup for CFD analysis

Until now, cryogenic tanks operating conditions have been typically studied in CFD using a transient approach, modeling the tank as 2D axisymmetric, and introducing a two-phase model, in order to treat the interface region. The most widely used two-phase models have been the Sharp Interface (SI) model, developed by Kassemi and his research group, and the Volume-of-Fluid (VOF) model. In the Sharp Interface model [16, 49–51], the interface is represented as a sharp boundary that divides the liquid and vapor regions. For each phase, the governing equations are individually solved, and interface balances are imposed at the liquid-vapor interface. A drawback of the Sharp Interface model is that it is currently limited to stationary flat interfaces, such as pressurization in normal gravity. In the VOF model [38], the interface is captured diffusively. Only one set of governing equations is solved for both phases, and an evolution equation for the volume fraction of the vapor is added to this set. The volume fraction is then used to weight material properties and field variables, creating the impression of the presence of two distinct "fluids" within the solution. Although, in literature, the Eulerian VOF method has been mostly used to track the interface between the liquid and vapor phases in cryogenic tanks simulations, also other approaches have been tested. For example, in [99], a 3D adaptive Eulerian-Lagrangian method, with a phase change model, has been used to study the self-pressurization of a liquid H_2 tank.

Alongside the interface treatment, in CFD self-pressurization studies, a proper model has to be selected in order to take into account the interfacial phase change mass transfer rate. The most common models for implementing mass transfer in two-phase schemes are the Rankine-Hugoniot jump condition, the one proposed by Schrage, and the one proposed by Lee. In the first [31], mass transfer rate is calculated from the net energy transfer across the interface. Schrage [95] proposed a formulation based on kinetic theory of gases and applicable for near equilibrium conditions. Instead, Lee [64] developed a simplified saturation model for evaporation and condensation processes. In this model, phase change rate is proportional to the deviation of the interface temperature from the saturation temperature.

In this chapter, we will see the details of the numerical setup that we have used to obtain the results presented in the following chapters. In particular, after presenting the governing equations, details of the chosen two-phase model, namely the Volume-of-Fluid model will be given. Then, the selected models to account for the mass transfer due to phase change and for the effect of surface tension, i.e. the Lee model and the Continuum Surface Force (CSF) model, respectively, will be presented. Later, the main Reynolds-Averaged Navier-Stokes (RANS) turbulence modelings will be

shown. Next, the selected approaches for assigning the thermophysical and transport properties will be explained. Finally, the conjugate heat transfer model will be shortly introduced.

3.1 Governing equations

The equations describing the behavior of the fluid are the continuity, Navier-Stokes, and energy equations:

$$\frac{\partial \rho}{\partial t} + \nabla \cdot (\rho \boldsymbol{v}) = 0 \tag{3.1}$$

$$\frac{\partial}{\partial t}(\rho \boldsymbol{v}) + \nabla \cdot (\rho \boldsymbol{v}\boldsymbol{v}) = -\nabla p + \nabla \cdot \left[\mu_{eff}\left(\nabla \boldsymbol{v} + \nabla \boldsymbol{v}^T\right)\right] + \rho \boldsymbol{g} + \boldsymbol{F}_{vol} \tag{3.2}$$

$$\frac{\partial}{\partial t}(\rho E) + \nabla \cdot [\boldsymbol{v}(\rho E + p)] = \nabla \cdot (\lambda_{eff} \nabla T) + S_h \tag{3.3}$$

This set of equations can be used in both the laminar and turbulent cases, through the definition of effective transport properties, where effective is defined as the sum of the molecular contribution and of the possible turbulent contribution. μ_{eff} and λ_{eff} are, respectively, the effective viscosity and the effective thermal conductivity.

3.2 The Volume-of-Fluid method

Common Eulerian schemes used to simulate two-phase flows are termed interface-capturing methods. In these methods, the computational grid remains fixed. The Volume-of-Fluid method [38] is part of interface-capturing methods, and it is based on the definition of the volume fraction of a specific phase, whose value is one if the cell is completely occupied by that phase, is zero if it is completely occupied by the other phase, and is between zero and one for interface cells, as it is schematized in Fig. 3.1.

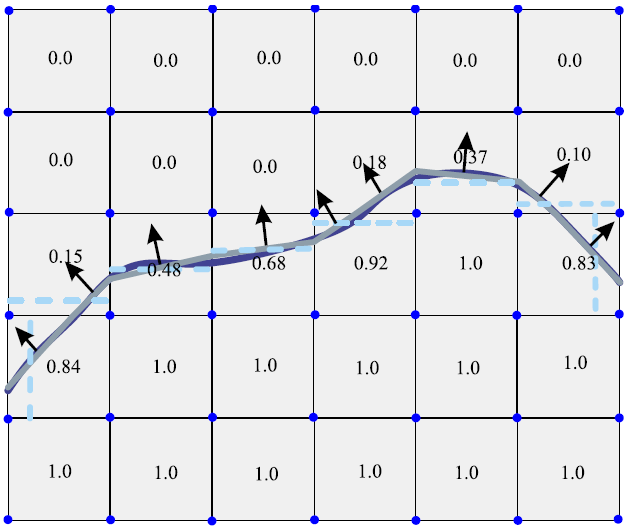

Figure 3.1: Schematic of fluid volume fraction and fluid interface, from [52].

In the VOF method, a unique set of governing equations, Eqs. (3.1) - (3.3), is solved for both phases, and an evolution equation for the volume fraction of the vapor is added to this set (in order

to track the interface between the liquid and vapor phases):

$$\frac{1}{\rho_v}\left[\frac{\partial}{\partial t}(\alpha_v\rho_v) + \nabla\cdot(\alpha_v\rho_v\boldsymbol{v}_v) = \dot{m}_{lv} - \dot{m}_{vl}\right] \tag{3.4}$$

The liquid volume fraction can be computed using the constraint that the sum of the volume fractions of each q^{th} phase must be equal to unity:

$$\sum_{q=l,v}\alpha_q = 1 \tag{3.5}$$

Average field variables and properties are, typically, defined in terms of the phases volume fractions:

$$\rho = \sum_{q=l,v}\alpha_q\rho_q \quad \mu_{eff} = \sum_{q=l,v}\alpha_q\mu_{eff_q} \quad \lambda_{eff} = \sum_{q=l,v}\alpha_q\lambda_{eff_q} \tag{3.6}$$

The specific total energy (i.e., the sum of the specific internal and kinetic energies) is treated as a mass averaged variable:

$$E = \frac{\sum_{q=1}^{2}\alpha_q\rho_q E_q}{\sum_{q=1}^{2}\alpha_q\rho_q} = \frac{\sum_{q=1}^{2}\alpha_q\rho_q e_q}{\sum_{q=1}^{2}\alpha_q\rho_q} + \frac{v^2}{2} \tag{3.7}$$

The velocity, v, resulting from Eq. (3.2), is shared among the phases.

Finally, VOF methods are inherently conservative, but they suffer inability to capture the interface accurately.

3.3 The Lee model

The source term, in the evolution Eq. (3.4), is written using the Lee model [64], which is a simplified saturation model used to calculate phase change due to evaporation and condensation. The model assumes that mass is transferred at constant pressure and quasi-thermo-equilibrium state. In this model, the driving force for the volumetric mass sources, $\dot{m}_{lv}$ and $\dot{m}_{vl}$, in [kg/(m^{3}s)], is the difference between local temperature and saturation temperature, T_s:

$$\dot{m}_{lv} = r\alpha_l\rho_l\frac{T_l - T_s}{T_s} \qquad if\ \ T_l > T_s\ \ (evaporation) \tag{3.8}$$

$$\dot{m}_{vl} = r\alpha_v\rho_v\frac{T_s - T_v}{T_s} \qquad if\ \ T_v < T_s\ \ (condensation) \tag{3.9}$$

where r, which has the units of [1/s], is an empirical coefficient, called mass transfer intensity factor, which is typically adjusted to match experimental data. It is the inverse of a relaxation time, and researchers have used a wide range of values, ranging from 0.1 to $1\cdot10^7$ 1/s [54]. In general, the optimal value of r depends on numerous factors, which encompass, but are not restricted to, specific phase change phenomenon, flow rate, mesh size, and computational time step. Even if, theoretically, it should be different for evaporation and condensation processes, in this thesis, equal values of r have been used for both processes, as it has been done in previous numerical studies [69, 71].

It is clear, from Eqs. (3.8) and (3.9), that an accurate representation of the saturation line is fundamental for a precise calculation of phase change mass transfer. In our simulations, NIST [65] data have been used for either a linear or a piecewise linear approximation of the saturation line.

In addition, the volumetric mass source estimated using the Lee model is multiplied by the latent heat of phase change in order to compute the source term, S_h, in Eq. (3.3), which is a volumetric heat source due to phase change.

Finally, some researchers [7, 70] have demonstrated that Lee model is fundamentally derived from the Schrage model. But, unlike the Schrage model, which allows phase change only along the interface, the Lee model allows to simulate full scale flow boiling and flow condensation processes, with relative ease.

3.4 The Continuum Surface Force model

In order to accurately capture the interface, a method for modeling surface tension force effects has to be used. This holds especially true under conditions of reduced gravity, where the relative influence of surface tension force with respect to gravity can be high. The source term $\boldsymbol{F}_{vol}$, in Eq. (3.2), represents the contribute of surface tension force at the interface, which is modeled as a volumetric force, using the Continuum Surface Force (CSF) model [12, 54]. With fixed grid methods, the surface tension force, according to the CSF model for constant surface tension, σ, is defined as:

$$\boldsymbol{F}_{vol} = \sigma \kappa \delta_s \hat{\boldsymbol{n}} \tag{3.10}$$

where δ_s is the Dirac delta function, which allows the surface tension force to have a finite value at the interface, and to be zero everywhere else away from the interface.

Moreover, the surface unit normal, $\hat{\boldsymbol{n}}$, and the surface curvature, κ, are defined as:

$$\hat{\boldsymbol{n}} = \frac{\nabla c}{|\nabla c|} \tag{3.11}$$

$$\kappa = \nabla \cdot \hat{\boldsymbol{n}} \tag{3.12}$$

where, c is a parameter defined based on the method used, and, with the VOF method, it is the volume fraction. Thus, when the VOF is used, the term $\boldsymbol{F}_{vol}$, in Eq. (3.2), becomes:

$$\boldsymbol{F}_{vol} = \sigma \frac{\rho \kappa_l \nabla \alpha_l}{\frac{1}{2}(\rho_l + \rho_v)} \tag{3.13}$$

where ρ is the volume fraction averaged density, computed using Eq. (3.6). Even though the CSF model has been successfully applied in numerical schemes, it is known, as well as other other methods used to describe the effect of surface tension, to artificially induce spurious currents when capturing the interface. These are nonphysical vortex currents induced close to the interface, resulting in unrealistic distortions, and, therefore, lowering the accuracy of interface curvature calculations. The inability to balance pressure gradient with surface tension force is the main cause of these currents. Recently, investigators have proposed techniques to eliminate these spurious currents. For example, an accurate representation of the body force due to surface tension, which effectively

suppresses spurious currents, is proposed in [86].

3.5 Contact angle model

When using a surface tension model, a contact angle model has to be chosen, too. The contact angle is the angle between the gas-liquid phase boundary and the solid container wall at the contact line. This angle establishes the shape of the free-surface in the tanks, and thus the location of the liquid bulk. The knowledge of the liquid position is important for the retreat of liquid from the tank, as well as for the prediction of the heat and mass transfer. The contact angle, which is determined by the interfacial energy of the components, is no longer constant if the contact line moves over a solid.

In case of isothermal conditions the advancing dynamic contact angle, γ_d, mainly depends on the capillary number [30], $Ca = \mu\overline{u}/\sigma$, where $\overline{u}$ denotes the advancing velocity of the meniscus, μ the viscosity of the liquid, and σ the surface tension. Many models for the dependency between the dynamic contact angle and the Ca number have been developed over the years [13, 22, 42]. Experiments at isothermal conditions, made in [30], showed a good agreement with the dynamic contact angle model developed by Jiang et al. [42]:

$$\frac{\cos\gamma_s - \cos\gamma_d}{\cos\gamma_s + 1} = \tanh\left(4.96Ca^{0.702}\right) \tag{3.14}$$

where γ_s stands for the static contact angle. In [42], Eq. (3.14) is recommended for any macroscopic geometry in the cases when the effects of gravity, of inertia, and of adsorption are absent.

In case of non-isothermal conditions, the dynamic contact angle is affected by different thermal effects, among which there are the Marangoni flow due to surface tension gradients, evaporation and condensation at the liquid-ullage interface, and the vapor recoil. Both experimental and numerical studies have been carried out by Dreyer et al. to investigate the effect of the Marangoni flow on the dynamic contact angle at compensated gravity conditions [30, 58]. The measured data showed that Marangoni convection causes an increase of the apparent dynamic contact angle. In particular, in [30], they used the correlation by Jiang [42] as a basis for a dynamic contact angle model in the non-isothermal case. In particular, the model of Jiang was modified by a substitution of the static isothermal contact angle by a shift contact angle, γ_{shift}, which characterizes the shift of the dynamic contact angle caused by Marangoni convection:

$$\frac{\cos\gamma_{shift} - \cos\gamma_d}{\cos\gamma_{shift} + 1} = \tanh\left(4.96Ca^{0.7}\right) \tag{3.15}$$

Moreover, a relation has been determined for γ_{shift}, which depends on the thermocapillary Reynolds number, Re_M, and the ratio between the Weber number and the thermocapillary Weber number, We/We_M:

$$\gamma_{shift} = 20.9\left\{\frac{We}{We_M}\left[Re_M\left(\frac{L}{D}\right)\right]^{1/3}\right\}^{1/3} \tag{3.16}$$

where the ratio between the Weber number and the thermocapillary Weber number can be expressed in terms of the surface tension, the surface tension gradient, σ_T, and the temperature difference

between the hot wall and the cold liquid, ΔT:

$$\frac{We}{We_M} = \frac{\sigma_T \Delta T}{\sigma} \tag{3.17}$$

and Re_M is defined as:

$$Re_M = \frac{\rho \sigma_T \Delta T L}{\mu^2} \tag{3.18}$$

In the present study, the contact angle has been prescribed as a boundary condition. In particular, it has been set as constant and equal to 90° for all the analyses, except for the parametric study on the gravity level (see Sec. 6.3), where it has been set to 5°. It stands out, observing the Eq. (3.14), that the dynamic contact angle would be equal to the static one in the case of null Ca, i.e. when the advancing velocity of the meniscus is zero. Thus, the assumption of a constant static contact angle at the wall is accurate for the studies performed in normal gravity (see Cap. 4 and Cap. 5), and for the validation carried out in reduced gravity (see Sec. 6.2), as a settling acceleration was used in the latter case. Indeed, in these cases, the contact line does not move in time. Instead, for the parametric study on the gravity level (see Sec. 6.3), the free-surface is subject to reorientation, thus a model for a dynamic contact angle would have been needed. However, the used value of contact angle, 5°, is a good approximation, being a typical contact angle for cryogenic liquids in contact with typical tank wall materials (aluminum or stainless steel) [10, 14]. Moreover, it stands out from Eq. (3.16) that γ_{shift} nulls either for $Re_M = 0$ or for $\frac{We}{We_M} = 0$, thus in the cases when $\Delta T = 0$, and, consequently, also the surface tension gradient is zero. Thus, neglecting the γ_{shift}, we have also neglected the temperature gradient between the hot wall and the liquid, which, in cryogenic tanks, is typically not negligible in proximity of the liquid-ullage interface.

3.6 Reynolds Averaged Navier-Stokes turbulence modeling

One of the most used approaches in solving the Navier-Stokes equations is the Reynolds Averaged Navier-Stokes simulation, in which only the mean flow field behavior is described by the averaged Navier-Stokes equations. Fine turbulent scales are not resolved, and a steady mean flow field, that satisfies the averaged Navier-Stokes equations, is obtained.

When the flow is strongly unsteady with non-turbulent origin (e.g., externally-enforced unsteadiness), the unsteady mean flow is resolved, and the turbulent fluctuations are described by the turbulence model. This is possible because the time scale of the turbulence dynamics is smaller than the dynamics of the phenomenon that caused the unsteadiness. Such transient simulations are named Unsteady Reynolds-Averaged Navier-Stokes (URANS) simulations. URANS simulations require a higher computational cost with respect to their steady-state version, and show a stronger sensitivity to the model chosen.

The non-linearity of the Navier-Stokes equations leads to the appearance of momentum fluxes (the Reynolds stress terms) that act as apparent stresses throughout the flow. Since these momentum fluxes are unknown a priori, the system of the equations is no longer closed, and additional equations have to be derived. A turbulence model can be used to close the system. Turbulence modeling consists in creating a mathematical model that approximates the physical behavior of turbulent flows. This has to be made by introducing the minimum amount of complexity, while capturing the relevant flow physics.

Most turbulence modeling focuses on the Reynolds stress terms. These are either solved directly, as in full second-moment Reynolds stress models, or defined via a constitutive relation for simpler models. Less attention is typically given to the other terms that need to be modeled. For zero-, one-, and two-equation models, the Boussinesq approximation, with suitable generalization for compressible flows, is the most used approach. Denoting the eddy viscosity by μ_t , the following form is assumed for the Favre-averaged Reynolds Stress Tensor, $\bar{\rho}\tau_{ij}^R$:

$$\bar{\rho}\tau_{ij}^R = -\overline{\rho v_i'' v_j''} = 2\mu_t \left(\widetilde{S_{ij}} - \frac{1}{3}\frac{\partial \widetilde{v_k}}{\partial x_k}\delta_{ij} - \frac{2}{3}\bar{\rho}k\delta_{ij} \right) \tag{3.19}$$

where $\widetilde{S_{ij}}$ is the mean strain rate tensor. In the mean strain rate tensor, the Favre-averaged velocity, $\tilde{v}_i$, is used:

$$\tilde{v}_i(x_i,t) = \frac{1}{\overline{\rho}(x_i,t)}\overline{\rho(x_i,t,\omega)v_i(x_i,t,\omega)} \tag{3.20}$$

The most important consideration in postulating Eq. (3.19) is to guarantee that:

$$tr\left(\tau_{ij}^R\right) = -2k \tag{3.21}$$

where, k, is the turbulence kinetic energy, which means that the second eddy viscosity is identically $-\frac{2}{3}\mu_t$. It is worth to notice that the Boussinesq hyphotesis implies the anisotropy tensor $\widetilde{a_{ij}}$ to be aligned with the deviatoric part of the Favre-mean strain rate tensor:

$$\widetilde{a_{ij}} = \overline{\rho v_i'' v_j''} - \frac{2}{3}\bar{\rho}k\delta_{ij} = -2\nu_T \widetilde{S_{ij}}^D \tag{3.22}$$

Being symmetric and deviatoric, both $\widetilde{a_{ij}}$ and S_{ij}^D have five independent components. According to the turbulent viscosity hypothesis, these five components are related to each other through the scalar coefficient ν_T, but, even in simple shear flow, it is found that this alignment does not occur. Specification, by the turbulence model, of $\nu_T(x_i,t)$ solves the problem of the Reynolds stress tensor closure. In creating a mathematical model that approximates the physical behavior, the most used approach is applying the Boussinesq hypothesis (Eq. (3.19)), and trying to provide a scalar value of the eddy viscosity to close the RANS equations (Linear Eddy Viscosity Models (LEVM)). Since the beginning of the history of turbulence modeling, many researchers tried to provide equations for ν_T , developing n-equation models, which require the solution of n additional differential transport equations. Zero-equation or algebraic models (mixing-length model), one-equation models (Spalart-Allmaras model), and two-equations (SST $k-\omega$, $k-\omega$, and $k-\varepsilon$ models) all belong to this category of closure strategies.

3.6.1 $k-\varepsilon$ model

In the $k-\varepsilon$ turbulence model [62] two transport equations, one for the turbulence kinetic energy, k, and the other for its dissipation rate, ε, are used. The transport equations are:

$$\frac{\partial}{\partial t}(\bar{\rho}k) + \frac{\partial}{\partial x_j}(\bar{\rho}\tilde{v}_j k) = -\tau_{ij}\frac{\partial \tilde{v}_i}{\partial x_j} + \frac{\partial}{\partial x_j}\left[\left(\bar{\mu} + \frac{\mu_t}{\sigma_k}\right)\frac{\partial k}{\partial x_j}\right] - \bar{\rho}\varepsilon\left(1 + 2M_t^2\right) \tag{3.23}$$

$$\frac{\partial}{\partial t}(\bar{\rho}\varepsilon) + \frac{\partial}{\partial x_j}(\bar{\rho}\tilde{v}_j\varepsilon) = -c_{1\varepsilon}\frac{\varepsilon}{k}\tau_{ij}\frac{\partial \tilde{v}_i}{\partial x_j} + \frac{\partial}{\partial x_j}\left[\left(\bar{\mu} + \frac{\mu_t}{\sigma_\varepsilon}\right)\frac{\partial \varepsilon}{\partial x_j}\right] - c_{2\varepsilon}\bar{\rho}\frac{\varepsilon^2}{k} \tag{3.24}$$

In these equations, the first and last terms at the right-hand side account for production and dissipation, respectively; and $M_t = \sqrt{2k}/a$ is the turbulent Mach number, where a is the sound speed. The eddy viscosity is evaluated as:

$$\mu_t = \bar{\rho}c_\mu\frac{k^2}{\varepsilon} \tag{3.25}$$

The values of the model constants are $c_{1\varepsilon} = 1.44$, $c_{2\varepsilon} = 1.92$, $c_\mu = 0.09$, $\sigma_k = 1.0$, and $\sigma_\varepsilon = 1.3$.

3.6.2 $k - \omega$ model

The standard $k - \omega$ model [119] is based on model transport equations for k and $\omega = \varepsilon/k$. The eddy viscosity is evaluated as:

$$\mu_t = \alpha^*\bar{\rho}\frac{k}{\omega} \tag{3.26}$$

where α^* is the low-Reynolds-number damping term. The transport equations are:

$$\frac{\partial}{\partial t}(\bar{\rho}k) + \frac{\partial}{\partial x_j}(\bar{\rho}\tilde{v}_j k) = -\tau_{ij}\frac{\partial \tilde{v}_i}{\partial x_j} + \frac{\partial}{\partial x_j}\left[\left(\bar{\mu} + \frac{\mu_t}{\sigma_k}\right)\frac{\partial k}{\partial x_j}\right] - \bar{\rho}\beta^* f_{\beta^*} k\omega \tag{3.27}$$

$$\frac{\partial}{\partial t}(\bar{\rho}\omega) + \frac{\partial}{\partial x_j}(\bar{\rho}\tilde{v}_j\omega) = -\alpha\frac{\omega}{k}\tau_{ij}\frac{\partial \tilde{v}_i}{\partial x_j} + \frac{\partial}{\partial x_j}\left[\left(\bar{\mu} + \frac{\mu_t}{\sigma_\omega}\right)\frac{\partial \omega}{\partial x_j}\right] - \bar{\rho}\beta f_\beta \omega^2 \tag{3.28}$$

with:

$$\alpha^* = \alpha^*_\infty\left(\frac{\alpha^*_0 + Re_t/R_k}{1 + Re_t/R_k}\right), \qquad \alpha = \frac{\alpha_\infty}{\alpha^*}\left(\frac{\alpha_0 + Re_t/R_\omega}{1 + Re_t/R_\omega}\right) \tag{3.29}$$

$$f_{\beta^*} = \begin{cases} \dfrac{1 + 680\chi_k^2}{1 + 400\chi_k^2} & if\ \chi_k > 0 \\ 1 & if\ \chi_k \leq 0 \end{cases}, \qquad f_\beta = \frac{1 + 70\chi_\omega}{1 + 80\chi_\omega} \tag{3.30}$$

$$\chi_k = \frac{1}{\omega^3}\frac{\partial k}{\partial x_j}\frac{\partial \omega}{\partial x_j}, \qquad \chi_\omega = \left|\frac{\tilde{\Omega}_{ij}\tilde{\Omega}_{jk}\tilde{S}_{ki}}{(\beta^*_\infty\omega)^3}\right| \tag{3.31}$$

$$\beta^* = \beta^*_i\left[1 + \zeta^* F(M_t)\right], \qquad \beta = \beta_i - \beta^*_i\zeta^* F(M_t) \tag{3.32}$$

$$\beta^*_i = \beta^*_\infty\left(\frac{4/15 + (Re_t/R_\beta)^4}{1 + (Re_t/R_\beta)^4}\right), \qquad Re_t = \frac{\bar{\rho}k}{\bar{\mu}\omega} \tag{3.33}$$

$$F(M_t) = \left[M_t^2 - M_{t0}^2\right]\mathcal{H}(M_t - M_{t0}), \qquad M_t^2 = \frac{2k}{a^2} \tag{3.34}$$

Here, $\mathcal{H}(x)$ is the Heaviside step function; and the values assigned to the model constants are $\alpha^*_\infty = 1$, $\alpha_\infty = 0.52$, $\alpha^*_0 = \beta_i/3$, $\alpha_0 = 1/9$, $\beta^*_\infty = 0.09$, $\beta_i = 0.072$, $R_\beta = 8$, $R_k = 6$, $R_\omega = 2.95$, $\zeta^* = 1.5$, $M_{t0} = 0.25$, $\sigma_k = 2$, $\sigma_\omega = 2$.

3.6.3 SST $k-\omega$ model

The Shear Stress Transport (SST) $k-\omega$ model of Menter [74] successfully blends the near-wall robust and accurate formulation of the $k-\omega$ model, with the freestream independence of the $k-\varepsilon$ model. The eddy viscosity is obtained from:

$$\mu_t = \frac{\bar{\rho}k}{\omega}\frac{1}{max\left[(1/\alpha^*),(\Omega F_2/a_1\omega)\right]} \tag{3.35}$$

and the transport equations are similar to the parent models:

$$\frac{\partial}{\partial t}(\bar{\rho}k) + \frac{\partial}{\partial x_j}\left(\bar{\rho}\tilde{v}_j k\right) =| -\tau_{ij}\frac{\partial \tilde{v}_i}{\partial x_j} + \frac{\partial}{\partial x_j}\left[\left(\bar{\mu}+\frac{\mu_t}{\sigma_k}\right)\frac{\partial k}{\partial x_j}\right] - \bar{\rho}\beta^* k\omega \tag{3.36}$$

$$\begin{aligned}\frac{\partial}{\partial t}(\bar{\rho}\omega) + \frac{\partial}{\partial x_j}\left(\bar{\rho}\tilde{v}_j \omega\right) = &-\alpha\frac{\bar{\rho}}{\mu_t}\tau_{ij}\frac{\partial \tilde{v}_i}{\partial x_j} + \frac{\partial}{\partial x_j}\left[\left(\bar{\mu}+\frac{\mu_t}{\sigma_\omega}\right)\frac{\partial \omega}{\partial x_j}\right] \\ &- \bar{\rho}\beta\omega^2 + D_\omega\end{aligned} \tag{3.37}$$

where α is determined from Eq. (3.29), by replacing the (constant) α_∞ with:

$$\begin{aligned}&\alpha_\infty = F_1\alpha_{\infty,1} + (1-F_1)\,\alpha_{\infty,2}, \quad \alpha_{\infty,1} = \frac{\beta_{i,1}}{\beta^*_\infty} - \frac{\kappa_v^2}{\sigma_{\omega,1}\sqrt{\beta^*_\infty}}, \\ &\alpha_{\infty,2} = \frac{\beta_{i,2}}{\beta^*_\infty} - \frac{\kappa_v^2}{\sigma_{\omega,2}\sqrt{\beta^*_\infty}}\end{aligned} \tag{3.38}$$

and

$$\beta_i = F_1\beta_{i,1} + (1-F_1)\beta_{i,2} \tag{3.39}$$

The cross-diffusion term D_ω is defined as:

$$D_\omega = 2\,(1-F_1)\,\bar{\rho}\sigma_{\omega,2}\frac{1}{\omega}\frac{\partial k}{\partial x_j}\frac{\partial \omega}{\partial x_j} \tag{3.40}$$

The blending functions F_1 and F_2 are evaluated from:

$$F_1 = \tanh\left(\Phi_1^4\right), \quad F_2 = \tanh\left(\Phi_2^2\right) \tag{3.41}$$

$$\begin{aligned}&\Phi_1 = \min\left[\max\left(\frac{\sqrt{k}}{0.09\omega d}, \frac{500\bar{\mu}}{\bar{\rho}d^2\omega}\right), \frac{4\bar{\rho}k}{\sigma_{\omega,2}D^+_\omega d^2}\right], \\ &\Phi_2 = \max\left[2\frac{\sqrt{k}}{0.09\omega d}, \frac{500\bar{\mu}}{\bar{\rho}d^2\omega}\right]\end{aligned} \tag{3.42}$$

$$D^+_\omega = \max\left[2\bar{\rho}\frac{1}{\sigma_{\omega,2}}\frac{1}{\omega}\frac{\partial k}{\partial x_j}\frac{\partial \omega}{\partial x_j}, 10^{-20}\right], \quad \Omega = \sqrt{2\tilde{\Omega}_{ij}\tilde{\Omega}_{ij}} \tag{3.43}$$

$$\sigma_k = \frac{1}{F_1/\sigma_{k,1} + (1-F_1)/\sigma_{k,2}}, \quad \sigma_\omega = \frac{1}{F_1/\sigma_{\omega,1} + (1-F_1)/\sigma_{\omega,2}} \tag{3.44}$$

where Ω_{ij} is the mean rotation rate, d is the distance from the nearest wall, and D_{ω^+} is the positive portion of the cross-diffusion term. The model constants are here set to $\sigma_{k,1} = 1.176$, $\sigma_{\omega,1} = 2$, $\sigma_{k,2} = 1$, $\sigma_{\omega,2} = 1.168$, $a_1 = 0.31$, $\beta_{i,1} = 0.075$, and $\beta_{i,2} = 0.0828$. The additional model

constants assume the same values as in the standard $k-\omega$ model.

3.6.4 Realizable $k-\varepsilon$ model

The realizable $k-\varepsilon$ model was introduced by Shih et al. [98] to guarantee positivity of the normal Reynolds stresses and Schwarz inequality for the turbulent shear stress. The transport equation for k is the same as for the standard model (Eq. (3.23)), except for the model constants, instead the equation for ε is:

$$\frac{\partial}{\partial t}(\bar{\rho}\varepsilon)+\frac{\partial}{\partial x_j}\left(\bar{\rho}\tilde{v}_j\varepsilon\right)=\bar{\rho}c_1 S\varepsilon+\frac{\partial}{\partial x_j}\left[\left(\bar{\mu}+\frac{\mu_t}{\sigma_\varepsilon}\right)\frac{\partial\varepsilon}{\partial x_j}\right] -\bar{\rho}c_2\frac{\varepsilon^2}{k+\sqrt{\bar{\nu}\varepsilon}} \tag{3.45}$$

where:

$$c_1=\max\left[0.43,\frac{\eta}{\eta+5}\right],\quad \eta=S\frac{k}{\varepsilon},\quad S=\sqrt{2\tilde{S}_{ij}\tilde{S}_{ij}} \tag{3.46}$$

and a variable c_μ is used for the evaluation of μ_t (Eq. (3.25)):

$$c_\mu=\frac{1}{A_0+A_s\left(kU^*/\varepsilon\right)},\quad U^*=\sqrt{\tilde{S}_{ij}\tilde{S}_{ij}+\tilde{\Omega}_{ij}\tilde{\Omega}_{ij}} \tag{3.47}$$

$$A_0=4.04,\quad A_s=\sqrt{6}\cos\phi \tag{3.48}$$

$$\phi=\frac{1}{3}\cos^{-1}(\sqrt{6}W),\quad W=\frac{\tilde{S}_{ij}\tilde{S}_{jk}\tilde{S}_{ki}}{\sqrt{\tilde{S}_{ij}\tilde{S}_{ij}}} \tag{3.49}$$

The model constants are set to $c_2=1.92$, $\sigma_k=1.0$, and $\sigma_\varepsilon=1.2$.

3.6.5 Near-wall treatment of $k-\varepsilon$ models

For the $k-\varepsilon$ models, the flow is divided into two layers: a fully turbulent region far away from the wall, which obeys the $k-\varepsilon$ model equations; and a viscous region, where ε and μ_t are both specified algebraically [120]:

$$\varepsilon=\frac{k^{3/2}}{l_\varepsilon} \tag{3.50}$$

$$\mu_{t,2l}=\bar{\rho}c_\mu\sqrt{k}l_\mu \tag{3.51}$$

where the damping effects are taken into account in:

$$l_\varepsilon=dc_l\left[1-\exp\left(-Re_d/A_\varepsilon\right)\right] \tag{3.52}$$

$$l_\mu=dc_l\left[1-\exp\left(-Re_d/A_\mu\right)\right]\sqrt{\frac{\bar{\rho}_w}{\bar{\rho}}} \tag{3.53}$$

Eq. (3.53) accounts for the effect of compressibility through the density ratio, where $\bar{\rho}_w$ is the wall density [34]. The blending between the two layers is smoothly and implicitly achieved for steady-state solutions, introducing the blending function $\lambda_\varepsilon(Re_d)$, as proposed in [43]:

$$\lambda_\varepsilon=\frac{1}{2}\left[1+\tanh\left(\frac{Re_d-200}{20/\operatorname{atanh}(0.98)}\right)\right] \tag{3.54}$$

which is close to zero for $Re_d < 200$ (i.e., in the near-wall region) and one otherwise. The blended eddy viscosity is computed easily as the convex combination of the two:

$$\mu_{t,\text{sth}} = \lambda_\varepsilon \mu_t + (1 - \lambda_\varepsilon)\, \mu_{t,2l} \tag{3.55}$$

where μ_t is the one of the fully turbulent layer. The blended dissipation is computed in a similar way, but acting on the differential equations, Eq. (3.24) or Eq. (3.45), by multiplying all the terms (but the temporal derivative) by λ_ε, and by adding the term:

$$(1 - \lambda_\varepsilon) \left(\frac{k^{3/2}}{l_\varepsilon} - \varepsilon \right) \tag{3.56}$$

Hence, in the fully turbulent layer, where $\lambda_\varepsilon \simeq 1$, Eq. (3.24) or Eq. (3.45) is recovered; whereas in the viscous layer, where $\lambda_\varepsilon \simeq 0$, we have:

$$\frac{d\varepsilon}{dt} = \frac{k^{3/2}}{l_\varepsilon} - \varepsilon \tag{3.57}$$

which reduces to Eq. (3.50) under steady conditions. The constants are, here, set to [15]:

$$c_l = k c_\mu^{-3/4}, \quad A_\mu = 70, \quad A_\varepsilon = 2c_l \tag{3.58}$$

3.7 Thermophysical and transport properties

Two different approaches have been used for thermophysical and transport properties. In the first approach (Sec. 4.6.3), the propellant and the vapor contained in the ullage, which are of the same chemical species, are modeled as an unique species, with time varying real thermophysical and transport properties, taken from the National Institute of Standards and Technology (NIST) Chemistry WebBook [65] database.

Driven by the will to speed up the really time-consuming two-phase simulations, we have looked for an approach which does not require access to the NIST functions at each time step in order to compute the properties. In this second approach, even if the propellant and the vapor are of the same chemical species, they are treated as if they were two different species. The ideal gas equation of state is used to model the vapor phase density. Whereas, the Boussinesq approximation is used to account for density variations in the liquid phase. Boussinesq approximation is typically applied for incompressible flows in the case of natural convection. In the Boussinesq approximation, variations in fluid properties other than density are ignored, and density is considered constant in the governing equations, except where it appears in terms multiplied by $\boldsymbol{g}$, the acceleration due to gravity (i.e. the buoyancy force term, $\rho\boldsymbol{g}$, in the momentum equation, Eq. (3.2)). In the buoyancy force term, density is assumed to have a linear dependence on temperature:

$$\rho = \rho_0 - \beta\rho_0(T - T_0) \tag{3.59}$$

where ρ_0 is the (constant) density of the flow, T_0 is the operating temperature, and β is the coefficient of thermal expansion. This last is computed from NIST data, and using this formula,

which is derived from thermodynamic relations (see Appendix A):

$$\beta = \sqrt{\frac{c_p}{T}\left(\frac{c_p}{c_v} - 1\right)} \cdot \frac{1}{a} \tag{3.60}$$

where a is the speed of sound. The Boussinesq approximation is accurate as long as changes in actual density are small; specifically, when $\beta(T - T_0) << 1$.

As concerns the other properties, the specific heat, c_p, thermal conductivity, k, and dynamic viscosity, μ, of the liquid phase are modeled as constant. Instead, vapor properties are modeled as constant if the vapor does not experience large temperature variations during the simulated test case (Chap. 4). On the contrary, vapor properties are modeled as temperature varying if the ullage is characterized by large temperature excursions (Chap. 5 and Chap. 6). In the latter case, the vapor c_p is modeled with a piecewise linear approximation of data taken from NIST database, at various temperature values. Instead, the thermal conductivity and viscosity are modeled either with a piecewise linear approximation of NIST data, or with the Sutherland's law [110].

Sutherland's law formulation for thermal conductivity is:

$$\frac{\lambda}{\lambda_0} = \left(\frac{T}{T_0}\right)^{3/2} \frac{T_0 + S_k}{T + S_k} \tag{3.61}$$

where Sutherland's law parameters for thermal conductivity depend on the species considered (for example for N_2 they are $\lambda_0 = 0.0242$ W/(m K), $T_0 = 273$ K, and $S_k = 150$ K).

Sutherland's law formulation for dynamic viscosity is:

$$\frac{\mu}{\mu_0} = \left(\frac{T}{T_0}\right)^{3/2} \frac{T_0 + S_\mu}{T + S_\mu} \tag{3.62}$$

where Sutherland's law parameters for dynamic viscosity depend on the species considered (for example for N_2 they are $\mu_0 = 1.663 \cdot 10^{-5}$ Pa s, $T_0 = 273$ K, and $S_\mu = 107$ K).

The saturation curve is approximated either as linear or as piecewise linear using NIST data.

Characteristic thermophysical and transport properties at cryogenic temperatures have been used for the wall material. In particular, they have been modeled as constant if the wall does not experience large temperature variations during the test (Chap. 4). Otherwise (Chap. 5), wall thermal conductivity and specific heat have been modeled as piecewise linear, using data taken from NIST database for solid materials [53].

3.8 The conjugated heat transfer model

In most of the analyses presented in the following chapters, a conjugated heat transfer model is used. Tank wall temperature distribution is solved from the wall energy equation:

$$\frac{\partial}{\partial t}\left(\rho_w c_w T_w\right) = \nabla\left(\lambda_w \nabla T_w\right) \tag{3.63}$$

where ρ_w, c_w, λ_w, and T_w are the wall density, specific heat, thermal conductivity, and temperature, respectively. Wall temperature distribution is coupled to the fluid energy equations through

the wall fluid boundary condition:

$$\lambda_w \nabla T_w = \lambda_{eff} \nabla T \tag{3.64}$$

where λ_{eff} is the effective thermal conductivity. Finally, a heat flux determined from the experiments is imposed at the external boundary of the wall.

Chapter 4

Self-pressurization of a liquid N_2 tank: "BOG cell" test case

The validation test case presented in this chapter involves liquid N_2 self-pressurization in a small-scale tank, exposed to the heat flux generated by three heaters [84]. This experimental test case has been selected because, in the test apparatus, a large number (thirty-five) of Resistance Temperature Detector (RTD) sensors had been immersed in the liquid and in the ullage, to measure thermal stratification over time. In addition, CFD simulations of this test case are still missing in literature, but the experiment was successfully reproduced using a non-equilibrium multilayer thermodynamic model in [116].

Previous CFD reproductions of experimental results of ground-based self-pressurization in cryogenic tanks were mostly focused on the accurate representation of the self-pressurization rate and of the temporal evolution of the liquid and ullage temperatures in the very few locations where suitable thermocouples were installed. Consequently, researchers have rarely assessed the ability of their computational methodology to reproduce in detail the liquid temperature stratification close to the free-surface. Since the developing of such a thermal stratification is a driving factor in propellant vaporization and in the consequent pressure rise, with this validation we assess the potentialities and the weaknesses of various numerical models in reproducing experimental temperature stratification profiles, as well as pressure rise rates. This validation includes several analyses. First, a comparison is shown between the experimental results and the numerical ones obtained varying two thermophysical modelings and various computational models and parameters: pressure-velocity coupling algorithm; mass transfer intensity factor for phase change computation; conjugated and non-conjugated wall heat transfer; laminar and turbulent flow. Then, the problem of the uncertainty of the experimental data and of its influence on numerical results is discussed. Finally, a comparison between CFD and reduced order models results is presented.

4.1 Self-pressurization literature survey

In literature, despite the abundance of self-pressurization experiments conducted within cryogenic tanks, not all of them have clear and reproducible initial and boundary conditions, making them acceptable for comparison with CFD results. Among the valuable experiments for numerical methodologies validations, there are the ones performed in the early 1990's in the K-site test facility at

NASA Glenn Research Center [36, 112], and the ones performed in the early 2000's at the Multi-purpose Hydrogen Test Bed (MHTB) facility at NASA Marshall Space Flight Center [37]. In the K-site test facility, self-pressurization experiments of liquid H_2 in an ellipsoidal tank were done. In particular, in [36], the effect of different initial conditions and imposed heat fluxes was studied, and, in [112], the effect of the filling level was investigated. In the MHTB facility, a liquid H_2 self-pressurization test series, in a cylindrical tank with elliptical domes, was carried out, varying the heat transfer rate and the filling level.

Besides experimental data of flight tanks, self-pressurization results in small-scale ground-based tanks, suitable for validation purposes, can be found, among them there are the ones obtained in the Zero-Boil-Off Tank (ZBOT) apparatus [8]. These results were obtained in a cylindrical tank with spherical domes, and the effect of different filling levels and heat transfer rates was studied for the low boiling point refrigerant HFE-7000.

While most of the self-pressurization test cases found in literature involve tanks experiencing moderate heat fluxes, there is also a presence of experimental data obtained for tanks exposed to elevated heat fluxes. An example is the experimental data reported in [5], where the self-pressurization results of tests performed in a spherical liquid H_2 tank, subjected to various combinations of three parameters: filling percentage, heat flux (which reached a maximum value of 405 W/m^2 in the uniform heating configuration), and heating configuration, were presented.

Researchers extensively employed the previously mentioned test cases to validate their numerical approaches. The self-pressurization process of the 50% filled K-site tank, implementing the detailed tank geometry and the multilayer insulation was simulated in [102]. The VOF model, with Schrage relationship for mass transfer rate calculation, was used, and the flow was modeled as laminar. The sensitivity of the initial pressure rise to the initial temperature profile near the interface was shown, and several issues related to cryogenic fluid simulations were identified. The self-pressurization process in the 50% filled K-site tank was also simulated in [51]. The case in which the tank was subjected to a heat flux of 3.5 W/m^2 was considered, and laminar and turbulent conjugated and non-conjugated VOF model predictions of pressure evolution were compared. Results demonstrated that the laminar VOF model provides a more accurate calculation of the self-pressurization rate, and that wall conduction plays a large role in distributing the heat between the ullage and liquid in the laminar case. Moreover, the ZBOT self-pressurization experiment in which a 1 W of heat was imparted into the tank, through a band heater, was simulated using an axisymmetric conjugated Sharp Interface two-phase CFD model. The computational predictions for this test case were in excellent agreement with the experimental counterpart. Furthermore, Kassemi et al. [49] presented the CFD results of a ground-based ZBOT experiment in which the tank was self-pressurized through uniform heating provided by radiation through a vacuum jacket, simulating heat leaks in the tank from the space environment, and obtaining, also in this case, a good agreement between the numerical results and the experimental measurements of tank pressure rise and local temperature evolutions. Simulations of self-pressurization experiments in the MHTB facility were carried out in [50], and the results showed that computation of mass transfer using Schrage relationship is insensitive to the magnitude of accomodation coefficient, both in the Sharp Interface model and in the VOF method. In the previous numerical validations, a comparison with experimental data of self-pressurizing tanks exposed to moderate heat fluxes was carried out, instead, in [39], some of the high heat flux self-pressurization data from [5] were used to validate the proposed numerical methodology.

Alongside the numerical replication of experimental test cases, in literature, there are interesting parametric analyses, without an experimental counterpart. For example, in [59], CFD computations on the stratification of large liquid H_2 tanks subject to different heat fluxes were performed, and different stratification behaviors during the pre-evaporation and the evaporation phases for tanks of different aspect ratios were found.

More recently, in [26], numerical simulation of liquefied natural gas (LNG) self-pressurization in a small-scale tank was carried out. Temperature stratification, boil-off, and self-pressurization phenomena, for various tank filling levels and insulation layer thicknesses, were studied using conjugate heat transfer and SST $k-\omega$ turbulence models.

4.2 Test case description

The selected validation experiment is a self-pressurization experiment, performed in a relatively small-scale liquid N_2 tank [84], in normal gravity. The test tank, defined BOG cell, was placed in a system characterized by a suitable insulation from the external environment, and an average heat transfer rate of 2.2 W was imparted to the tank radiatively, using three heaters, mounted on the lateral walls of a copper can that surrounded the test tank. A schematic of the experimental apparatus is shown in Fig. 4.1. The tank was equipped with a large number (thirty-five) of RTD

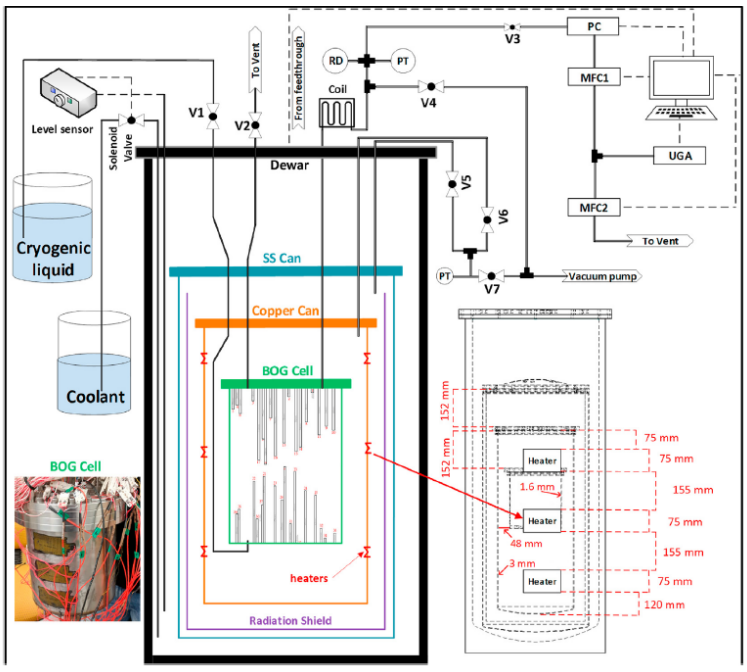

Figure 4.1: Experimental apparatus, from [84].

sensors, immersed in the liquid and in the ullage, to measure thermal stratification over time, their position is schematized in Fig. 4.2. The experiment underwent two distinct phases: the first one was characterized by self-pressurization, during which the tank was closed, and the second one was characterized by pressure set to a fixed value, by the use of a pressure regulator. During both phases the heaters imparted a heat flux to the tank. Our numerical analysis encompasses a maximum of the initial 4 hours of the experiment, which corresponds to the complete self-pressurization phase. According to the data provided in [84], the simulated tank is a cylinder characterized by a height,

H, of 213 mm and an inner diameter, D, of 200.5 mm, as represented in Fig. 4.3. The tank wall material is AISI 316 SS, and the thickness of the side wall is 1.6 mm. Finally, initial liquid volume fraction and initial pressure, for the selected experiment, are 88% and 106 kPa, respectively.

4.3 Thermophysical and transport properties

The vapor N_2 is modeled using the ideal gas equation of state and constant specific heat and transport properties. Such constant values are taken from the NIST Chemistry WebBook [65] database, at the average experimental pressure and temperature [84]. Liquid phase density is modeled with the Boussinesq approximation (see Sec. 3.7), so it is left constant in the governing equations, except in the buoyancy force term in the momentum equation, where density variation is written as a linear function of temperature. Thermophysical and transport properties have been

Top Lid		Bottom	
Sensor N	Position from bottom (mm)	Sensor N	Position from bottom (mm)
1	207	19	99
2	201	20	93
3	195	21	87
4	189	22	81
5	183	23	75
6	177	24	69
7	171	25	63
8	165	26	57
9	159	27	51
10	153	28	45
11	147	29	39
12	141	30	33
13	135	31	27
14	129	32	21
15	123	33	15
16	117	34	9
17	111	35	3
18	105		

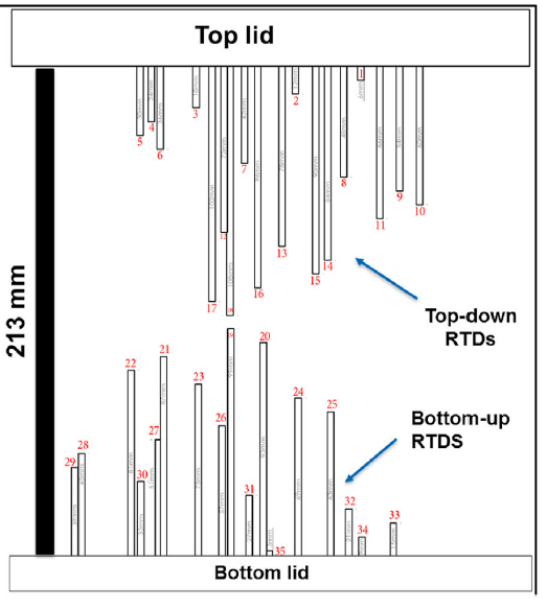

Figure 4.2: Scheme showing the positions of the thirty-five RTD sensors inside the BOG cell, from [84].

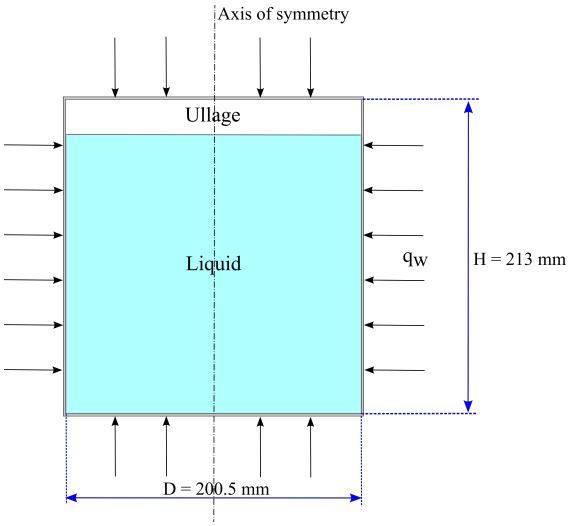

Figure 4.3: Tank scheme with the indication of the characteristic dimensions and of the boundary conditions used in CFD.

left constant also for the liquid N_2 phase, and they have been extracted from NIST database, at the average experimental pressure and temperature. Moreover, a volumetric thermal expansion coefficient, β, of 0.0057 1/K is used for the liquid phase, which has been computed from NIST data, and using Eq. (3.60) of Sec. 3.7. A standard state enthalpy of -1.211 $\cdot 10^7$ J/kmol and of 0 J/kmol, both at the reference temperature of 298.15 K, are used for the liquid N_2 and for the gaseous N_2, respectively. These values have been retrieved from [73]. A linear approximation is used for the N_2 saturation curve, using two saturation temperature/saturation pressure combinations, taken from NIST [65] database. Moreover, a constant value of the surface tension coefficient, equal to 0.0087925 N/m, is used.

When the conjugate heat transfer model is used, the solution of the conduction through the tank wall is coupled to the fluid-dynamics solution inside the liquid and vapor phases. For these cases, the solid considered is, in agreement with the experiment [84], AISI 316 SS, for which constant values of density, thermal conductivity and specific heat, extracted from NIST database for solid materials at cryogenic temperatures [53], are used. All constant liquid, vapor, and wall properties are listed in Tab. 4.1.

Table 4.1: Physical properties for the liquid, vapor, and wall materials, taken from [53, 65]. For the liquid and vapor phases, the indicated value of c is the specific heat at constant pressure, c_p.

	$\boldsymbol{\rho}$ $\mathbf{[kg/m^3]}$	$\boldsymbol{\lambda}$ $\mathbf{[W/(m \cdot K)]}$	$\boldsymbol{c}$ $\mathbf{[J/(kg \cdot K)]}$	$\boldsymbol{\mu}$ $\mathbf{[Pa \cdot s]}$
Liquid phase	803.2	0.14359	2044.4	$1.567 \cdot 10^{-4}$
Vapor phase	-	$7.59 \cdot 10^{-3}$	1133.5	$5.714 \cdot 10^{-6}$
Wall material	8067.2	8.1	214.7	-

4.4 Computational setup

Transient simulations have been carried out using the the pressure-based solver of the commercial CFD software Ansys Fluent® [1]. The flow is modeled as 2D axisymmetric, which is a reasonable assumption for the given geometry (cylindrical) and boundary conditions (see Fig. 4.3). A second order implicit time scheme is used for time discretization, with a time step size of $2.5 \cdot 10^{-2}$ s, with 30 iterations per time step, and a Courant number of 1. These parameters have been selected appropriately by making a trade-off between computational cost and numerical accuracy. Second order upwind schemes are used for spatial discretization of the convective terms in density, momentum, energy, and turbulence equations, and Ansys Fluent®'s "Compressive" scheme [1] is selected for the volume fraction equation, with the selection of sharp interface regime modeling. "PRESTO!" scheme [1] is used to interpolate pressure values at the cell faces. "Coupled" scheme [1] is used as pressure-velocity coupling scheme. For the validation case of our interest, as we will see in Sec. 4.6.4, we have made a comparison between the results obtained with the use of the coupled algorithm "Coupled", and those obtained with the segregated algorithm "PISO". This comparison has shown that the coupled algorithm allows to obtain results of pressurization rate and of thermal stratification comparable to those obtained with the segregated algorithm, but with a time step 2.5 times larger than that required with the segregated algorithm. For this reason, the coupled algorithm has been deemed more appropriate for such time-consuming simulations and, therefore, has been

chosen. Green-Gauss cell based scheme is used to calculate the properties' gradients, which are necessary to discretize the convection and diffusion terms in the flow conservation equations.

The following boundary conditions are imposed in simulations coupled with the solid wall: a heat flux of 10.8 W/m^2 (given by the ratio between the heat transfer rate to the tank and the tank external surface) on the external tank walls and a no-slip coupled wall (with a contact angle of 90°) boundary condition at the interface between the fluid and the wall. The liquid and vapor phases are initialized as quiescent, at a pressure of 106 kPa and at a temperature corresponding to the saturation temperature at the initial tank pressure. The wall is initialized at the same uniform temperature as the fluid phases.

4.5 Grid convergence study

A grid convergence study has been done considering three grids with an increasing level of spatial accuracy. Details of the used grids are reported in Tab. 4.2.

Table 4.2: Details of the computational grids used for grid independence study, in the case with conjugate heat transfer.

	No. of cells [-]	**Wall-Interface spacing [mm]**
Coarse	2232	0.5 - 0.5
Baseline	7392	0.5 - 0.5
Fine	26250	0.2 - 0.5

Due to the high computational cost of two-phase flow simulations, for grid independence study a time interval of half an hour has been simulated because, even if the duration of the self-pressurization part of the experiment was longer, the effect of the grid was already evident in this limited time. In Fig. 4.4, the pressurization curves obtained with the three grid levels are shown. The results obtained with the medium grid level, defined as "Baseline" in Tab. 4.2, show a limited discrepancy with the ones obtained with the finest grid. Hence, the "Baseline" grid allows for a trade-off between accuracy and computational cost. For this reason, it has been selected for subsequent analyses.

The chosen grid, represented in Fig. 4.5, is characterized by an average cell length of 2 mm in the fluid regions and of 1 mm in the wall region. Moreover, for this grid, the height of the fluid cells that face the wall, and of those that face the interface (this grid parameter is defined "spacing" in Tab. 4.2) is 0.5 mm. The selection of appropriate wall and interface spacings is very important for an accurate calculation of thermal and velocity boundary layers at the wall and of mass and energy transfer at the interface between the two phases. Indeed, a grid convergence study carried out only in the fluid region (i.e. without conjugate heat transfer, and distributing the heat flux between the liquid phase and the ullage as suggested in Sec. 4.6.2), using the three grid levels whose details are summarized in Tab. 4.3, has shown that halving the spacing yields results similar to those obtained with a grid twice as fine. This aspect is evident in Fig. 4.6, showing numerical pressurization curves obtained with the three grid levels used for the grid independence study, in the case without conjugate heat transfer.

It can be concluded that, once the appropriate spacing is found, one can halve the number of

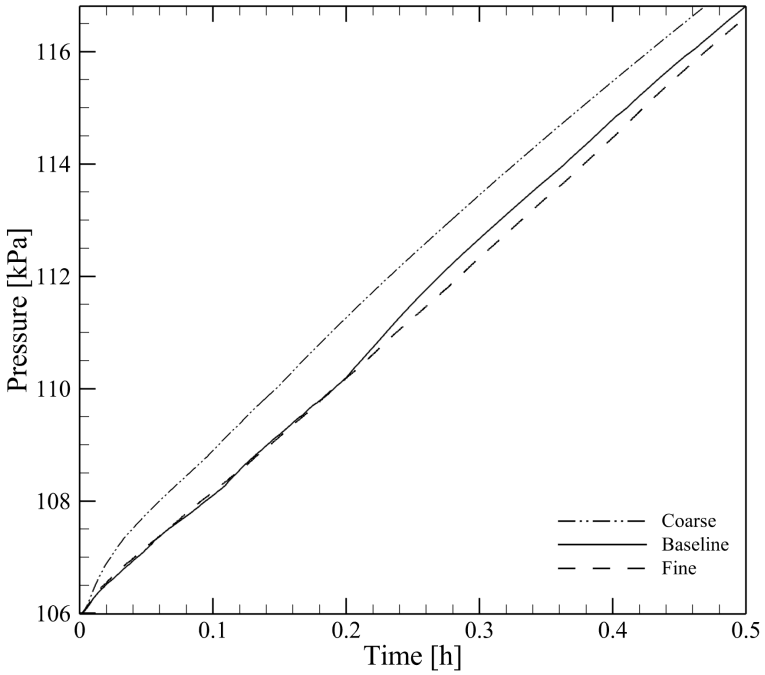

Figure 4.4: Grid convergence study, case with conjugate heat transfer: Numerical pressurization curves obtained with the three grids whose details are summarized in Tab. 4.2.

Table 4.3: Details of the computational grids used for grid independence study, in the case without conjugate heat transfer.

	No. of cells [-]	**Wall-Interface spacing [mm]**
Base	5782	1 - 1
2 x finer	23128	0.5 - 0.5
Base with half spacing	5782	0.5 - 0.5

grid points in both directions in the bulk region without any change in the results, leading to a reduction in computational time. For the reasons just explained, in this study, for the analyses carried out without the solid wall, grid defined as "Base with half spacing", in Tab. 4.3, has been used. This grid is equal to the "Baseline" grid, but is without the wall area.

4.6 Results

In this section, numerical results are presented, discussed and compared with experimental data. The objective of the discussion is twofold. On the one hand, the objective is the explanation of the main physical phenomena occurring in self-pressurizing tanks, and influencing the pressure rise rate and thermal stratification behavior. On the other hand, the focus of the discussion is the different numerical modelings used in simulations, exploring the reasons for which some choices produce more reliable results than others, and justifying the choice of a certain numerical methodology.

4.6.1 Thermo-fluid-dynamics phenomena of self-pressurization

Many thermo-fluid-dynamics phenomena occur during tank self-pressurization. First of all, the heat transfer rate entering the tank causes self-pressurization, which is due to both vaporization of the propellant and heating of the ullage. Moreover, the application of a heat flux to the tank walls causes heating of the fluid layers adjacent to it, which, due to buoyancy, move upward into the denser fluid, and generate convective recirculations, both in the liquid and in the ullage. Convective recirculations, in the ullage, cause its thermal stratification, indeed the hottest and lightest vapor layers move in the uppermost part of the ullage, while the coldest and heaviest layers reach the lowest part of the ullage. Convective recirculations, in the liquid, transport heat towards the interface between the two phases. The interface temperature is approximately the saturation temperature corresponding to tank pressure at a given time [6]. Additionally, the heat input causes the liquid's bulk temperature to rise, although at a slower rate than the interface temperature does since, as previously stated, the interface temperature rise is correlated with the rise in tank pressure via the saturation curve. This difference in the rate of growth causes a liquid thermal stratification close to the free-surface, whose extension grows over time, as will be better explained in Sec. 4.6.6, in a closed self-pressurizing tank.

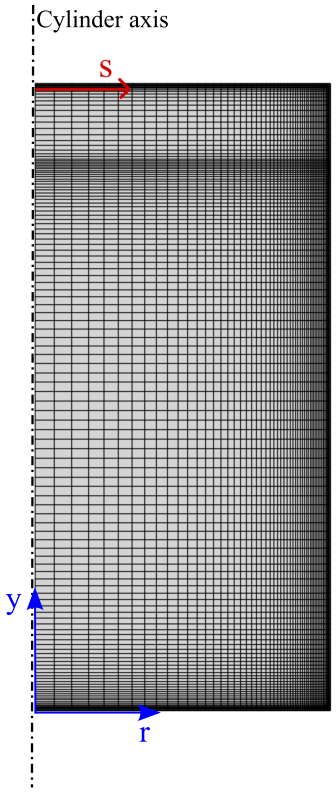

Figure 4.5: Selected computational grid for wall coupled simulations (the domain has been modeled as 2D axisymmetric), with indication of the origin of the axisymmetric axes "r" and "y" and of the curvilinear abscissa, "s".

4.6.2 Uncoupled simulations: Heat flux distribution

In the case when the simulation of this test case is carried out without the wall region, the heat flux distribution between the liquid and the ullage is not known a priori. Indeed, of the average heat transfer rate of 2.2 W imparted to the tank, a bigger part will be absorbed from the liquid phase, and a lower part will go into the ullage, as it will be better explained in Sec. 4.6.6. In order to estimate the ratio between the heat flux entering the liquid phase, q_l, and the heat flux entering the ullage, q_v, a parametric analysis has been done. In particular, the following values of $q_l/q_v = [2, 4, 9]$, and also the case in which all the heat flux enters the liquid phase ($q_v = 0$), have been considered. Fig. 4.7 shows the laminar pressure evolutions obtained for the different values of q_l/q_v. The simulation with $q_l/q_v = 4$ has not been continued for the same physical time as the others because, even from the initial instants, it is evident that the agreement with the experimental pressurization rate is poor. The heat flux distribution between the two phases which best fits the experimental pressurization rate is $q_l/q_v = 9$, to which these values correspond: $q_l = 14.2$ W/m^2 and $q_v = 1.6$ W/m^2. So, this distribution is used in the case when the simulation of this test case is carried out without the wall conjugate heat transfer model.

4.6.3 Effect of the thermophysical modeling

Two different thermophysical modelings for the liquid and the ullage have been compared. In one case, real thermophysical and transport properties for liquid and gaseous N_2, taken from the NIST Chemistry WebBook [65] database, have been used. In the second case, the ideal gas assumption has been made for the vapor phase, and the liquid has been modeled with the Boussinesq approxi-

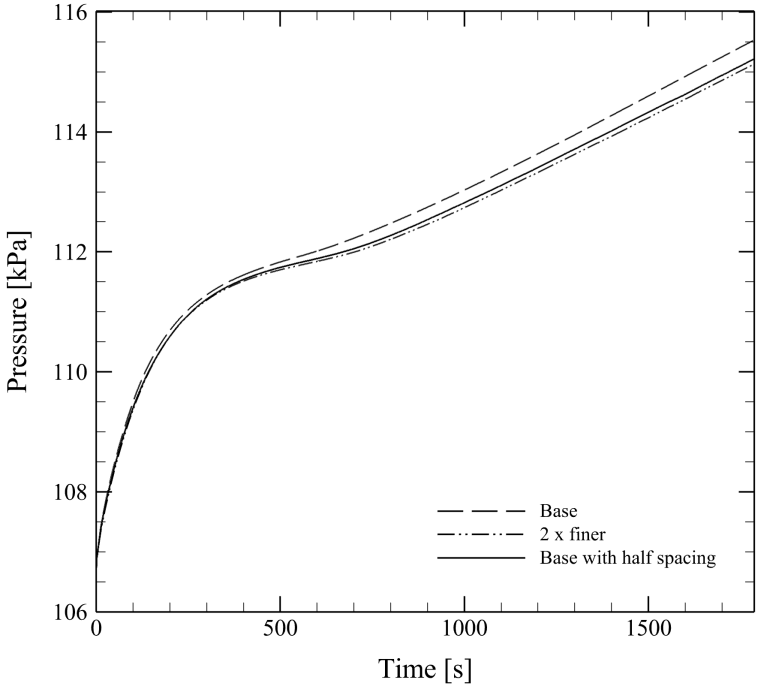

Figure 4.6: Grid convergence study, case without conjugate heat transfer: Numerical pressurization curves obtained with the three grids whose details are summarized in Tab. 4.3.

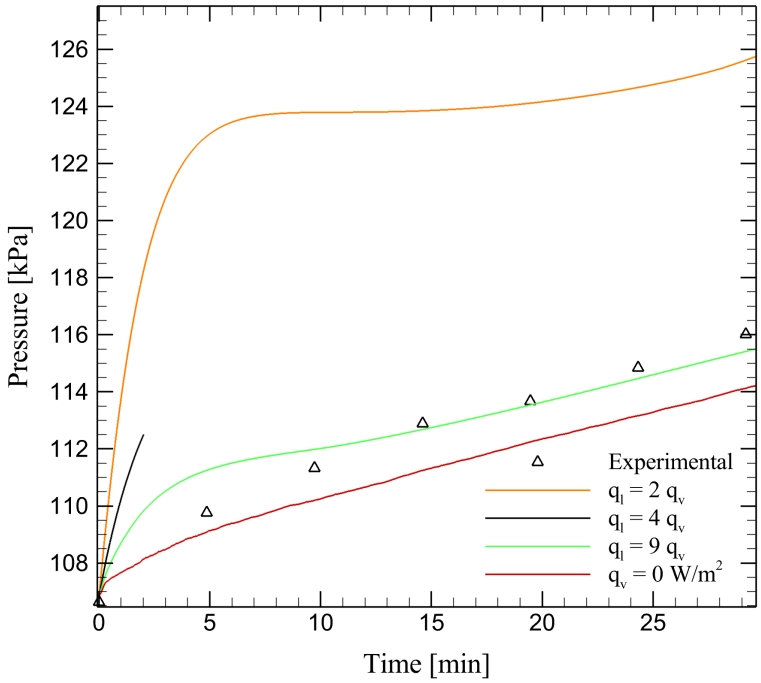

Figure 4.7: Pressure evolutions for different values of the ratio between the heat flux entering the liquid phase, q_l, and the heat flux entering the ullage, q_v. Results refer to wall decoupled simulations, with a laminar model.

mation (see Sec. 3.7). Fig. 4.8 shows the experimental and numerical results of pressure evolution (Fig. 4.8 (a)), and temperature stratification (Fig. 4.8 (b)). Numerical predictions refer to wall decoupled laminar simulations, carried out with the two different thermophysical modelings just exposed. Moreover, the heat flux distribution between the two phases has been chosen as explained in Sec. 4.6.2.

Thermal stratification profiles at tank axis of symmetry, in Fig. 4.8 (b), show the value of the ratio y/H as a function of temperature for two times, the initial time (blue curves) and after 2 h (red curves). In the y/H expression, y represents tank vertical dimension (as can be seen in Fig. 4.5), and H represents tank height. Moreover, dotted lines represent the saturation temperature corresponding to experimental tank pressure at a given time. In addition, the interface level is represented using a continuous black line. This level remains almost unchanged throughout the experiment because the amount of evaporated mass is low. Since numerical simulations have been initialized at the saturation temperature corresponding to initial tank pressure, numerical temperatures at the initial time are uniform, differently from the experimental temperature.

The difference in the pressurization rate estimated with the two models is of about 7%, and the temperature stratification profiles are almost the same with the two models. Instead, the computational time reduces of about 3.25 times with the use of the ideal gas law for the vapor phase and the Boussinesq approximation for the liquid phase. Indeed, with the latter modeling, 1.23 min are required to simulate a physical time of 1 s, using 10 CPUs. Instead, when the NIST properties are used, a time of 4 min is needed to simulate the same physical time with the same number of CPUs. As two-phase flow simulations are very time consuming, and given that the results

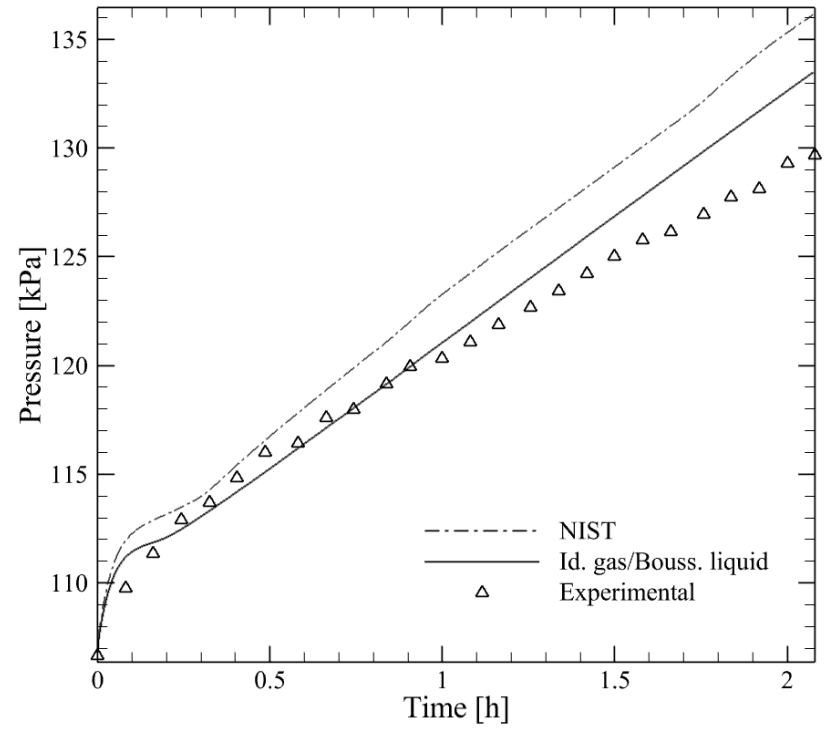

(a)

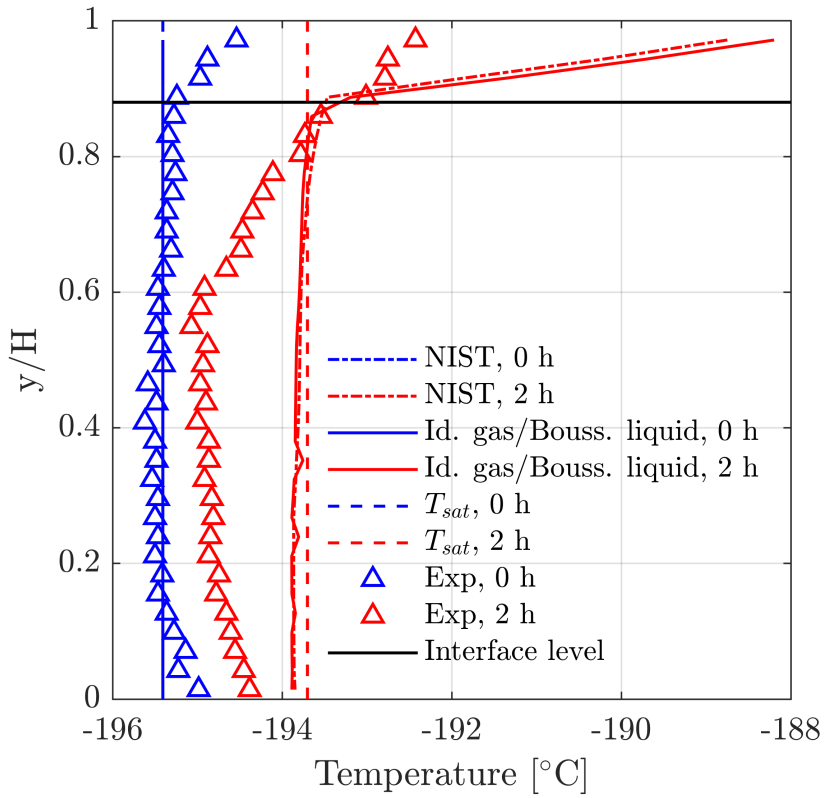

(b)

Figure 4.8: Comparison between experimental and numerical results of (a) pressure evolution and (b) temperature stratification at tank axis of symmetry. Numerical predictions refer to wall decoupled laminar simulations carried out with two different thermophysical modelings (either using the NIST properties, or modeling the gaseous N_2 as an ideal gas and the liquid N_2 with the Boussinesq approximation).

obtained with the NIST model do not show high discrepancies with respect to the ones obtained with the other modeling, it has been decided to retain, in the subsequent analyses, the modeling made by the ideal gas law for the vapor phase and the Boussinesq approximation for the liquid phase, in order to reduce the computational time.

4.6.4 Effect of the numerical setup

For the validation case of our interest, we have made a comparison between the results obtained with two different setups. The first, indicated as "Setup 1", is characterized by the use of the segregated algorithm "PISO" for pressure-velocity coupling, of the "Least Squares Cell Based" scheme to calculate the properties' gradients, of the "Body Force Weighted" scheme to interpolate pressure values at the cell faces, and of a computational time step equal to 0.01 s. The second, indicated as "Setup 2", is characterized by the use of the coupled algorithm "Coupled" for pressure-velocity coupling, of the "Green-Gauss Cell Based" scheme to calculate the properties' gradients, of the "PRESTO!" scheme to interpolate pressure values at the cell faces, and of a computational time step equal to 0.025 s.

Difference between Ansys Fluent® segregated and coupled schemes is that segregated algorithm solves the momentum and pressure-based continuity equations separately and, being a semi-implicit solution method, it is characterized by a relatively slow convergence, while, the coupled algorithm solves the momentum and pressure-based continuity equations together, and allows transient phenomena to be simulated with a larger time step than the previous algorithm [1].

Fig. 4.9 shows laminar results of pressure evolution (Fig. 4.9 (a)) and of temperature stratification at tank axis of symmetry (Fig. 4.9 (b)). Experimental data are also reported in the figure for comparison. Numerical results are presented for both "Setup 1" and "Setup 2". The simulations have been carried out without the solid wall, with a mass transfer intensity factor equal to 0.1 1/s, and using a heat flux distribution between the two phases such as to allow the numerical results to fit as much as possible the experimental pressurization rate ($q_l/q_v = 9$, as seen in Sec. 4.6.2). Numerical results show that the coupled algorithm ("Setup 2") allows to obtain results of pressurization rate and of thermal stratification comparable to those obtained with the segregated algorithm ("Setup 1"), but with a time step 2.5 times larger than that required in the segregated algorithm. The agreement between the experimental and numerical results of pressure evolution is even better in the case when the coupled algorithm is used. For these reasons, the coupled algorithm has been deemed more appropriate for such time-consuming simulations and, therefore, has been chosen for subsequent analyses.

4.6.5 Mass transfer intensity factor parametric study

As seen in Sec. 3.3, computation of mass transfer using the Lee model lies on the choice of a parameter, the mass transfer intensity factor, r (see Eqs. (3.8) and (3.9)). Optimum value of this parameter depends on many factors, both physical, for example the specific phase-change phenomenon, and numerical, for example the mesh size and computational time step. This means that, for a given combination of experimental test case and numerical setup, it has to be chosen in order to best fit the experimental data. For this test case, a parametric study has been carried out, using four values of this parameter, starting from 0.1 1/s, and increasing the value by a factor of 10

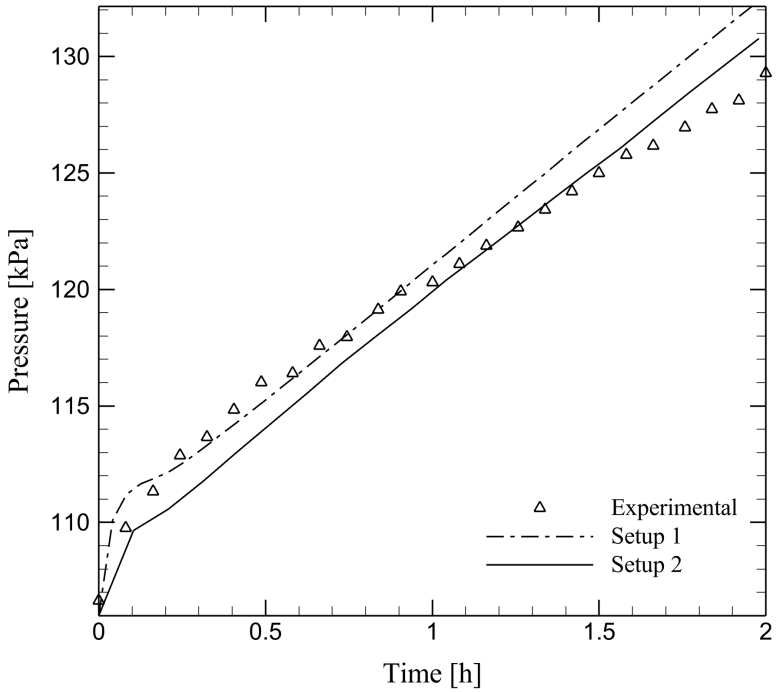

(a)

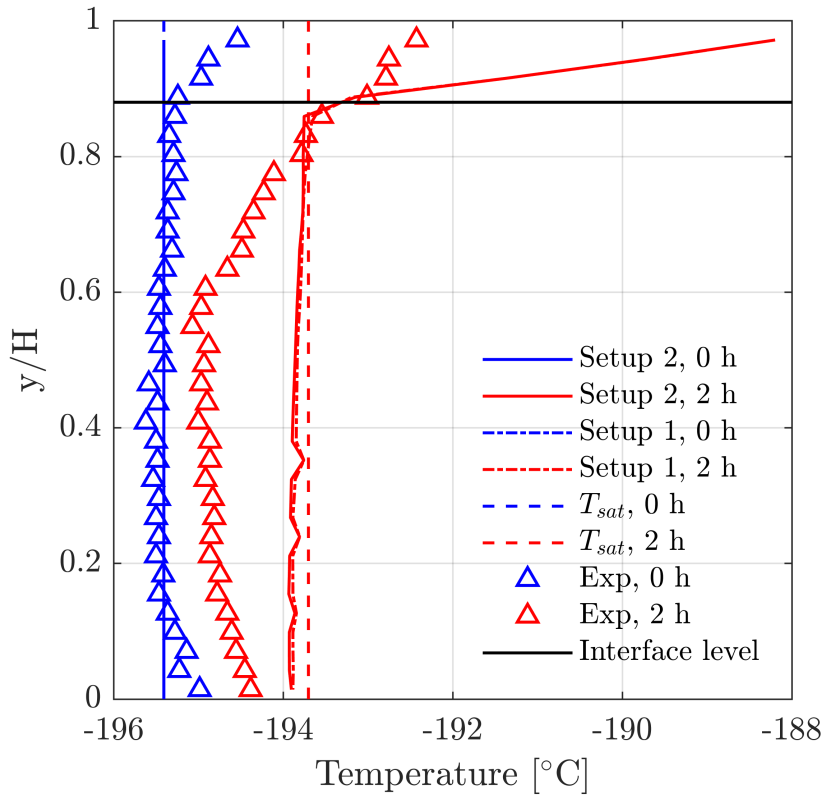

(b)

Figure 4.9: Comparison between experimental and numerical results of (a) pressure evolution and (b) temperature stratification at tank axis of symmetry. Numerical predictions refer to wall decoupled laminar simulations, carried out with two different numerical setups.

1/s, up to 100 1/s.

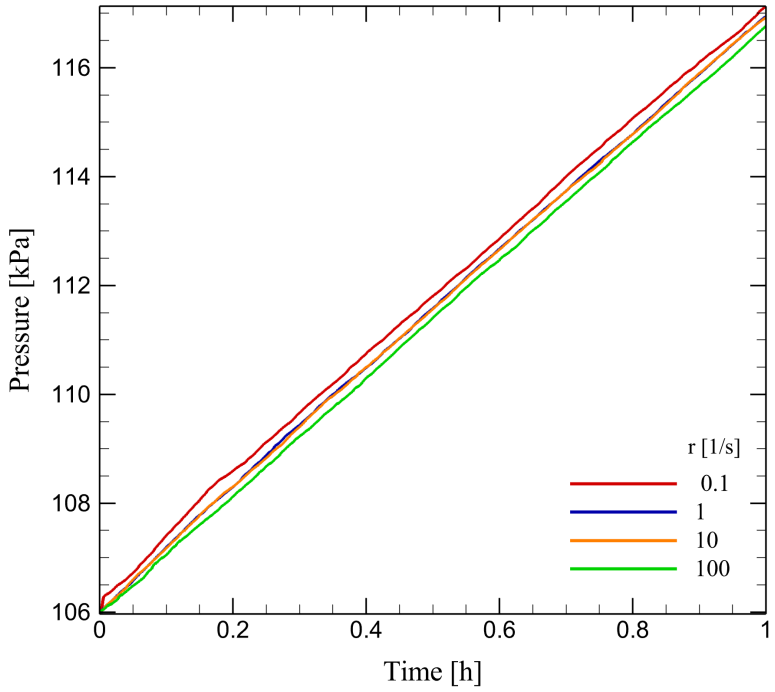

Figure 4.10: Pressure evolutions for values of the mass transfer intensity factor from 0.1 1/s up to 100 1/s. Results refer to wall decoupled simulations, with a laminar model, and with the assumption that all the heat flux is applied to the liquid phase.

To simplify this parametric study, wall decoupled simulations have been done, using a laminar model, and assuming that all the heat flux was applied to the liquid phase. Fig. 4.10 shows the self-pressurization curves obtained. It is possible to notice that pressure rise rate is insensitive to the value of r parameter, having variations less than 1% for variations of this parameter of three orders of magnitude. A very important issue is that, even if pressure results seem to be not influenced by the mass transfer intensity factor value, its choice plays a role in the stability of the numerical computation, so, for example, using a value of r equal to 1 1/s allows to run the simulation with a higher computational time step than the one that it is possible to use with r equal to 0.1 1/s. Finally, because the numerical results have proved not to be much affected by the value of this parameter, an intermediate value, equal to 1 1/s, has been used for subsequent calculations.

4.6.6 Importance of the use of a conjugate heat transfer model

As it will be cleared in the following, introducing the wall region in the numerical simulation is a fundamental aspect. Indeed, neglecting wall conduction leads to inability of numerical results to reproduce liquid temperature stratification close to the free-surface.

For evaluating the laminar or turbulent nature of the flow, the modified Rayleigh number, Ra_x^*, which describes the natural convection in case of uniform wall heat flux, can be used [69]:

$$Ra_x^* = \frac{g\rho^2 c_p \beta q_w x^4}{\mu\lambda^2} \tag{4.1}$$

where g is the acceleration due to gravity, ρ is the density, c_p is the specific heat, β is the volumetric thermal expansion coefficient, q_w is the uniform heat flux applied to the wall, x is the vertical coordinate measured from the origin of the boundary layer, μ is the dynamic viscosity, and λ is the thermal conductivity. The estimated maximum modified Rayleigh number, in the ullage, is highly below the critical value for the transition from laminar to turbulent, which is equal to 10^{11}. Instead, the estimated maximum modified Rayleigh number, in the liquid phase (i.e. that located in proximity of the liquid interface), resulted slightly above the critical value, so most of the fluid in the tank is in a laminar condition.

In Fig. 4.11, laminar results of pressure evolution (Fig. 4.11 (a)) and of temperature stratification at tank axis of symmetry (Fig. 4.11 (b)) are shown, and compared with experimental data. Numerical results are reported for both the case in which the simulation included the wall (and a conjugate heat transfer model was used) and the case of a simulation without the wall. In the latter case, the heat flux distribution between the two phases has been chosen to allow the numerical results to fit as much as possible the experimental pressurization rate, as explained in Sec. 4.6.2, i.e. with a ratio of 9 to 1 between the heat flux entering the liquid phase and that entering the ullage. The self-pressurization rate is overestimated by the wall coupled solution, with a percentage error of 66.8%, so, if only the pressure result is considered, the wall decoupled solution could seem better. However, if the temperature stratification result is also taken into account, the situation appears different. Looking at the thermal stratification profiles at tank axis of symmetry, in Fig. 4.11 (b), it is evident from the comparison with experimental data at 2 h, that temperature is overestimated by the numerical results obtained both in the case with and in the case without the solid wall. However, while the solution obtained in the case with the solid wall provides a more accurate representation of the shape of the liquid temperature stratification close to the free-surface, the solution obtained in the case without the solid wall demonstrates nearly uniform temperature distribution within the liquid. The extension of the liquid temperature stratification close to the free-surface, ΔT, can be quantified through the difference between the free-surface temperature and the bulk liquid temperature. This quantity increases in time during self-pressurization, reaching a value of approximately 1.2 K at 2 h, both in the experiment and in the results of the simulation coupled with the solid wall. Furthermore, in the case without the solid wall, there is a much greater overestimation of the ullage temperature. This is due to the lack of heat conduction through the wall, which would otherwise restrict the inflow of heat into the ullage. Indeed, calculations involving conjugate heat transfer have revealed that the heat flux entering the liquid phase significantly exceeds that entering the ullage.

Concerning the thermal stratification observed at the tank's bottom in the experimental results, neither of the numerical models manages to replicate it. However, this is not due to a deficiency of numerical models, since, in [84], it is stated that "the apparent slight increase in temperature near the bottom of the cell is an experimental artefact".

The reason why doing the coupled simulation with the solid wall is essential to represent liquid temperature stratification close to the free-surface is that the wall heat flux paths play a crucial role in the distribution of the entering heat fluxes between the liquid and the ullage. Indeed, even if the heat flux applied, as a boundary condition, to the external surface of the tank, is constant over the entire surface, the heat fluxes entering the liquid and vapor phases are different from each other. This can be attributed to the variation in thermophysical properties between the liquid and

vapor phases. In fact, the volumetric heat capacity, ρc_p, of liquid N_2 is about three hundred times that of vapor N_2, so that the latter will tend to heat up more if exposed to the same heat transfer rate, reaching, in a short time, a higher temperature than that of the liquid. The wall temperatures reflect the increase in temperature of the adjacent phases and, as a result, the heat coming from the upper section of the tank, in correspondence of the ullage, is redirected towards the lower section of the tank, by conduction. This phenomenon can be clarified by observing, in Fig. 4.12, the wall temperatures as a function of the curvilinear abscissa, "s", at various time instants. The curvilinear abscissa, moves tangentially to the wall, at the interface with the fluid, from the tank axis of symmetry, and its origin is shown, for clarity, in Fig. 4.5. The wall temperature attains its peak values at the uppermost part of the tank, undergoes a rapid decline in the lateral region of the wall adjacent to the ullage phase, and further diminishes within the wall region adjacent to the liquid temperature stratification close to the free-surface, eventually reaching a constant value in the wall zone adjacent to the bulk liquid.

Due to the pronounced heat transfer from the wall in contact with the ullage to the wall in contact with the liquid, the heat flux at the interface between the fluid and the wall experiences a peak in proximity to the free-surface. The wall to fluid heat flux at the interface between the fluid and the wall, as a function of the curvilinear abscissa, is shown in Fig. 4.13, for four time instants. In correspondence of the heat flux peak, a region of high evaporation develops, which is shown in Fig. 4.14 (a). This phenomenon had already been noticed by Stewart et al. [102], in the numerical simulation of a liquid H_2 self-pressurization test case. In the wall uncoupled simulation, the intensity of the evaporation in this specific area, while greater in comparison to the rest of the domain, is lower than that obtained in the wall coupled simulation (see Fig. 4.14 (b)). The aforementioned difference between the outcomes of coupled and uncoupled simulations provides supplementary proof of the higher heat flux that reaches the liquid in proximity of the interface, in the case in which the wall is taken into account in the simulation.

Since, as we have shown, not modeling the wall involves neglecting important thermal phenomena for the representation of the self-pressurization phenomenon, the wall coupling approach has been retained in the following analyses.

4.6.7 Effect of turbulence modeling

From the laminar simulation with the conjugate heat transfer model, an overestimation of both the pressure rise rate and the temperature values at 2 h has been obtained. For this reason, it is worth investigating the effect of a turbulence model. Using the Realizable $k-\varepsilon$ [98], whose details can be seen in Sec. 3.6.4, with Enhanced Wall Treatment [1], has resulted in an improved agreement between the experimental and numerical pressure results (as can be seen in Fig. 4.15 (a)), lowering the percentage error on self-pressurization rate from 66.8% to 10.2%.

Nevertheless, from temperature profiles in Fig. 4.15 (b), it is evident that liquid bulk temperature is overestimated by a comparable extent as observed in the laminar result, and that the turbulent model fails to represent the liquid temperature stratification close to the free-surface. The latter aspect is due to the fact that the turbulent model produces more intense convective recirculations than the laminar model, predicting more fluid mixing than the actual one. As a result, it is not possible to achieve an accurate reproduction of thermal stratification.

In conclusion, it can be inferred that the turbulent model is not suitable for numerically repli-

cating this test case. Additionally, it is worth considering the presence of another factor that might contribute to the overestimation of the pressurization rate and temperature when using the laminar model. In particular, this factor could be the experimental uncertainty on the entering heat transfer rate, as will be discussed in the next section.

4.6.8 The experimental uncertainty on the entering heat transfer rate

A primary challenge in numerically simulating the self-pressurization phenomenon stems from the uncertainty associated with the experimental data. Unfortunately, a small error in the experimental data produces a large error in the numerical estimates. In this particular test case, the overestimation of the self-pressurization rate and of the temperature by the laminar model, with the conjugate heat transfer, might potentially arise from a disparity between the heat flux mentioned in the experimental paper and the actual heat flux. A proof of this hypothesis can be found in a calculation made by Wang et al. [116]. They selected the experimental data from the same test case which has been chosen in this analysis, and they used them to validate their non-equilibrium multilayer thermodynamic model. However, they calculated the total heat transfer rate to the tank through an enthalpy balance, using experimental temperature and pressure data, and found it to be equal to 1.24 W, that is lower than the 2.2 W, declared in the experimental article.

In Fig. 4.16, results of pressure evolution (Fig. 4.16 (a)) and temperature stratification at tank axis of symmetry (Fig. 4.16 (b)), obtained imposing, as boundary condition, the wall heat flux derived by the total heat transfer rate to the tank of Wang et al. [116], are shown. Results achieved with the old heat flux value (calculated from the experimental heat transfer rate) and the experimental ones are also represented for comparison. Employing the lower heat flux boundary condition results in a slight underestimation of the pressurization rate. However, the lower heat flux boundary condition provides a more accurate representation of the actual pressurization rate compared to the outcome obtained with the higher heat flux, indeed the percentage error is lowered from 66.8% to 12.1%, as summarized in Tab. 4.4.

Table 4.4: Pressurization rate, percentage error, $E_{r\%}$, on pressure slope, and average $E_{r\%}$ on temperature, for laminar coupled simulations, with the heat flux values from Perez et al. [84] and Wang et al. [116].

	Pressurization rate $\left[\frac{\mathbf{kPa}}{\mathbf{h}}\right]$	$\boldsymbol{E_{r\%}}$ **on pressure slope** **[-]**	**Mean** $\boldsymbol{E_{r\%}}$ **on temperature** **[-]**
Experimental	8.98	-	-
Perez et al. [84] q_w	14.98	66.8%	0.53 %
Wang et al. [116] q_w	7.90	12.1 %	0.33%

Also the liquid temperature profile at tank axis of symmetry at 2 h is reproduced with greater accuracy with the lower heat flux value (see the mean percentage error on temperature in Tab. 4.4). But, with the new boundary condition, both the temperature in the ullage and the extension of the liquid temperature stratification close to the free-surface are slightly underestimated.

The case with the new boundary condition has been simulated also with a different initial condition, i.e. with an initial temperature profile which is an interpolation of the initial experimental temperature profile. Fig. 4.17 shows pressure evolutions (Fig. 4.17 (a)) and temperature stratifications (Fig. 4.17 (b)), obtained both in the case with a uniform initial temperature and in the

case with a stratified initial temperature. Both temperature and pressure results turn out to be not very sensitive to the initial temperature condition. The only difference is in the pressure evolution in the first 1.5 h, which is better described with the more realistic initial condition, but the final numerical pressurization rate is the same with both initial temperature profiles.

Since by using the new heat flux we obtain temperature and pressure values closer to the experimental ones, but both the temperature in the ullage (at 2 h) and the pressurization rate (in the first half hour of self-pressurization) are still underestimated, it is reasonable to deduce that the actual incoming heat transfer rate had an intermediate value, between the experimental one and the one calculated by Wang et al. [116]. Finally, a simulation with an intermediate value of the entering heat transfer rate, 1.48 W, such to achieve the closest match with the experimental pressure rise rate, has been carried out. The whole self-pressurization phase, i.e. the first 4 hours of the experiment have been simulated, obtaining the pressure evolution and temperature profiles shown in Fig. 4.18. Using this value of heat transfer rate, the pressurization rate in the first half hour of self-pressurization is estimated with greater accuracy with respect to the one derived using the heat transfer rate computed by Wang et al. [116]. As a consequence, there is less discrepancy between experimental and numerical pressures in the remaining part of the self-pressurization phase. Moreover, the thermal profile at 2 h exhibits a greater resemblance to the experimental counterpart with respect to the ones obtained using both the heat transfer rate by Perez et al. [84] and the one by Wang et al. [116]. In particular, with the intermediate heat transfer rate, temperatures are better described in the ullage, at the interface, and under the free-surface, instead bulk liquid temperatures are described slightly better using the heat transfer rate by Wang et al. [116]. Lastly, employing the intermediate heat transfer rate also results in an accurately described temperature profile at 4 h.

4.6.9 Comparison between CFD and reduced order models' results

The in-house 0D model and the 1D model developed by NASA [20], presented in Chap. 2, can be used to estimate both the temperature stratification and the pressure evolution of the selected validation test case, and to compare their results with those obtained with our CFD methodology. Fig. 4.19 shows a comparison between experimental data, reduced order models' results, and numerical results of pressure evolution (Fig. 4.19 (a)) and temperature stratification at tank axis of symmetry at 2 h (Fig. 4.19 (b)). Numerical predictions refer to the computation carried out with the intermediate entering heat flux, such as to fit the experimental pressurization rate (see Sec. 4.6.8). It is evident both in Fig. 4.19 and in Tab. 4.5 that the reduced order models are able to describe the pressure rise rate with reasonable accuracy. Moreover, the average percentage error, $E_{r\%}$, on pressure is slightly above 2% with the 0D model, which is the reduced order model which performs worse, hence there is a very good agreement between the reduced order models' results and experimental data for pressure.

As concerns the temperature, the predictive capabilities of the CFD model compared with the reduced models are much more evident. Both the 0D and the 1D models underestimate the ullage temperature, and are not able to represent well the temperature stratifications arising both in the ullage and close to the free-surface. The latter aspect is more obvious for the 0D model, which describes both the ullage and the liquid with an average temperature, but is less obvious for the 1D model.

Table 4.5: Comparison between CFD and reduced order model's results: pressurization rate, and average percentage error, $E_{r\%}$, on pressure.

	Pressurization rate [kPa/h]	**Mean $E_{r\%}$ on pressure [-]**
Experimental	8.98	-
CFD	9.36	1.4%
1D	9.88	0.82%
0D	9.79	2.11%

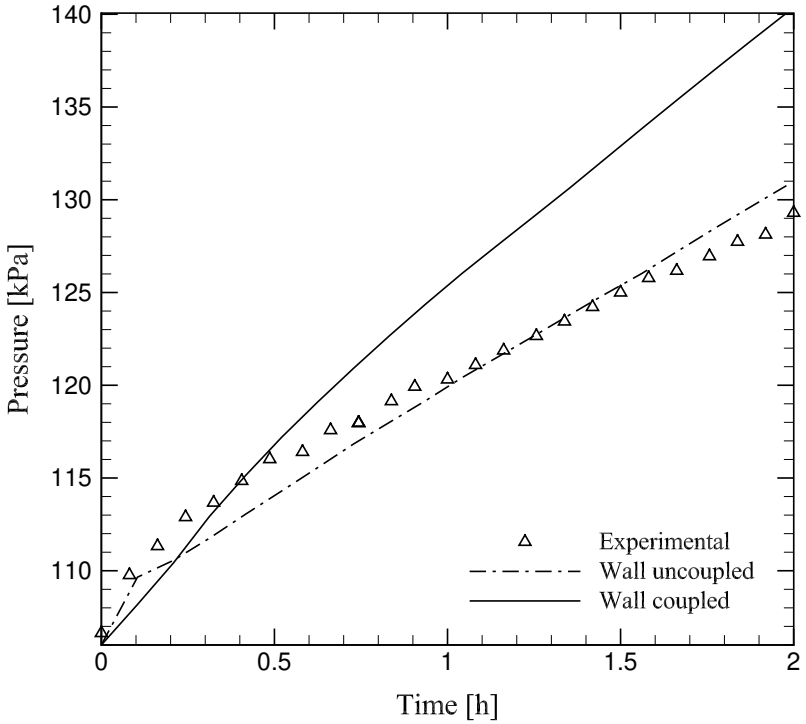

(a)

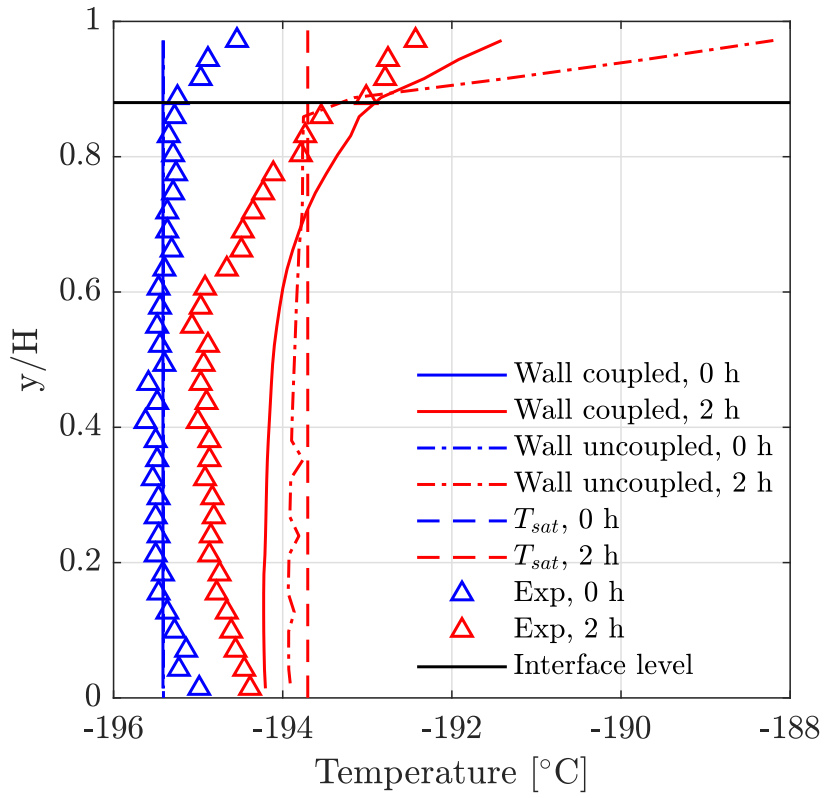

(b)

Figure 4.11: Comparison between experimental and numerical results of (a) pressure evolution and (b) temperature stratification at tank axis of symmetry. Numerical predictions refer to laminar simulations with and without wall coupling.

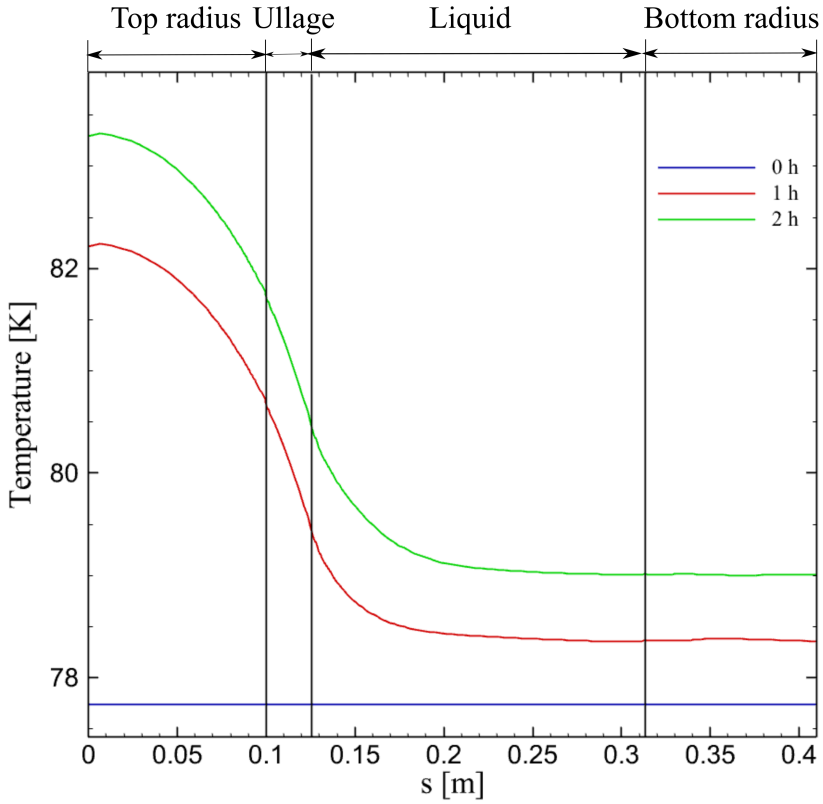

Figure 4.12: Laminar, wall coupled predictions of wall temperatures at the interface with the fluid, as a function of the curvilinear abscissa, for three time instants.

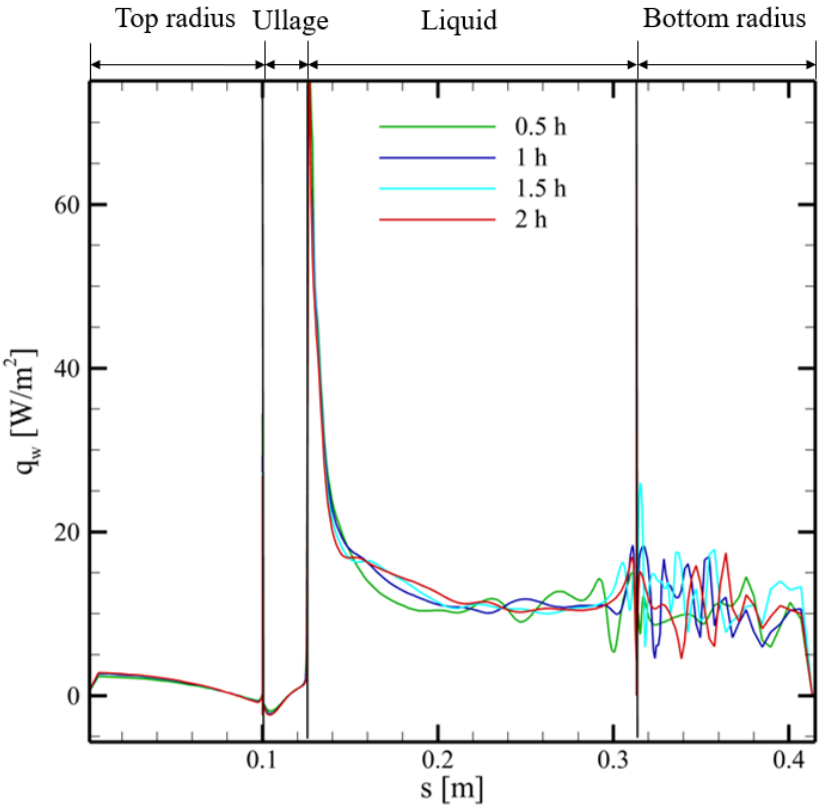

Figure 4.13: Laminar, wall coupled predictions of wall to fluid heat flux, as a function of the curvilinear abscissa, for four time instants.

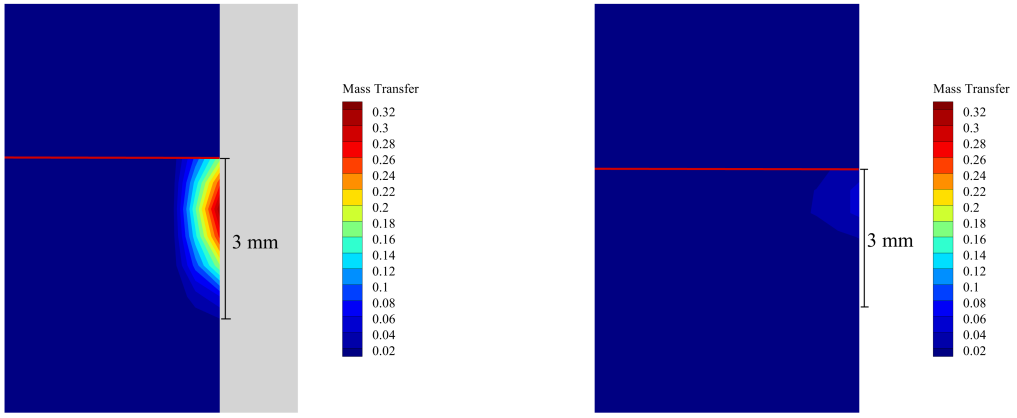

(a) (b)

Figure 4.14: Contour of mass transfer (i.e. the mass source term in Eq. (3.4)) at 2 h, for (a) the laminar simulation, coupled with the solid wall, (b) the laminar simulation, not coupled with the solid wall. Zoom of a tank region near the free-surface (red line).

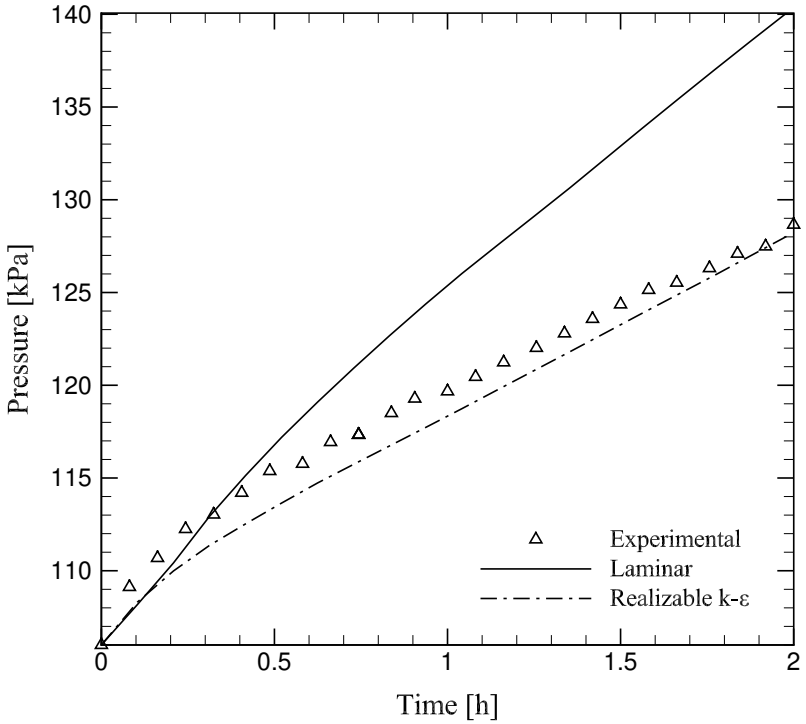

(a)

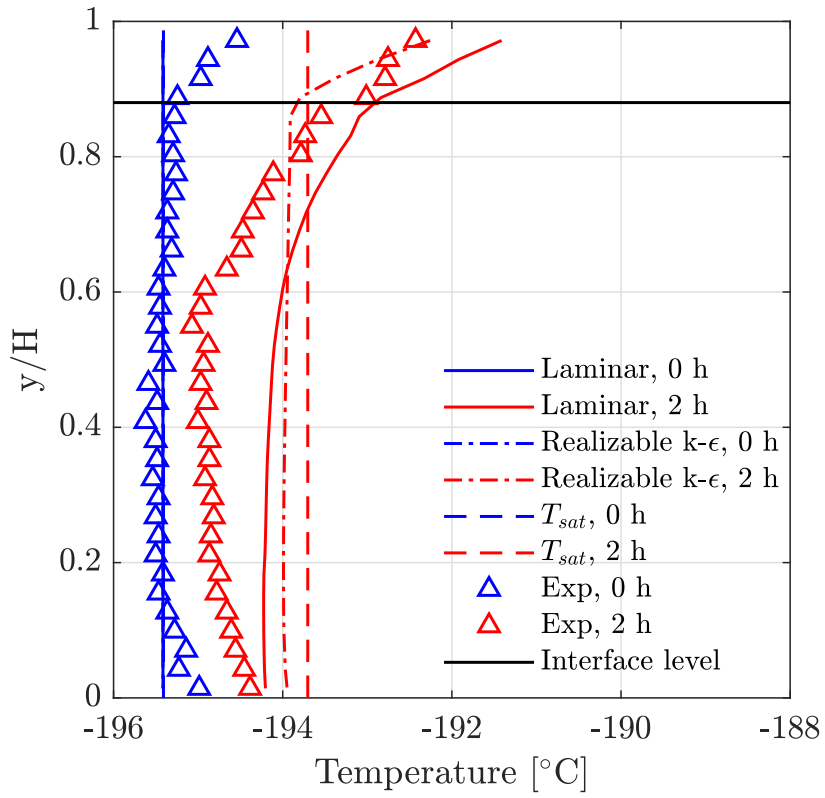

(b)

Figure 4.15: Comparison between experimental and numerical results of (a) pressure evolution and (b) temperature stratification at tank axis of symmetry. Numerical predictions refer to wall coupled simulations with a laminar and with a turbulence model.

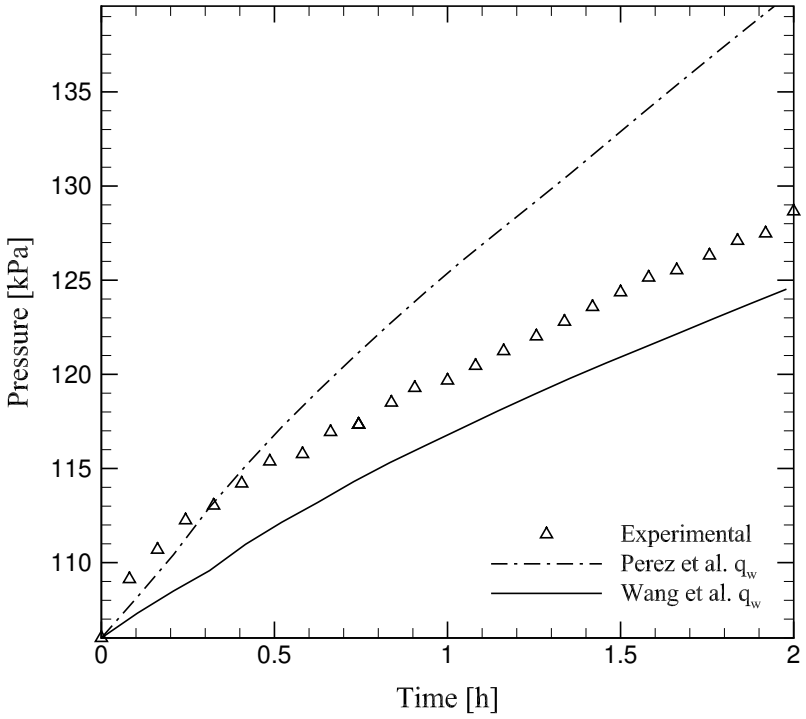

(a)

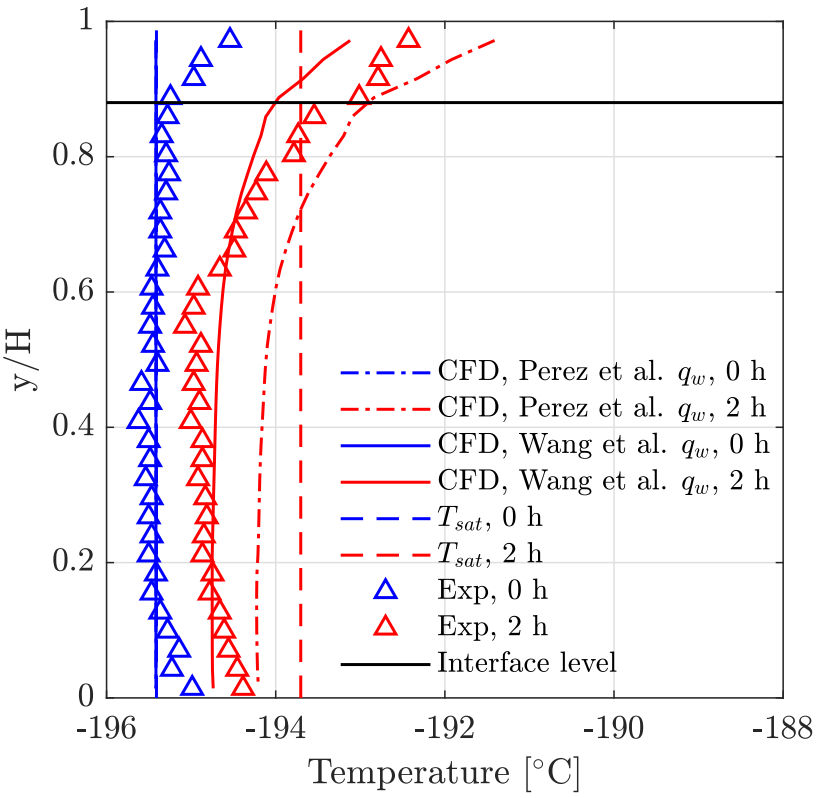

(b)

Figure 4.16: Comparison between experimental and numerical results of (a) pressure evolution and (b) temperature stratification at tank axis of symmetry. Numerical predictions refer to laminar, wall coupled simulations, with the heat flux values from Perez et al. [84] and from Wang et al. [116].

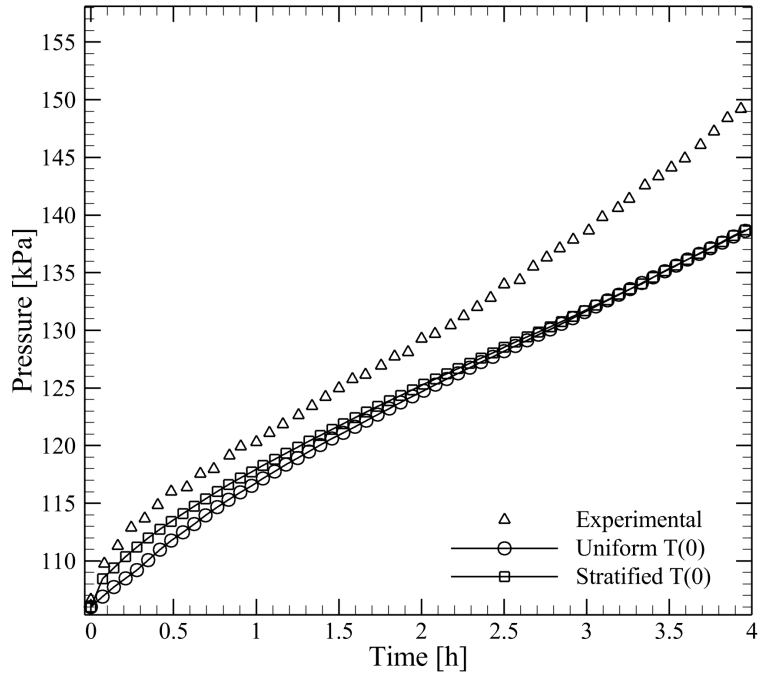

(a)

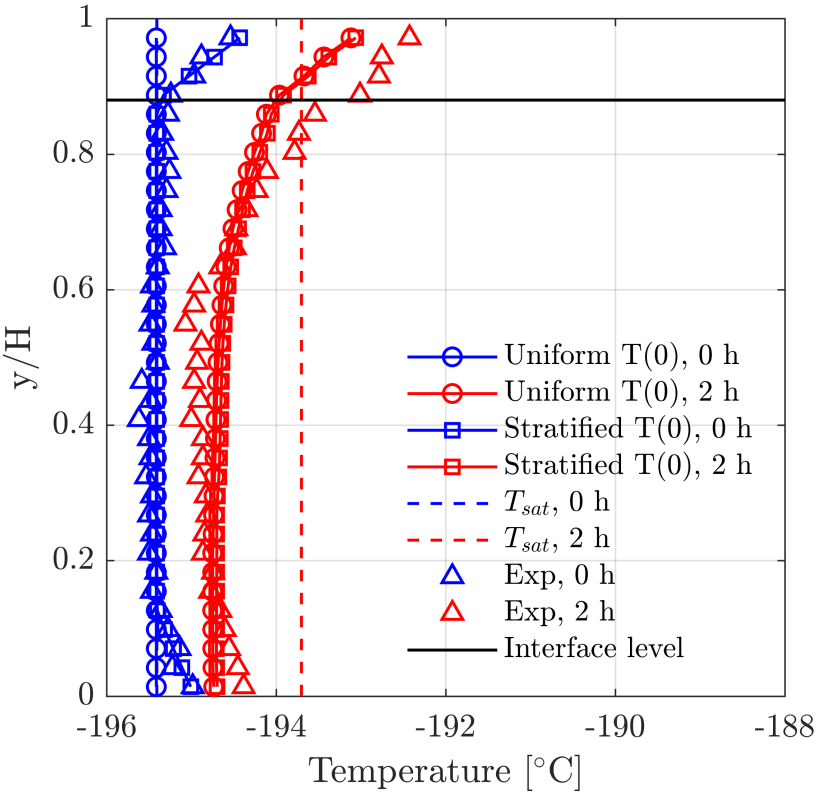

(b)

Figure 4.17: Comparison between experimental and numerical results of (a) pressure evolution and (b) temperature stratification at tank axis of symmetry. Numerical predictions refer to laminar, wall coupled simulations, with the heat flux values from Wang et al. [116], and either with a uniform or with a stratified initial temperature profile.

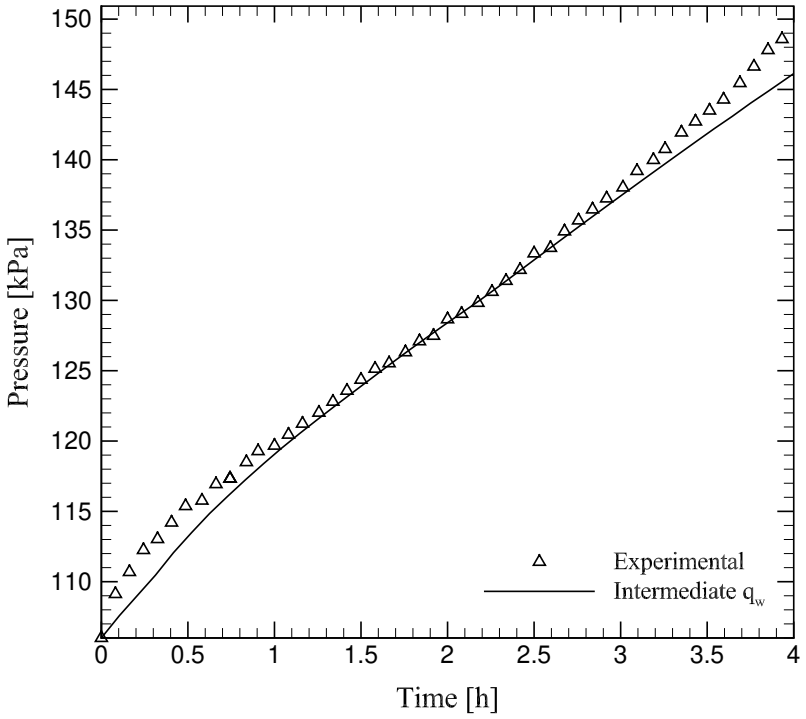

(a)

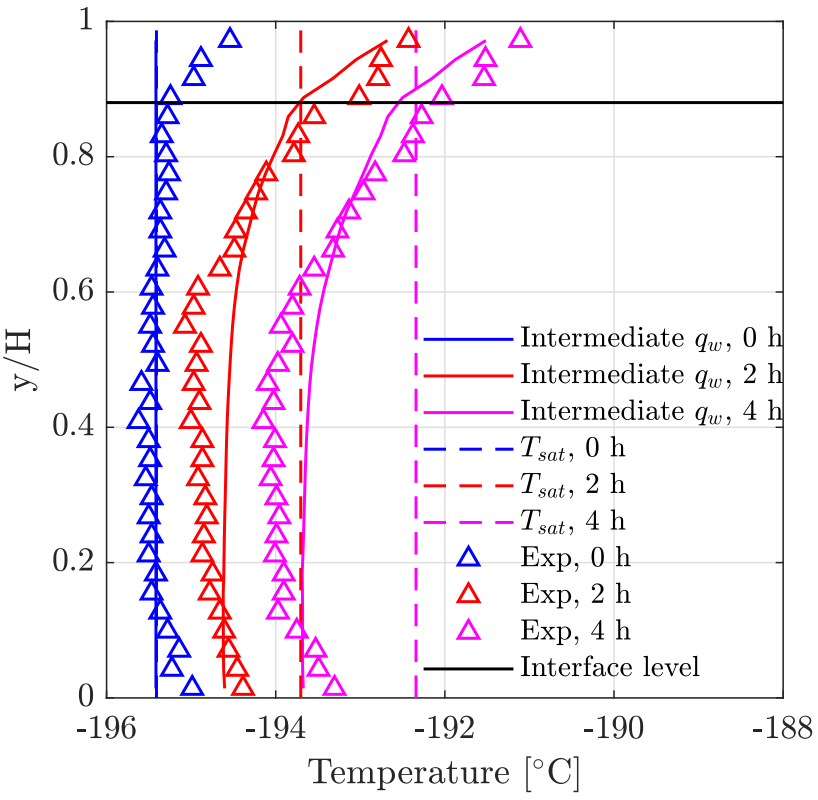

(b)

Figure 4.18: Comparison between experimental and numerical results of (a) pressure evolution and (b) temperature stratification at tank axis of symmetry. Numerical predictions refer to the computation carried out with an intermediate entering heat flux, such as to fit the experimental pressurization rate.

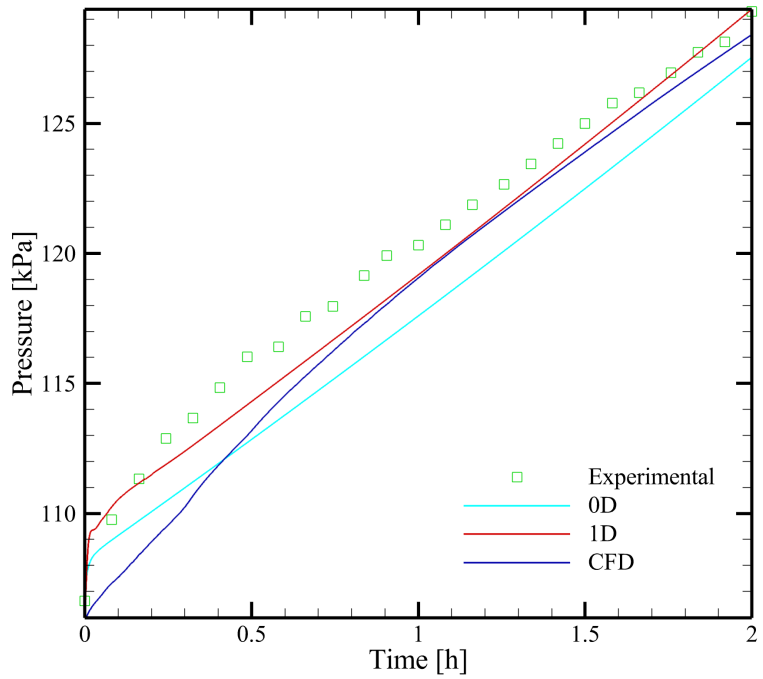

(a)

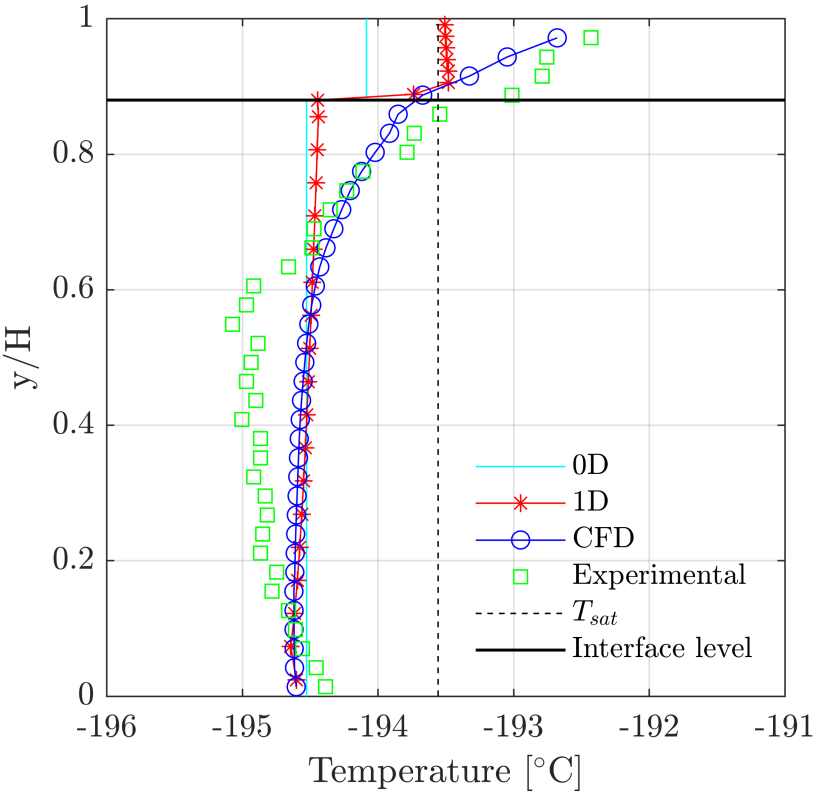

(b)

Figure 4.19: Comparison between experimental data, reduced order models' results, and numerical results of (a) pressure evolution and (b) temperature stratification at tank axis of symmetry. CFD predictions refer to the computation carried out with an intermediate entering heat flux, such as to fit the experimental pressurization rate.

Chapter 5

Active-pressurization of a liquid N_2 tank

In this chapter, the CFD results of a ground-based active-pressurization experiment, inside a liquid N_2 tank [72], are presented. The selected test case differs from the one presented in the previous chapter for the type of operating condition (active-pressurization instead of self-pressurization) and for the boundary conditions (there is no longer a heat flux applied on all the external walls in this case). This active-pressurization experiment has been chosen for the validation because of the accuracy of the initial and boundary conditions provided in [72]. Previous numerical studies have not emphasized the effect that particular numerical modeling choices regarding the phenomenon of active-pressurization have on the results. Instead, in this study, the reason why some modeling choices (for example a gradual termination of the pressurant gas injection) have a positive impact on the reliability of the results is explained. The goal of this validation is to define a numerical methodology able to describe the main thermo-fluid-dynamics phenomena occurring in an actively pressurized cryogenic tank, without propellant expulsion, in the case when the pressurant gas is of the same chemical species as the propellant. In particular, the proper numerical methodology is defined comparing the experimental data of the selected validation experiment with the numerical ones obtained with various numerical models.

Ludwig et al. [72] already carried out simulations of their own experiment, obtaining an active-pressurization rate highly consistent with the experimental one. However, they largely overpredicted the pressure decrease at the end of active-pressurization. Instead, with our methodology, a high fidelity reproduction of both the active-pressurization rate and of the pressure decrease after the end of gas injection is obtained.

This chapter is organized as follows. First, a literature survey on the active-pressurization phenomenon is presented. Later, the chosen validation experiment and the used thermophysical and transport properties are described. Then, the computational setup and the results of grid convergence study are presented. Next, the problem of the uncertainty of the experimental data and of its influence on numerical results is discussed. Then, a comparison is shown between the experimental results and the numerical ones obtained varying the flow regime (laminar or turbulent) and the modeling setup (effect of various turbulence models, of the profile of the pressurant gas mass flow rate, etc.). Finally, a comparison between CFD results and results obtained with the 0D model, presented in Chap. 2, is made.

5.1 Active-pressurization literature survey

Active-pressurization is commonly carried out in cryogenic propellant tanks for rockets and satellites for multiple reasons. Among these, there is the need to subcool the propellant, in order to suppress bulk boiling; to produce propellant expulsion during the engine operation; and, sometimes, to stiffen the structure of the tank. Moreover, during turbopump-fed rocket engine operation, tank pressurization is essential to provide pressurized fuel and oxidizer to the turbopumps, to prevent cavitation.

Active-pressurization is commonly achieved through the injection of a pressurant gas directly into the ullage, by the use of a diffuser. The pressurant gas can come from a pressurant supply tank or, otherwise, pressurization can be autogenous. In the latter case, pressurization is done by removing a small amount of liquid from the tank, heating it until it becomes gaseous, and then using it to pressurize the tank.

Interest in minimizing the pressurant mass requirements originates from the desire to decrease the dimension and number of pressurant supply tanks, in order to reduce the mass of the vehicle. Earlier experimental tests and computational investigations have revealed the influence of several factors on the pressurant gas requirement: the inlet gas temperature [103–106, 115], the diffuser design [105, 106, 115], the heat and mass transfer at the liquid-ullage interface [79], the pressurant gas species [113], and the tank wall thickness [115]. Predicting the pressurant mass requirement is crucial in defining cryogenic propulsion systems, and it is a complex task. This complexity derives from the thermo-fluid-dynamics processes characterizing these systems, among which the prevalent are linked to the heat transfer between the ullage and the tank wall and the heat and mass transfer between the ullage and the liquid.

In the 1960s and 1970s, the first experimental investigations of the active-pressurization phenomenon in cryogenic tanks in normal gravity were carried out at NASA. In particular, the problem of tank pressurization during propellant expulsion was widely investigated. For example, in [32, 91], ten liquid H_2 discharge experiments, using ambient temperature H_2 or He as pressurant gas, were conducted. Tests varying the liquid outflow rate and the tank pressure were carried out. During the experiments the gas was continually supplied, in order to keep the ullage pressure, and, thus, the propellant outflow rate, constant. Between 1969 and 1970, four experimental studies, regarding the active-pressurization during liquid H_2 expulsion, from two spherical tanks of different dimensions, pressurized either with gaseous H_2 [105, 106], or with gaseous He [103, 104], were performed. The related experimental results showed that the parameters having a strong influence on the pressurant gas requirements are the inlet gas temperature, the diffuser geometry, and the tank pressure level.

In the literature, there are also experimental results regarding the active-pressurization of cryogenic tanks without propellant expulsion. For example, three active-pressurization experiments in a liquid H_2 tank, pressurized either with gaseous H_2 or with gaseous He, at about room temperature were carried out in [79]. During the test procedure, pressurization was done rapidly, and, then, the desired target pressure was held constant. Results showed that the condensation at the liquid-ullage interface creates a substantial heat transfer to the liquid, which must be taken into account in stratification studies. Moreover, in [79], it was stated that the effect of the mass transfer on the pressurant requirement estimation has to be considered, while the effect of the heat transfer at the liquid-ullage interface can, probably, be neglected.

Besides experimental studies, CFD analyses are a valid tool for the study of active-pressurization inside cryogenic tanks, as they allow both to reduce the costs associated with complex experiments, and to speed up the design process of the active-pressurization system. In various studies presented in the literature, a numerical methodology is proposed and validated with available experimental results. For example, in [94], a numerical model, which combines a weakly compressible multiphase solver, based on the VOF method, with a suitable phase change model, was developed. Moreover, it was validated with both two analytical solutions and with the data of a cryogenic active-pressurization experiment [72]. In the last case, the use of the turbulence SST $k-\omega$ model did not influence the quality of the results during the active-pressurization phase, but had a negative effect on the simulation of the remaining part of the experiment. In [101], a numerical methodology, based on the Eulerian Multiphase model, combined with a subgrid model, was presented. The subgrid model was used to solve the Schrage equation for the mass transfer and the 1D heat equation at the interface. This methodology was used to simulate an active-pressurization experiment, in which liquid H_2 was pressurized with gaseous H_2 at high temperature. In [16], a liquid N_2 autogenous pressurization experiment was simulated, using different multiphase models, flow regimes, and enabling or not the phase change. Results showed that the setup characterized by the Sharp Interface model and laminar model, with the phase change activated, best matched the experimental data.

Also the problem of pressurization during propellant expulsion has been thoroughly examined through CFD. Wang et al. [113–115] presented three CFD studies on this topic. In all cases, their methodology was validated using experimental data from [91]. In [114], they dealt with the thermal and pressurization behavior of a liquid O_2 tank, pressurized with gaseous He. Moreover, they modeled the outside aerodynamic heating, and considered the fluid and tank wall regions, as well as the external insulation layer, which was made of foam. In [113] and [115], the same liquid H_2 tank, pressurized with either gaseous H_2 or gaseous He, was considered. In particular, in [113], they highlighted the superior pressurization performance of gaseous H_2 compared to gaseous He, due to its higher specific heat. While, in [115], they analyzed the impact on pressurization behavior of various parameters, among which the inlet gas temperature, the wall thickness, the outflow rate, and the diffuser structure.

Several additional CFD investigations documented in the literature did not concentrate on replicating specific experimental test cases, rather, they aimed to simulate relevant operational conditions. For example, in [67], the active-pressurization during atmospheric flight and the pressurized discharge during the orbit flight were simulated in a final stage liquid O_2 tank. The tank was pressurized with high temperature gaseous O_2. The VOF model was used, mass transfer was considered using Lee model, and the low-Re $k-\varepsilon$ turbulence model was selected. Moreover, both aerodynamic heat and space solar radiation were imposed as boundary conditions. Their numerical methodology had been validated in previous works, using data from [91]. Numerical results showed ullage mass condensation during the active-pressurization phase. Later, they simulated the active-pressurization during the pre-launch phase [68], in the same tank as in [67], with the same propellant and pressurant gas. They employed a similar setup as before but, this time, adopted the standard $k-\varepsilon$ turbulence model. They took into account the external forced convection heat exchange, and considered the effect of different environmental temperatures. Numerical results showed condensation during the whole pressurization.

Finally, many reduced order models have been developed over the years to simulate tank opera-

tions. An example is the 1D model developed, in [91], to simulate the problem of tank pressurization during propellant expulsion, in a cylindrical tank. This model was validated against the results of nineteen liquid H_2 experiments, taken from both [32] and [4], characterized by a variation of the following parameters: tank pressures, outlet flow rates, and pressurizing gases.

5.2 Test case description

The selected validation experiment is a ground-based active-pressurization experiment, performed in a liquid N_2 tank [72]. Throughout the experimental procedure, the test tank was placed in a vacuum casing, for better insulating it from the external environment. The experiment was carried out in two phases. During the first phase, whose duration, t_{press}, was of 60.7 s, gaseous N_2 was injected directly in the ullage, through the use of a radial diffuser, until a target pressure of 300 kPa was reached. Hence, in this test, the pressurant gas was of the same species as the propellant. Then, the tank inlet valve was closed and the second phase, which lasted 152.3 s, was characterized by a pressure decrease, until pressure reached a constant value, and the experiment was completed. According to the data provided in [72], the simulated tank is cylindrical, with a round shaped bottom. Fig. 5.1 shows a scheme of the tank, together with its characteristic dimensions. The liquid-ullage interface is set at a height, H_l, of 0.445 m; the height of the ullage, H_v, is 0.205 m; and the tank inner radius, R, is 0.148 m.

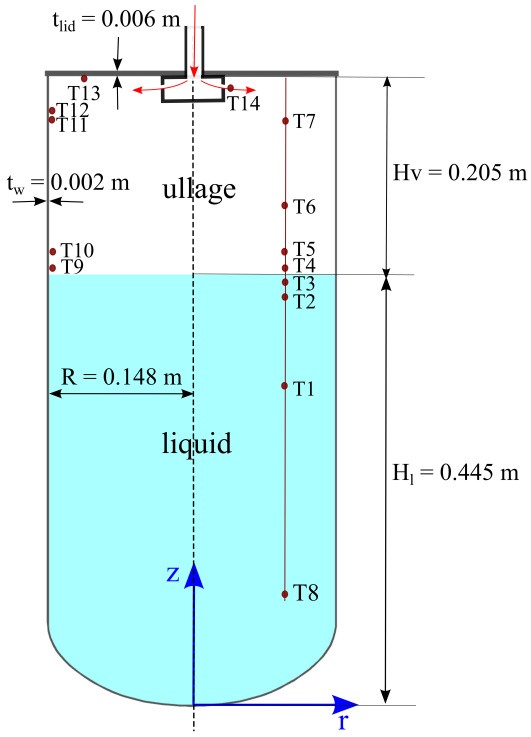

Figure 5.1: Tank scheme with the indication of the origin of the axisymmetric axes "r" and "z", of the tank characteristic dimensions, and of the position of the temperature probes (T1 to T14).

The wall thickness, t_w, is 1.5 mm in the top third of the tank and 2 mm below. In the numerical analysis, a thickness of 2 mm is used for all the tank wall, after verifying, as we will see in Sec. 5.6.2,

that using a thickness of 1.5 mm produces approximately equal results. Instead, the lid, is modeled with a thickness, t_{lid}, of 6 mm, which has been chosen approximately, looking at a tank schematics in [72], because this data lacked in [72]. Initial pressure for the selected experiment is 104.2 kPa. Before the beginning of pressurization, the tank ullage is filled only with evaporated N_2. When the experiment is started, relatively hot gaseous N_2, characterized by a temperature of 352 K, is injected with a constant mass flow rate of $8.3 \cdot 10^{-4}$ kg/s. During the experiment, temperature is measured by numerous probes, whose locations are specified in Tab. 5.1, and indicated in Fig. 5.1.

Table 5.1: Locations of the experimental temperature probes.

Probe	T1	T2	T3	T4	T5	T6	T7
r [m]	0.098	0.098	0.098	0.098	0.098	0.098	0.098
z [m]	0.33	0.43	0.44	0.45	0.46	0.51	0.61
Probe	T8	T9	T10	T11	T12	T13	T14
r [m]	0.098	-0.148	-0.148	-0.148	-0.148	-0.098	0.0063
z [m]	0.11	0.45	0.46	0.625	0.63	0.65	0.644

5.3 Thermophysical and transport properties

Liquid phase density is modeled with the Boussinesq approximation (see Sec. 3.7), so it is left constant in the governing equations, except in the buoyancy force term in the momentum equation, where density variation is written as a linear function of temperature. As the liquid N_2 phase does not experience large temperature variations throughout the duration of the experiment, its thermophysical and transport properties have been left constant, and they have been extracted from the NIST Chemistry WebBook [65] database, at the average experimental temperature and pressure. During the experiment, the injection of pressurant gas, at a relatively high temperature, leads to a noticeable increase in temperature for both the ullage and the wall. For this reason, temperature varying properties are used for them. In particular, the ideal gas equation of state is used to model the gaseous N_2 density, and the Sutherland's law [110], whose details can be seen in Sec. 3.7, is used to model its viscosity and thermal conductivity. Whereas, gaseous N_2 specific heat is modeled with a piecewise linear approximation of the data taken from the NIST database, at the average experimental pressure. The wall material considered is, in agreement with the experiment [72], stainless steel. Because the precise indication of the type of stainless steel was missing in [72], AISI 316 SS has been chosen, as it is sometimes used for cryogenic tank structures. However, if we had considered another type of stainless steel, the properties would have changed only slightly. The wall specific heat and thermal conductivity are modeled with a piecewise linear approximation of the temperature dependent data, taken from the NIST database for solid materials at cryogenic temperatures [53]. Instead, the wall density is modeled as constant, and equal to 8053.7 kg. All constant liquid properties are listed in Tab. 5.2.

It is clear from Eqs. (3.8) and (3.9), in Sec. 3.3, that an accurate representation of the saturation line is fundamental for a precise calculation of phase change mass transfer. In our simulations, NIST

Table 5.2: Constant physical properties for the liquid N_2, taken from [65].

	ρ [kg/m^3]	λ [W/(m · K)]	c_p [J/(kg · K)]	μ [Pa · s]
Liquid phase	804.14	0.144	2042.5	$1.579 \cdot 10^{-4}$

data have been used for a piecewise linear representation of the N_2 saturation line. Moreover, a constant value of the surface tension coefficient, equal to 0.0072183 N/m, is used. A standard state enthalpy of -1.211 $\cdot 10^7$ J/kmol and of 0 J/kmol, both at the reference temperature of 298.15 K, are used for the liquid N_2 and for the gaseous N_2, respectively. These values have been retrieved from [73]. Moreover, a liquid volumetric thermal expansion coefficient of 0.0057 1/K is used, which has been computed from NIST data, using Eq. (3.60) of Sec. 3.7.

5.4 Computational setup

Transient simulations have been carried out using the pressure-based solver of the commercial CFD software Ansys Fluent® [1]. The flow is modeled as 2D axisymmetric, which is a reasonable assumption for the given geometry and boundary conditions. A second order implicit time scheme is used for time discretization. After preliminary convergence studies, time steps of 10^{-2} s and of $5 \cdot 10^{-3}$ s, for turbulent and laminar analyses, respectively, have been selected. The Courant number is set to 0.5. These parameters have been selected appropriately, by making a trade-off between computational cost and numerical accuracy. Second order upwind schemes are used for spatial discretization of the convective terms in density, momentum, energy, and turbulence equations, and Ansys Fluent®'s "Compressive" scheme [1] is selected for the volume fraction equation, with the selection of the sharp interface regime modeling. "PRESTO!" scheme [1] is used to interpolate pressure values at the cell faces. "Coupled" scheme [1] is used as pressure-velocity coupling scheme. Green-Gauss cell based scheme is used to calculate the properties' gradients, which are necessary to discretize the convection and diffusion terms in the flow governing equations.

The boundary conditions imposed in simulations, represented in Fig. 5.2, are the following: all the tank external surfaces (except the lid's ones) are set as adiabatic walls, indeed, the heat flux on that walls can be neglected due to the short duration of the experiment and to the insulation provided by the presence of the vacuum casing; a temperature of 280 K is imposed on the lid exterior surfaces, as suggested in [72]; and the interfaces between the fluid and the wall are set as no-slip coupled walls with a contact angle of 90°. Moreover, since the tank was equipped with a radial diffuser, a uniform and normal to the inlet surface mass flow rate, $\dot{m}_{pg}$, is imposed at the diffuser inlet surface, during the active-pressurization phase. After that phase, an adiabatic wall boundary condition is imposed on that surface. The temperature of the pressurant gas is modeled as an interpolation of the experimental gas temperature, measured at the probe located immediately downstream of the diffuser. This probe is the T14, as indicated in Fig. 5.1. It is important to highlight that the actual inlet gas temperature was lower than the one measured upstream of the connecting pipe between the inlet valve and the diffuser (which was equal to 352 K).

The liquid and vapor phases are initialized as quiescent, at a pressure of 104.2 kPa. The liquid and the wall in contact with the liquid are initialized at a temperature of 77 K. A piecewise linear fit of the temperatures measured by the probes at the beginning of the experiment is used as the initial

condition for the ullage and for the wall in contact with the ullage. Finally, the lid is initialized using a linear stratification between the temperatures of its lower surface and of its upper surface, which were 278 K and 280 K, respectively, as stated in [72].

For the validation test case under consideration both the laminar and the turbulent modeling have been considered. In particular, three turbulence models have been tested: the Realizable $k-\varepsilon$ [98] with Enhanced Wall Treatment [1], the SST $k-\omega$ of Menter [74], and the SST $k-\omega$ with low-Re corrections [1]. Differently from the Standard $k-\varepsilon$ model, the Realizable $k-\varepsilon$ model (see Sec. 3.6.4) uses an improved dissipation rate equation, and this model is "realizable" in the sense that it satisfies certain mathematical constraints (the positivity of normal Reynolds stresses and Schwarz' inequality for turbulent shear stresses) consistent with the physics of turbulent flows. The SST $k-\omega$ model of Menter [74], whose details are given in Sec. 3.6.3, combines the advantages

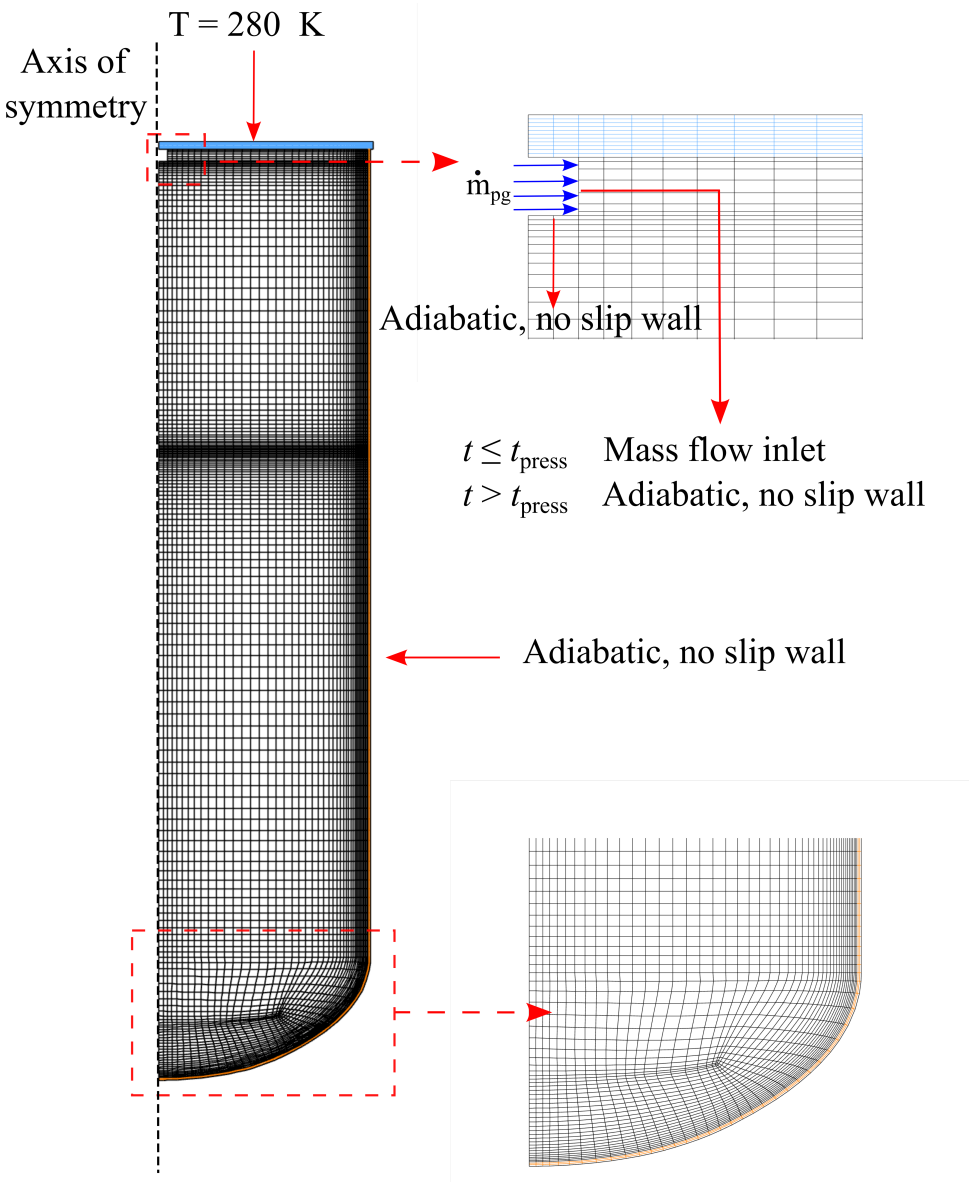

Figure 5.2: Selected computational grid (the domain has been modeled as 2D axisymmetric), with indication of the boundary conditions used in simulations. Different colors than that in the fluid region are used to color the wall (orange) and lid (light blue) grids. In the right half of the figure, a zoom of the grid in proximity of the diffuser and a zoom of the grid in the round shaped bottom section of the tank are shown.

of the standard $k-\omega$ model of Wilcox [119] and of the $k-\varepsilon$ model. Moreover, it accounts for the transport of the turbulent shear stress in the definition of the turbulent viscosity. In the case when the low-Re corrections are included in the SST $k-\omega$ model, the accuracy in predicting low Reynolds number flows is improved.

5.5 Grid convergence study

A grid convergence study with four grids characterized by an increasing level of spatial accuracy has been carried out. The used grids are structured and their details, together with the time average of the percentage error, $E_{r\%}$, on pressure of the various grid levels with respect to the finest grid, "Grid 4", are reported in Tab. 5.3.

Table 5.3: Details of the computational grids used for grid independence study and time average of the percentage error, $E_{r\%}$, on pressure of the various grid levels with reference to the finest grid, "Grid 4".

	No. of cells [-]	**Wall-Interface spacing [mm]**	$\boldsymbol{E_{r\%}}$ **w.r.t. Grid 4 [%]**
Grid 1	2443	0.6	2.2
Grid 2	7690	0.6	2.5
Grid 3	31649	0.3	1.2
Grid 4	68294	0.2	[-]

Pressure evolutions obtained with the four grid levels are shown in Fig. 5.3. The grid levels from "Grid 2" to "Grid 4" are in the asymptotic range of convergence (being the average percentage error of "Grid 2" with respect to "Grid 3" of 1.3% and the one of "Grid 3" with respect to "Grid 4" of 1.2%). Instead, the coarsest grid, "Grid 1", produces results outside the range of asymptotic convergence, for this reason it has been discarded. As the results obtained with the "Grid 2" show a limited discrepancy with respect to the ones obtained with the finest grid (the average percentage error between the two is of 2.5%, as can be seen in Tab. 5.3), it has been selected for subsequent analyses, in order to reduce the computational cost. The selected computational grid is represented in Fig. 5.2. In the right half of the figure, a zoom of the grid in proximity of the diffuser and a zoom of the grid in the round shaped bottom section of the tank are shown, too. The characteristic average cell size of the "Grid 2" is of 4 mm and of 2 mm, in the fluid regions and in the wall region, respectively.

5.6 Results

5.6.1 The experimental uncertainty

An inconsistency can be observed by examining the experimental data relative to the initial condition. Specifically, if the initial ullage mass is computed using the experimental data (pressure of 104.2 kPa, ullage volume, and temperature reconstructed with a piecewise linear fit of the initial measures of the temperature probes), it is found to be equal to 32.8 g. Whereas, in [72], it is stated to be practically equal to 35 g. Although this difference of about two grams might seem insignificant, in reality, a good representation of the initial vapor mass is crucial to obtain an accurate estimate of the pressurization rate, as it will be clear in the subsequent discussion. The influence of

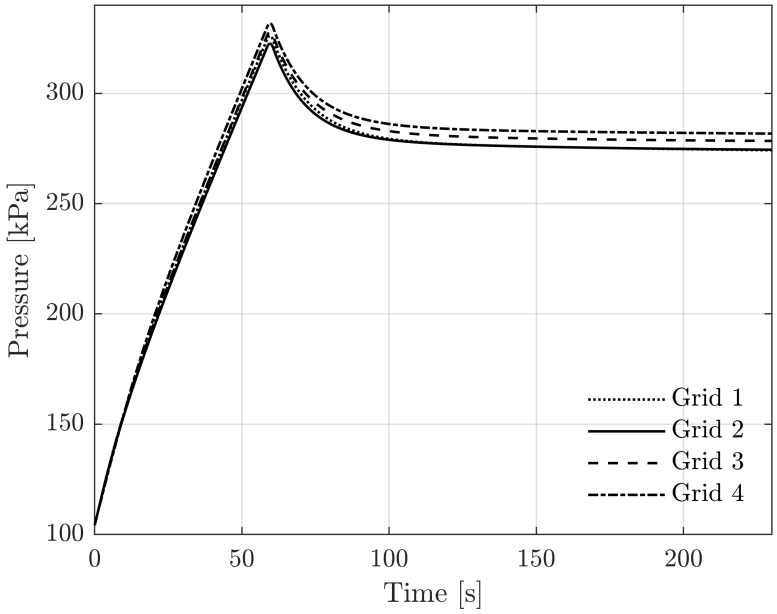

Figure 5.3: Numerical pressurization curves obtained with the four grids used for grid independence study. The characteristics of the used grids are summarized in Tab. 5.3.

the initial ullage mass value on the pressurization rate implies that this mass has to be accurately quantified by experimental measures, in order to allow accurate CFD analyses. The error in the calculation of the initial vapor mass made using experimental data is related to the uncertainties in the experimental measurements of pressure, temperature, and fill level. However, comprehending how to simultaneously vary all these parameters in order to reconstruct the initial vapor mass is a complex task. In this study, it has been decided to change only the ullage volume, in order to obtain an initial ullage mass of 35 g. In particular, the ullage volume has been incremented by 3.4%, by increasing its height by 7 mm, from 0.205 m to 0.212 m. Indeed, adjusting the ullage volume results in a change of negligible amount with respect to the overall size of the tank, and that does not impact the thermodynamic characteristics of the system. In this study, it has been done by adding a vapor layer, having the height of 7 mm, above the liquid-ullage interface, and initializing it at the same temperature of the liquid.

Pressure evolutions obtained both with the nominal and with the incremented initial ullage volume are shown in Fig. 5.4, together with the corresponding experimental measures. These numerical results have been obtained with the SST $k-\omega$ with low-Re corrections turbulence model. Being the active-pressurization a rapid mainly mechanical process, only slightly impacted by the heat transfer, it is evident that the pressurant gas injection is more effective (higher pressurization rate) in the case where the ullage contains less mass at the initial instant (case with the nominal ullage volume). The use of the increased vapor volume allows to better represent the active-pressurization phase and, consequently, to start the study of the subsequent pressure decrease phase from a more realistic condition. Therefore, this method has been maintained in all the subsequent analyses.

5.6.2 Effect of the wall thickness

The experimental tank had a wall thickness, t_w, of 1.5 mm in the top third and of 2 mm below, as reported in [72]. Since there were no details on how the transition between one part and the other of the wall was made, and in order to simplify the analysis, it has been decided to assign a single thickness to the wall. In Fig. 5.5, a comparison between the experimental and numerical pressure evolutions obtained with an uniform wall thickness, t_w, equal either to 1.5 mm or to 2 mm, is shown. Numerical predictions have been obtained with the SST $k-\omega$ with low-Re corrections turbulence model. The ullage temperatures and the liquid temperatures, relative to the same analyses, are presented in Fig. 5.6 (left) and in Fig. 5.6 (right), respectively. Given that the results of both pressure and temperature obtained with the two values of wall thickness exhibit negligible discrepancies between them, in our numerical analysis, we have retained the value of 2 mm for all the tank wall thickness.

5.6.3 Numerical modeling of the pressurant gas injection

The experiment starts with an active-pressurization phase, which lasts 60.7 s, during which the pressurant gas is injected with a constant mass flow rate, $\dot{m}_{pg}$, of $8.3 \cdot 10^{-4}$ kg/s. After this phase, the gas injection is stopped, and a pressure decrease phase begins. The modeling of the final instants of the pressurant gas injection requires some attention from a numerical standpoint, to avoid having unphysical results. Indeed, if the pressurant gas injection is stopped instantaneously (changing the boundary condition at the inlet surface of the diffuser from mass flow inlet to no-slip wall at 60.7 s), an unphysical temperature decrease occurs in proximity of the diffuser, as well as at the axisymmetric boundary, i.e., at the tank axis. This phenomenon is observable in Fig. 5.7, showing

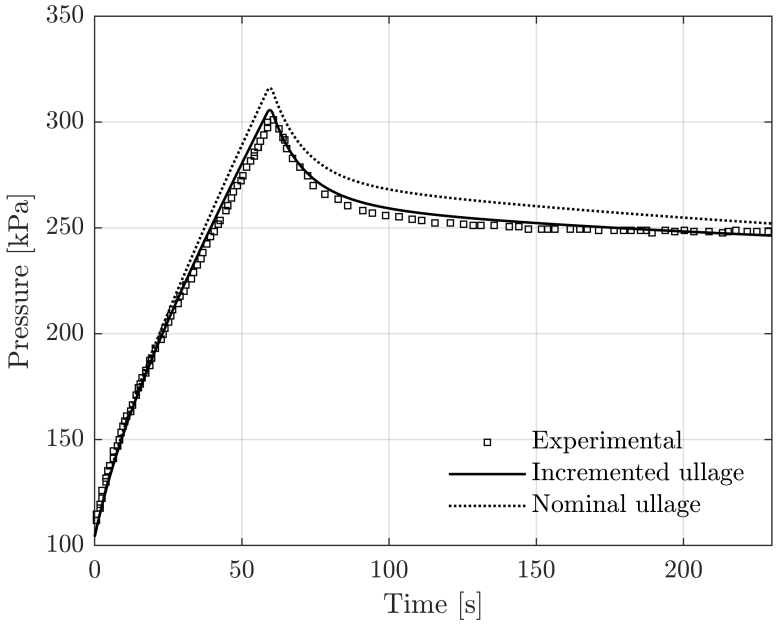

Figure 5.4: Comparison between experimental and numerical results of pressure evolution. Numerical predictions have been obtained with the SST $k-\omega$ with low-Re corrections turbulence model, both for the case with the nominal ullage volume from [72], and for the case with the ullage volume incremented by 3.4% (in order to fit the initial ullage mass of the experiment).

temperature contours, obtained with the SST $k-\omega$ with low-Re corrections turbulence model, at two time instants, one (figure on the left) just before the end of pressurant gas injection, precisely

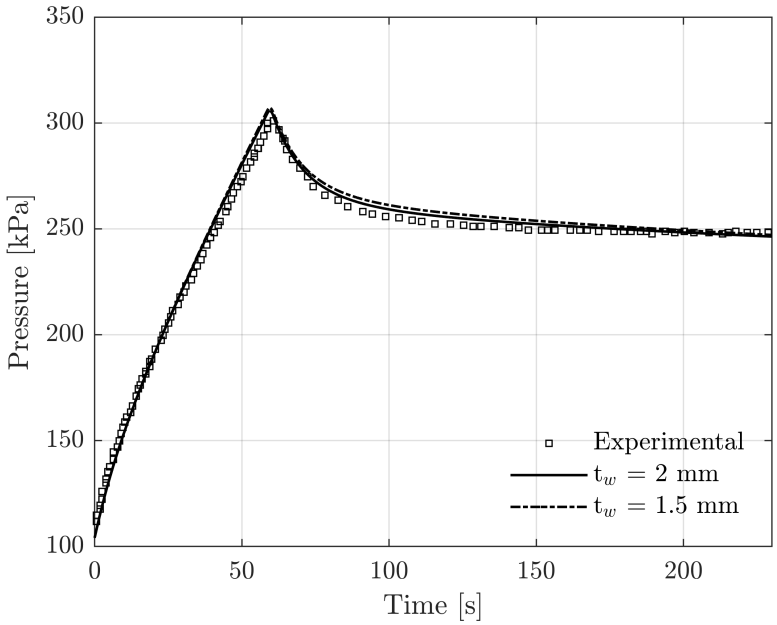

Figure 5.5: Comparison between experimental and numerical pressure evolutions obtained with a wall thickness, t_w, equal either to 1.5 mm or to 2 mm. Numerical predictions have been obtained with the SST $k-\omega$ with low-Re corrections turbulence model.

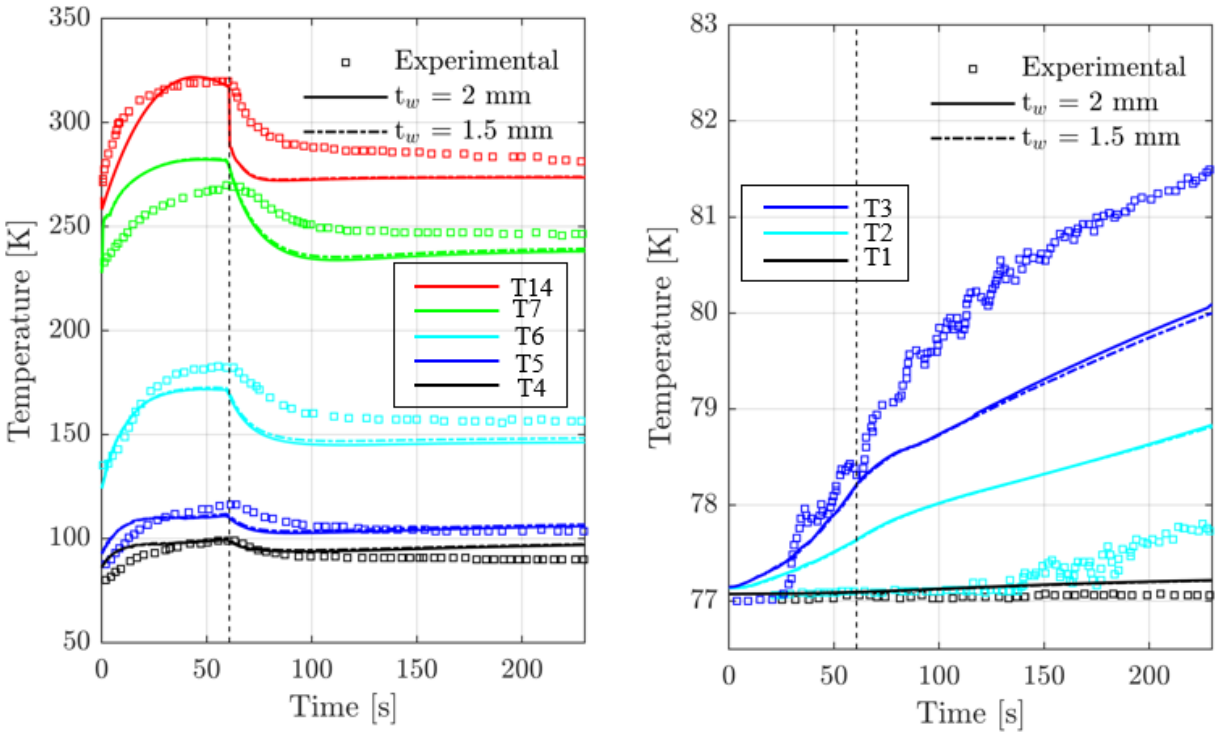

Figure 5.6: Comparison between experimental and numerical results of ullage temperatures (left) and liquid temperatures (right). Numerical predictions have been obtained with the SST $k-\omega$ with low-Re corrections turbulence model, and using a wall thickness, t_w, equal either to 1.5 mm or to 2 mm.

at 60 s, and the other (figures on the right) just after the end of pressurant gas injection, precisely at 62 s. The temperature contours at 62 s are shown both for the case in which the pressurant gas injection is stopped instantaneously at 60.7 s, and for the case in which the pressurant gas injection shutdown is modeled with a linear decrease. In addition, the same behavior observed in Fig. 5.7 is

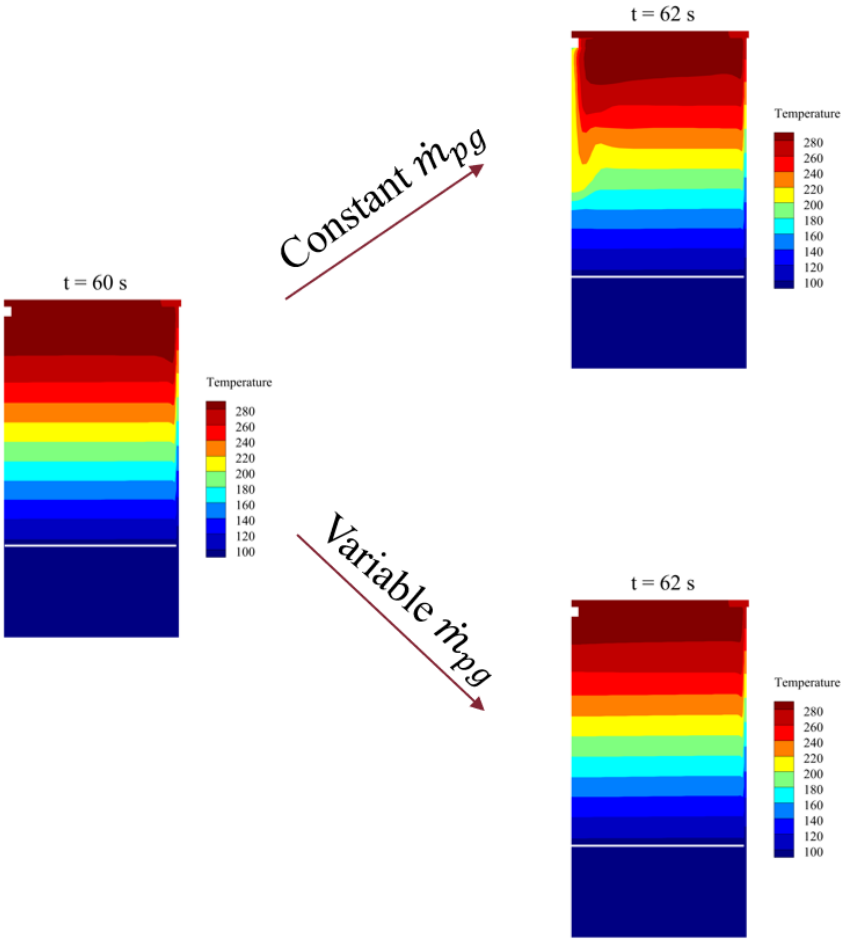

Figure 5.7: Temperature contours, obtained with the SST $k - \omega$ with low-Re corrections turbulence model, in the upper part of the tank, at a few time instants before (left) and after (right) the end of the pressurant gas injection. Contours are shown both for the case in which the pressurant gas injection is stopped instantaneously at 60.7 s, and for the case in which the pressurant gas injection shutdown is modeled with a linear decrease. The liquid-ullage interface is indicated with a white line.

visible also when using the laminar model, as shown in Fig. 5.8.

Do not stopping the pressurant gas injection instantly is a more credible modeling because, in the actual experiment, it is expected that, when the valve regulating the pressurant gas injection is closed, the mass input does not end instantaneously. In the numerical analysis, this effect has been taken into account by modeling the pressurant gas mass flow rate with a profile characterized by a constant value, equal to $8.44 \cdot 10^{-4}$ kg/s, for 58.7 s, and by a linear decrease during the last two seconds of active-pressurization. The initial constant value of the mass flow rate has been selected to ensure that the total pressurant gas mass injected into the tank remains equal to the experimental one. However, the profile used for the pressurant gas mass flow rate is an approximation of the real valve shutdown behavior, which is not provided in the experimental data.

If the pressure evolutions obtained using either a constant value for the mass flow rate, which is instantaneously stopped at 60.7 s, or the aforementioned profile are compared (see Fig. 5.9), no

relevant differences between them can be noticed. The only discrepancies are the slightly higher pressurization rate, the smoothing of the pressure peak, and its slight anticipation, in the case when the profile for the pressurant gas mass flow rate is used. The use of the tested turbulence model, namely the SST $k-\omega$ with low-Re corrections, together with the selected more realistic model for the pressurant gas injection shutdown, allow to reproduce the experimental pressure evolution with high accuracy during both the active-pressurization phase and the pressure decrease phase.

In Fig. 5.10, a comparison between experimental and numerical results of the ullage temperature, at probe T14 (left), and liquid temperatures, at various positions where the experimental probes are located (right), is presented. The reader can refer to Tab. 5.1 and Fig. 5.1 for the locations of the experimental temperature probes. Numerical results are shown both for the case in which the pressurant gas mass flow rate is modeled as constant, and for the case in which a profile is used. In both cases, the SST $k-\omega$ with low-Re corrections turbulence model has been used. The time evolution of the numerical temperature at the probe T14, which is the one located immediately downstream of the inlet surface of the diffuser, shows that, when the pressurant gas injection is stopped instantaneously, a downward peak develops at the end of active-pressurization. However, this figure confirms that this numerical effect is corrected by the use of a smooth profile for the mass flow rate. But, even when the smooth profile is used, a mismatch between experimental and numerical T14 temperature values is created at the moment when the pressurant gas injection is

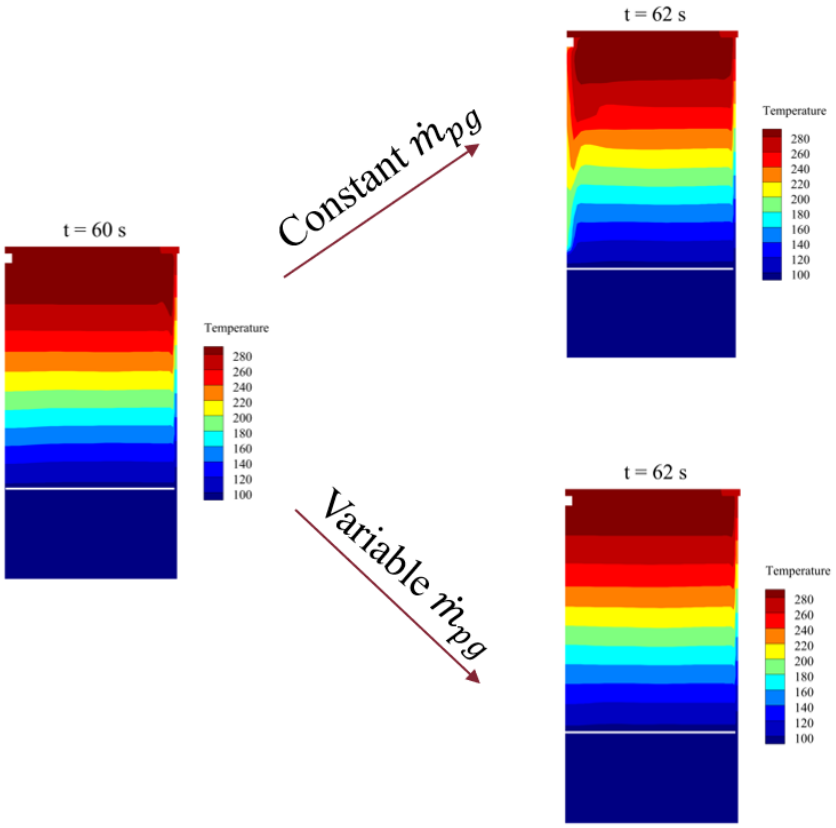

Figure 5.8: Temperature contours, obtained with the laminar model, in the upper part of the tank, at a few time instants before (left) and after (right) the end of the pressurant gas injection. The temperature contours at 62 s are shown both for the case in which the pressurant gas injection is stopped instantaneously at 60.7 s, and for the case in which the pressurant gas injection shutdown is modeled with a linear decrease. The liquid-ullage interface is indicated with a white line.

stopped. The trends of the liquid temperature profiles follow the experimental data with reasonable accuracy, with the highest discrepancies found for the temperatures at the probe T3, which, among the probes located inside the liquid, is the closest to the interface and at the underlying probe T2. Liquid bulk temperature remains approximately constant, and equal in T1 and T8 probes, both in the simulations and in the experiment. So, the temperature at probe T8 has not been shown for visual clarity. Moreover, the use of the profile for the pressurant gas mass flow rate corrects the aforementioned unphysical numerical effect, and does not alter the numerical temperature results from those obtained when the pressurant gas injection is arrested instantly. This is valid for both the ullage temperatures (see Fig. 5.11 (left)) and the wall temperatures (see Fig. 5.11 (right)).

The phase change mass flow rate (see Fig. 5.12), obtained as the volume integral of the source terms of Eq. (3.4) in Sec. 3.2, shows that both the models for the pressurant gas injection predict condensation during the whole experiment, apart from an evaporation spike in the initial instants. Indeed, from the right hand side of Eq. (3.4), it is visible that the phase change is positive if evaporation is greater than condensation, and negative otherwise. The obtained phase change result agrees with the analytical estimation made in [72], using the experimental data. Finally, it is apparent in Fig. 5.12 that, in the case when the pressurant gas injection is stopped instantly, an unphysical spike forms in the phase change mass flow rate. This effect is again corrected with the use of a smooth profile for the mass flow rate.

5.6.4 Effect of turbulence modeling

If the numerical results are used to estimate the Rayleigh number in proximity of the liquid-ullage interface, as its estimation with the experimental data is impracticable, it turns out to be of the order of 10^{11}, so highly above the critical value, both during the active-pressurization phase and

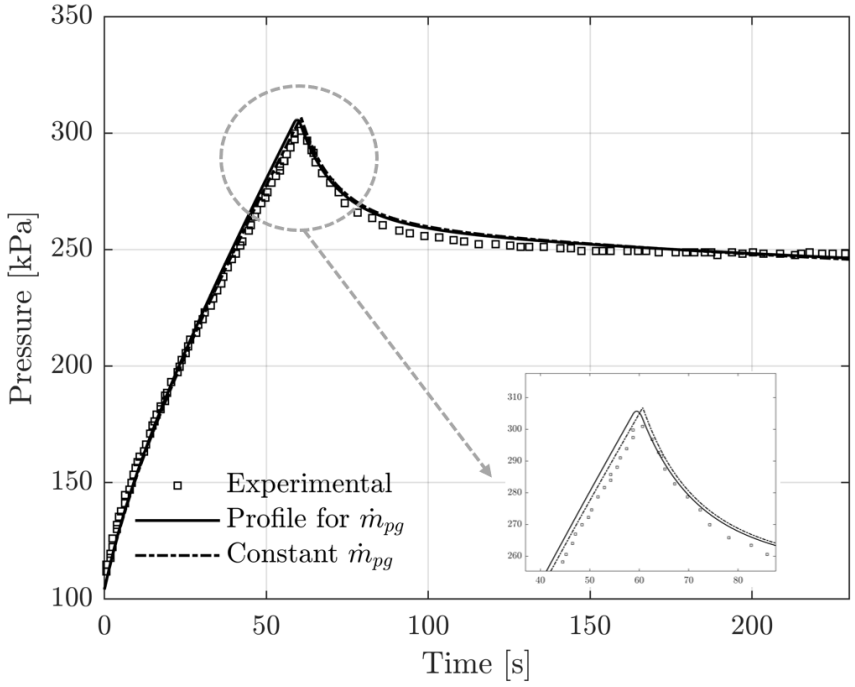

Figure 5.9: Comparison between experimental and numerical results of pressure evolution. A zoom of the pressure peak is shown in the bottom right corner of the figure. Numerical predictions have been obtained either by modeling the pressurant gas mass flow rate as constant, or by modeling it with a profile.

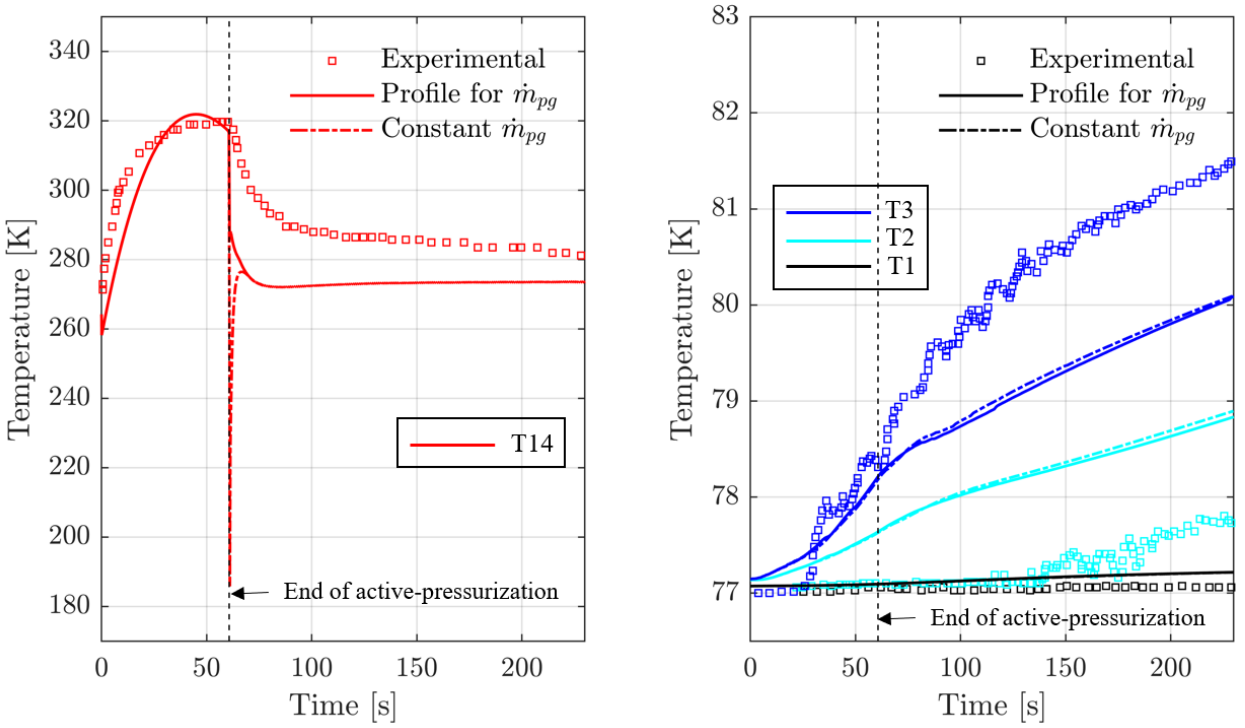

Figure 5.10: Comparison between experimental and numerical results of ullage temperature, at probe T14 (left) and liquid temperatures, at various positions where the experimental probes are located (right). Numerical results refer to simulations carried out with the SST $k-\omega$ with low-Re corrections turbulence model, in which the pressurant gas mass flow rate is modeled either as constant, or with a profile.

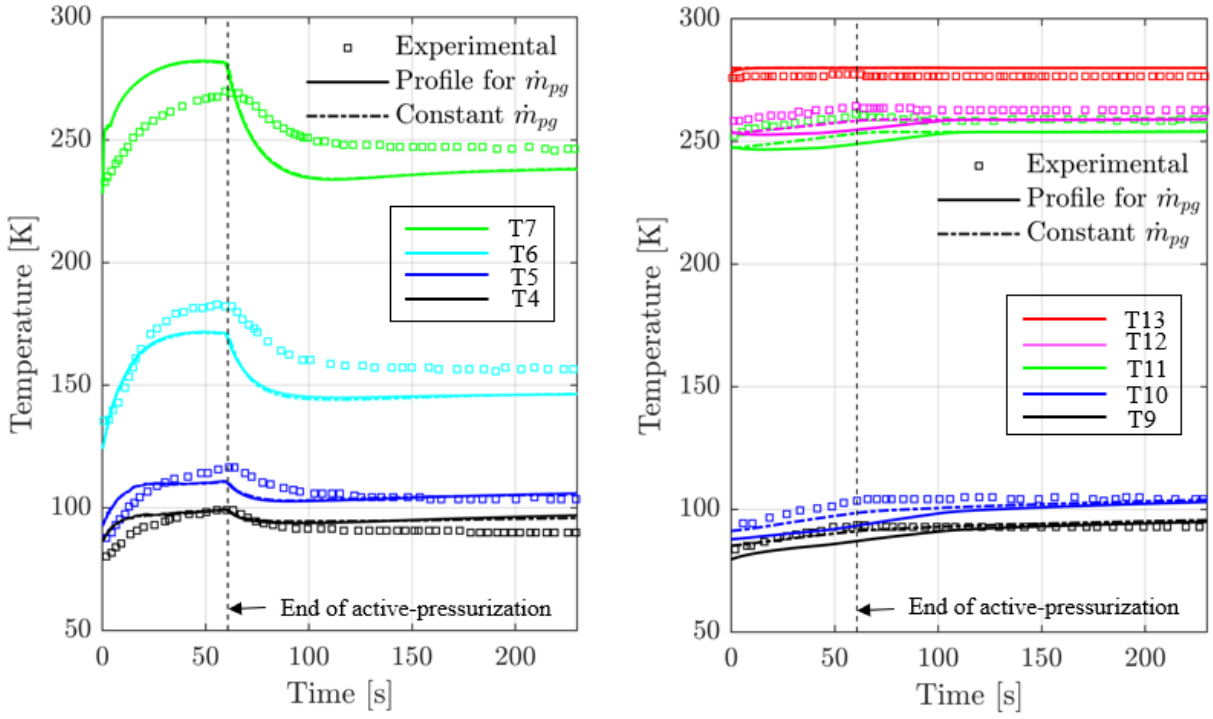

Figure 5.11: Comparison between experimental and numerical results of ullage temperatures (left) and wall temperatures (right), at various positions where the experimental probes are located. Numerical results refer to simulations carried out with the SST $k-\omega$ with low-Re corrections turbulence model, in which the pressurant gas mass flow rate is modeled either as constant, or with a profile.

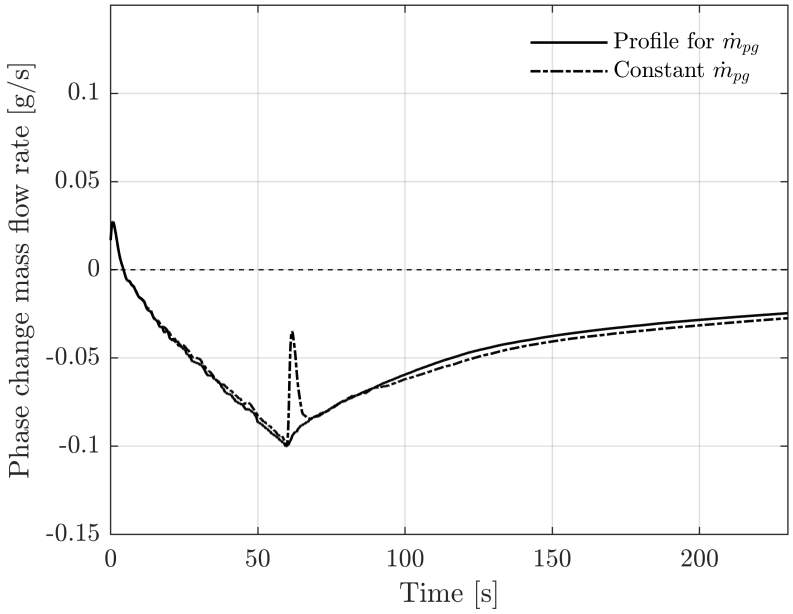

Figure 5.12: Phase change mass flow rate for the cases with the pressurant gas mass flow rate modeled either as constant, or with a profile.

during the pressure decrease phase, where the Rayleigh number is even higher. Indeed, the critical Rayleigh number for the transition from laminar to turbulent in a free convection boundary layer on a vertical plate is approximately equal to 10^9 [41].

In this study, three different turbulence models have been tested: the Realizable $k-\varepsilon$ [98] with Enhanced Wall Treatment [1], the SST $k-\omega$ [74], and the SST $k-\omega$ with low-Re corrections [1]. However, in order to consider the possible inadequacy of the Rayleigh number to establish whether the flow is laminar or turbulent in a problem of this complexity, it is considered useful to compare the results obtained with these three turbulence models with the ones obtained with the laminar model. In particular, a comparison between the experimental pressure evolution and the numerical ones is shown in Fig. 5.13. The percentage error between the experimental active-pressurization rate and its laminar estimation is equal to 6.5%. On the contrary, it is evident that all the turbulent models describe the active-pressurization rate with higher accuracy with respect to the laminar one, allowing to better describe the pressure peak, as can be seen in the zoom presented in Fig. 5.13. In the laminar case, beginning the simulation of the pressure decrease phase with a higher pressure value causes a shift between the experimental and numerical pressure measurements for all the remaining part of the test. This shift is slightly lower than 19 kPa at the end of the test. Instead, the use of the SST $k-\omega$ with low-Re corrections model allows the best replication of the experimental values during the pressure decrease part of the test. While, both the Realizable $k-\varepsilon$ with Enhanced Wall Treatment and the SST $k-\omega$ models show an overestimation of the pressure decrease rate in the last 100 s.

In terms of temperature evolutions in the fluid and at the wall, laminar and turbulent models produce similar results, as shown in Figs. 5.14 and 5.15, respectively.

An exception is the temperature at the probe T7 estimated by the Realizable $k-\varepsilon$ with Enhanced Wall Treatment model, which, with respect to the other models, fits better with experimental data during the active-pressurization phase, and fits worse with experimental data during the pressure

decrease phase. Another exception is the deviation between the laminar and turbulent estimations of the temperature at T2. This last is better described by the laminar model. Indeed, the turbulent models, due to their tendency to overestimate the convective recirculations, are worse in predicting the temperature stratification developing under the liquid-ullage interface, as we had already noticed in Sec. 4.6.7.

Fig. 5.15 shows a satisfactory agreement between the experimental wall temperatures and the numerical ones calculated both with the laminar and with the tested turbulence models.

Even if some discrepancies between the numerical and the experimental local fluid temperature values are present, as seen in Fig. 5.14, if the temperature stratification at a time instant when these discrepancies are high, for example 200 s, is plotted (see Fig. 5.16), it is evident that the thermal behavior of the tank is described with reasonable accuracy by both the laminar and the turbulent models. The temperature stratification profile has been extracted at the tank radial coordinate corresponding to the one where the rake with the temperature probes from T1 to T8 is located. Moreover, the results have shown that the variations arising from modeling the flow as either laminar or turbulent are more noticeable in pressure outcomes compared to temperature outcomes.

Now, it is interesting to examine the representation of the wall to fluid heat fluxes over the tank axial coordinate, "z", in Fig. 5.17, at 60 s (left) and 200 s (right). The figure at 60 s shows the wall to fluid heat flux during the active-pressurization. During this phase, a high temperature pressurant gas is injected into the ullage, causing a relatively high heat flux being transferred from the ullage to the wall adjacent to it. Wall thermal conduction, in the vertical direction, causes the transfer of a portion of this heat to the lower part of the tank, and the heating of the wall region located immediately below the liquid-ullage interface. This wall region, in turn, heats the liquid layers adjacent to it, as it is proven by the high heat flux value below the liquid-ullage interface (Fig. 5.17), and by the thermal stratification developing under the liquid-ullage interface (Fig. 5.16).

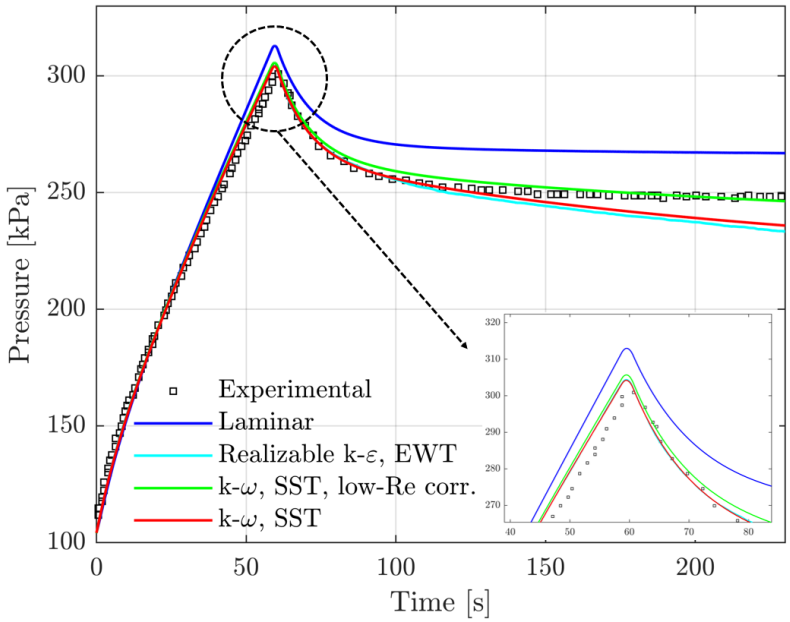

Figure 5.13: Comparison between experimental and numerical results of pressure evolution. Numerical predictions are shown both for the laminar analysis and for the turbulent analyses carried out with three different turbulence models.

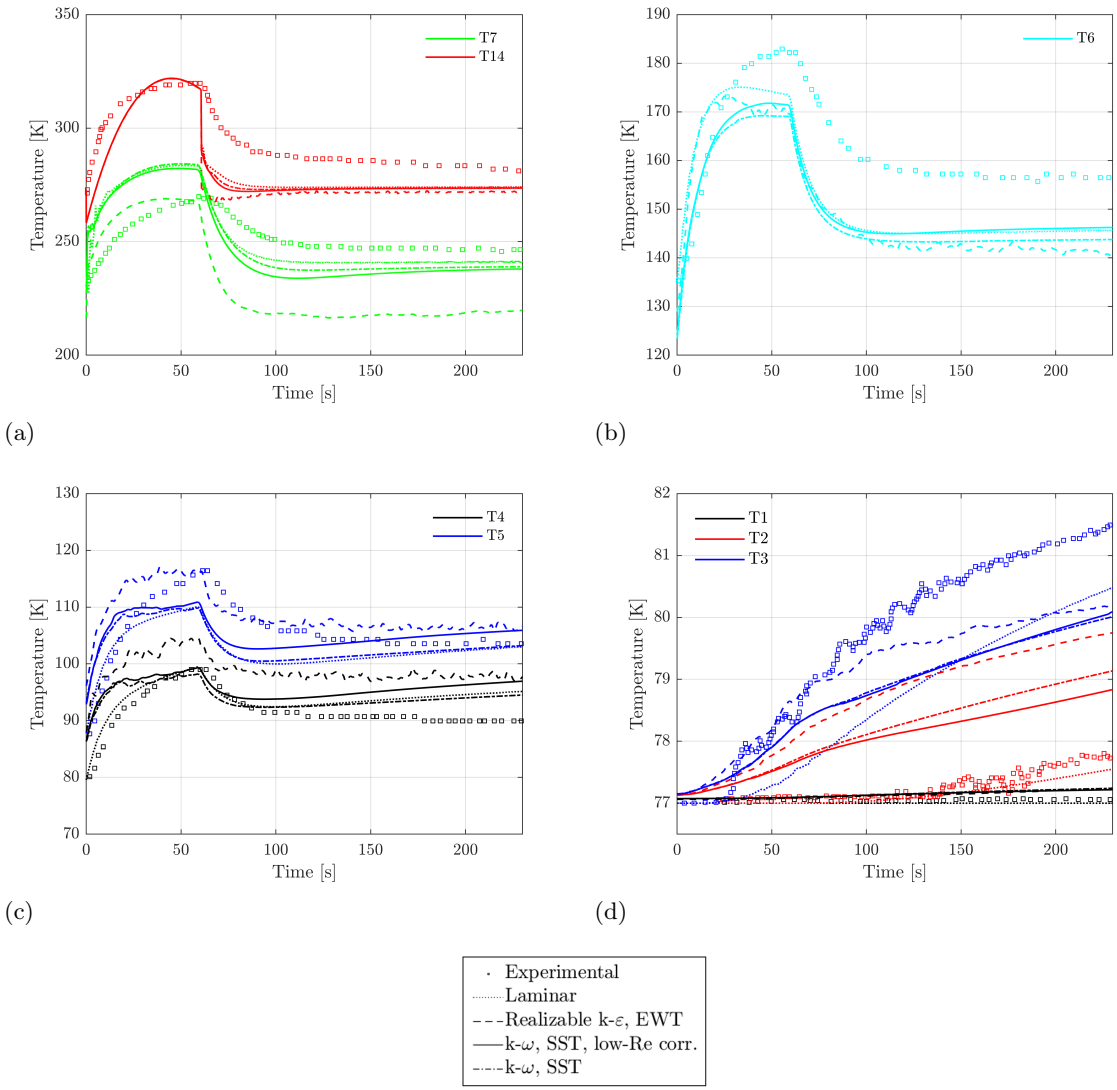

Figure 5.14: Comparison between experimental and numerical results of ullage temperatures at the locations of the probes T7 and T14 (a), ullage temperature at the location of the probes T6 (b), ullage temperatures at the locations of the probes T4 and T5 (c), and liquid temperatures at the locations of the probes T1, T2, and T3 (d). Numerical predictions refer to both laminar analysis and to turbulent analyses carried out with three different turbulence models.

The Fig. 5.17 (right) shows the wall to fluid heat flux, almost at the end of the pressure decrease phase (200 s). At this time instant, the thermal imbalances induced in the ullage by the pressurant gas injection have relaxed, and the heat flux between the ullage and its adjacent wall is averagely null, both in the laminar and in the turbulent case. Instead, the peak of heat flux below the liquid-ullage interface, which was noticeable also at 60 s, is still present.

Fig. 5.18 shows the temperature difference between the wall and the fluid adjacent to the wall (calculated only on the cylindrical part of the tank, both at 60 s and at 200 s), which is the driving force for the heat flux. This figure refers to the turbulent case with the SST $k-\omega$ with low-Re corrections model. It is evident that this temperature difference shows the same qualitative behavior as the wall to fluid heat flux.

Wall to fluid heat fluxes over the tank axial coordinate, "z", at various times, obtained with the SST $k-\omega$ with low-Re corrections model, are shown in Fig. 5.19 (left). It is interesting to observe

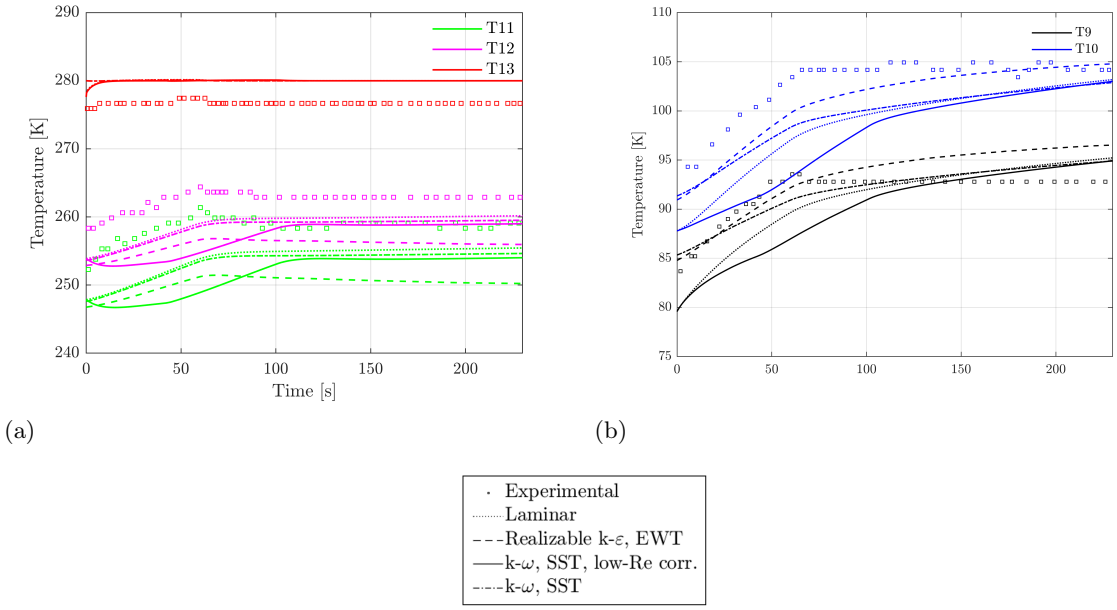

Figure 5.15: Comparison between experimental and numerical results of tank wall temperatures at the locations of the probes T11, T12, and T13 (a), and at the locations of the probes T9 and T10 (b). Numerical predictions refer to both laminar analysis and to turbulent analyses carried out with three different turbulence models.

how the heat flux profile varies in time from the initial condition, to the configuration assumed during the active-pressurization, and, finally, to the configuration assumed at the end of the relaxation phase. During the active-pressurization phase, the heat flux from the ullage to the wall increases in time. Then, during the relaxation phase, it decreases, reaching an approximately adiabatic condition at the end of the test. On the contrary, the peak of heat flux which develops under the free-surface increases in time both during the active-pressurization and during the relaxation phase,

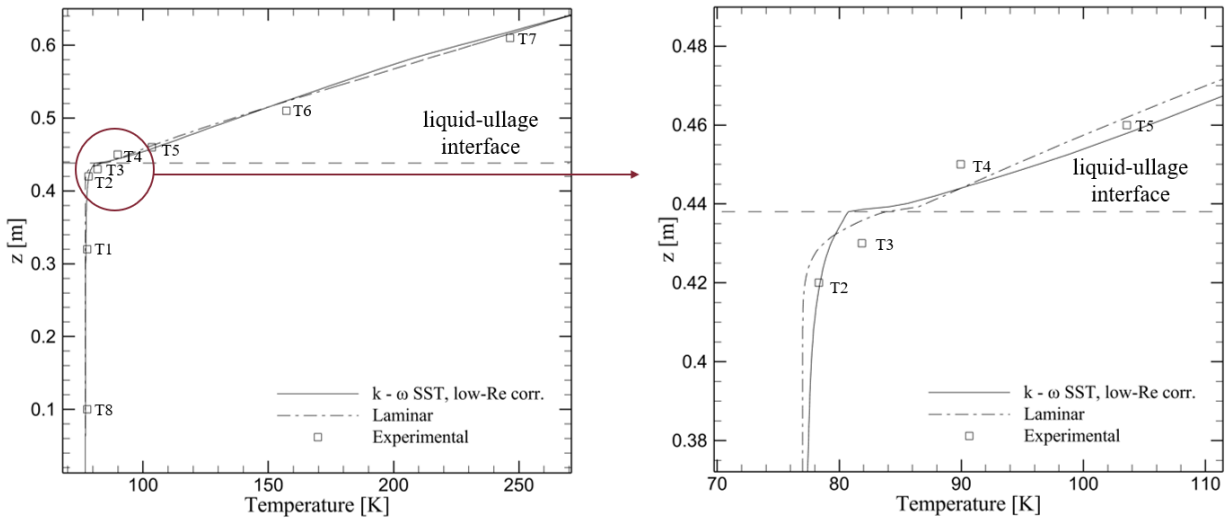

Figure 5.16: Comparison between experimental and numerical (with laminar and with SST $k-\omega$ with low-Re corrections models) temperature stratifications at 200 s (left), together with a zoom of the region close to the liquid-ullage interface (right). The liquid-ullage interface level is represented with a horizontal dotted line.

as it is evident in the zoom in Fig. 5.19 (right). The peak of heat flux under the free-surface is correlated with the presence of a recirculation bubble, indeed the height of the bubble and of the region characterized by the peak of heat flux are comparable. Velocity magnitude contours and streamlines, at 60 s, obtained for the turbulent case with the SST $k-\omega$ with low-Re corrections model, are shown in Fig. 5.20 (left). The zoom of these contours, in Fig. 5.20 (right), highlights the presence of the recirculation bubble under the free-surface.

We have seen in the previous analyses that the wall plays an important role in the distribution of the heat between the ullage and the liquid. Hence, it can be concluded that simulating the wall

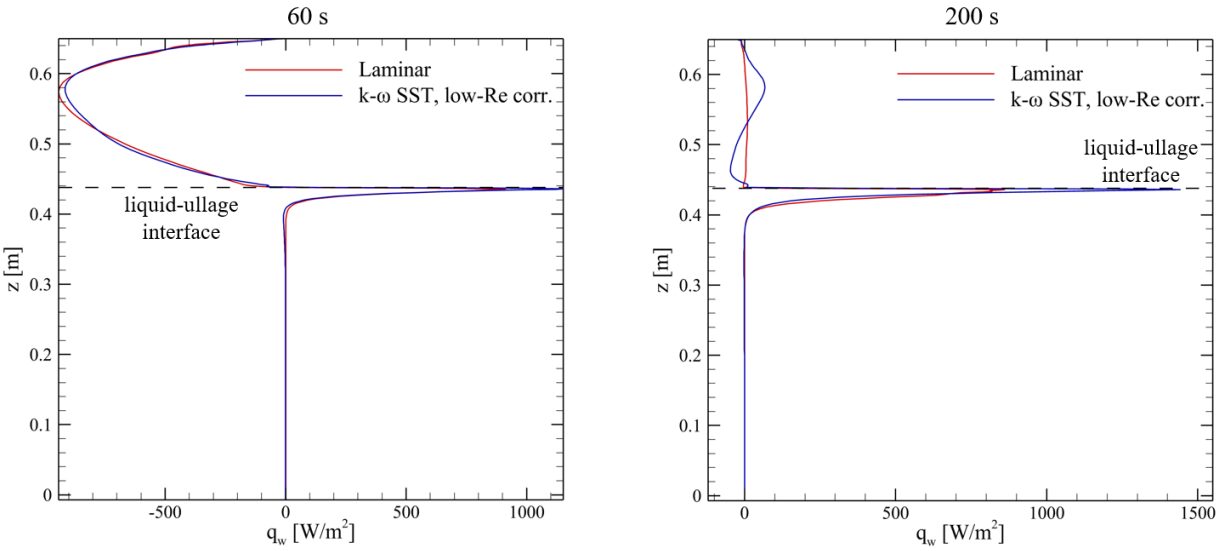

Figure 5.17: Wall to fluid heat fluxes over the tank axial coordinate, "z", at 60 s (left) and at 200 s (right), obtained with the laminar and with the SST $k-\omega$ with low-Re corrections models. The liquid-ullage interface level is represented with a horizontal dotted line.

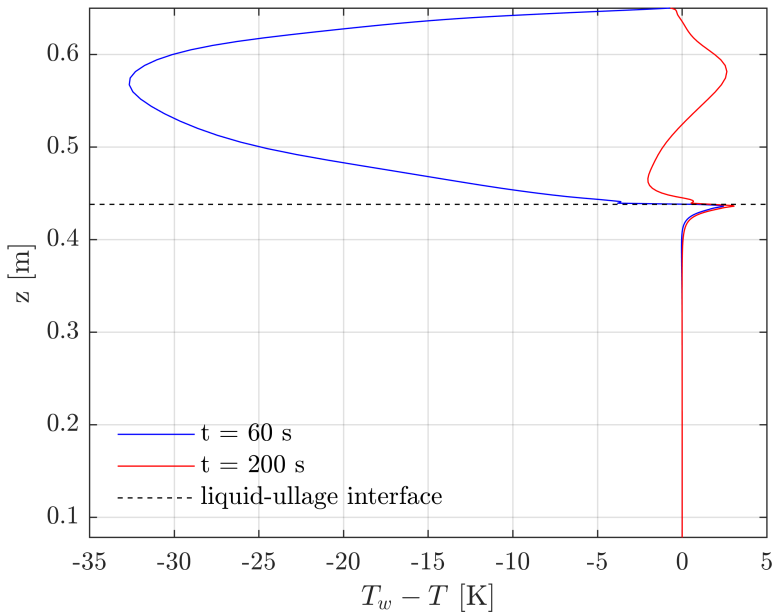

Figure 5.18: Temperature difference (obtained with the SST $k-\omega$ with low-Re corrections model) between the wall and the fluid adjacent to the wall, calculated only on the cylindrical part of the tank.

region, through the use of a conjugate heat transfer model, is fundamental in the case of cryogenic tanks actively-pressurized with a relatively hot pressurant gas.

As concerns the phase change, both models predict an evaporation peak at the initial instants of the experiment, followed by condensation during both the active-pressurization phase and the pressure decrease phase, as can be seen in Fig. 5.21. In addition, both models show that the mass transfer rate due to condensation increases during the active-pressurization, and decreases during the following phase, but the turbulent model predicts a higher mass transfer rate.

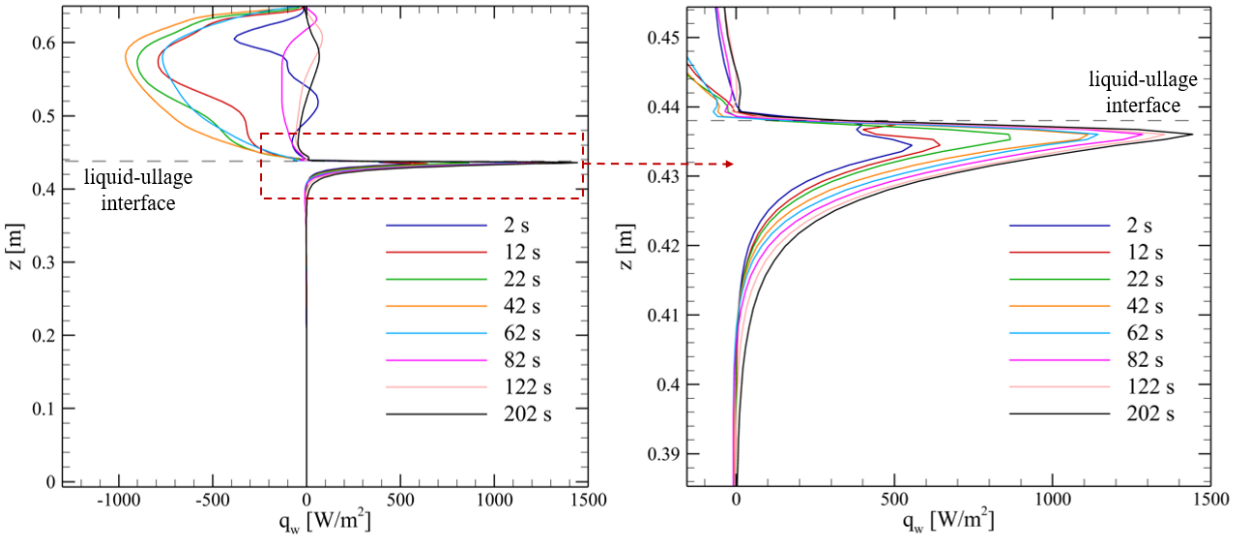

Figure 5.19: Wall to fluid heat fluxes over the tank axial coordinate, "z", at various times, obtained with the SST $k-\omega$ with low-Re corrections model (left). Zoom of the region close to the liquid-ullage interface (right).

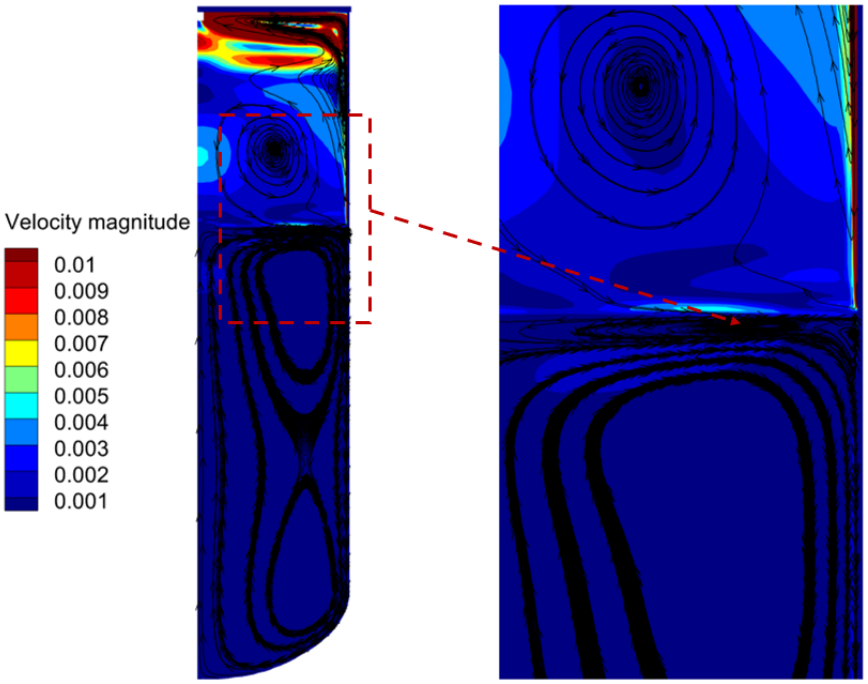

Figure 5.20: Velocity magnitude contours and streamlines, at 60 s, with a zoom, on the right, of the recirculation bubble developing under the free-surface. These contours refer to the turbulent case with the SST $k-\omega$ with low-Re corrections model.

If the experiment would be continued beyond the pressure decrease phase, it is reasonable to expect that a self-pressurization phase would begin, caused by the thermal input due to the high temperature boundary condition imposed on the outer surface of the lid. In Fig. 5.22, the pressure evolutions continued beyond the experimental duration, obtained with the laminar and with the SST $k-\omega$ with low-Re corrections models, are shown. The vertical dashed dotted lines denote the local pressure minimum, marking the conclusion of the pressure relaxation phase, for both laminar

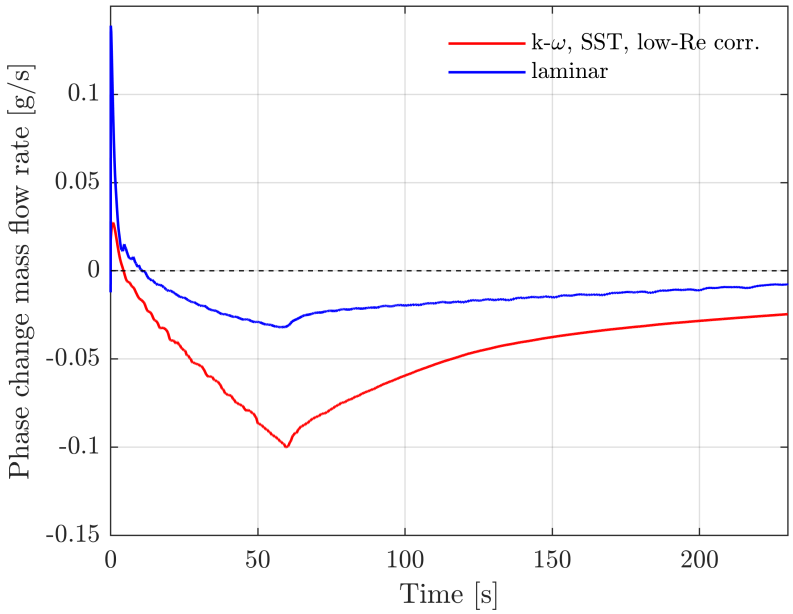

Figure 5.21: Phase change mass flow rate for laminar and turbulent (with SST $k-\omega$ with low-Re corrections model) analyses.

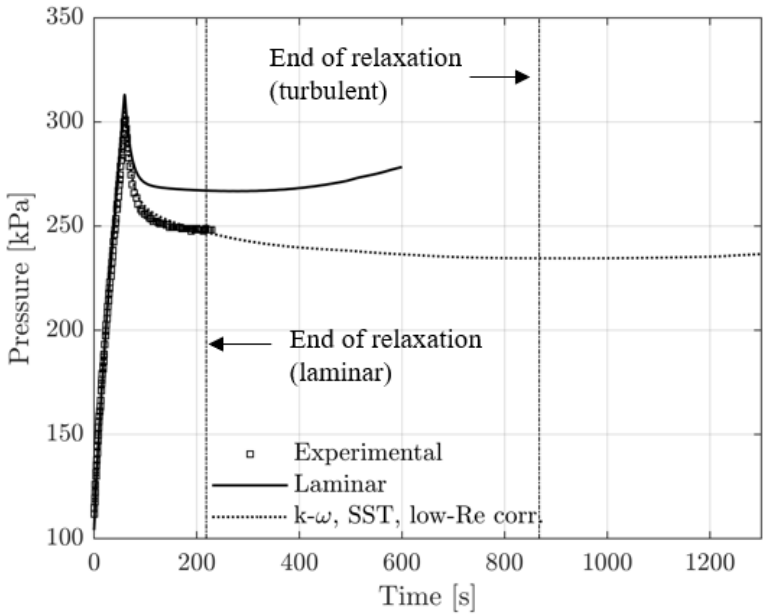

Figure 5.22: Pressure evolutions, obtained with the laminar and with the SST $k-\omega$ with low-Re corrections models, during and after the experimental duration. Vertical dashed dotted lines indicate the end of the pressure decrease phase for laminar and turbulent cases.

and turbulent cases. It is evident that, even if the turbulent model is more adequate than the laminar to describe the pressure evolution during the experimental duration, it predicts a pressure decrease phase longer than the experimental one. Indeed, in [72], the relaxation phase is said to end at 213 s. On the contrary, the laminar model is more adequate in predicting the duration of the pressure decrease phase. After the pressure decrease, both models predict self-pressurization, but with different rates. For times longer than the experimental duration, the laminar model might be more appropriate than the turbulent one since, once the jet and the thermal input into the tank due to the hot pressurant gas are removed, the flow might laminarize. Further experimental data would be needed to understand which model is the most accurate for describing the self-pressurization phase occurring after the pressure relaxation.

5.6.5 Comparison between CFD and 0D model results

The 0D model, presented in Chap. 2, can be used to estimate both the average temperature of the liquid and the ullage at any time and the pressure evolution for the selected validation test case. Moreover, the results of the 0D model can be compared with those obtained with our CFD methodology. Fig. 5.23 shows a comparison between experimental data, 0D model results, and numerical results of pressure evolution (Fig. 5.23 (a)) and temperature stratification at 200 s (Fig. 5.23 (b)). CFD predictions refer to the computation carried out with the SST $k-\omega$ with low-Re corrections turbulence model. The temperature stratification profile has been extracted at the tank radial coordinate corresponding to the one where the rake with the temperature probes from T1 to T8 is located. It is evident in Fig. 5.23 (a) that the 0D model is able to describe the pressure rise rate, with reasonable accuracy, during the active-pressurization phase. But, it is characterized by poor agreement with the experimental data during the relaxation phase, as it overestimates the depressurization rate. As for the temperature results (Fig. 5.23 (b)), the liquid temperature estimated by the 0D model, at 200 s, is very similar to the experimental one and to the one estimated with the CFD simulation, except for the fact that the CFD model predicts a thin thermal stratification zone close to the free-surface. Finally, regarding the temperature within the ullage, the one estimated by the 0D model closely matches the average of both the experimental and CFD temperature distributions at 200 s.

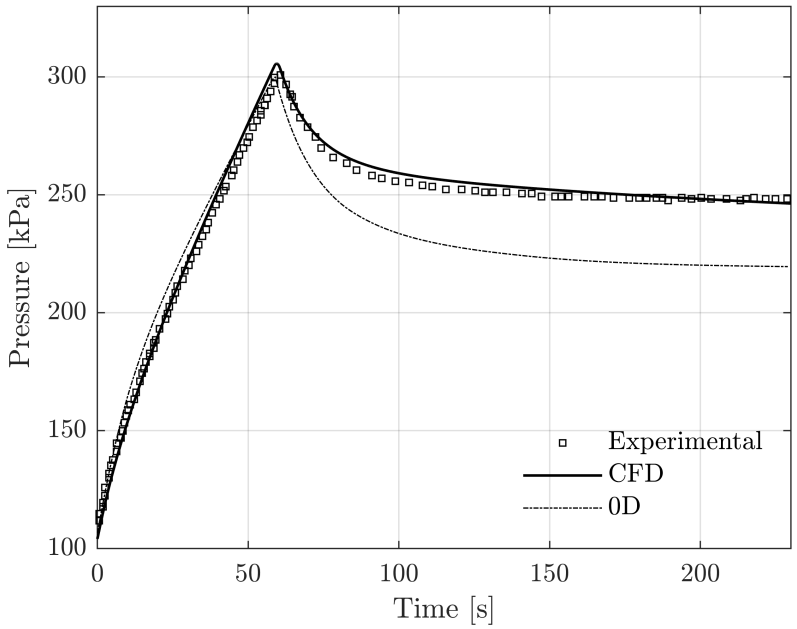

(a)

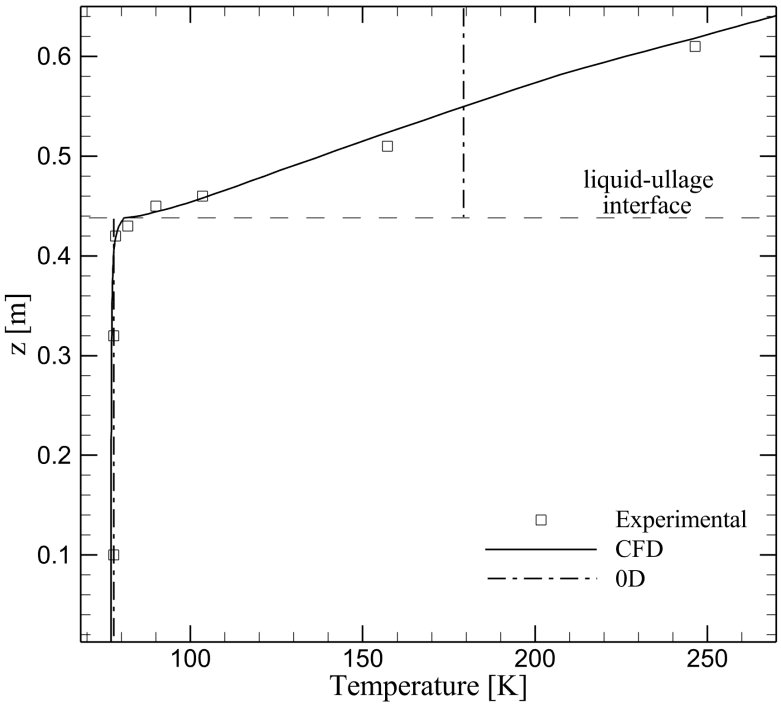

(b)

Figure 5.23: Comparison between experimental data, numerical results, and 0D model results of (a) pressure evolution and (b) temperature stratification at 200 s. CFD predictions refer to the computation carried out with the SST $k-\omega$ with low-Re corrections turbulence model.

Chapter 6

Reduced gravity analyses

After validating our methodology with pressurization results in normal gravity, in the previous chapters, we present the results of the application of our CFD methodology to the first self-pressurization experiment, in reduced gravity, with data sufficiently detailed for validating storage tank models [117]. The test tank is the liquid H_2 tank of the second stage of the Saturn IB AS-203 vehicle, and the self-pressurization experiment was carried out while it was into circular low Earth orbit. Due to the orbital environment, this tank absorbed the heat flux due to solar radiation. Moreover, it was subjected to an axial acceleration resulting from the balance between an axial thrust and the drag force. This acceleration, although low, was sufficient to keep the propellant stabilized during all the experiment. All the experiments chosen for validation purposes, in this thesis, concern a liquid with a non-moving interface, which is a significant simplification compared to reality (see Sec. 1.5). In addition, the time-varying acceleration and heat flux to which the tank was exposed during the experiment have been modeled in our analysis.

The results of the validation show that the proposed CFD methodology allows to describe the main thermo-fluid-dynamics phenomena occurring in cryogenic tanks during self-pressurization in reduced gravity with a reasonably good accuracy.

After carrying out the validation of the CFD methodology in reduced gravity, we also present the results of a parametric study involving four gravity levels, from normal gravity ($g_E = 9.81$ m/s^2), to the reduced gravity value of $10^{-3} g_E$. This study has been performed using the same geometry, fluid, and operating conditions of the validation test case presented in Chap. 4. This study has allowed to see the effect of the gravity level on the pressurization behavior, phase change, liquid-ullage interface shape, etc. Further investigations would be needed, and the parameter space should be further expanded (for example studying the effect of the applied heat flux level) in order to extend the knowledge of cryogenic fluid behavior under reduced gravity.

6.1 Literature survey on pressurization in reduced gravity

Studying the thermo-fluid-dynamics behavior of cryogenic propellant at different gravity levels is crucial for the design of upper stage cryogenic storage tanks. Indeed, these last, during their operating life, experience extremely variable gravity levels. The gravity level influences the boiling process, as pointed out in both numerical and experimental studies on pool boiling. Also the dynamics of the free-surface is influenced by the gravity level, indeed, in conditions of low Bond

number, the surface tension force prevails over the gravity force, leading to motions of the free-surface along the tank walls.

The first self-pressurization experiment in reduced gravity with data sufficiently detailed for validating storage tank models was carried out in the liquid H_2 tank of the second stage of the Saturn IB AS-203 vehicle [117]. Details of this experiment will be presented in Sec. 6.2.1. More recently, self-pressurization data sufficiently detailed for CFD methodologies validation were obtained in the framework of the Zero-Boil-Off (ZBOT) experiments [48]. These last were several small-scale experiments, carried out aboard the ISS, in a transparent tank, partially filled with the Perfluoro-n-Pentane refrigerant.

Experimental data are fundamental for validation of CFD methodologies, but there are a few issues with experiments. Firstly, there is a lot of uncertainty in the experimental data. Secondly, experiments in microgravity environment are very expensive and complex to design. These limitations highlight the potentialities of CFD simulations.

Data collected during the self-pressurization experiment in the Saturn IB AS-203 tank [117], have been used in a fair number of studies concerning CFD methodologies validation. Among these, in [3] a multi-phase numerical framework, utilizing real fluid properties, was proposed, and its applicability to different classes of propellant tank applications, among which the self-pressurization in orbit, was demonstrated, replicating experimental data from [117]. While, in [69], a CFD model to study the effect of gravity level on the thermal behavior, in a liquid H_2 tank, was selected and validated with data from [117]. Moreover, in [44], two two-phase CFD models for cryogenic tanks pressurization, based either on the Sharp Interface approach, or on the VOF method, were presented. Both models were validated using data from [117], and the VOF model produced better agreement.

Other promising CFD methodologies were also presented in the open literature, and validated with more recent experimental data. For example, in [28], a computational methodology based on the Coupled Level-Set and the Volume-of-Fluid (CLSVOF) method was validated against experimental results by Seo and Jeong [96], and used to study the evaporation and its effect on vapor pressure under microgravity. A self-pressurizing tank, partially filled with liquid H_2, was taken into account, and the effects of reduced gravity, contact angle of the vapor bubble, and surface tension were investigated. Moreover, in [46], a CFD methodology (based on a 3D VOF model) for simulating both the self-pressurization and the pressure control, through jet mixing, in a Freon-113 tank in microgravity was presented. In addition, it was validated through comparison with the experimental results of the Tank Pressure Control Experiment (TPCE), carried out aboard the Space Shuttle in 1991 [11]. Later, in [49], results from experiments carried out both on ground and in the microgravity environment of the ISS, as part of the ZBOT experimental program, were presented. These experiments included both self-pressurization and pressure control, through jet mixing, analyses, and were made using the refrigerant Perfluoro-n-Pentano (PnP) as simulant fluid. Moreover, a two-phase CFD model, based on the Sharp Interface approach for self-pressurization analyses and on VOF model for the jet mixing cases, was presented, and validated through comparison with the ZBOT experimental data.

6.2 Validation with liquid H_2 self-pressurization data in microgravity

In this section, the validation of the CFD methodology with the results of the self-pressurization experiment carried out in low Earth orbit will be presented.

6.2.1 Test case description

The test case under consideration is a self-pressurization experiment carried out in the liquid H_2 tank of the second stage of the Saturn IB AS-203 vehicle [117].

This tank has a height, H, of 11.3 m, and a radius, R, of 3.3 m. The initial liquid mass is 7103.3 kg, corresponding to an initial liquid height, H_l, of 4.1 m, and the ullage contains only evaporated H_2. The tank characteristic dimensions are schematized in Fig. 6.1. The tank shares a common

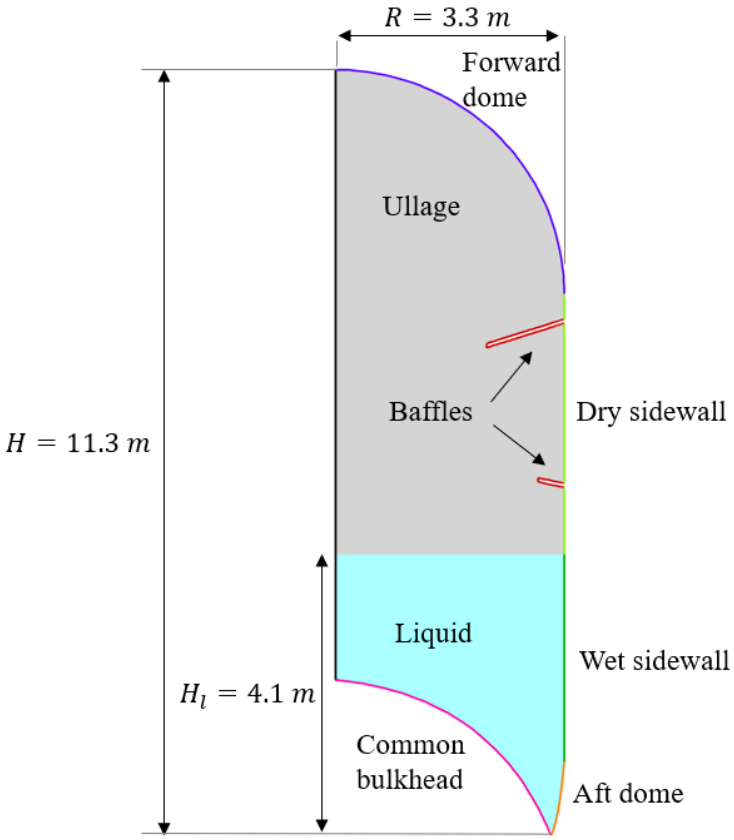

Figure 6.1: Tank scheme with the indication of the characteristic dimensions and of the names of the various parts in which the wall can be divided.

bulkhead with the liquid O_2 tank, which is placed below it.

The test tank was in a circular low Earth orbit, and, thus, absorbed a time-varying heat flux due to solar radiation, which caused self-pressurization. Moreover, it was subjected to a time-varying axial acceleration resulting from the balance between an axial thrust and the drag force.

6.2.2 Thermophysical and transport properties

For the liquid H_2, the Boussinesq approximation is selected for the density, and constant thermophysical and transport properties, taken from the NIST Chemistry WebBook [65] database, at the average pressure and liquid temperature, are used. All constant liquid properties are listed in Tab. 6.1.

Table 6.1: Constant physical properties for the liquid H_2, taken from [65].

	$\boldsymbol{\rho}$ [kg/m^3]	$\boldsymbol{\lambda}$ [W/(m · K)]	$\boldsymbol{c_p}$ [J/(kg · K)]	$\boldsymbol{\mu}$ [Pa · s]
Liquid phase	70.48	0.10108	9927	$1.3147 \cdot 10^{-5}$

The gaseous H_2 is modeled as an ideal gas, with temperature dependent specific heat, thermal conductivity, and viscosity. The latter are modeled, as shown in Fig. 6.2, as a piecewise linear fit of the NIST data, at the average pressure. The H_2 saturation curve (see Fig. 6.3) is approximated

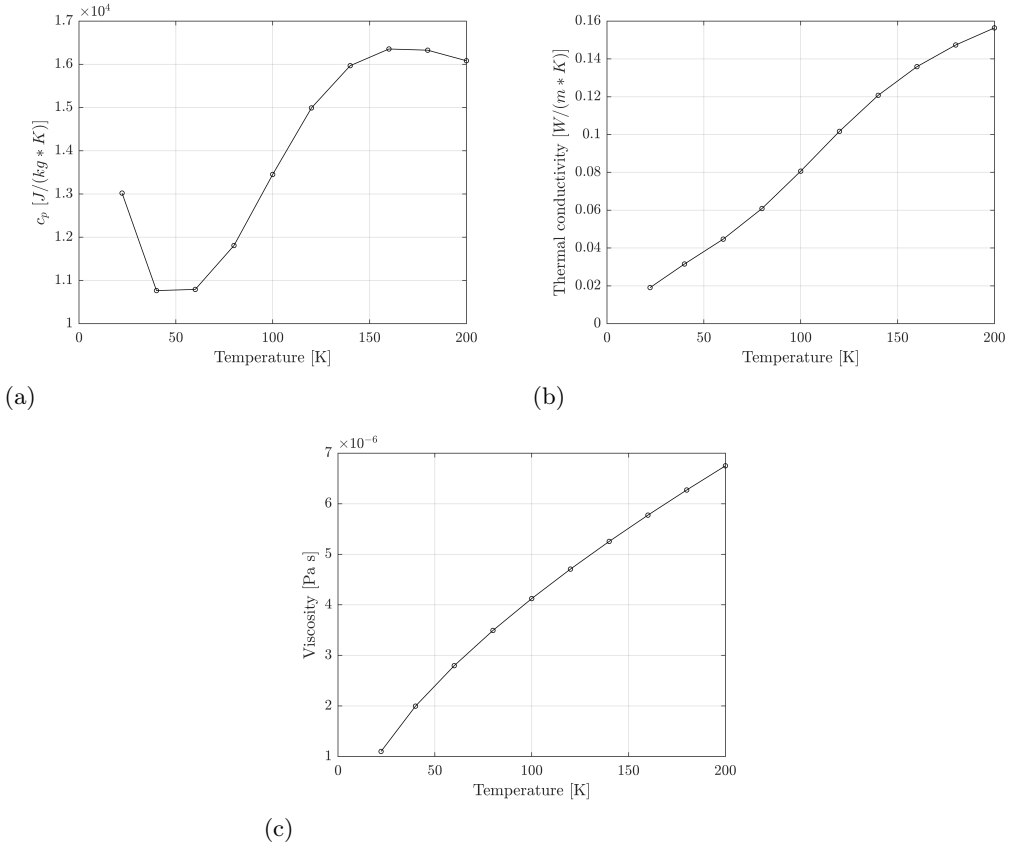

Figure 6.2: Gaseous H_2 specific heat, thermal conductivity, and viscosity. The latter are modeled as a piecewise linear fit of the NIST data, at the average pressure.

with a piecewise linear fit of the NIST data. Moreover, a constant value of the surface tension coefficient, equal to 0.0016158 N/m, is used. A standard state enthalpy of -9.012 $\cdot 10^6$ J/kmol and of 0 J/kmol, both at the reference temperature of 298.15 K, are used for the liquid H_2 and for the gaseous H_2, respectively. These values have been retrieved from [73]. Moreover, a liquid volumetric thermal expansion coefficient of 0.0171 1/K is used, which has been computed from the NIST data, using Eq. (3.60), in Sec. 3.7.

6.2.3 Computational setup

The pressure-based solver of the commercial CFD software Ansys Fluent® [1] is used to simulate the transient self-pressurization phenomenon. The flow is modeled as 2D axisymmetric. A second order implicit time scheme is used for time discretization, and a minimum time step of 0.005 s is used in order to keep the residuals below a proper limit. Second order upwind schemes are used for spatial discretization of the convective terms in the governing equations. Ansys Fluent®'s "Compressive" scheme [1] is used for the volume fraction equation with the selection of sharp interface regime modeling. "PRESTO!" scheme [1] is used to interpolate pressure values at the cell faces. The chosen pressure-velocity coupling scheme is SIMPLE. Green-Gauss node based scheme is used to calculate the properties' gradients. All the walls are set as no-slip walls, with a contact angle of 90°. An interpolation of the experimental time-varying heat flux is imposed, as boundary condition, on each part of the tank wall, instead the walls of the baffles are treated as adiabatic. The different parts of the tank wall are indicated in Fig. 6.1. Fig. 6.4 represents the evolution of both the experimental and the interpolated heat transfer rate on the different parts of the tank wall. The tank axial acceleration level is modeled as an interpolation of its experimental values. This interpolation, together with the experimental acceleration, are represented in Fig. 6.5. The tank is initialized at a pressure of 85495 Pa; the initial liquid temperature is 19.72 K; the ullage is initialized using a linear stratification between the liquid temperature and a temperature of 22.5 K [117]; and both phases are initialized as quiescent.

If the modified Rayleigh number, based on the liquid level, is estimated using Eq. (4.1), it results to be of the order of 10^{14}, so higher than the critical value for the transition from laminar to turbulent. For this reason, the flow has been modeled as turbulent, and the SST $k-\omega$ turbulence model of Menter [74] has been used.

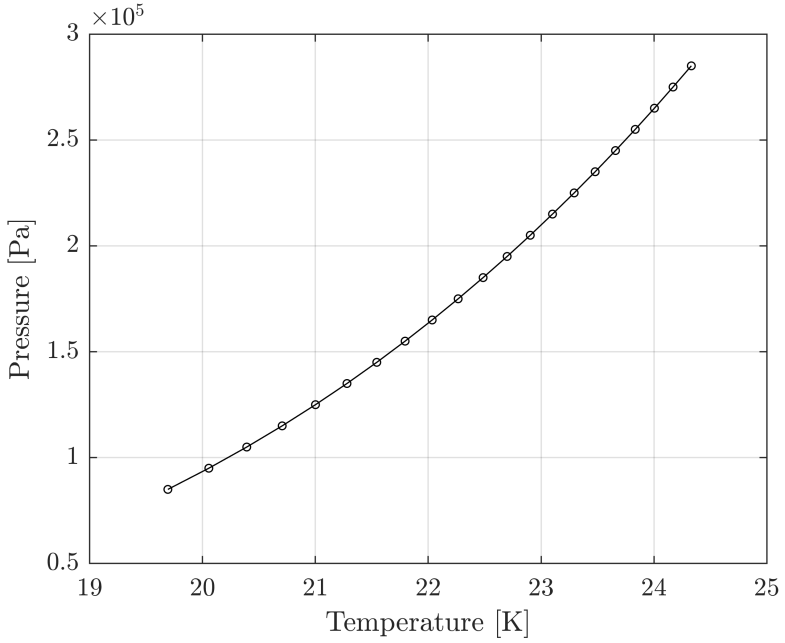

Figure 6.3: Used approximation of H_2 saturation curve (piecewise linear fit of the NIST data).

6.2.4 Grid convergence study

A grid convergence study with three grids, characterized by an increasing level of spatial accuracy, has been carried out. The used grids are hybrid structured-unstructured. Indeed, they are unstructured in the central region, where there are the baffles, and structured elsewhere. Details of the used computational grids are reported in Tab. 6.2. Pressure evolutions obtained with the three grid levels are shown in Fig. 6.6. The pressure results obtained with the coarsest grid show a limited

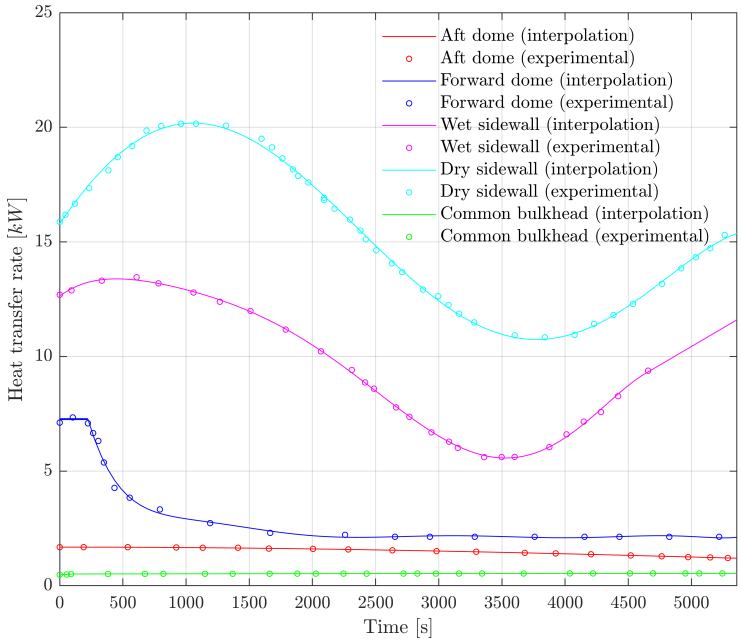

Figure 6.4: Experimental and interpolated heat transfer rates on the different parts of the tank wall, whose names are indicated in Fig. 6.1.

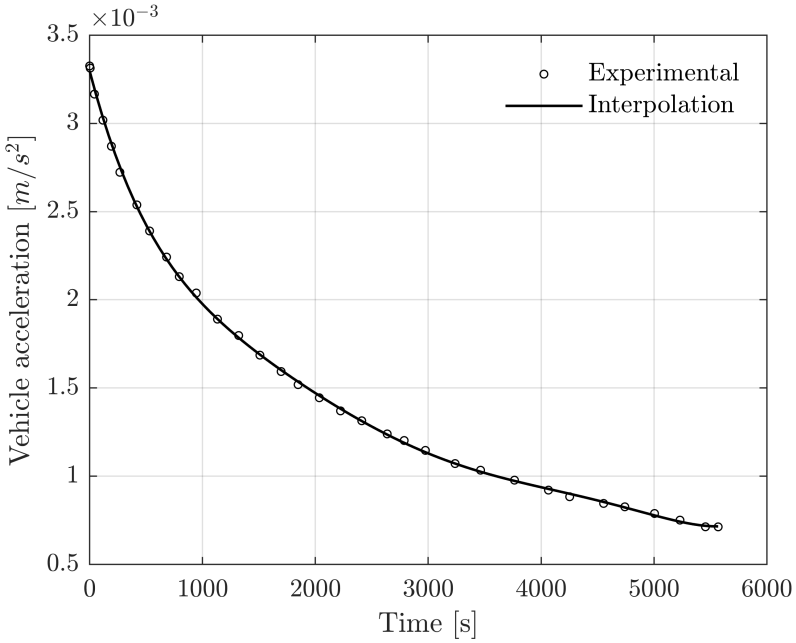

Figure 6.5: Experimental and interpolated acceleration.

Table 6.2: Details of the computational grids used for grid independence study.

	No. of cells [-]	Wall-Interface spacing [mm]
Grid 1	23401	4
Grid 2	34017	4
Grid 3	84694	2

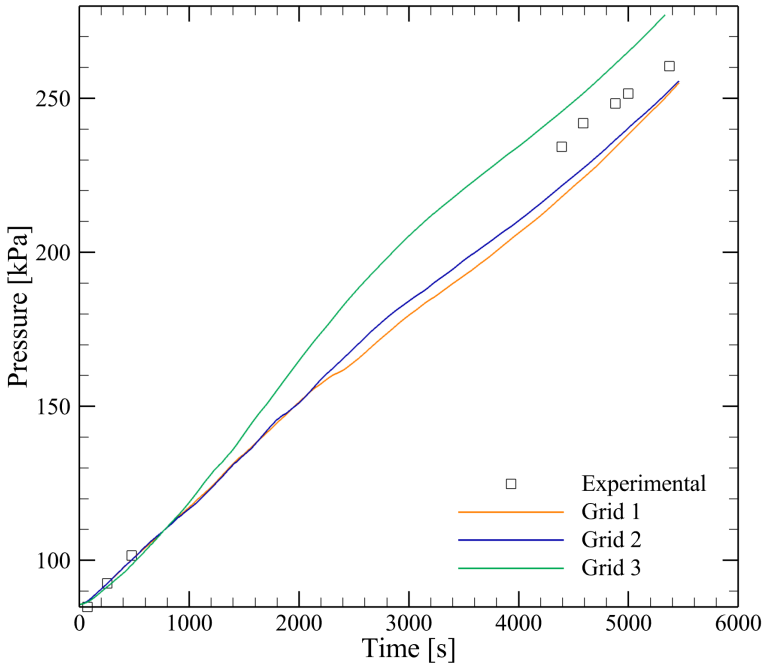

Figure 6.6: Numerical pressurization curves obtained with the three grids used for grid independence study. The characteristics of the used grids are summarized in Tab. 6.2.

discrepancy with respect to the ones obtained with the medium grid. Instead, the pressure results of these two grids show a not negligible discrepancy with respect to the one obtained with the finest grid. However, with the finest grid the numerical solution is too time-consuming for practical use, and so the medium grid, which is indicated as "Grid 2" in Tab. 6.2, has been selected for a trade-off between accuracy and computational time. "Grid 2" is represented in Fig. 6.7. On the right half of the figure there are a zoom of the tank region comprising the baffles and of the edge region developing near the common bulkhead.

Thermal stratification profiles in Fig. 6.8, show the value, at tank axis of symmetry, of the ratio y/H as a function of temperature, at the final instant of the test, for the two coarsest grid levels. In the y/H expression, y represents tank vertical dimension, and H represents tank height. The difference between the temperature at the top of the tank and that at the liquid-ullage interface is about 152 K for both grid levels. Instead, an experimental value of 107.8 K is reported in [117]. The overestimation of the ullage temperature stratification in CFD analyses may probably be attributed to the lack of the conjugate heat transfer model. Indeed, the wall conduction plays a role in diverting part of the heat toward the lower part of the tank, as we have seen in the case of self-pressurization

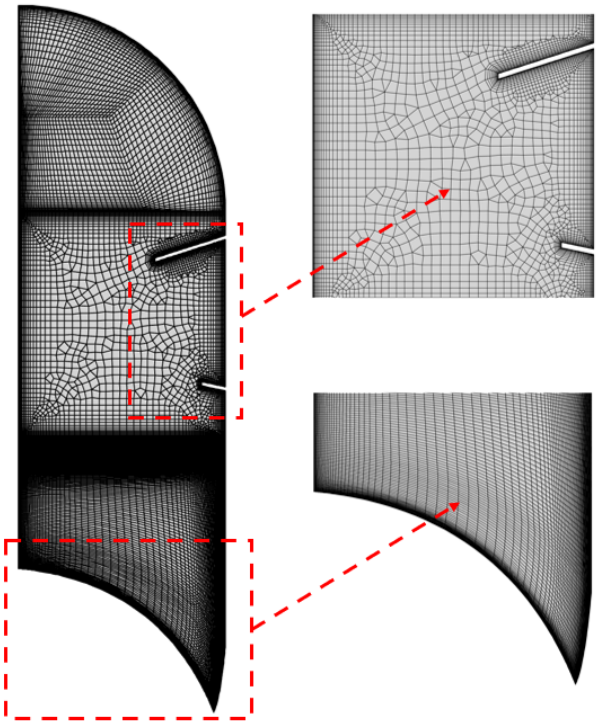

Figure 6.7: Representation of "Grid 2", whose details are given in Tab. 6.2. On the right half of the figure there are a zoom of the tank region comprising the baffles and of the edge region developing near the common bulkhead.

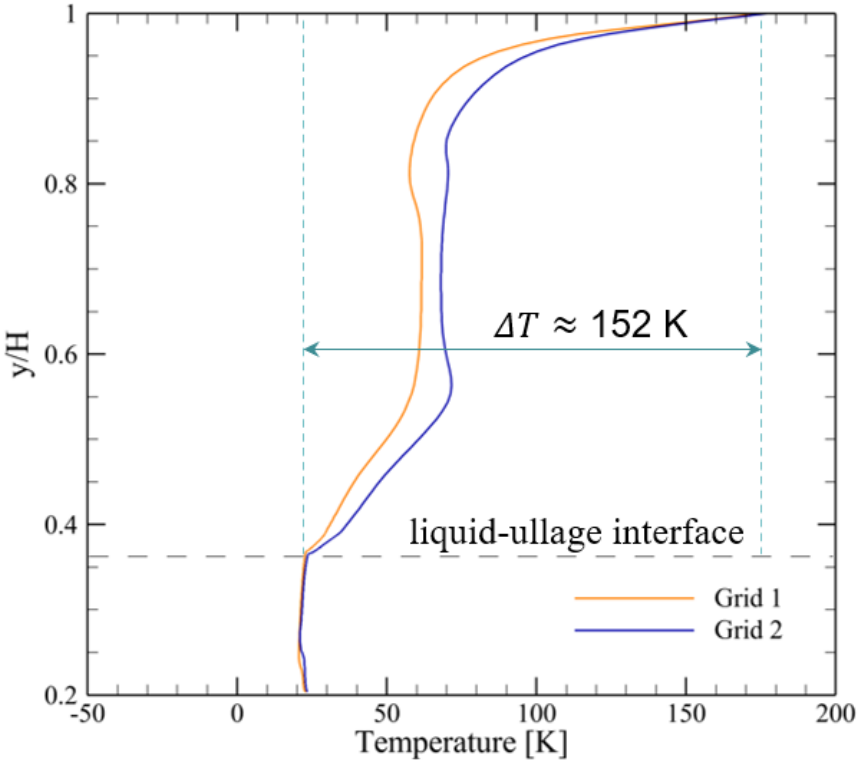

Figure 6.8: Thermal stratification profiles at tank axis of symmetry, at the final instant of the test, for the two coarsest grid levels.

in normal gravity (see Sec. 4.6.6). Another reason of the mismatch can be the selected turbulence model.

6.2.5 Results: physical phenomena in reduced gravity

An analysis of some physical phenomena occurring during this experiment will be presented in this section. All the presented results have been obtained with the selected grid (i.e. "Grid 2").

Contours of liquid H_2 volume fraction in the bottom part of the tank, at various times, ranging from 0 min to 15 min, are shown in Fig. 6.9. It is evident that boiling occurs at the tank walls. The

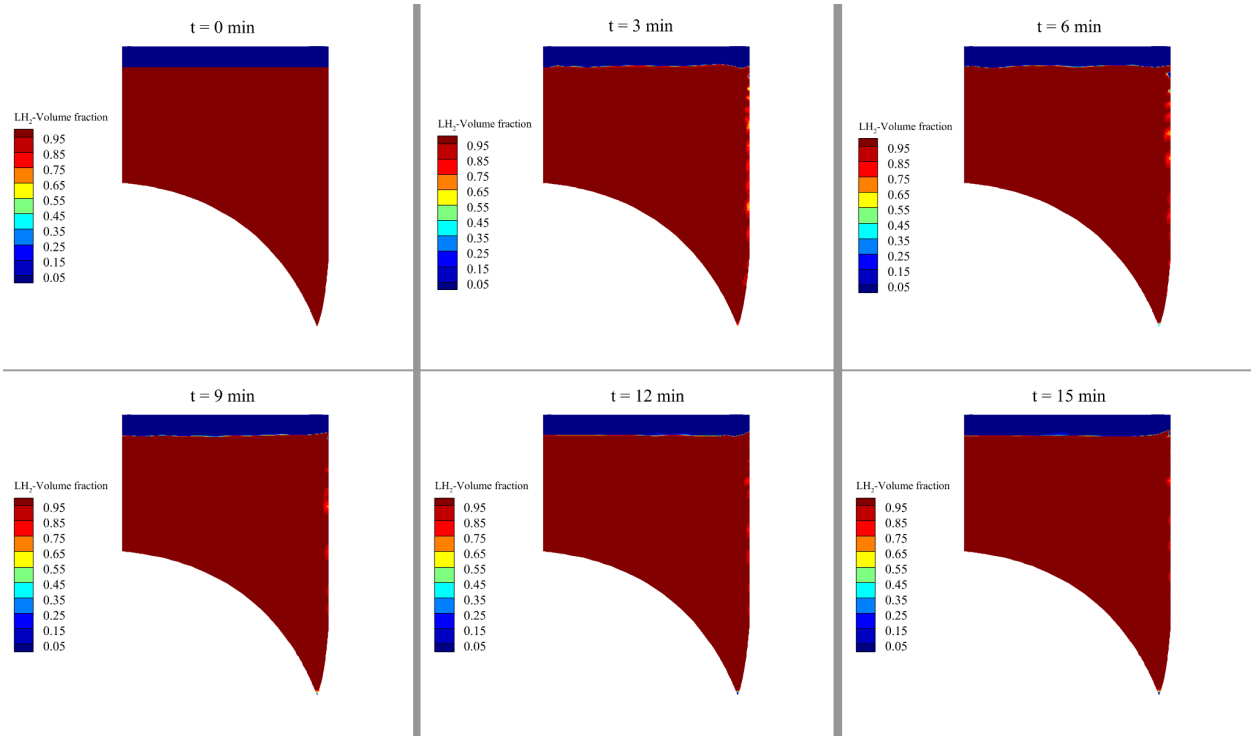

Figure 6.9: Contours of liquid H_2 volume fraction in the bottom part of the tank, at various times, ranging from 0 min to 15 min.

boiling has not the characteristics of boiling in microgravity, indeed, there is not the coalescence of many bubbles into a single large bubble, which remains attached to the wall, but the formation of many bubbles raising upward. This means that the gravity level is sufficient to give rise to buoyancy forces. Moreover, the boiling intensity decreases after 6 min, as it is evidenced by the reduction in the amount of wall bubbles for longer times. This is due to the profile of the heat transfer rate entering the liquid from the wet sidewall. Indeed, the interpolated profile, which is the one that has been used to compute the heat flux used as boundary condition, shows a decreasing behavior after about 8 min and until about 58 min. Also Fig. 6.10, which shows liquid H_2 volume fraction in the bottom part of the tank, at higher times, ranging from 24 min to 42 min, witnesses that the boiling intensity continues to decrease during the phase characterized by a decreasing behavior of the imposed wall heat flux. Moreover, from Fig. 6.9 and Fig. 6.10, it is evident that there is no rising of liquid on the walls, even if the experiment is carried out in a reduced gravity environment. This behavior is due to the Bond number, which is the ratio of buoyancy forces to surface tension force (see Eq. (1.4)). Indeed, if the Bond number is estimated using the medium acceleration level

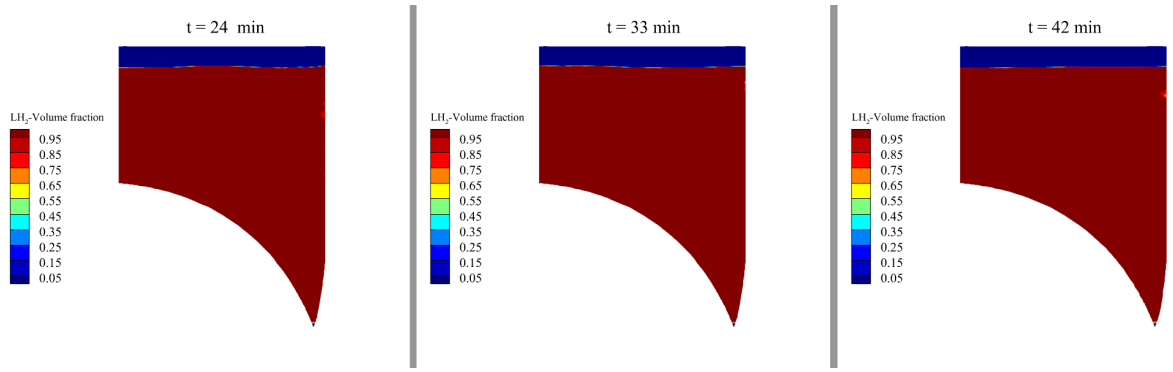

Figure 6.10: Contours of liquid H_2 volume fraction in the bottom part of the tank, at various times, ranging from 24 min to 42 min.

$(1.7 \cdot 10^{-4} g_E)$, it results to be of the order of 10^3, both if it is based on the liquid height and if it is based on the tank diameter. This means that the level of acceleration, although low, is sufficient to keep the liquid stabilized throughout the experiment.

As regards the temperature, Fig. 6.11 shows temperature contours at the beginning (0 min), at about the middle (45 min), and at about the end (89 min) of the test. Streamlines are also shown in the right half of each figure. The figure at 0 min shows the initial condition, which, as already said in Sec. 6.2.3, is characterized by temperature stratification in the ullage, uniform temperature in the liquid, and null velocity in both phases. Figures at 45 and 89 min show that the ullage continues

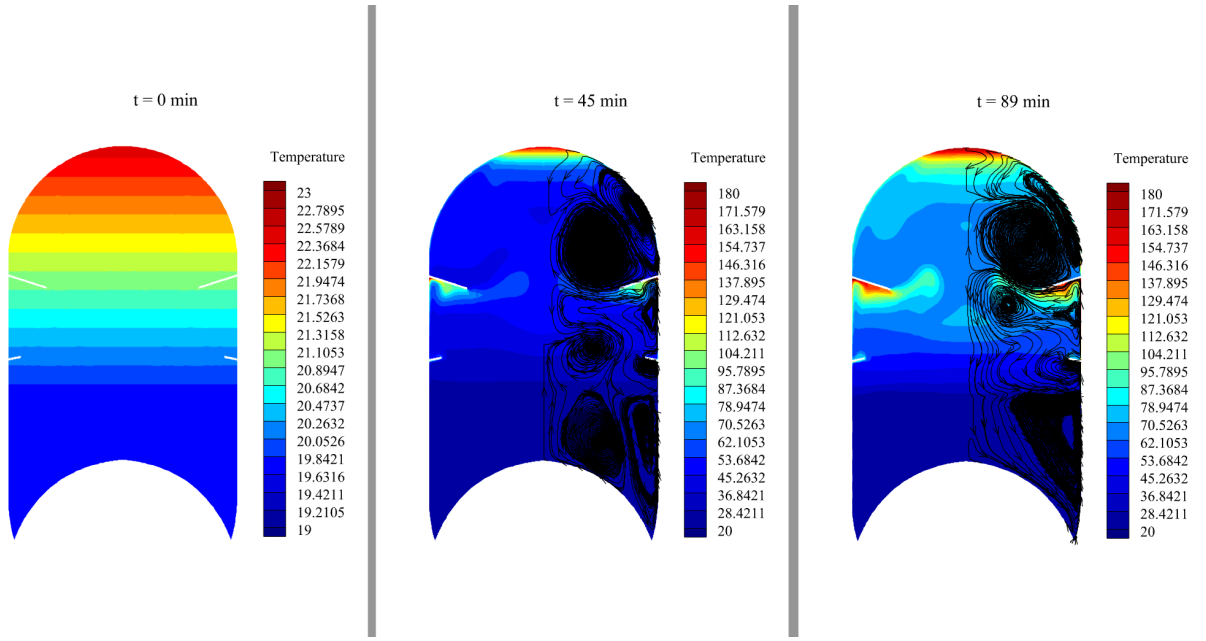

Figure 6.11: Temperature contours and streamlines at 0 min, 45 min, and 89 min.

to be thermally stratified, as it has already been shown in Fig. 6.8. Moreover, the presence of the baffles highly influences the thermal behavior of the tank, as it creates an obstacle for the convective recirculations. Indeed, the highest temperature values in the tank are reached at the edge located below the upper baffle. This is due both to the heat flux applied on the wet sidewall, which has the largest values compared to those on the other walls, and to the presence of the baffle.

It is interesting to highlight that even the very low acceleration level is sufficient to support

convective motions in both the liquid and the ullage. The presence of convective recirculations, which are shown in Fig. 6.11, is also witnessed by the thermal stratification.

6.3 Parametric study on the gravity level

In this section, the parametric study carried out for four gravity levels (g_E, $10^{-1}g_E$, $10^{-2}g_E$, and $10^{-3}g_E$) will be presented. The geometry, fluid, wall material, and operating conditions are the same of the validation test case [84] presented in Chap. 4. The selected test case involves liquid N_2 self-pressurization, inside a cylindrical tank, made of 316 SS. Details about the geometry can be read in Sec. 4.2. The initial liquid volume fraction is equal to 88%, and the initial pressure is 106 kPa. Moreover, the intermediate value of the entering heat transfer rate (see Sec. 4.6.8), 1.48 W, has been used to calculate the heat flux applied to the wall. The thermophysical and transport properties have been chosen as in Sec. 4.3.

6.3.1 Computational setup

The same computational setup of Sec. 4.4 has been used. Different computational grids, whose details are summarized in Tab. 6.3, have been used for the cases characterized by different gravity levels. Indeed, being the liquid-ullage interface not flat under reduced gravity conditions, the grid has been refined in the regions where the interface is expected to be during the test, in order for the shape of the interface to be reconstructed well. All the used grids are structured, and they are

Table 6.3: Details of the simulations carried out for the parametric study: gravity level, grid name, number of grid cells, grid spacing at the wall, time step, and number of iterations per time step.

Gravity level [m/s^2]	Grid name [-]	No. of cells [-]	Wall spacing [mm]	Time step [s]	Iter/time step [-]
g_E	Grid 1*	8344	0.23	0.01	30
$10^{-1}g_E$	Grid 2*	26052	0.23	0.001	30
$10^{-2}g_E$	Grid 2*	26052	0.23	0.001	30
$10^{-3}g_E$	Grid 3*	67392	0.23	0.001	40

characterized by an increasing number of cells as gravity decreases (except for the cases at $10^{-1}g_E$ and $10^{-2}g_E$, for which the same grid has been used). The used grids are represented in Fig. 6.12. The time step and number of iterations per time step used for each simulation are summarized in Tab. 6.3, and have been selected in order to keep the residuals below proper limits.

The laminar model has been used, as the flow is expected to be laminar for all the gravity levels considered, as it is clear from Fig. 6.13. The latter shows the modified Rayleigh number (see Eq. (4.1)), Ra^*, calculated both based on the wet sidewall and on the dry sidewall, as a function of the ratio between the gravity level and normal gravity (both axes are in logarithmic scale). A horizontal dashed-dotted line, corresponding to Ra^*=10^{11}, is also shown to indicate the transition from laminar to turbulent. From the figure, it is evident that the flow becomes weakly turbulent only in normal gravity and only in the liquid. For this reason, the laminar model has been adopted.

The following boundary conditions are imposed: a heat flux of 7.281 W/m^2 on the external tank walls and a no-slip coupled wall boundary condition at the interface between the fluid and the wall, with a contact angle of 5°. This last value has been selected as it is in the range of the contact

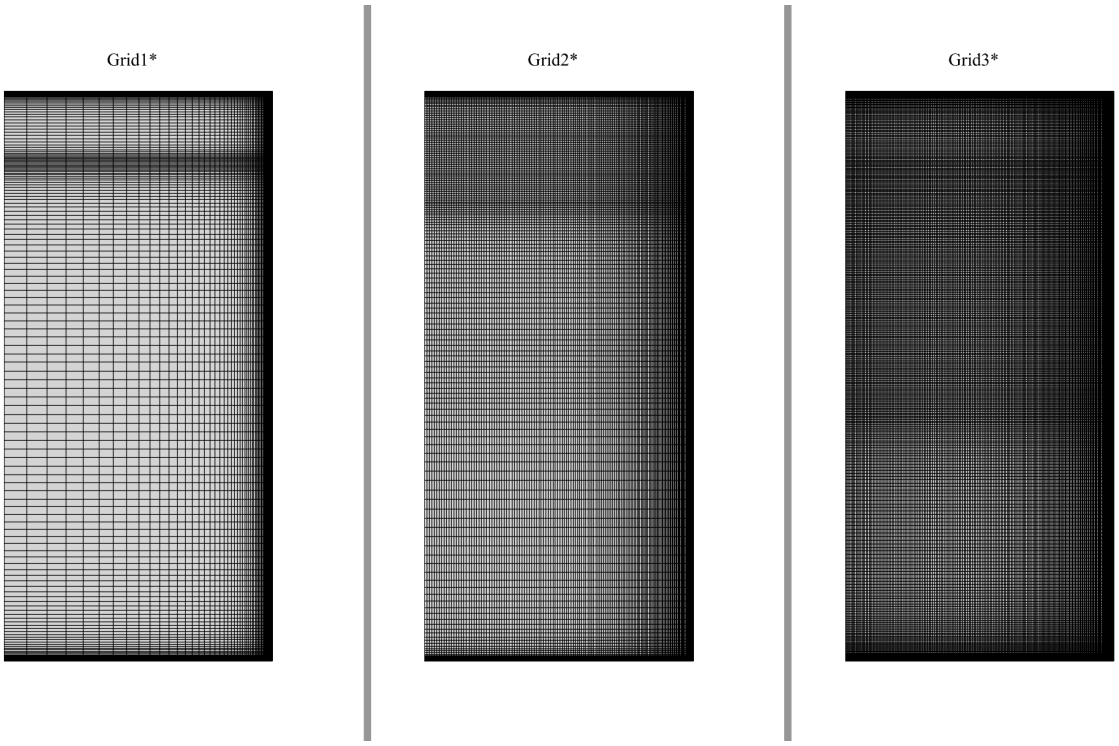

Figure 6.12: Grids used for the simulations of the parametric study on the gravity level. Details of the represented grids can be found in Tab. 6.3.

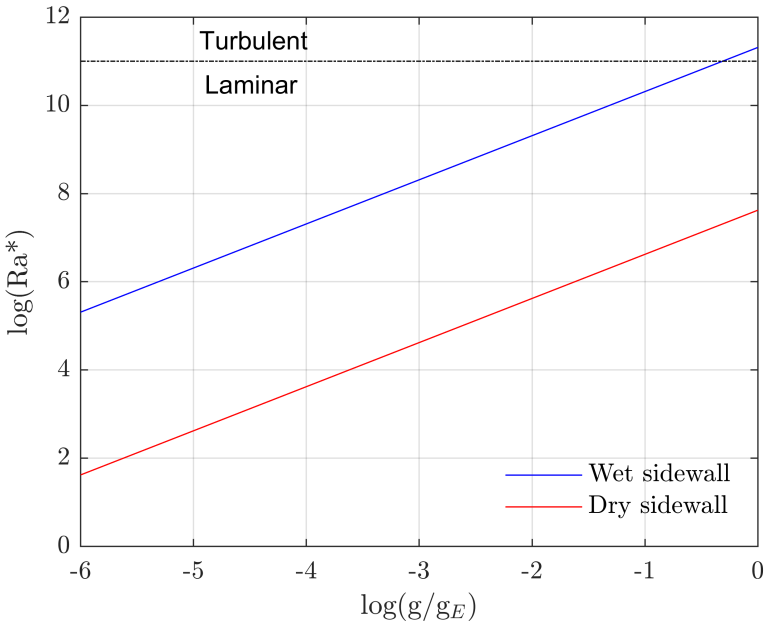

Figure 6.13: Modified Rayleigh number, Ra^*, calculated both based on the wet sidewall and on the dry sidewall, as a function of the ratio between the gravity level and normal gravity (both axes are in logarithmic scale).

angles for cryogenic liquids in contact with typical tank wall materials (aluminum or stainless steel) [10, 14]. The liquid and vapor phases are initialized as quiescent, at a pressure of 106 kPa and at a temperature corresponding to the saturation temperature at the initial tank pressure. The wall is initialized at the same uniform temperature as the fluid phases.

6.3.2 Results

Varying the gravity level from normal gravity, g_E, to $10^{-3}g_E$, the Bond number (see Eq. (1.4)), Bo, is characterized by large excursions, as it is shown in Fig. 6.14. This last shows the Bond number,

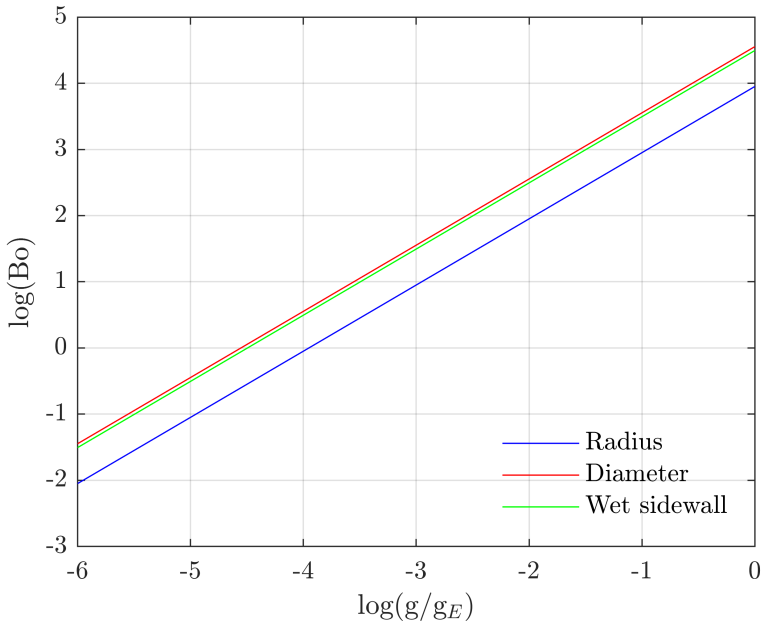

Figure 6.14: Bond number, Bo, calculated based either on the wet sidewall, or on the tank radius, or on the tank diameter, as a function of the ratio between the gravity level and normal gravity (both axes are in logarithmic scale).

calculated based either on the wet sidewall, or on the tank radius, or on the tank diameter, as a function of the ratio between the gravity level and normal gravity (both axes are in logarithmic scale). As the gravity level decreases, the Bond number decreases, and the surface tension force assumes an increasing influence over the buoyancy force. As a consequence, the liquid-vapor interface does not remain flat in time. Fig. 6.15 shows contours of liquid N_2 volume fraction at 60 s, obtained for the four tested gravity levels. As the gravity level decreases, the amount of liquid rising on the tank wall increases. The liquid-ullage interface begins to have a not negligible distortion for $g = 10^{-2}g_E$, and, for $g = 10^{-3}g_E$, the liquid has completely risen up along the wall initially in contact with the vapor.

The pressure evolutions in the tank, obtained for the four considered gravity levels, are shown in Fig. 6.16. It is evident that the pressurization rate increases as gravity level decreases, but, below $10^{-2}g_E$, the effect of gravity on the pressurization rate becomes less pronounced. Moreover, the difference in the pressurization rate for the various gravity levels is higher at the initial instants, and reduces as time progresses. The pressure behavior as gravity changes can be explained looking at the phase change mass flow rate evolutions for the four gravity levels, in Fig. 6.17. At the initial instants, the slopes of the curves reflect the behavior with gravity of the slopes of the pressure curves. Instead, after about 20 seconds, all the curves obtained in reduced gravity tend to assume similar trends. This behavior can be explained by the entity of the buoyancy forces. Indeed, in normal gravity, the convective motions cause the hot fluid zones which form near the wall to move upwards, while, in reduced gravity, these hot fluid layers are not pushed upwards by convection, and continue

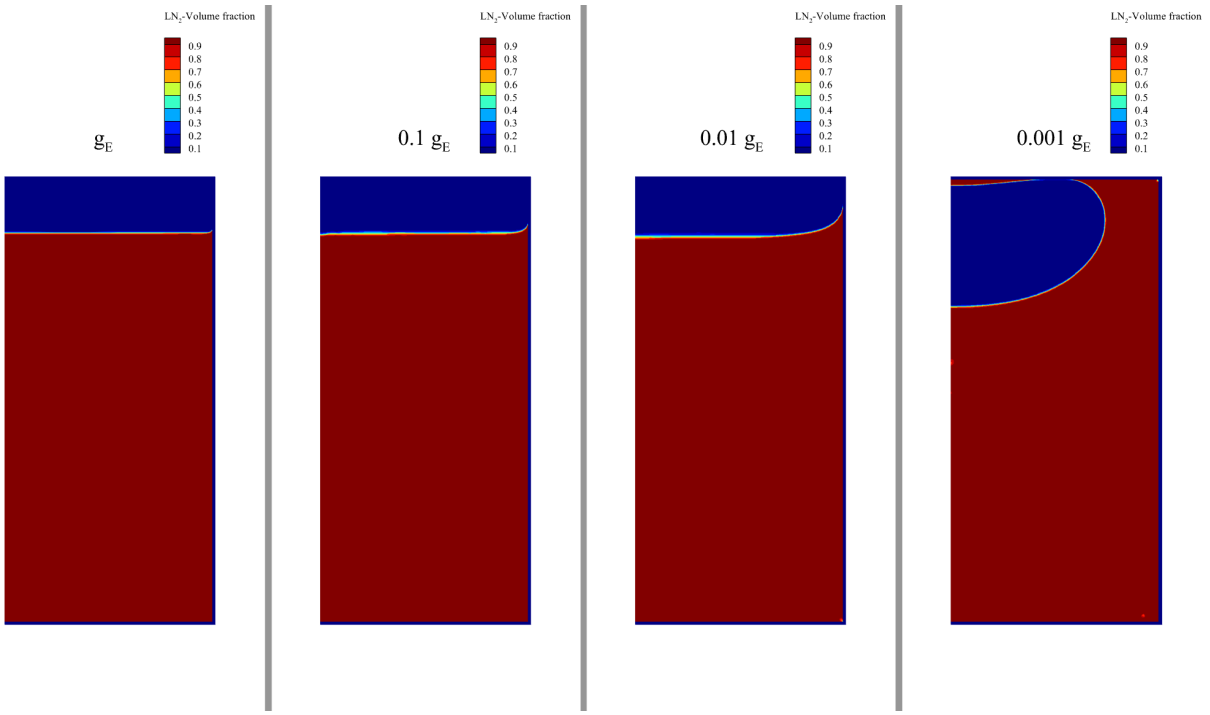

Figure 6.15: Contours of liquid N_2 volume fraction, at 60 s, for the four gravity levels considered in the parametric study.

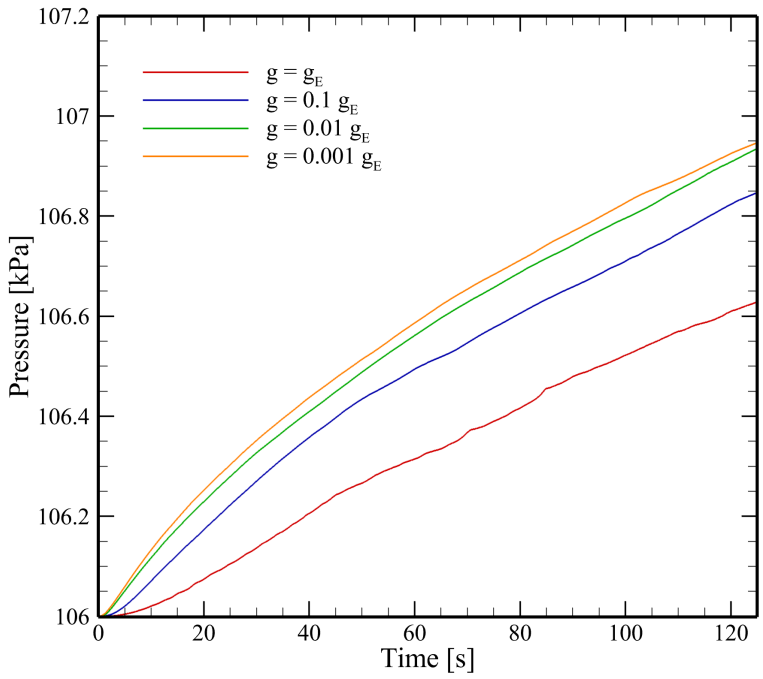

Figure 6.16: Pressure evolutions for the four gravity levels considered in the parametric study.

to heat up. Thus, the superheated state is reached earlier, and boiling has a higher intensity in the lowest gravity case. Nevertheless, within a few seconds, even in the other cases at reduced gravity, a superheated layer develops on the wetted wall, and that explains why, after about 20 s, all the

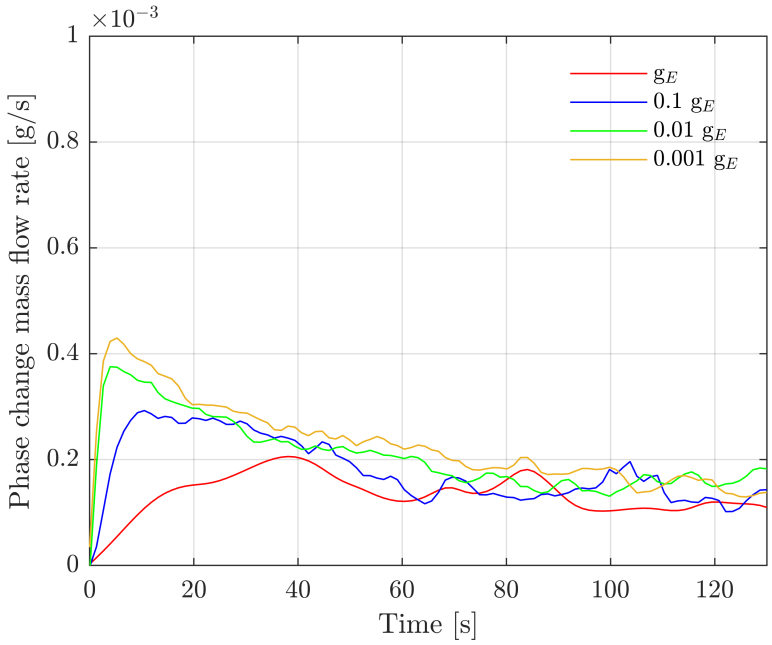

Figure 6.17: Phase change mass flow rate evolutions for the four gravity levels considered in the parametric study.

curves of phase change mass flow rate obtained in reduced gravity tend to assume similar trends. Once the difference in the phase change mass flow rate has diminished, also the difference in the pressurization rates reduces.

Chapter 7

Conclusions and future work

A thermo-fluid-dynamics characterization of the behavior of cryogenic propellant inside tanks has been carried out for two types of cryogenic propellant (H_2 and N_2), under various operating conditions (the self-pressurization and the active-pressurization on ground, and the self-pressurization in reduced-gravity conditions). Thermo-fluid-dynamics characterization, in addition to the study of fluid-dynamics behavior and of heat transfer characteristics of cryogenic propellant, is aimed at estimating the following observables: the pressurization rate, the temperature stratification, and the phase change mass flow rate. Carrying out this kind of analysis is very important from both a scientific and technological standpoint. Indeed, heat leaks from the outside environment are inevitable in cryogenic tanks, causing propellant vaporization. This last, together with the heating of the ullage, causes tank self-pressurization, in the case of a closed tank without venting. Pressurization can also be actively performed in some situations. In the design phase of cryogenic tanks, tank pressure levels as well as local temperature values must be reliably quantified and controlled in order to ensure proper inlet conditions for the turbopumps. Besides these aspects, additional phenomena increase the complexity of thermo-fluid-dynamics characterization in the case of reduced gravity (the different characteristics of boiling, the role of surface tension etc.). The study of these phenomena is critical for the design of cryogenic tanks, and has been extensively carried out in the literature by means of experiments, reduced order models, and numerical simulations. Experiments are expensive and complex to design, especially in the microgravity environment, and there is a lot of uncertainty in the experimental data. Reduced order models, of various levels of sophistication, are an engineering tool useful to make quick estimates of the main observables. Nevertheless, they do not allow to consider all the physical phenomena at play, and to monitor the local characteristics of the propellant in the tank (temperature distribution, bubble formation, fluid-dynamics paths etc.), as in CFD simulations. These last, instead, for cryogenic tank operations, have the drawback of being time-consuming, due to the two-phase flow modeling (interface reconstruction) and to the unsteadiness of the phenomenon. Despite this critical issue, CFD simulations represent an important complementary tool to the experiments to approach the study of thermo-fluid-dynamics behavior of cryogenic propellant in tanks.

The objective of this thesis is twofold. On the one hand, a reduced 0D model has been implemented in Matlab, verified with a 1D model developed by NASA, and utilized to perform the simulation of benchmark test cases retrieved from the literature. On the other hand, a state of the

art CFD methodology has been set up, and validated with the experimental data of three validation test cases.

As concerns the 0D model, the comparison between its results and the ones obtained with the 1D code, for two characteristic operating conditions, namely the storage regime and the blowdown regime, has shown that the 0D model is able to describe, with reasonable accuracy, the main observables of the thermo-fluid-dynamics characterization for both the operating conditions. This result underscores the usefulness of the 0D model, which, moreover, requires less effort to be implemented with respect to the 1D model. The 0D model has been also used, alongside the CFD methodology, to perform the simulation of two benchmark validation experiments. The following results have been obtained:

- A ground-based self-pressurization experiment, in a small-scale liquid N_2 tank, has been simulated. The experimental pressure rise rate has been reproduced with reasonable accuracy (with a percentage error on pressure slightly above 2%). Obviously, the 0D model is inherently not able to reproduce the temperature stratifications arising both in the ullage and close to the free-surface, and the estimated average liquid and ullage temperatures at 2 h have, respectively, overestimated and underestimated the experimental values.
- A ground-based active-pressurization experiment in a small-scale liquid N_2 tank has been simulated. The 0D model has resulted able to describe the pressure rise rate with reasonable accuracy, during the active-pressurization phase. But, there has been poor agreement with the experimental data during the relaxation phase, due to an overestimation of the depressurization rate. As for the temperature results, the liquid temperature estimated by the 0D model, at 200 s, has resulted very similar to both the one estimated with the CFD simulation and to the experimental one. Regarding the temperature within the ullage, the one estimated by the 0D model, at 200 s, has closely matched the average of both the CFD and experimental distributions.

As regards the developed CFD methodology, it is based on the use of the Volume-of-Fluid method to reconstruct the liquid-ullage interface, of the Lee model to compute the mass transfer due to phase change, and of the Continuum Surface Force model to take into account the effect of surface tension. The tank is schematized as 2D axisymmetric, due to the symmetry of the geometry, boundary condition, and flow field. Transient simulations have been carried out using the commercial software Ansys Fluent®, and three validation test cases have been simulated.

The first validation test case involves liquid N_2 self-pressurization in a small-scale tank, exposed to the heat flux generated by three heaters. With this validation we have assessed the potentialities and the weaknesses of various numerical models in reproducing experimental temperature stratification profiles close to the free-surface, as well as pressure rise rates. The main results are the following:

- Phase change computation using Lee model is insensitive to the value of mass transfer intensity factor. Indeed, pressure rise rate shows variations less than 1% for variations of this parameter of three orders of magnitude. However, the choice of the mass transfer intensity factor plays a role in the stability of the numerical computation.

- In order to describe the liquid temperature stratification close to the free-surface, it is necessary to simulate the self-pressurization phenomenon including the solid wall region, and using a conjugate heat transfer model. This is due to the fact that heat flux paths within the tank wall play a fundamental role in distributing the entering heat transfer rate between the liquid and the ullage.

- Using a turbulence model leads to an overestimation of convective recirculations, and, consequently, to a prediction of a higher mixing than the actual one. This causes the inability of the turbulence models to represent the liquid temperature stratification close to the free-surface. Instead, for the ullage, a higher thermal stratification than the actual one is obtained.

- The experimental uncertainty on the entering heat transfer rate may substantially affect the numerical predictions.

- Modeling the vapor as an ideal gas and the liquid with the Boussinesq approximation leads to results of pressure and temperature stratification comparable with respect to the ones obtained when using real thermodynamic and transport properties for liquid and gaseous N_2, taken from the NIST Chemistry WebBook. Instead, the computational time reduces of about 3.25 times with respect to the case when real properties are used.

- Numerical results show that using a coupled algorithm for pressure-velocity coupling allows to obtain results of pressurization rate and of thermal stratification comparable to those obtained with a segregated algorithm, but with a time step 2.5 times larger than that required in the segregated algorithm.

The second validation experiment is a ground-based active-pressurization experiment, inside a liquid N_2 tank. With our methodology, a high fidelity reproduction of both the active-pressurization rate and of the pressure decrease following the end of gas injection is obtained. The main results obtained are:

- The active-pressurization rate is dependent on the initial ullage mass value. Thus, the experimental uncertainty on this parameter affects the numerical predictions.

- The numerical modeling of the final instants of the pressurant gas injection requires some attention, to avoid having unphysical results. In particular, the gas injection should not be stopped instantaneously, but using a decreasing profile for the pressurant gas mass flow rate, in order to avoid sudden unphysical temperature drops near the diffuser and at the axisymmetric boundary.

- All the three tested turbulence models allow for a better estimation of the active-pressurization rate, compared to the one obtained with the laminar model. While, the pressure decrease phase of the experiment is described with the highest accuracy when the SST $k-\omega$ with low-Re corrections turbulence model is used.

- The discrepancies caused by modeling the flow either as laminar or as turbulent are more pronounced on pressure results with respect to temperature results.

- Even if the turbulent models have proven to be more adequate than the laminar one to describe the pressure evolution during the experimental duration, they predict a pressure decrease phase longer than the experimental one. Instead, the laminar model is more adequate in predicting the duration of the pressure decrease phase.

- Simulating the wall region, through the use of a conjugate heat transfer model, is fundamental in the case of cryogenic tanks actively-pressurized with a high temperature pressurant gas. This is due to the fact that heat flux paths within the tank wall play a fundamental role in distributing, between the two phases, the energy input carried by the pressurant gas.

After validating our CFD methodology with pressurization results in normal gravity, a validation of our methodology with the experimental data of the first self-pressurization experiment in reduced gravity, with data sufficiently detailed for validating storage tank models, has been carried out. The test tank is the liquid H_2 tank of the second stage of the Saturn IB AS-203 vehicle, and the self-pressurization experiment was carried out while it was into circular low Earth orbit. Thus, the time-varying acceleration and heat flux to which the tank was exposed during the experiment have been modeled in our analysis. The main results are the following:

- With the tested turbulence model (the SST $k-\omega$) the experimental pressurization rate is described quite well.

- The temperature stratification in the ullage at the end of the experiment is overestimated of about 40 K, this is probably due to the lack of the conjugate heat transfer model.

- Although the low level of average acceleration ($1.7 \cdot 10^{-4} g_E$), the Bond number is high enough (of the order of 10^3) to keep the liquid stabilized throughout the experiment.

- Thermal stratification develops within the ullage, and this is the proof that very low accelerations are sufficient to support convective motions.

- The presence of the baffles highly influences the thermal behavior of the tank, as it creates an obstacle for the convective recirculations. This causes the highest temperature values in the tank to be reached at the edge located below the upper baffle.

The successfully validated methodology has been, finally, used to carry out a parametric study on the gravity level. Four gravity levels, from normal gravity ($g_E = 9.81$ m/s^2), until the reduced gravity of $10^{-3} g_E$, have been considered. This study has been performed using the same geometry, fluid, and operating conditions of the first validation test case. The parametric study has shown that the pressurization rate increases with the decrease of the gravity level. This is due to the decrease of convective motions in reduced gravity, which causes hot fluid layers to remain adherent to the wall, and continue to heat up, reaching more easily the superheated state. Thus, at the initial instants, the increased boiling causes an increased pressurization rate, in the lowest gravity case. Within a few seconds, the superheated state near the wall is reached also in the other cases in reduced gravity, hence, the corresponding curves of phase change mass flow rate tend to assume similar trends, and also the difference in the pressurization rates reduces.

The objective of this study has been the thermo-fluid-dynamics characterization of the behavior of the cryogenic propellant in tanks under numerous operating conditions. This has been done, with two different levels of detail, using either the implemented and validated 0D model, or the proposed CFD methodology. The proposed and validated methodology, as well as the results of the parametric studies constitute a solid base from which to start, nevertheless some aspects have not been considered yet, and should be tackled in the future. First of all, the influence of the sloshing on the thermo-fluid-dynamics characterization should be considered, as it has been demonstrated by experimental and numerical work that the sloshing has a strong impact on the thermal physical processes occurring in cryogenic tanks, and because the sloshing is very common in upper-stage liquid propellant tanks. Indeed, during sloshing there is thermal de-stratification induced by fluid mixing, as well as heat and mass transfer at the liquid-ullage interface, which cause large pressure drops in the tank. The quantification of these phenomena for cryogenic propellant tanks is crucial, as large pressure collapse due to strong sloshing can induce engine pump cavitation and thrust degeneration. Moreover, it is also fundamental to ensure that the pressure does not decrease beyond the buckling limit, in order to guarantee the structural integrity. Secondly, in the present thesis, the surface tension has been modeled as constant. This simplification, although accurate in the normal gravity environment, is quite strong in the reduced gravity case, where the presence of thermocapillary convection influences the bubbles behavior in case of boiling, as well as the free-surface deformations. Hence, our CFD methodology could be improved, in the future, in order to make it capable to take into account the effects of surface tension gradients. Furthermore, the assumption of a constant static contact angle at the wall, which has been used in all the analyses, is accurate enough for the cases without sloshing or without liquid surface reorientation due to reduced gravity. Indeed, in these cases, the contact line does not move in time. Instead, in the other cases, it would be desirable to use a model for the dynamic contact angle. Hence, in the future, some work could be done on the proposed numerical methodology, in order to incorporate a proper contact angle model, this would certainly be beneficial to the future parametric studies carried out in reduced gravity. In addition, regarding the active-pressurization studies, it can be noticed that, in the case analyzed, the pressurant gas is of the same chemical species as the propellant. It is well known that, in real applications, He is often used as pressurant gas for cryogenic tanks. When the pressurant gas species differs from the propellant already present in the tank additional physical phenomena arise (e.g., the species diffusion), thus it would be important to make the numerical methodology capable of taking into account all of them. Other phenomena that could play a role in some situations, but that have not been considered in this thesis are: the presence of a non-condensable gas, the formation of fog in the ullage, etc. Furthermore, because the analyses carried out under reduced gravity conditions that we have presented are quite preliminary, further parametric analyses (e.g., varying the incoming wall heat flux) and studies under different operating conditions could also be conducted. Finally, once the proposed numerical methodology is enhanced, it could be used to simulate a real mission profile of a high-stage tank, or even two tanks in a common bulkhead configuration (e.g., a liquid O_2 tank and a liquid CH_4 tank, as in the case of the third stage of Vega E), from ground hold, to insertion into orbit and orbital phase.

Bibliography

[1] ANSYS fluent documentation. Release 2022 R1. 2022.

[2] H. N. Abramson. The dynamic behavior of liquids in moving containers, with applications to space vehicle technology. *NASA Technical Report*, NASA SP-106, 1966.

[3] V. Ahuja, A. Hosangadi, S. Mattick, C. Lee, R. Field, and H. Ryan. Computational analyses of pressurization in cryogenic tanks. In *44th AIAA/ASME/SAE/ASEE Joint Propulsion Conference & Exhibit*, page 4752, 2008.

[4] Anon. Main propellant tank pressurization system study and test program. In *Prog. Rep.*, pages FTRL–TOR–61–23 (ER 5238), Lockheed–Georgia Co., 1961.

[5] J. C. Aydelott. Normal gravity self-pressurization of 9-inch-/23 cm/diameter spherical liquid hydrogen tankage. *NASA Technical Report*, NASA TN D-4171, 1967.

[6] H. Baehr and K. Stephan. *Heat and mass transfer*. Springer, 2006.

[7] M. Bahreini, A. Ramiar, and A. A. Ranjbar. Numerical simulation of bubble behavior in subcooled flow boiling under velocity and temperature gradient. *Nuclear Engineering and Design*, 293:238–248, 2015.

[8] S. Barsi and M. Kassemi. Investigation of tank pressurization and pressure control—part I: experimental study. *Journal of Thermal Science and Engineering Applications*, 5(4):041005, 2013.

[9] S. Barsi and M. Kassemi. Investigation of tank pressurization and pressure control—part II: numerical modeling. *Journal of Thermal Science and Engineering Applications*, 5(4):041006, 2013.

[10] K. Bellur, V. Konduru, M. Kulshrestha, D. Tyrewala, E. Medici, J. S. Allen, C. K. Choi, D. S. Hussey, D. C. Jacobson, J. B. Leão, et al. Contact angle measurement of liquid hydrogen (LH_2) in stainless steel and aluminum cells. *Journal of Heat Transfer*, 138(2):020904, 2016.

[11] M. D. Bentz. Tank pressure control in low gravity by jet mixing. *NASA Contractor Report*, NASA CR-191012, 1993.

[12] J. Brackbill, D. Kothe, and C. Zemach. A continuum method for modeling surface tension. *Journal of Computational Physics*, 100(2):335–354, 1992.

[13] M. Bracke, F. De Voeght, and P. Joos. The kinetics of wetting: the dynamic contact angle. *Trends in Colloid and Interface Science III*, pages 142–149, 2007.

[14] P. Brennan and E. Skrabek. Design and development of a prototype static cryogenic heat transfer system. *NASA Contractor Report*, NASA CR-121939, 1971.

[15] H. Chen and V. Patel. Near-wall turbulence models for complex flows including separation. *AIAA journal*, 26(6):641–648, 1988.

[16] B. Ciccotosto and D. M. Hauser. Autogenous pressurization of a cryogenic tank using computational fluid dynamics. In *AIAA Propulsion and Energy 2021 Forum*, page 3558, 2021.

[17] J. Clark. Universal equations for saturation vapor pressure. In *40th AIAA/ASME/SAE/ASEE Joint Propulsion Conference and Exhibit*, page 4088, 2004.

[18] J. H. Corpening. Analytic modeling of pressurization and cryogenic propellant conditions for liquid rocket based vehicle designs. In *NASA MSFC ER-22*, 2010.

[19] M. Daigle, M. Foygel, V. Smelyanskiy, and J. Boschee. LH2Sim [computer software]. https://github.com/nasa/LH2Sim, 2017.

[20] M. J. Daigle, V. N. Smelyanskiy, J. Boschee, and M. Foygel. Temperature stratification in a cryogenic fuel tank. *Journal of Thermophysics and Heat Transfer*, 27(1):116–126, 2013.

[21] S. De Brock, R. Grove, R. Sloma, D. Balzer, Y. BRILL, and G. Yankura. A survey of current developments in surface tension devices for propellant acquisition. *Journal of Spacecraft and Rockets*, 8(2):83–98, 1971.

[22] P.-G. De Gennes, F. Brochard-Wyart, D. Quéré, et al. *Capillarity and wetting phenomena: drops, bubbles, pearls, waves*. Springer, 2004.

[23] V. K. Dhir. Nucleate pool boiling under reduced gravity conditions—role of numerical simulations. In *Advances in Heat Transfer*, volume 47, pages 167–202. Elsevier, 2015.

[24] F. Dodge. Fluid management in low gravity. *Low-Gravity Fluid Dynamics and Transport Phenomena*, pages 3–14, 1990.

[25] A. Faghri and Y. Zhang. *Transport phenomena in multiphase systems*. Elsevier, 2006.

[26] J. L. Ferrín and L. J. Pérez. Numerical simulation of natural convection and boil-off in a small size pressurized LNG storage tank. *Computers & Chemical Engineering*, 138:106840, 2020.

[27] W. Friz. Maximum volume of vapor bubbles. *Physic. Zeitschz.*, 36:379–354, 1935.

[28] J. Fu, B. Sunden, X. Chen, and Y. Huang. Influence of phase change on self-pressurization in cryogenic tanks under microgravity. *Applied Thermal Engineering*, 87:225–233, 2015.

[29] E. Fuhrmann, M. Dreyer, S. Basting, and E. Bänsch. Free surface deformation and heat transfer by thermocapillary convection. *Heat and Mass Transfer*, 52:855–876, 2016.

[30] J. Gerstmann and M. E. Dreyer. The dynamic contact angle in the presence of a non-isothermal boundary condition. *Microgravity Science and Technology*, 19:96–99, 2007.

[31] F. Gibou, L. Chen, D. Nguyen, and S. Banerjee. A level set based sharp interface method for the multiphase incompressible Navier–Stokes equations with phase change. *Journal of Computational Physics*, 222(2):536–555, 2007.

[32] D. Gluck and J. Kline. Gas requirements in pressurized transfer of liquid hydrogen. In *Advances in Cryogenic Engineering: Proceedings of the 1961 Cryogenic Engineering Conference University of Michigan Ann Arbor, Michigan August 15–17, 1961*, volume 7, pages 219–233. Springer, 1962.

[33] S. N. Govindan and M. E. Dreyer. Experimental investigation of liquid interface stability during the filling of a tank in microgravity. *Microgravity Science and Technology*, 35(3):1–23, 2023.

[34] D. Guezengar, J. Francescatto, H. Guillard, and J.-P. Dussauge. Variations on a k–ε turbulence model for supersonic boundary layer computations. *European Journal of Mechanics-B/Fluids*, 18(4):713–738, 1999.

[35] J. W. Hartwig. A detailed historical review of propellant management devices for low gravity propellant acquisition. In *52nd AIAA/SAE/ASEE Joint Propulsion Conference*, page 4772, 2016.

[36] M. Hasan, C. S. Lin, and N. Vandresar. Self-pressurization of a flightweight liquid hydrogen storage tank subjected to low heat flux. In *1991 ASME/AIChE National Heat Transfer Conference*, number E-6095, 1991.

[37] L. Hastings, R. Flachbart, J. Martin, A. Hedayat, M. Fazah, T. Lak, H. Nguyen, and J. Bailey. Spray bar zero-gravity vent system for on-orbit liquid hydrogen storage. *NASA Technical Report*, NASA TM-2003-212926, 2003.

[38] C. Hirt and B. Nichols. Volume of fluid (VOF) method for the dynamics of free boundaries. *Journal of Computational Physics*, 39(1):201–225, 1981.

[39] J. I. Hochstein, H. C. Jit, and J. C. Aydelott. Prediction of self-pressurization rate of cryogenic propellant tankage. *Journal of Propulsion and Power*, 6(1):11–17, 1990.

[40] D. K. Huzel. *Modern engineering for design of liquid-propellant rocket engines*, volume 147. AIAA, 1992.

[41] F. P. Incropera, D. P. DeWitt, T. L. Bergman, A. S. Lavine, et al. *Fundamentals of heat and mass transfer*, volume 6. Wiley, New York, 1996.

[42] T.-S. Jiang, O. H. Soo-Gun, and J. C. Slattery. Correlation for dynamic contact angle. *Journal of colloid and interface science*, 69(1):74–77, 1979.

[43] T. Jongen and Y. Marx. Design of an unconditionally stable, positive scheme for the k-ε and two-layer turbulence models. *Computers & fluids*, 26(5):469–487, 1997.

[44] O. Kartuzova and M. Kassemi. Modeling interfacial turbulent heat transfer during ventless pressurization of a large scale cryogenic storage tank in microgravity. In *47th AIAA/ASME/SAE/ASEE Joint propulsion conference & exhibit*, page 6037, 2011.

[45] O. Kartuzova and M. Kassemi. Validation of a CFD model predicting the effect of high level lateral acceleration sloshing on the heat transfer and pressure drop in a small-scale tank in normal gravity. In *Fluids Engineering Division Summer Meeting*, volume 51579, page V003T18A002. American Society of Mechanical Engineers, 2018.

[46] O. V. Kartuzova and M. Kassemi. A CFD prediction of microgravity self-pressurization and pressure control and validation against the tank pressure control experiment. In *53rd AIAA/SAE/ASEE Joint Propulsion Conference*, page 4660, 2017.

[47] O. V. Kartuzova, M. Kassemi, Y. Umemura, K. Kinefuchi, and T. Himeno. CFD modeling of phase change and pressure drop during violent sloshing of cryogenic fluid in a small-scale tank. In *AIAA Propulsion and Energy 2020 Forum*, page 3794, 2020.

[48] M. Kassemi and D. Chato. The zero boil-off tank experiment. *Cold Facts, Cryogenics Society of America*, 33(3), 2017.

[49] M. Kassemi, S. Hylton, and O. Kartuzova. Zero-boil-off tank (ZBOT) experiment–CFD self-pressurization model validation with ground-based & microgravity results. In *AIAA Propulsion and Energy Forum*, 2018.

[50] M. Kassemi and O. Kartuzova. Effect of interfacial turbulence and accommodation coefficient on CFD predictions of pressurization and pressure control in cryogenic storage tank. *Cryogenics*, 74:138–153, 2016.

[51] M. Kassemi, O. Kartuzova, and S. Hylton. Validation of two-phase CFD models for propellant tank self-pressurization: crossing fluid types, scales, and gravity levels. *Cryogenics*, 89:1–15, 2018.

[52] N. D. Katopodes. *Free-Surface Flow: Computational Methods, Chapter 12 - Volume of Fluid Method*. Butterworth-Heinemann, 2019.

[53] A. D. Keni and J. Taillon. Cryogenic material properties calculators. `https://trc.nist.gov/cryogenics/calculators/propcalc.html`, 2018. [Online; accessed July 2022].

[54] C. R. Kharangate and I. Mudawar. Review of computational studies on boiling and condensation. *International Journal of Heat and Mass Transfer*, 108:1164–1196, 2017.

[55] C. Konishi and I. Mudawar. Review of flow boiling and critical heat flux in microgravity. *International Journal of Heat and Mass Transfer*, 80:469–493, 2015.

[56] M. Konopka, P. Noeding, J. Klatte, P. Behruzi, J. Gerstmann, A. Stark, and N. Darkow. Analysis of LN2 filling, draining, stratification and sloshing experiments. In *46th AIAA fluid dynamics conference*, page 4272, 2016.

[57] M. Konopka, A. Stark, and J. Gerstmann. Liquid nitrogen experiments and simulations using a large-scale aluminum test tank. In *AIAA Propulsion and Energy 2021 Forum*, page 3560, 2021.

[58] R. Krahl, J. Gerstmann, P. Behruzi, E. Bänsch, and M. E. Dreyer. Dependency of the apparent contact angle on nonisothermal conditions. *Physics of Fluids*, 20(4), 2008.

[59] S. P. Kumar, B. Prasad, G. Venkatarathnam, K. Ramamurthi, and S. S. Murthy. Influence of surface evaporation on stratification in liquid hydrogen tanks of different aspect ratios. *International Journal of Hydrogen Energy*, 32(12):1954–1960, 2007.

[60] J. Lacapere, B. Vieille, and B. Legrand. Experimental and numerical results of sloshing with cryogenic fluids. *Progress in Propulsion Physics*, 1:267–278, 2009.

[61] R. F. Lark. Cryogenic positive expulsion bladders. *NASA Technical Memorandum*, NASA TM X-1555, 1968.

[62] B. E. Launder and D. B. Spalding. The numerical computation of turbulent flow. *Computer Methods in Applied Mechanics and Engineering*, 3:269–289, 1974.

[63] J. Lee, Y. Ahn, and Y. Kim. Experimental study on effect of density ratio and phase transition during sloshing impact in rectangular tank. *Ocean Engineering*, 242:110105, 2021.

[64] W. H. Lee. A pressure iteration scheme for two-phase flow modeling. *Computational Methods for Two-Phase Flow and Particle Transport*, pages 61–82, 2013.

[65] E. Lemmon, M. McLinden, and D. Friend. Thermophysical properties of fluid systems. In *NIST Chemistry WebBook, NIST Standard Reference Database Number 69, Eds. Linstrom, P.J., and Mallard, W.G., National Institute of Standards and Technology, Gaithersburg MD*, 20899.

[66] Z. Liu, Y. Feng, G. Lei, and Y. Li. Thermal physical process in a liquid oxygen tank under different sloshing excitations. *International Communications in Heat and Mass Transfer*, 117:104771, 2020.

[67] Z. Liu, Y. Li, and Y. Jin. Pressurization performance and temperature stratification in cryogenic final stage propellant tank. *Applied Thermal Engineering*, 106:211–220, 2016.

[68] Z. Liu, Y. Li, Y. Jin, and C. Li. Thermodynamic performance of pre-pressurization in a cryogenic tank. *Applied Thermal Engineering*, 112:801–810, 2017.

[69] Z. Liu, Y. Li, and G. Zhou. Study on thermal stratification in liquid hydrogen tank under different gravity levels. *International Journal of Hydrogen Energy*, 43(19):9369–9378, 2018.

[70] Z. Liu, B. Sunden, and J. Yuan. VOF modeling and analysis of filmwise condensation between vertical parallel plates. *Heat Transfer Research*, 43(1), 2012.

[71] Z. Liu, X. Yin, Y. Liu, Y. Li, and M. Andersson. Thermodynamic performance in a liquid oxygen tank during active-pressurization under different gas injection temperatures. *International Communications in Heat and Mass Transfer*, 140:106477, 2023.

[72] C. Ludwig and M. Dreyer. Investigations on thermodynamic phenomena of the active-pressurization process of a cryogenic propellant tank. *Cryogenics*, 63:1–16, 2014.

[73] B. J. McBride and S. Gordon. *Computer program for calculation of complex chemical equilibrium compositions and applications. II. User manual and program description.* NASA Reference Publication 1311, 1996.

[74] F. R. Menter. Two-equation eddy-viscosity turbulence models for engineering applications. *AIAA journal*, 32(8):1598–1605, 1994.

[75] H. Merte Jr. Momentum effects in steady nucleate pool boiling during microgravity. *Annals of the New York Academy of Sciences*, 1027(1):196–216, 2004.

[76] H. Merte Jr. Some parameter boundaries governing microgravity pool boiling modes. *Annals of the New York Academy of Sciences*, 1077(1):629–649, 2006.

[77] T. Oka, Y. Abe, Y. H. Mori, and A. Nagashima. Pool boiling of n-pentane, CFC-113, and water under reduced gravity: Parabolic flight experiments with a transparent heater. *Journal of Heat Transfer*, 117(2):408–417, 1995.

[78] T. Oka, Y. Abe, Y. H. Mori, and A. Nagashima. Pool boiling heat transfer in microgravity: experiments with CFC-113 and water utilizing a drop shaft facility. *JSME International Journal Series B Fluids and Thermal Engineering*, 39(4):798–807, 1996.

[79] W. A. Olsen. Experimental and analytical investigation of interfacial heat and mass transfer in a pressurized tank containing liquid hydrogen. *NASA Technical Note*, TN D-3219, 1966.

[80] V. V. Osipov, M. J. Daigle, C. B. Muratov, M. Foygel, V. N. Smelyanskiy, and M. D. Watson. Dynamical model of rocket propellant loading with liquid hydrogen. *Journal of Spacecraft and Rockets*, 48(6):987–998, 2011.

[81] C. H. Panzarella and M. Kassemi. On the validity of purely thermodynamic descriptions of two-phase cryogenic fluid storage. *Journal of Fluid Mechanics*, 484:41–68, 2003.

[82] C. H. Panzarella and M. Kassemi. Self-pressurization of large spherical cryogenic tanks in space. *Journal of spacecraft and rockets*, 42(2):299–308, 2005.

[83] C. H. Panzarella and M. Kassemi. Comparison of several zero-boil-off pressure control strategies for cryogenic fluid storage in microgravity. *Journal of Propulsion and Power*, 25(2):424–434, 2009.

[84] F. Perez, S. Z. Al Ghafri, L. Gallagher, A. Siahvashi, Y. Ryu, S. Kim, S. G. Kim, M. L. Johns, and E. F. May. Measurements of boil-off gas and stratification in cryogenic liquid nitrogen with implications for the storage and transport of liquefied natural gas. *Energy*, 222:119853, 2021.

[85] R. Raj, J. Kim, and J. McQuillen. Pool boiling heat transfer on the international space station: experimental results and model verification. *Journal of Heat and Mass Transfer*, 134(10), 2012.

[86] Y. Renardy and M. Renardy. PROST: A parabolic reconstruction of surface tension for the volume-of-fluid method. *Journal of Computational Physics*, 183(2):400–421, 2002.

[87] E. Ring. *Rocket Propellant and Pressurization Systems*. Prentice-Hall International Series in Space Technology, 1964.

[88] F. Rossetti, M. Pizzarelli, R. Pellegrini, E. Cavallini, and M. Bernardini. Setup of a numerical methodology for the study of active-pressurization of cryogenic tanks. In *Aerospace Europe Conference 2023 - 10^{th} EUCASS - 9^{th} CEAS*, 2023.

[89] F. Rossetti, M. Pizzarelli, R. Pellegrini, E. Cavallini, and M. Bernardini. Setup of a numerical methodology for the study of self-pressurization of cryogenic tanks. *Submitted to Cryogenics*, 2023.

[90] F. Rossetti, M. Pizzarelli, R. Pellegrini, E. Cavallini, and M. Bernardini. Development of a numerical methodology for the simulation of active-pressurization of cryogenic tanks. *Submitted to Cryogenics*, 2024.

[91] W. H. Roudebush. An analysis of the problem of tank pressurization during outflow. *NASA Technical Note*, TN D-2585, 1965.

[92] S. I. Sandler. *Chemical and Engineering Thermodynamics.* John Wiley and Sons, 1989.

[93] V. SB, S. Bhowmick, and B. T. Kuzhiveli. Experimental and numerical investigation of stratification and self pressurization in a high pressure liquid nitrogen storage tank. *Energy Sources, Part A: Recovery, Utilization, and Environmental Effects*, 44(1):2580–2594, 2022.

[94] H. Scheufler and J. Gerstmann. Heat and mass transfer in a cryogenic tank in case of active-pressurization. *Cryogenics*, 121:103391, 2022.

[95] R. W. Schrage. *A theoretical study of interphase mass transfer.* Columbia University Press, 1953.

[96] M. Seo and S. Jeong. Analysis of self-pressurization phenomenon of cryogenic fluid storage tank with thermal diffusion model. *Cryogenics*, 50(9):549–555, 2010.

[97] M. Shahid, B. Chambers, and S. Sankarasubramanian. Methane and oxygen from energy-efficient, low temperature in situ resource utilization enables missions to Mars. *AIChE Journal*, page e18010, 2023.

[98] T.-H. Shih, W. W. Liou, A. Shabbir, Z. Yang, and J. Zhu. A new $k-\varepsilon$ eddy viscosity model for high reynolds number turbulent flows. *Computers & Fluids*, 24(3):227–238, 1995.

[99] J. Sim, C.-K. Kuan, and W. Shyy. Simulation of spacecraft fuel tank self-pressurization using Eulerian-Lagrangian method. In *49th AIAA Aerospace Sciences Meeting including the New Horizons Forum and Aerospace Exposition*, page 1318, 2011.

[100] D. Sivolella. *To orbit and back again: how the space shuttle flew in space.* Springer Science & Business Media, 2013.

[101] M. Stewart. Pressurization of a flightweight, liquid hydrogen tank: Evaporation & condensation at the liquid/vapor interface. In *53rd AIAA/SAE/ASEE Joint Propulsion Conference*, page 4916, 2017.

[102] M. Stewart and J. P. Moder. Self-pressurization of a flightweight, liquid hydrogen tank: simulation and comparison with experiments. In *52nd AIAA/SAE/ASEE Joint propulsion conference*, page 4674, 2016.

[103] R. Stochl, J. Maloy, P. Masters, and R. DeWitt. Gaseous-helium requirements for the discharge of liquid hydrogen from a 1.52-meter- (5-ft-) diameter spherical tank. *NASA Technical Note*, NASA TN D-5621, 1970.

[104] R. Stochl, J. Maloy, P. Masters, and R. DeWitt. Gaseous-helium requirements for the discharge of liquid hydrogen from a 3.96-meter- (13-ft-) diameter spherical tank. *NASA Technical Note*, NASA TN D-7019, 1970.

[105] R. Stochl, P. Masters, R. DeWitt, and J. Maloy. Gaseous-hydrogen requirements for the discharge of liquid hydrogen from a 1.52-meter- (5-ft-) diameter spherical tank. *NASA Technical Note*, NASA TN D-5336, 1969.

[106] R. Stochl, P. Masters, R. DeWitt, and J. Maloy. Gaseous-hydrogen requirements for the discharge of liquid hydrogen from a 3.96-meter- (13-ft-) diameter spherical tank. *NASA Technical Note*, NASA TN D-5387, 1969.

[107] J. Straub. Microscale boiling heat transfer under 0g and 1g conditions. *International journal of thermal sciences*, 39(4):490–497, 2000.

[108] J. Straub. Origin and effect of thermocapillary convection in subcooled boiling: observations and conclusions from experiments performed at microgravity. *Annals of the New York Academy of Sciences*, 974(1):348–363, 2002.

[109] B. Sundén and J. Fu. *Heat transfer in aerospace applications*. Academic Press, 2016.

[110] W. Sutherland. LII. The viscosity of gases and molecular force. *The London, Edinburgh, and Dublin Philosophical Magazine and Journal of Science*, 36(223):507–531, 1893.

[111] W. Tam, P. Behruzi, and D. Jaekle. Propellant management devices-functional design methodologies and verifications. In *Space Propulsion 2018*, 2018.

[112] N. Van Dresar, C. Lin, and M. Hasan. Self-pressurization of a flightweight liquid hydrogen tank: Effects of fill level at low wall heat flux. In *30th Aerospace Sciences Meeting and Exhibit*, page 818, 1992.

[113] L. Wang, Y. Li, C. Li, and Z. Zhao. CFD investigation of thermal and pressurization performance in LH2 tank during discharge. *Cryogenics*, 57:63–73, 2013.

[114] L. Wang, Y. Li, Z. Zhao, and Z. Liu. Transient thermal and pressurization performance of LO2 tank during helium pressurization combined with outside aerodynamic heating. *International Journal of Heat and Mass Transfer*, 62:263–271, 2013.

[115] L. Wang, Y. Li, Z. Zhao, and J. Zheng. Numerical investigation of pressurization performance in cryogenic tank of new-style launch vehicle. *Asia-Pacific Journal of Chemical Engineering*, 9(1):63–74, 2014.

[116] Z. Wang, A. Sharafian, and W. Mérida. Thermal stratification and rollover phenomena in liquefied natural gas tanks. *Energy*, 238:121994, 2022.

[117] W. Ward, L. Toole, C. Ponder, M. Meadows, C. Simmons, J. Lytle, J. McDonald, and B. Kavanaugh. Evaluation of AS-203 low-gravity orbital experiment. *NASA Contractor Report*, CR-94045:13, 1967.

[118] N. H. Weber and M. E. Dreyer. Depressurization induced vapor bubble growth in liquid methane during microgravity. *Cryogenics*, 134:103716, 2023.

[119] D. C. Wilcox et al. *Turbulence modeling for CFD*, volume 2. DCW industries, 1998.

[120] M. Wolfshtein. The velocity and temperature distribution in one-dimensional flow with turbulence augmentation and pressure gradient. *International Journal of Heat and Mass Transfer*, 12(3):301–318, 1969.

Appendix A

Derivation of the formula to compute the thermal expansion coefficient from the NIST Chemistry WebBook properties

In the following section, the formula to compute the thermal expansion coefficient from the NIST Chemistry WebBook [65] properties is derived from the thermodynamic relations presented in [92]. It is possible to start from the relation for the speed of sound, a:

$$a^2 = \frac{c_p}{c_v}\left(\frac{\partial p}{\partial \rho}\right)_T \tag{A.1}$$

and, using the definition of specific volume, $v = \frac{1}{\rho}$:

$$a^2 = -\frac{c_p}{c_v}v^2\left(\frac{\partial p}{\partial v}\right)_T \tag{A.2}$$

The isothermal compressibility, κ_T, si defined as:

$$\kappa_T = -\frac{1}{v}\left(\frac{\partial v}{\partial p}\right)_T \tag{A.3}$$

The definition of κ_T can be replaced in Eq. (A.2), obtaining:

$$a^2 = \frac{c_p}{c_v}\frac{v}{\kappa_T} \tag{A.4}$$

Using the first principle of thermodynamics, and considering the internal energy and entropy as a function of pressure and specific volume, the following expression is given:

$$c_p - c_v = vT\frac{\beta^2}{\kappa_T} \tag{A.5}$$

Replacing Eq. (A.5) in Eq. (A.4), one has:

$$a^2 = c_p\left(\frac{c_p}{c_v} - 1\right)\frac{1}{T\beta^2} \tag{A.6}$$

From the last relation the expression of the thermal expansion coefficient can be derived:

$$\beta = \sqrt{\frac{c_p}{T}\left(\frac{c_p}{c_v} - 1\right)} \cdot \frac{1}{a} \tag{A.7}$$

The latter expression can be used to compute β starting from c_p, c_v, and a values, taken from the NIST Chemistry WebBook.

Acknowledgements

As the end of my academic journey as a student has come, I would like to take this opportunity to acknowledge and thank those who have believed in me, and have supported me in these beautiful and challenging years.

First and foremost, my thanks go to my supervisor, Prof. Bernardini, to my co-supervisor, Eng. Pizzarelli, and to Prof. Stella for all their scientific support, and for being an example both professionally and personally.

Next, I want to express my gratitude to my mom and sister, who supported me throughout my academic career, pushing me beyond the limits I set for myself, and always believing in my potential.

Then, I want to dedicate a special thought to my father, who I am certain would be very proud of me today.

I also want to say a special thanks to my husband, Simone, who is an endless source of love, patience, support, and joy in my life.

Thanks also to my husband's family, Gisella, Roberto, and Matteo, who welcomed me into their home and stood by me, especially when I needed it most.

Thanks to my best friend, Giorgia, who makes me feel her closeness, affection, and support even from many miles away. It has been an immense pleasure to share most of my academic journey with you!

I also want to say thank you to my "adoptive grandmother", Rosi, who has been one of the greatest supporters of my engineering career when everyone saw me as a future doctor. Thank you for caring about every single exam, and for encouraging me not to give up on the toughest days of my journey.

I then express my gratitude to my senior colleagues, Matteo and Giacomo, for being exemplary models to learn from and also very sensitive and helpful friends. Thanks also to my junior colleagues, Lorenzo, Marco, and Daniel, for bringing enthusiasm and vitality to our research group.

Finally, I want to thank the Italian Space Agency for the financial support.

This research was jointly funded by Sapienza University and the Italian Space Agency — Agenzia Spaziale Italiana (ASI) as part of the research project: "Technical Assistance for launchers and propulsion" N.2019-4-HH.0 carried out under a framework research agreement CUP:F86C17000080005.

Francesca Rossetti, Rome, January 2024